Nonlinear frequency conversion in fiber lasers

Svane, Ask Sebastian

Publication date:
2015

Document Version
Publisher's PDF, also known as Version of record

Nonlinear frequency conversion in fiber lasers

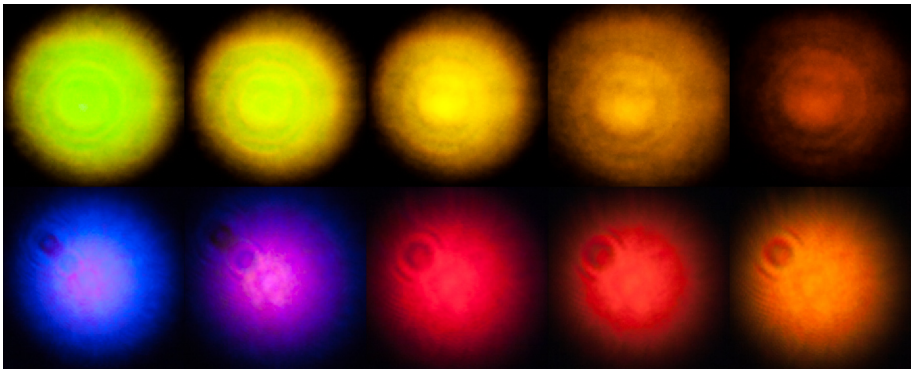

A dissertation
submitted to the Department of Photonics Engineering
at the Technical University of Denmark
in partial fulfillment of the requirements
for the degree of
philosophiae doctor

Ask Sebastian Svane
January 5, 2015

DTU Fotonik
Department of Photonics Engineering
Technical University of Denmark

Til Anton, Solveig og Line

If we knew what we were doing,
it wouldn't be called research,
would it?

- ALBERT EINSTEIN

Abstract

The concept of nonlinear frequency conversion entails generating light at new frequencies other than those of the source light. The emission wavelength of typical fiber laser systems, relying on rare-earth dopants, are constrained within specific bands of the infrared region. By exploiting nonlinear processes, light from these specific wavelength bands can be used to generate light at new frequencies otherwise not obtainable by rare-earth elements.

This thesis describes work covering Raman fiber lasers (RFLs) and amplifiers for nonlinear frequency down-conversion, and also the method of fiber-optic Cherenkov radiation (FCR) using ultrafast pulses as a means for generating tunable visible (VIS) light at higher frequencies.

Two different polarization maintaining (PM) RFL cavities are studied with an emphasis on stability and spectral broadening. The cavities are formed by inscription of fiber Bragg gratings (FBGs) in a PM Raman fiber. Active temperature control feedback of the cavity resonators is investigated as a means for obtaining a high degree of power and spectral stability. The impact of accurate cavity resonator alignment upon the RFL stability and emission characteristics is investigated and a highly stable PM RFL emitting at 1679 nm with a narrow spectral emission bandwidth is demonstrated. A driftless output was obtained for an output power of 680 mW at a 29 pm linewidth while having high output power and spectral stability; with a sub-pm standard deviation in the emission wavelength and linewidth. Subsequently, the RFL is used for the demonstration of a Raman amplifier, for which both the gain and noise characteristics in the vicinity of 1800 nm wavelength are examined.

The VIS FCR source can be considered for a broad range of applications in the field of biophotonics. FCR emission is characterized by a high temporal and spatial coherence, short temporal pulse duration, a tunable emission wavelength in the tens of nanometer range, along with a potential for having very low noise properties. The pursuit of a compact, portable, and robust VIS FCR source, suitable for applications outside of the optical lab, defined the work on an all fiber based system. Experimentally, the generation of VIS light using the FCR process is demonstrated in both uniform and tapered nonlinear fibers. VIS emission from the blue to the red parts of the VIS spectrum is demonstrated; extending across a 430 to 610 nm wavelength range for output powers up to 2 mW. Utilization of tapered nonlinear fibers resulted in a substantial increase in the obtainable wavelength tunability, with an increase from 20 to 118 nm, when compared to the results obtained for uniform nonlinear fibers.

Resumé

Den danske titel på projektet er: *Ikke-lineær frekvens konvertering i fiber lasere*

Konceptet for ikke-lineær frekvenskonvertering omfatter skabelsen af lys ved andre frekvenser end dem udsendt af den oprindelige lys kilde. Den typiske bølgelængde fra fiber laser systemer, der beror på sjældne jordartsdotering, er begrænset til specifikke bølgelængde-domæner i det infrarøde område. Lys fra disse specifikke bølgelængde-områder kan, ved at udnytte ikke-linære processer, blive omdannet til lys i nye frekvens-områder der ellers ikke er tilgængelige for lasere der beror på dotering med sjældne jordarter.

Denne afhandling beskriver arbejdet med at afdække egenskaber af Raman fiber lasere (RFLer) og til ikke-lineær frekvens ned-konvertering, og metoden for fiberoptisk Cherenkov stråling (FCS) ved brug af ultra hurtige pulser som et middel til at generere justerbart synligt lys (VIS) ved høje frekvenser.

To forskellige polarisationsbevarende (PB) RFL kaviteter bliver undersøgt med fokus på stabilitet og spektral forbredning. Kaviteterne er dannet ved at indskrive to fiber Bragg fibergittre (FBGer) i en PB Raman fiber. Aktiv temperatur styring af kavitetsresonatorerne bliver undersøgt som en metode til at opnå stabilitet af både udgangseffekt og spektrum. Virkningen af nøjagtig kavitetsresonator-tilpasning på RFL stabilitets- og emissionskarakteristika undersøges, og en meget stabil PB RFL, der udsender lys ved en 1679 nm bølgelængde med en smal spektral emissions båndbredde, demonstreres. En stabil laser blev opnået med en udgangseffekt på 680 mW og en 29 pm spektral linjebredde. Den høje udgangseffekt og spektrale stabilitet blev opnået med en sub-pm standardafvigelse i emissionsbølgelængden og linjebredden. RFL er efterfølgende anvendt til demonstration af en Raman forstærker, som karakteriseres for både forstærkning og støjegenskaber i nærheden af 1800 nm.

En VIS FCS kilde kan komme i betragtning til en bred vifte af anvendelser inden for biofotonik. FCS er karakteriseret ved en høj tidsmæssig og rumlig kohærens, kort tidsmæssig impulsvarighed, en variabel emissionsbølgelængde i nanometer området, sammen med et potentiale for at have meget lave støj egenskaber. Fokus på skabelsen af en kompakt, bærbar og robust VIS FCS kilde, egnet til anvendelser uden for det optiske laboratorium, definerede arbejdet på et rent fiber-baseret system. Synligt lys genereret ved hjælp af FCS processer er demonstreret i både ensartede og koniske ikke-lineære optiske fibre. VIS emission fra de blå til de røde dele af VIS-spektret, strækkende over 430-610 nm bølgelængdeområdet, er påvist for udgangseffekter op til 2 mW. Udnyttelse af koniske ikke-lineære optiske fibre resulterede i en betydelig forøgelse af båndbredden af opnåelige bølgelængder, med en stigning fra 20 til 118 nm, sammenlignet med de opnåede resultater for ensartede ikke-lineære optiske fibre.

Preface

> In the beginning there was
> nothing, which exploded
>
> Terry Pratchett

This thesis is a part of the formal requirements to obtain the Ph.D. degree at DTU Fotonik, Technical University of Denmark. The work was carried out mainly at DTU Fotonik from January 2011 to December 2014, and includes leave of absence due to paternity leave. The work relating to the manufacturing of fiber Bragg gratings was carried out at NKT Photonics A/S in Birkerød. All figures presented throughout this Thesis are made by the author unless otherwise stated.

The project was supervised by:

- Karsten Rottwitt (main supervisor), Professor, DTU Fotonik, Technical University of Denmark, Kgs. Lyngby, Denmark
- Jesper Lægsgaard (co-supervisor), Associate Professor, DTU Fotonik, Technical University of Denmark, Kgs. Lyngby, Denmark
- Xiaomin Liu (co-supervisor), Postdoc, DTU Fotonik, Technical University of Denmark, Kgs. Lyngby, Denmark

Ask Sebastian Svane
Kongens Lyngby, January 5, 2015

Acknowledgments

First of all i would like to thank my supervisors **Karsten Rottwitt**, **Jesper Lægsgaard**, **Xiaomin Liu** for their help and guidance and also for giving me the opportunity to pursue a PhD degree. Additionally, I also wish to thank **Dmitry Turchinovich** with whom I have collaborated on this project, and who also provided help with funding.

Secondly, I am indebted to everyone who helped me along the way in writing this work. In particular I would like to thank my office mates and my fellow group members for lots of cake, fun events and a good working environment.

Thirdly, I would like to acknowledge all the special people at DTU Fotonik: **Christophe Peucheret**, **Hans Christian Hansen Mulvad** and **Michael Galili** for always being ready to lend out equipment. **Christian Maibohm** for providing entertainment in the office and for rotating the coffee grinder on a daily basis. **Uffe Visbech Møller**, **Kristian Nielsen**, ***The Greek***, ***The Croatian***, and the rest of the "Bang gang" for sharing spectrometers, cleaving tiles, lab space, and other equipment. **Brian Michael Sørensen** for his help with electronics. **Jan Normann Mortensen** and the rest of the team at the mechanical workshop for bearing with me and all of my drawings. Not forgetting all of my friends at DTU for many fruitful discussions, company at the Friday bar, and for sharing both frustrations and challenges.

To **Anders Sig Olesen, Anders Mølbjerg Lund**, **Ken Lunn**, and **Casper Laur Byg** thank you for helping me burn the midnight oil and for meticulous proofreading.

I would like to express my gratitude to NKT Photonics A/S in Birkerød for providing the hollow-core and nonlinear fibers, and for allowing me use their UV laser and fiber Bragg grating facilities. Especially, I want to express my thanks to **Mikael Svalgaard** for taking time out of his busy schedule to help me. But also OFS Fitel Denmark in Brøndby and **Lars Grüner-Nielsen** for providing various optical fibers. Also a thank you to the *Otto Mønsteds Fond*, *Oticon Fonden* and *P.A. Fiskers Fond* for their financial support for various conferences.

I am deeply indebted to my family and friends for their dedicated support and for abiding with me during the stressful periods of carrying out this work.

Finally, I want to express my deepest regards to **Line** for always supporting me and for taking care of our children **Anton** and **Solveig** of whom I have seen far too little during the last few busy months.

List of publications

The work carried out during this PhD project has resulted in the following publications:

Journal publications

- Lars Søgaard Rishøj, Ask Sebastian Svane, Toke Lund-Hansen, Karsten Rottwitt, "Quantitative evaluation of standard deviations of group velocity dispersion in optical fibre using parametric amplification," Electronic Letters, Vol. 50, Issue 3, pp 199-200 (2014).
- Xiaomin Liu, Ask S. Svane, Jesper Lægsgaard, Haohua Tu, Stephen A. Boppart, Dmitry Turchinovich, "Progress in Cherenkov femtosecond fiber lasers," [in preparation].
- Ask S. Svane, Karsten Rottwitt, "Stability analysis of a PM Raman Fiber Laser at 1680 nm," [in preparation].

Conference contributions

- Xiaomin Liu, Ask Sebastian Svane, Jesper Lægsgaard, Haohua Tu, Stephen Boppart, Dmitry Turchinovich, "Tunable Femtosecond Cherenkov Fiber Laser," IEEE/ICAIT 2014, China.
- Ask Sebastian Svane, Xiaomin Liu, Jesper Lægsgaard, Haohua Tu, Stephen Boppart, Dmitry Turchinovich, "Electrically-Tunable Multi-Color Ultrafast Cherenkov Fiber Laser," CLEO US 2014, USA, 2014.
- Ask Sebastian Svane, Xiaomin Liu, Karsten Rottwitt, "Highly Stable PM Raman Fiber Laser at 1680 nm," CLEO US 2013, USA, 2013.
- Ask Sebastian Svane, Karsten Rottwitt, "Design of an 1800 nm Raman Amplifier," OSA Photonics North, Ottawa, Canada, 2013.
- Ask Sebastian Svane, Karsten Rottwitt, "Monolithic PM Raman fiber laser at 1679 nm for Raman amplification at 1810 nm," CLEO Europe 2013, Munich, Germany, 2013.
- Ask Sebastian Svane, Karsten Rottwitt, "PM Raman fiber laser at 1679 nm," Advanced Photonics Congress, Nonlinear Photonics, 2012.

- Ask Sebastian Svane, Karsten Rottwitt, "Linewidth optimization of a PM Raman Fiber laser at 1679 nm," Northern Optics, Snekkersten, Denmark, 2012.

Conference contributions outside the scope of this thesis

- Ask Sebastian Svane, Toke Lund-Hansen, Karsten Rottwitt "Wavelength Conversion by Cascaded FWM in a Fiber Optical Parametric Oscillator," Optical Fiber Communication Conference/National Fiber Optic Engineers Conference (OFC/NFOEC), 2011.

- Toke Lund-Hansen, Karsten Rottwitt, Christophe Peucheret, Zohreh Lali-Dastjerdi, Lars Søgaard Rishøj, Ask Sebastian Svane, Lasse Mejling Andersen, Valentina Cristofori, "Pump to signal noise transfer in parametric fiber amplifiers," 10th International Conference on Fiber Optics and Photonics, 2010.

Pending Patent Applications

- Jesper Lægsgaard, Dmitry Turchinovich, Xiaomin Liu, Ask S. Svane, "Wavelength-tunable laser based on nonlinear dispersive-wave generation in a tapered optical waveguide," European Patent Application No. 14171513.6, June 6th 2014

Contents

Chapter 1

Introduction

> Progress in science comes when experiments contradict theory.
>
> Richard Feynman

The process of *light amplification by stimulated emission of radiation*, also known by the acronym *laser*, was proposed by Albert Einstein in 1917 [1]. The optical amplification of light by stimulated emission entails the generation of a photon having the same phase, energy, polarization and direction as the initial photon.

The first demonstration of stimulated emission in 1954 [2] was in the microwave region of the electromagnetic spectrum. The theoretical groundwork for the laser was laid out in the 1950s [3], leading to the first demonstration of a laser operating at optical frequencies based on a ruby crystal by T. H. Maiman in 1960 [4]. The significance of the discovery was instantly recognized, and won the researchers the Nobel prize in Physics in 1964 [5].

The 1960's turned out to be an eventful decade in optics, where the first demonstration of light generated by a non-linear process in 1961 by Franken *et al.* [6] was followed by the demonstration of stimulated Raman scattering (SRS) in 1962 by Eckhardt *et al.* [7], and the development of the first fiber laser by Koester *et al.* in 1964 [8] and also the first demonstration of the ultrafast laser in 1966 by De Maria *et al.* [9].

1.1 Nonlinear frequency conversion in fibers

Nonlinear frequency conversion entails the concept of generating light at new frequencies other than the initial source light. The type and magnitude of the nonlinearity is dependent upon the material used and can be related the molecular structure. High electrical field strengths are required in order for the nonlinear processes to be efficient. The development of optical fibers has assisted in being able to scale up the intensity by confining light to small cross sections in the $\sim\mu\text{m}^2$-range. While the nonlinearity of silica is weak,

when compared to other glasses and crystals [10, 11], the low loss properties of silica based optical fibers enables long interaction lengths. The development of ultrafast lasers has further facilitated a wide range of spectacular processes; due to being able to concentrate the emitted light in time and thereby obtain very high intensities for extremely short durations. The shortest pulse durations created are in the attosecond (10^{-18}s) range [12]. To put this into perspective - an attosecond is to a second what a second is to twice the age of the Universe.

The typical method for constructing fiber lasers and amplifiers relies on doping the core of an optical fiber with rare-earth elements, such as Ytterbium, Erbium, Thulium, or Holmium. Optical pumping of these fibers with laser diodes can provide emission in different parts of the infrared (IR) spectrum. However, emission of such lasers is limited in wavelength by the relative absorption and emission spectrum of the dopant material. By exploiting nonlinear processes, light from these specific wavelength bands can be used to generate light at new frequencies not obtainable by rare-earth elements.

The process of second harmonic generation (SHG), which is a second order nonlinear process, enables frequency doubling of lasers and gives access to isolated emission windows based on the frequency of the pump source. For Ytterbium-based sources, which can emit from 976 to 1130 nm, this entails a frequency doubled emission wavelength between 488 and 575 nm [13]. While all silica glasses are centrosymmetric special nonlinear crystals are required for the SHG process.

The lowest order of nonlinearity in silica based fibers is the third order nonlinearity, which can give rise to the so-called *instantaneous Kerr-effect* in addition to a delayed nonlinear response [14]. The delayed nonlinear response engenders SRS and stimulated Brillouin scattering (SBS). Typically, these processes transfer energy from an optical field to another field at lower frequencies and hereby simultaneously creating vibrations in the material; through optical and acoustic phonons. While non-stimulated Raman scattering was observed in 1928 by Raman and Krishnan [15], the theory of SRS and SBS was formulated in 1965 by Shen *et al.* [16]. SRS can be utilized for amplification and thereby also be used in the construction of a laser, which will be described below. Meanwhile the Kerr effect gives rise to various nonlinear processes, such as self-phase modulation (SPM), which causes a chirp on the pulse and results in spectral broadening and the generation of new frequencies.

As many nonlinear processes are dependent on high spatial confinement in addition to accurate dispersion control, new possibilities have emerged with the development of endlessly single mode photonic crystal fibers (PCFs) in the end of the 1990s [17, 18]. Controlling the layout of the PCF microstructure enables engineering of the fiber dispersion, which in turn enables a range of applications in the field of nonlinear optics. Accurate control of microstructuring has resulting in intriguing concepts such as the photonic bandgap effect in optical fibers, which have enabled the guiding of light in air inside a hollow-core (HC) fiber [19].

This thesis describes work covering Raman fiber lasers and amplifiers for nonlinear frequency down-conversion, and also presents the method of fiber-optic Cherenkov radiation (FCR) using ultrafast pulses as a means for gener-

ating tunable visible (VIS) light at higher frequencies.

1.2 Raman fiber laser and amplifier

The development of the low loss silica transmission fiber in the 1970s [20, 21] marked the beginning of a continued and rapid growth in global telecommunication [22]. From the mid-1970s the record data transmission increased by a factor of 10 every 4^{th} year, owing to the development of optical rare-earth doped fiber amplifiers, wavelength-division multiplexing (WDM), and high-spectral efficiency encoding. Over the last decade we have reached, within a factor of two, the so-called nonlinear Shannon limit, which effectively limits the obtainable spectral efficiency of transmission systems using current technology [22]. Within the last 5 years the global IP traffic has increased fivefold, and a threefold growth is predicted over the next 5 years; with a projected annual global IP traffic exceeding 1 zettabyte (10^{12} GB) during the year 2016 [23]. To address the forthcoming capacity crunch, different approaches are being explored to enable further scaling in the capacity of transmission systems. While current transmission systems have exhausted the gain bandwidth of the Erbium doped fiber amplifier (EDFA), other degrees of freedom are being investigated. One approach that is being pursued, is the concept of spatial multiplexing, which has been demonstrated using multi-core fibers [24], higher-order mode (HOM) [25], and orbital angular momentum (OAM) [26].

Extending the bandwidth of the transmission system is another approach that could potentially scale the transmission performance further. This would require both new methods of amplifications and transmission; as the current transmission window is dictated by the low loss region of silica fibers and the gain bandwidth of current EDFAs.

For continuous wave (CW) operation, SRS can be used as a gain medium for an oscillator or amplifier. Raman lasers have been studied extensively since the first demonstration of stimulated Raman scattering (SRS) in the beginning of the 1960s [7, 27]. Forming a laser cavity by the inscription of fiber Bragg gratings (FBGs) allows precise control of the emission wavlength, and was demonstrated for the first time by Kean *et al.* in 1988 [28]. The development of cascaded Raman fiber lasers (RFLs) was initially motivated by telecommunication applications and the lack of available pump sources between the Ytterbium and Erbium band. In 1995 Grubb *et al.* [29] demonstrated a 5^{th} order RFL emitting at 1480 nm wavelength and pumped by a 1117 nm Ytterbium based pump source.

In an effort to extend the usable bandwidth of an optical communication system, there is a drive to move towards wavelengths longer than the conventional 1.55 μm band [30]. The measured transmission losses for different optical transmission fibers are shown in fig. 1.1. It is evident that the low-loss minimum of silica based optical fibers is conveniently located in the center of the Erbium amplification band stretching across the C-band (1530-1565 nm) and L-band (1565-1625 nm). However, the transmission loss in silica based fibers increases dramatically with increasing wavelengths; due to the increase in IR absorption loss. The theoretical low loss limit for HC PCFs is shown for

comparison in fig. 1.1 [31], and presents a wide potential transmission range. Utilization of SRS would allow for the construction of lasers and amplifiers within this range, thus bridging the gap between the Erbium and the Thulium amplification bands.

This work investigates a polarization maintaining (PM) RFL pumped in the Erbium band and emitting at a 1679 nm wavelength. Different laser cavity designs are studied with the emphasis on stability. Subsequently, the 1679 nm RFL is used to characterize a Raman amplifier (RA) with a peak gain at 1810 nm.

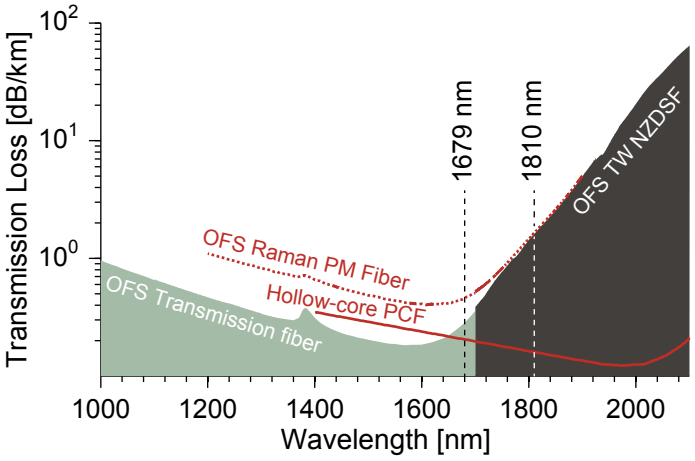

Figure 1.1: Comparison of the transmission loss for various fibers. The transmission of the OFS Transmission fiber *is reproduced from [32] and the predicted low loss limit for the hollow core fiber is reproduced from [31].*

1.3 Tunable visible Cherenkov laser

Accelerated by the development of PCFs [33] and advances in mode-locked all-fiber laser systems [34, 35], the supercontinuum (SC) source has matured into a commercially available product [36], which is now found on many lab benches and implemented in turnkey systems e.g. in biology labs. They are often high power system emitting several Watts of power spanning more than two octaves, but many applications only require selected wavelength bands/-lines. Therefore, the output must be filtered and only a fraction of the light utilized. An alternative and more efficient approach would be to only generate the wavelength desired. One solutions is to rely on VIS FCR and tune the wavelength of emission by controlling the pump laser and fiber geometry. FCR is the leakage of radiation across a zero-dispersion wavelength and arises by propagation of ultrashort pulses in suitable fibers (often PCFs).

The generation of FCR is a way to generate highly coherent light, potentially emitted as a single ultrafast pulse, with the possibility of very low noise properties. Advances in mode-locked fiber laser technology has enabled compact

pump sources, and recent fiber laser pumped FCR systems have demonstrated selective tunability across tens of nanometers in the VIS [37, 38]. While SC sources are currently used for various spectroscopy and imaging techniques, the above mentioned properties of the FCR emission makes these sources highly attractive and competitive for a wide range of applications in biophotonics.

The FCR source relies on an ultrafast femtosecond pump source along with a nonlinear fiber having anomalous dispersion characteristics. The emission wavelength is dictated by phase-matching, which can be controlled by utilizing an appropriate fiber design, i.e. dispersion engineering of the nonlinear PCF.

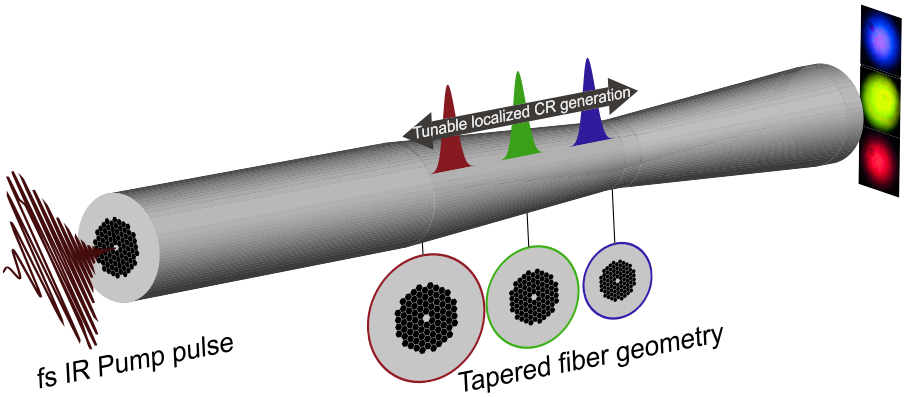

Figure 1.2: Illustration of the concept behind the tunable VIS FCR source.

To increase the wavelength tunability of current fiber based FCR an improved design is proposed. The concept of the tunable VIS Cherekov laser is outlined in fig. 1.2. The source relies on a tapered PCF, allowing a longitudinal variation in the fiber dispersion along the length of the fiber. The increased tunability is obtained by controlling the pump pulse parameters for a femtosecond pump pulse and by exploiting the localized nature of the pump pulse compression. Controlling the point of pump pulse compression along the taper structure, allows control of the FCR phase matching and hence also the FCR emission wavelength.

In this work a mode-locked Ytterbium based fiber laser is described, capable of emitting tunable femtosecond pulses, which is used to generate FCR in both uniform and tapered nonlinear fibers.

1.4 Project overview

When the work concerning this thesis was commenced in January 2011, the project was titled “Infrared fiberlaser utilising novel semiconductor optical fibers,” with the aim of characterizing and utilizing Silicon based optical fibers for Raman fiber lasers, that were manufactured by the group of John Ballato at Clemson University in South Carolina. The work was motivated by the strong nonlinear properties of Silicon combined with the prospect of integration using a fiber platform.

The project proposal relied on the utilization of silicon based optical fibers for the gain medium in a Raman fiber laser. The first stage of the Raman fiber laser was to be constructed using a silica host fiber, for the initial frequency down-conversion from the Erbium band around a 1550 nm wavelength. However, it turned out that the manufacturing and characterization of these fibers, which were to be manufactured at Clemson University USA, using the molten core drawing technique [39, 40], remained at a fundamental level.

While the work on improving the quality and transmission of the Silicon fibers at Clemson progressed, the work involving the construction and characterization of the first stage of the Raman fiber laser was initiated at DTU Fotonik. In the meantime, the development of Silicon based fibers was eventually superseded by the work done in the group of Anna Peacock at University of Southampton [40–47], where the nonlinear properties of said fiber structures were studied in detail. Due to the lack of available samples from University of Clemson, USA, the project was redefined in August 2013, focusing on the topic of nonlinear frequency conversion, and commencement of work on femtosecond fiber lasers and generation of VIS FCR was initiated.

1.5 Organization of the thesis

The thesis is divided into two parts; **part I** (chapters 2 and 3) concerning the work relating to Raman fiber lasers and amplifiers for nonlinear frequency down-conversion and **part II** (chapters 4 to 6) pertaining to the work performed on ultrafast femtosecond fiber lasers for creating visible light using fiber-optic Cherenkov generation.

Chapter 2 describes the theory governing fiber Bragg gratings (FBGs) along with the inscription method of ultraviolet (UV) induced index change in silica based fibers using a phase-mask. The experimental results are described with emphasis on manufacturing and characterizing FBGs for defining a Raman fiber laser (RFL) cavity.

Chapter 3 describes the experimental results for the RFLs investigated. Two different cavity designs are described and examined. Subsequently, a study of the power and spectral stability of the RFL emission is presented. The RFL is used for constructing a Raman amplifier (RA), leading to an investigation of the RA gain, noise, and polarization properties.

Chapter 4 introduces the passively-modelocked femtosecond pump source that is used in the subsequent experiments concerning the generation of fiber-optic Cherenkov radiation (FCR). The different pulse characterization techniques which are used for the characterization of the said source are introduced. The femtosecond oscillator is described along with the all-fiber based chirped pulse amplification (CPA) system. A detailed characterization of the emitted pump pulses is also presented for two different hollow-core (HC) compression fibers, in addition to the obtainable degree of tunability of the final pulse duration. Finally, the results of the work involved in replicating the femtosecond laser oscillator are described.

Chapter 5 presents the theory underpinning FCR generation. The concept of solitons and pump pulse compression is reviewed along with a brief description of different types of noise governing both FCR and supercontinuum (SC) generation. The FCR phase-matching is described along with estimates of the expected emission range. The numerical results relating to generation of FCR in both uniform and tapered fibers are also presented and discussed. Finally, the fundamental differences and limitations associated with generation of FCR in different taper structures is discussed.

Chapter 6 reviews the experimental results obtained for the generation of visible (VIS) FCR in uniform and tapered fibers. The VIS FCR emission is characterized and compared for different taper geometries with an emphasis on increasing the wavelength tunability.

Chapter 7 concludes the thesis with a summary of the most important conclusions and a presentation of recommendations for continuation of research in this area.

A list of acronyms is included in the appendix on page 129. The acronyms are defined the first time they are used in each chapter. Appendices A to D which mainly contains additional figures and supplementary information are included before the bibliography.

Part I

Continuous wave Raman fiber laser and amplifier

Chapter 2

Fiber Bragg gratings

> Only two things are infinite, the universe and human stupidity, and I'm not sure about the former.
>
> Albert Einstein

The method of inscribing fiber Bragg gratings (FBGs) in optical fibers is instrumental to the manufacturing of Raman fiber lasers (RFLs). The following section deals with the theory and manufacturing of FBGs inscribed by the method of ultraviolet (UV) induced index change in germanium doped silica based optical fibers. The emphasis of this chapter lies on the inscription of suitable gratings for the RFL described in chapter 3.

2.1 Theory and background

This section deals with the theory underpinning fiber Bragg gratings. Distributed Bragg reflectors are used in optical waveguides such as optical fibers, but are also used in solid state structures. Semiconductor based Bragg gratings are widely used in high performance optical devices such as the compact vertical-cavity surface-emitting laser (VCSEL), along with the semiconductor saturable absorber mirror (SESAM) which is used for passive mode-locking. In solid state materials, Bragg gratings are formed by creating stacks of alternating layers of material with different effective refractive index, such as GaAs and AlGaAs. At the boundary between the two materials light is reflected following the Fresnel equations. Depending on thickness of the respective layers, light at the proper frequency will interfere constructively or destructively, leading to distributed reflection.

FBGs relies on the same principle of distributed reflection. While the principle is the same, the manufacturing of FBG in silica fibers relies on modulating the refractive index of the glass core by exploiting the method of UV-induced index change, demonstrated for the first time in an optical fiber by Hill *et al.*

in 1978 [48]. The permanent modulation of the refractive index of the fiber core is termed photosensitivity, and depends on the glass composition of the host fiber. While the induced index change is orders of magnitude lower than what can be obtained when alternating between semiconductor materials, very strong gratings can be manufactured by inscribing long FBG structures. In 1989, Meltz *et al.* [49] demonstrated photosensitivity in a germanium doped fiber when exposed to UV light between 240 and 250 nm. For the *Hill experiment* in 1978 [48] two-photon absorbtion at 240 nm is believed to be responsible for the inscribed grating [50]. The mechanism behind the UV sensitivity has been studied in great detail, and is related to a GeO defect with a $\sim$240 nm absorption peak [51]. Models describing the photosensitivity include the color-center-model [52, 53] and the compaction model [54]. Subsequently, fiber bragg gratings have been researched extensively during the 1990s, in particular motivated by the applications within telecommunications, both theoretically and experimentally [55–59]. The most widely used method for manufacturing of fiber Bragg gratings structures is using a UV laser between 240 and 250 nm, by either point by point inscription [60] or by the phase mask technique [61–63].

Type-I gratings are in the mm to cm length range and contain a 10^{-6} to 10^{-3} index modulation, while spanning spectral bandwidths from a few GHz and up to a few hundred GHz [64]. Type-II gratings on the other hand, have mm or sub-mm length with index modulations between 10^{-3} to 10^{-2} with spectral widths up to the THz range.

Uniform grating structures that have a constant pitch and an average index profile, can be described analytically based on coupled-mode theory. More complex non-uniform grating structures, e.g. containing either apodization profiles, chirp or discrete π phase shift or superstructures, are typically described using the transfer matrix formalism [65]. In this chapter the focus is centered on the specific application of inscribing FBGs for RFLs; this includes a description of uniform FBGs along with apodization profiles.

2.1.1 Induced index shape

The inscription of fiber gratings in optical fibers, relies on doping with a photosensitive material, such as germanium, but other photo-sensitive materials include cerium [66]. Typical optical fibers relies on Germanium to increase the refractive index of the core, which has a higher refractive index than silica. Increasing the mol. % of GeO_2 in a silica host fiber can increase the mode-confinement, but offers also higher non-linearity and increased UV induced refractive index change. Typical values for the index modulation ranges between 10^{-6} and 10^{-3}. The UV sensitivity of a fiber can be increased by orders of magnitude by the process of loading the fiber with either Hydrogen or Deuterium under high pressure [67]. Using this method, index modulations of the order $\delta n = 10^{-2}$ can be achieved. This is of particular importance if strong FBG structures are required. The use of Deuterium instead of Hydrogen for the loading process, shifts the induced absorption peak of OH at 1380 nm to longer wavelengths [68].

The inscribed grating structure is quasi-permanent and decays slowly with

time, with typical designed life-spans of 25 years. Annealing of the FBG can be used to "accelerate the aging of the grating", in order to remove the initial fast decay of the grating. E.g. annealing at 480 K for 1 min is similar to 25 years at room temperature [58].

Following the notation of [65] the pertubation in the effective index, when exposing a photosensitive fiber with UV light, is given by:

$$\delta n_{\text{eff}}(z) \quad = \quad \bar{n}_{\text{eff}}(z)\left(1 + v\cos\left[\frac{2\pi}{\Lambda_{\text{FBG}}}z + \phi(z)\right]\right) \tag{2.1}$$

where $\bar{n}_{\text{eff}}$ is termed the “dc” index change averaged across a grating period, $\bar{n}_{\text{eff}}(z)v\cos\left[\frac{2\pi}{\Lambda}z + \phi(z)\right]$ is the “ac” index change, v is the fringe visibility for the index change, Λ is the period, and $\phi(z)$ denotes the grating chirp.

For an optical fiber with a typical step index profile and an induced index change $\delta n_{\text{co}}(z)$, it is given that $\delta n_{\text{eff}}(z) \simeq \Gamma\delta n_{\text{co}}(z)$, where Γ is the power confinement factor. The power confinement depends on the particular mode and can be calculated from the fiber parameters.

2.1.2 Phase-mask method

The grating inscription can be performed using the phase-mask technique, the process of which is outlined in fig. 2.1. The phase-mask is manufactured, optimized for certain emission wavelength where the 0^{th} order is suppressed. For a phase-mask with a pitch Λ The +/- 1^{st} order diffracted beams interfere, and give rise to an interference pattern imposed on the fiber at a 2:1 ratio, such that the resulting grating period inside the fiber is $\Lambda_{\text{FBG}} = \Lambda/2$. The resulting Bragg wavelength is therefore given by:

$$\lambda_{\text{bragg}} = 2n_{\text{eff}}\Lambda_{\text{FBG}} \qquad , \tag{2.2}$$

where n_{eff} is the effective index at the design wavelength.

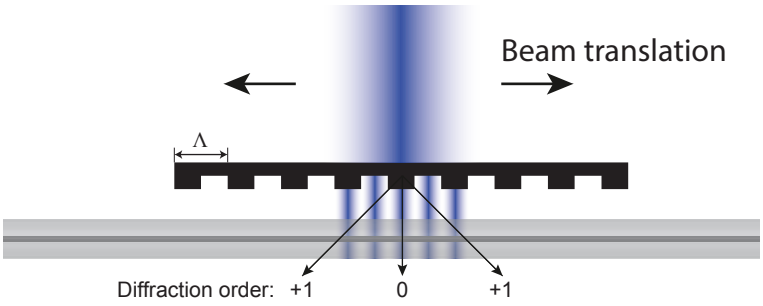

Figure 2.1: Outline of the setup used for inscription of gratings using a phase-mask along with a UV laser into a UV sensitive fiber.

2.1.3 Theoretical predictions

The theory underpinning FBGs is described extensively in the litterature [56, 65]. The reflection and transmission characteristics for a perfect and uniform FBG, having a constant longitudinal refractive index profile, can be derived based on coupled mode theory [69]. The reflectivity of a uniform FBG can be described by [56]:

$$R(l,\lambda) = \frac{\Omega^2 \sinh^2(sl)}{\Delta k^2 \sinh^2(sl) + s^2 \cosh^2(sl)} \quad , \tag{2.3}$$

where Ω is the coupling coefficient, Δk is the detuning wave vector, λ is the wavelength, l is the grating length and s is defined by $\sqrt{\Omega^2 - \Delta k^2}$. The detuning coefficient is defined to be:

$$\Delta k \equiv k - \frac{\pi}{\Lambda_{\mathrm{FBG}}} \tag{2.4}$$

$$= 2\pi n_{\mathrm{eff}} \left(\frac{1}{\lambda} - \frac{1}{\lambda_D} \right) \quad , \tag{2.5}$$

where λ_{Bragg} is defined as the design wavelength for the FBG. The coupling coefficient, Ω, is defined by:

$$\Omega = \frac{\pi \Delta n \eta(V)}{\lambda} \quad . \tag{2.6}$$

The parameter $\eta(V)$ represents the fraction of the integrated fundamental-mode intensity contained in the core (see appendix A.7). In the case of no

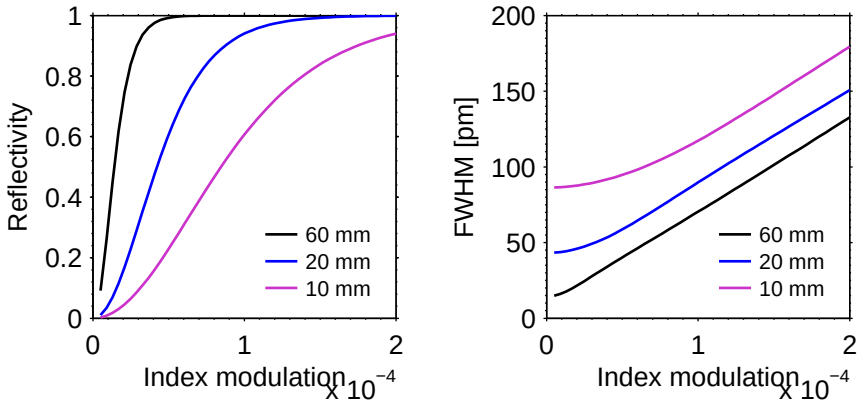

Figure 2.2: ***(left)*** *Calculated grating reflectivity for a uniform FBG for three different grating lengths and calculated for different index modulation strengths.* ***(right)*** *Spectral grating full-width half maximum (FWHM) calculated for three different grating lengths and for varying index modulation strength.*

wave-vector detuning, the reflectivity is given by:

$$R(l,\lambda) = \tanh^2(\Omega l) \quad , \tag{2.7}$$

from which it is seen that the peak reflectivity depends simply on the product of the coupling coefficient and the grating length. The scaling in peak reflectivity and spectral bandwidth obtained for a FBG with increasing index modulation is represented in fig. 2.2.

The piecewise-uniform approach is a method that can be used to model nonuniform gratings [65]. In this process the grating is divided into m uniform sections which are each described by a single 2×2 matrix containing the field amplitudes traversing that particular segment. By this method, the transmission properties of more complex grating structures can be calculated, such as grating having a chirp, apodization or a discrete π phase-shift [65].

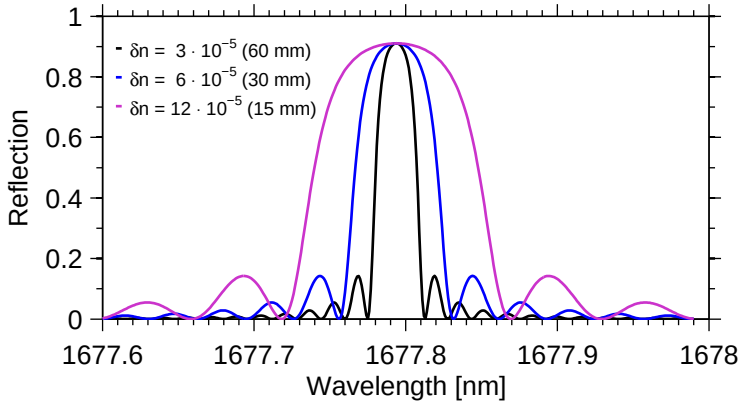

Figure 2.3: Comparison of different FBGs lengths and degrees of index modulation. Calculated for $n_0 = 1.446$ and $\Gamma = 580.15 \cdot 10^{-9}$.

For a typical type-I grating, the grating reflection spectrum (R) is complementary to the transmission spectrum (T); $R = 1 - T$ [58]. In fig. 2.3 the predicted grating reflection is shown for a constant product of $\delta n \cdot l$, yielding a constant peak reflection as predicted by eq. (2.7). Meanwhile, the spectral grating FWHM decreases with increasing grating length. The grating was calculated for typical fiber parameters for a $580.15 \cdot 10^{-9}$ nm grating pitch.

Increasing δn for a fixed grating length, increases both the reflectivity and spectral FWHM, as illustrated in fig. 2.4. As the grating strength is increased the side-lobe structure becomes more pronounced.

Apodization

Apodization of a FBG structure entails a non-uniform index modulation across the grating. Different apodization types include Gaussian-apodized, raised-cosine-apodized and chirped [65, 70].

If a Gaussian-apodization profile is introduced by varying the UV beam intensity during the FBG inscription process, the “ac” index modulation will be accompanied by a non-zero “dc” index modulation, that gives rise to a chirp in the grating structure and the formation of side-lobes in the reflectivity spectrum [65]. By applying a Gaussian or raised-cosine apodization of the

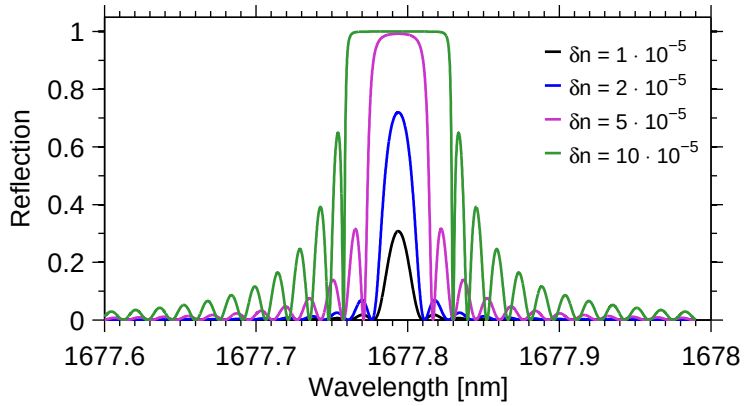

Figure 2.4: Comparison of different index modulation strengths for a long FBG. With a peak reflectivity of 30.8, 72.0, 99.2 and ≥ 99.99% reflectivity. The fiber parameters are identical to fig. 2.3.

"ac" index modulation, while the "dc" index remains constant, a strong side-lobe suppression can be ontained [71]. This can be realized experimentally by different fabrication methods [71–73]. An apodization to the "dc" and/or "ac" index can be applied intentionally or be the result of imperfections, that could originate from the phase-mask, alignment, bending of the fiber, temperature variations, and variation in the UV illumination intensity.

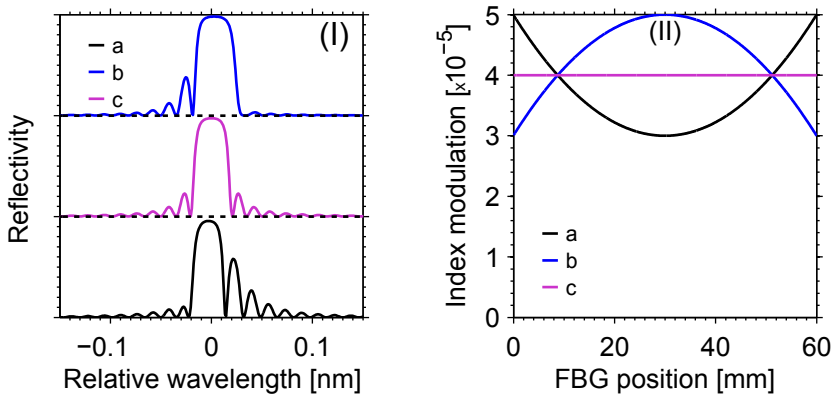

Figure 2.5: (I) Transmission for FBGs (a-c) having the different index apodization profiles shown in (II). 10% reflectivity/div. (II) Corresponding index apodization structure for the FBGs (a-c). Calculated using the transfer matrix approach for a 60 mm grating structure.

The grating reflectivity, calculated using the transfer matrix formalism, for grating having different apodization profiles are shown in fig. 2.5. The results show that variations in the index modulation along grating structure, introduces asymmetries and enhances the formation of side-lobes, on either the red or blue side of the central grating wavelength.

2.2 Inscribing fiber Bragg gratings

The experimental work on optimizing and manufacturing fiber gratings, has been performed at the facilities of NKT Photonics A/S in Birkerød. As a result this has imposed some time limitations, due to the limited availability of the required equipment. The work presented in this section was carried out across a combined duration of less than two weeks, with the purpose of writing the FBG for the RFL described in chapter 3.

2.2.1 Experimental setup and manufacturing methodology

The fiber Bragg gratings were inscribed using the phase-mask technique which was outlined in section 2.1.2, and all test gratings were inscribed in the polarization maintaining (PM) Raman specialty fiber described in section 3.3. Prior to the inscription of each grating, the fiber coating was removed along a 6-8 cm segment of the fiber using a hot solution of sulfuric acid. This method was used in stead of mechanical stripping of the coating, as removal by acid does not degrade the fiber strength for bending and stretching if the fiber is properly re-coated afterwards [74]. The acid stripping was followed by ultrasonic cleaning, before the fiber was mounted in the grating setup.

The fiber was mounted in the setup with a set pre-tension, stretching the fiber slightly, that could be adjusted to fine-tune the final grating wavelength. This ensured that the fiber was mounted completely straight below the phase-mask, as the small bends that could occur for a non-taut fiber, would potentially degrade the grating structure. Also the orientation of the phase-mask relative to the fiber was adjusted for each phase-mask, to ensure that there would be no tilt in the grating structure.

For the grating inscription a *Coherent LPX* KrF UV-excimer laser, with an 248 nm emission wavelength and nanosecond pulses operated at a 50 Hz repetition rate, with an approximate pulse energy of ∼38.5 mJ. Prior to the inscription of each grating, the UV-excimer laser would be warmed up, and the emission intensity calibrated. The gratings were typically inscribed using an intensity of ∼5.4 W/cm^2. The UV exposure is controlled by setting the specified total accumulated UV fluence for the particular grating structure, specified in J/cm^2. The UV beam which is shaped to a rectangular beam ∼2x17.7 mm, is scanned along the fiber and phase-mask during inscription, to average out the UV exposure.

2.2.2 Phase mask

The phase mask is manufactured by Ibsen photonics for the +/- 1. order with a 60 × 10 mm grating size, and is optimized for a 248 nm unpolarized laser with a 0$^{\text{th}}$ order below 3%. The phase-mask details are listed in table 2.1: From the estimated effective index of the host fiber, the design wavelength is 1564.6 nm for the gratings using phase-mask $\underline{\Lambda}_{1a}$ and $\underline{\Lambda}_{1b}$, and 1677.8 nm using phase-mask $\underline{\Lambda}_2$.

Phasemask	Phase-mask pitch [nm]	n_{eff}	Design wavelength [nm]
$\underline{\Lambda}_{1a}$	1080.5	1.448	1564.6
$\underline{\Lambda}_{1b}$	1080.5	1.448	1564.6
$\underline{\Lambda}_{2}$	1160.3	1.446	1677.8

Table 2.1: List of the utilized phase-masks.

2.2.3 Grating characterization

In fig. 2.6 the transmission profile is shown for a FBG inscribed in a D_2 loaded PM Raman fiber using phase mask $\underline{\Lambda}_2$ from table 2.1. The FBG transmission was measured using an unpolarized broadband light source, a *NKT Photonics compact SuperK*, both prior and after annealing. In fig. 2.6 a dip in the measured transmission spectrum is observed at two distinct peaks separated by 300 pm. Due to the difference in effective index for the two different principal fiber axes, the grating along the fast axis appears at a slightly lower wavelength than the grating along the slow axis. As a result a ∼3 dB transmission loss is observed for each grating when using an unpolarized source. The 300 pm wavelength shift is close to the predicted ∼325 pm wavelength shift corresponding to the $2.8 \cdot 10^{-4}$ specified fiber birefringence. It was also found that the annealing process, down-shifted the FBG central wavelength 1.87 nm, due to dissipation of the loaded D_2 gas.

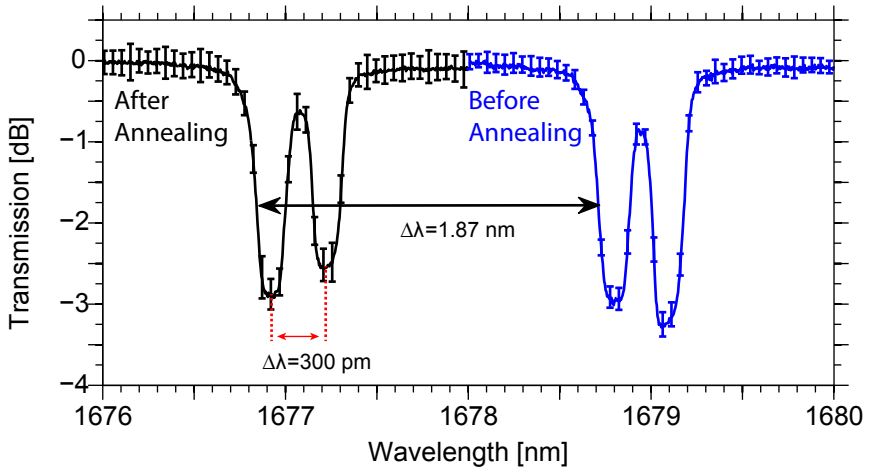

Figure 2.6: Transmission of the FBG, measured with a supercontinuum (SC) light-source, launched in both the fast and slow axis of the PM Raman fiber. Inscribed with a 50 J/cm^2 fluence in D_2 loaded fiber, using phase mask $\underline{\Lambda}_2$ at a 500 mN pre-tension. The error bars indicate the standard deviation for the measured transmission spectrum due to variations in the output power and spectrum of the SC source.

The fiber lacks rotational symmetry due to the presence of stress rods along the fiber structure. The stress rods affects the inscribed grating, depending on the fiber rotation with respect to the phase-mask and the incident UV exposure

[75]. The utilized experimental setup at NKT Photonics did not allow for active alignment of the fiber rotation prior to the grating inscription. As a result hereof, some variations between subsequent inscribed gratings are expected. However, no significant variance in the manufactured gratings were found.

To properly characterize the gratings along the principal fiber axis, the light from the broadband SC source is linearly polarized with a optical polarizer, and aligned with the appropriate principal fiber axis. To ensure a high polarization extinction ratio (PER) during the FBG characterization the PM fiber output from the polarizer is spliced directly to the FBG fiber using an *Ericsson FSU 995 PM Arc Fusion splicer*. The typical estimated PER for the splices were ∼40 dB. The measured grating transmission spectrum is shown in fig. 2.7. The inscribed grating has a central wavelength of 1677.25 nm with a 10 dB grating width of 134 pm and a peak reflection of 18 dB.

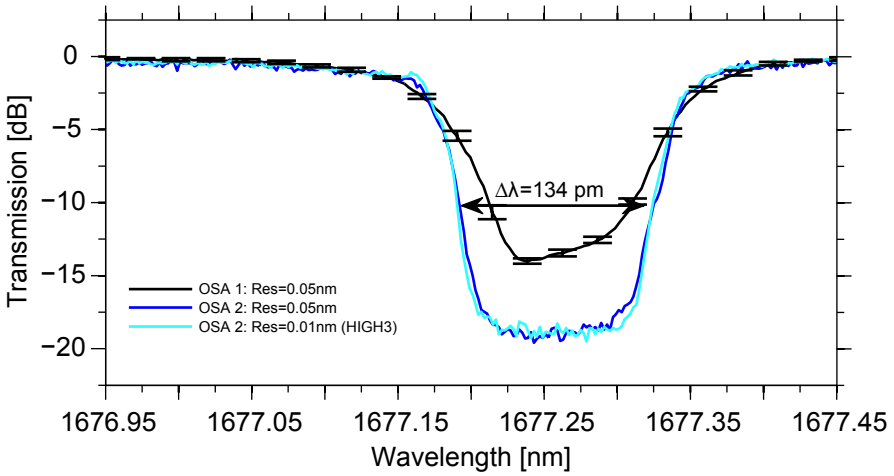

Figure 2.7: Transmission of the inscribed FBG shown in fig. 2.6, measured with a SC light-source that was linearly polarized and launched along the fast fiber axis. The figure shows measurements performed with a Yokowawa AQ-6375 optical spectrum analyzer (OSA) with a 1200 to 2400 nm measruement range (OSA 1) and an Ando AQ-6317B OSAwith a 600 to 1750 nm measurement range (OSA 2), listed along with the spectral resolution.

Due to the limited resolution of the OSA, the grating fine-structure and side-lobes described in section 2.1.3 cannot be properly resolved when using a broadband SC source. However, when using the Ando AQ-6317B OSA along with a AQ4321D tunable laser source (TLS), accurate grating characterization can be performed in the 1520 to 1620 nm wavelength range. This is done using the *TLS synchronized measurement* technique where the OSA takes control of the Ando laser, which has a sub-MHz linewidth.

2.2.4 Estimating the photo-sensitivity

For weaker *Type-I* gratings the reflectivity is complimentary to the measured transmission profile, given by $R = 1 - T$. The measured grating reflectivity

is plotted for 5 different individual gratings in fig. 2.8, inscribed using $\underline{\Lambda}_{1a}$ for different UV fluences and measured both before and after annealing.

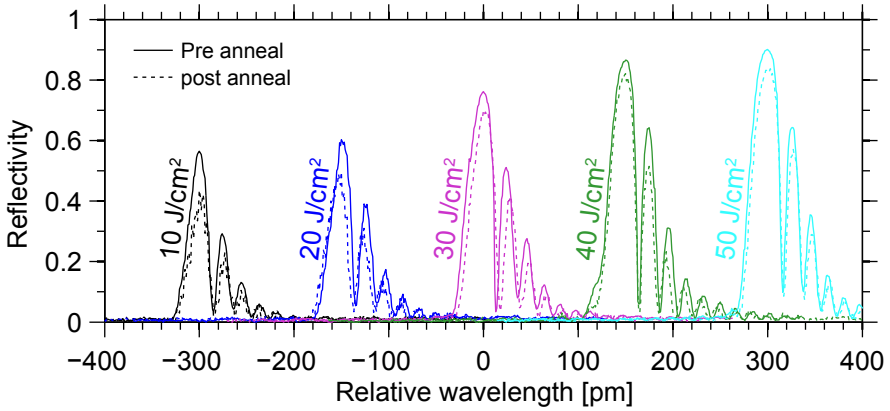

Figure 2.8: Reflectivity of gratings inscribed using $\underline{\Lambda}_{1a}$ for different UV fluences in PM Raman fiber without D_2 loading. The 5 gratings are plotted with a 150 pm displacement relative to each other.

The grating strength versus accumulated exposure without D_2 loading of the fiber is plotted in fig. 2.9. Due to a high photosensitivity of the PM Raman fiber, very small UV doses are required for inscribing fiber gratings with a reflectivity below 0.9.

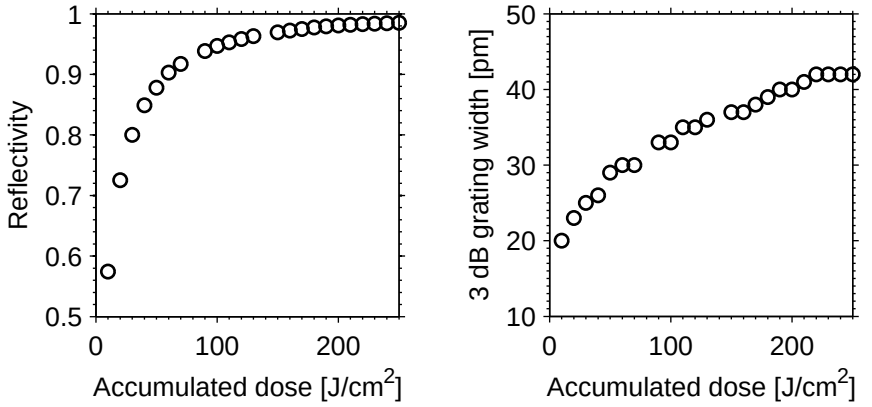

*Figure 2.9: **(left)** Measured peak FBG reflectivity, estimated from the measured transmission spectrum, versus the accumulated UV dose. **(right)** Measured grating width versus accumulated UV dose. Inscribed in a non-D_2 loaded PM Raman fiber.*

The amplitude of the "ac" index modulation can be calculated from the maximum reflectivity [65]:

$$\Delta n_{ac} = \frac{\lambda_b}{L_{\mathrm{FBG}} \cdot \pi} \cdot \operatorname{arctanh}(\sqrt{R_{\max}}) \quad . \tag{2.8}$$

For weak output gratings shown in fig. 2.9, the index modulations is estimated to be in the range from $8 \cdot 10^{-6}$ to $2 \cdot 10^{-5}$. The "dc" index modulation can be calculated for the induced wavelength shift [76].

A comparison between the gratings inscribed with and without prior D_2 loading of the fiber is included in appendix A.5. Measurements on the induced red-shift in the central grating wavelength, from the "dc" index modulation, are also included in appendix A.5.

2.2.5 Investigating the spectral grating shape

To investigate the origin of the side-lobes, two gratings were inscribed with identical parameters with two different phase masks $\underline{\Lambda}_{1a}$ and $\underline{\Lambda}_{1b}$ having the same specified uniform 1080.5 nm pitch. The transmission spectrum was characterized with both a tunable laser source shown in fig. 2.10a and using a broadband SC source in fig. 2.10b. For comparison, the grating transmission spectrum is plotted for $\underline{\Lambda}_2 = 1160.3$ nm at 1679 nm in fig. 2.10b. The 1679 nm grating was characterized with a broadband SC source and an OSA with a 10 pm resolution.

The grating parameters extracted from fig. 2.10 are listed in table 2.2. From the comparison it is evident that when using the broadband source, the grating shape cannot be resolved, and as a result the grating bandwidth is overestimated while the reflectivity is underestimated.

Phase-mask	**TLS**		**SuperK**	
	FWHM [pm]	R [%]	FWHM [pm]	R [%]
$\underline{\Lambda}_{1a}$	61	99.7	81	98.8
$\underline{\Lambda}_{1b}$	49	99.4	65	97.5
$\underline{\Lambda}_2$	-	-	71	96.5-98.0

Table 2.2: Summary of grating details from fig. 2.10

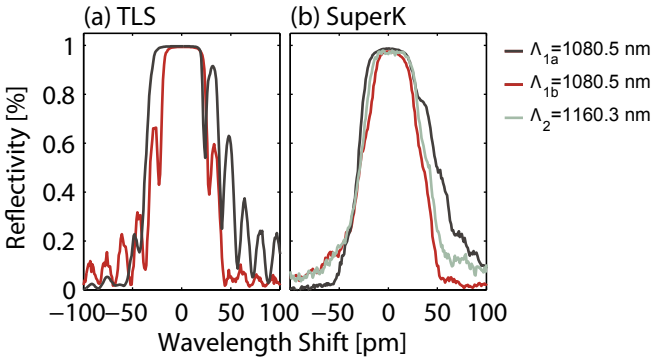

Figure 2.10: Grating reflectivity estimated from the measured transmission, with a comparison of the gratings inscribed using the three different phase-masks listed in table 2.1. (a) Measured using a TLS. (b) measured using a broadband SC source (NKT Photonics compact SuperK). The grating parameters are summarized in table 2.2.

For the two gratings characterized by a *TLS synchronized measurement* the grating fine-structure could be resolved as shown in fig. 2.10. From the figure it is evident that the side-lobe structure is more pronounced for $\underline{\Lambda}_{1\mathrm{a}}$, with strong side-lobes appearing on the *red* side of the grating, opposed to the $\underline{\Lambda}_{1\mathrm{b}}$ grating which is more symmetric.

Initial comparison of the measured FBG spectrum, when using phase-mask $\underline{\Lambda}_{1a}$ and $\underline{\Lambda}_{2b}$, reveals significant variations. While the grating structure is clearly visible when characterized with the tunable laser in fig. 2.10a, the structure appears smeared out using the broadband source in fig. 2.10b.

Evident from fig. 2.10a, the FBG inscribed with $\underline{\Lambda}_{1a}$ is asymmetric in shape and has distinct side-lobes at the red side of the spectrum, opposed to the FBG inscribed with $\underline{\Lambda}_{1b}$, which has a symmetric transmission spectrum.

The observed side-lobes could originate from apodization profiles in the grating structure, similar to the predictions shown in fig. 2.5 on page 16, caused by misalignment or variations in the UV beam power. However, direct comparison between FBGs inscribed using the phase-masks $\underline{\Lambda}_{1b}$ and $\underline{\Lambda}_{1b}$, that were aligned in a similar manner and with the same experimental setup, indicate differences in the phase-mask uniformity.

2.2.6 Thermal and mechanical tuning

It can be advantageous to fine tune the FBG wavelength, i.e. by mechanically changing the FBG pitch. As the Bragg wavelength depends on the grating period, the central wavelength of the FBG can be shifted to higher wavelengths by stretching the fiber. For the fabricated FBGs a 2.36 pm/mN mechanical tunability was found (see appendix A.2). By adjusting the tension prior to the grating exposure enables compensation of the red-shift in the grating wavelength caused by the "dc" term in the index modulation. This is of particular importance for stronger gratings and especially for D_2 loaded fibers, where the DC term in the induced refractive index can shift the grating wavelength by hundreds of picometer or even nanometer (see appendix A.5).

Further fine-tuning of the central FBG wavelength can be obtained by heating or cooling the fiber. The grating temperature sensitivity depends on the grating and fiber type, and is typically of the order 7-10.5 pm/^{o}C [77]. The wavelength shift for a ΔT temperature change of the FBG is given by [76]:

$$\Delta\lambda_{\mathrm{B}} = \lambda_{\mathrm{B}}(\alpha_{\Lambda} + \alpha_{\mathrm{n}})\Delta T \quad . \tag{2.9}$$

The thermal expansion coefficient is given by $\alpha_{\Lambda} = (1/\Lambda)(\partial\Lambda/\partial T)$, which is approximately $0.55 \cdot 10^{-6}$ for silica. The thermo-optic coefficient $\alpha_n = (1/n)(\partial n/\partial T)$ and is approximately $8.6 \cdot 10^{-6}$ for a typical germanium-doped silica fiber. The temperature tunability is demonstrated in fig. 2.11 where the grating temperature was controlled in the range from 20^{o}C to 95^{o}C, with a wavelength tuning of 11.95 pm/^{o}C.

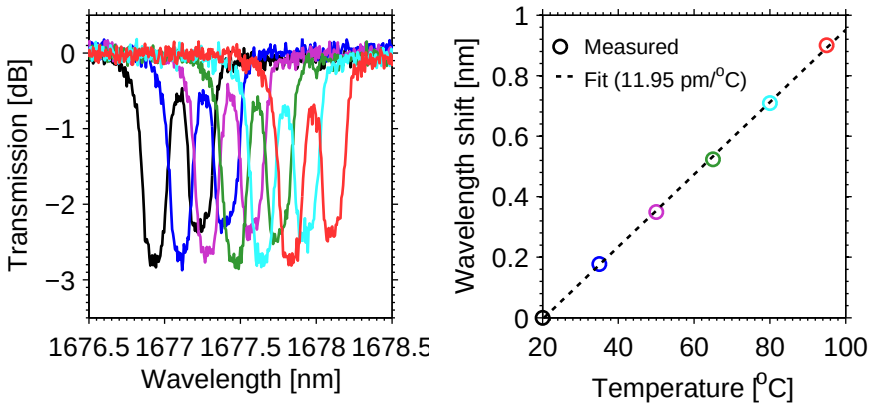

Figure 2.11: ***(left)*** *Measured FBG transmisson for different FBG temperatures using an unpolarized broadband light source.* ***(right)*** *Measured shift in the central wavelength with increasing grating temperature.*

Thermal grating alignment and stabilization setup

To control and stabilize the cavity FBGs, a temperature control setup was build. Each FBG was mounted and enclosed in an aluminum block mounted to a peltier element, capable of both cooling and heating. By embedding a thermocouple inside each grating mount a proportional-integral-derivative (PID) temperature feedback controller routine could be implemented in a LabView program, capable of tuning and stabilizing the individual FBGs. The typical standard deviation (σ) for the grating mount temperature is within a 10 and $\sim$ 20 mK range. A photo of the FBG temperature control setup is listed in appendix A.1.

2.2.7 Manufacturing the laser cavity gratings

The RFL described in chapter 3 comprises a laser cavity defined by the inscription of a high reflectivity (HR) and a low reflectivity (LR) FBG in a single segment of PM Raman fiber. The design wavelength of the RFL is at 1679 nm, located at the Raman gain peak, at a 13 THz frequency downshift from a 1564 nm pump source. The following section describes the inscribed FBGs for a 61 m and a 140 m RFL cavity.

Lacking a tunable laser at the 1679 nm signal wavelength, the low spectral bandwidth of the 50 mm long inscribed FBGs could not be resolved using a broadband SC light-source. Therefore, the FBG inscription parameters were optimized using a 1080.5 nm phase-mask pitch ($\underline{\Lambda}_{1a}$), yielding a test wavelength of 1564 nm. At this wavelength the grating could be characterized with a TLS synchronized with an OSA. The resulting recipe was then transferred to the 1160.3 nm phase-mask ($\underline{\Lambda}_2$), which was used to inscribe the final cavity gratings. With an estimated effective index $n_{\text{eff}} = 1.446$ for the PM Raman fiber a $\sim$1679 nm grating wavelength is predicted using phase-mask $\underline{\Lambda}_2$. The

final FBG wavelength is fine-tuned by applying fiber-stretch prior to the UV exposure.

	Pitch	Tension	UV dose	Loading
Signal reflection grating	1160.3 nm	100 mN	250 J/cm^2	D_2
Signal output grating	1160.3 nm	100 mN	250 J/cm^2	–
Pump reflection grating	1080.5 nm	600 mN	250 J/cm^2	D_2

Table 2.3: List of the FBG parameters for the 61 m RFL cavity gratings.

For the 61 m cavity, the HR signal and pump FBG were inscribed in D_2 loaded fiber. Before inscription of the LR FBG, the D_2 loaded fiber was annealed to remove the D_2. Without the D_2 loading, the reduced photosensitivity allowed for more accurate control of the final LR FBG reflectivity. The parameters for the 61 m high-Q cavity are listed in table 2.3. The measured FBG transmission of the test gratings, inscribed at 1564 nm, is plotted along with the estimated reflectivity in fig. 2.12.

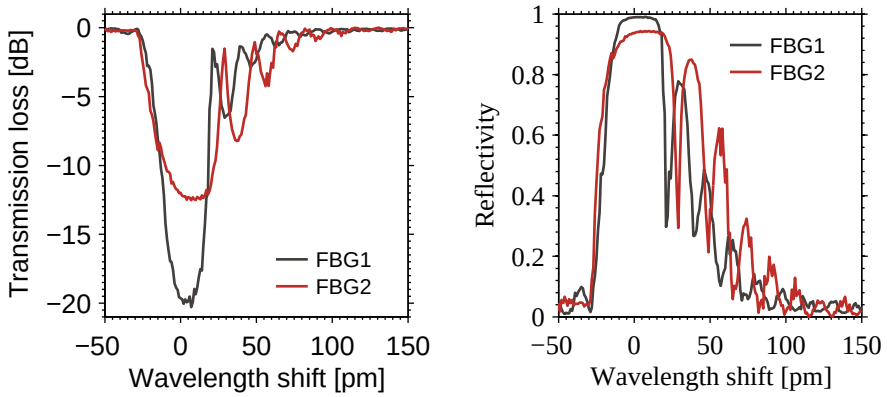

*Figure 2.12: Measured transmission **(left)** and estimated reflection **(right)** for two test gratings inscribed at a 1564 nm central wavelength for the for the 61 m RFL cavity.*

The parameters for the 140 m high-Q cavity are listed in table 2.4. The measured FBG transmission of the test gratings, inscribed at 1564 nm, is plotted along with the estimated reflectivity in fig. 2.13.

	Pitch	Tension	UV dose
Signal reflection grating	1160.3 nm	100 mN	2000 J/cm^2
Signal output grating	1160.3 nm	100 mN	30 J/cm^2
Pump reflection grating	1080.5 nm	600 mN	2000 J/cm^2

Table 2.4: List of the FBG parameters for the 61 m RFL cavity gratings.

Following inscription, the gratings were annealed, to ensure long term grating stability. While symmetric side-lobes to the grating shape is expected for a uniform FBG, asymmetric side-lobes at the red wavelength side of the grating

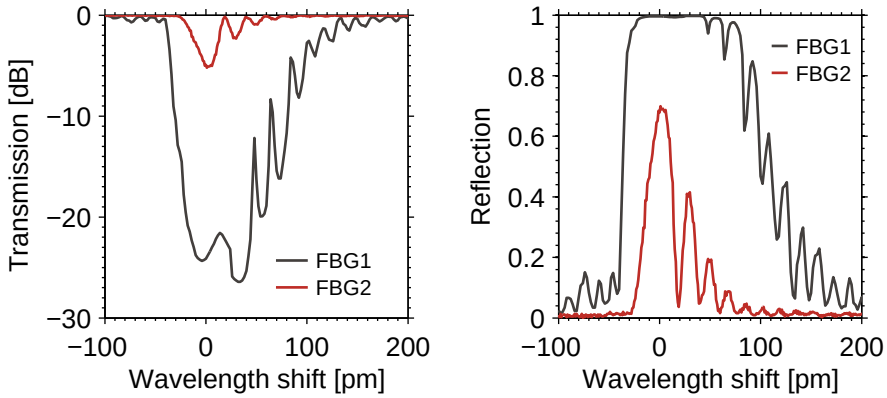

*Figure 2.13: Measured transmission **(left)** and estimated reflection **(right)** for two test gratings inscribed at a 1564 nm central wavelength for the for the 140 m RFL cavity.*

spectrum were observed for the inscribed gratings. These can arise due to an apodization in the grating structure [65].

2.3 Summary

In this chapter the theory and experiments regarding the inscription of FBGs were described. It was found that spectrally narrow FBGs could be inscribed with varying reflectivity in the utilized PM Raman fiber while using the phase-mask technique. Due to a high photosensitivity of said fiber, hydrogenation was not required for achieving the desired FBG properties. The findings were used as a basis for manufacturing the RFL cavity gratings with the desired reflectivity. However, side-lobes in the FBG spectrum were observed which may influence the RFL performance; a topic which is described further in the next chapter containing the experimental results for the investigated RFLs.

Chapter 3

Raman fiber lasers and amplifiers

> An expert is a man who has made all the mistakes that can be made in a very narrow field.
>
> Niels Bohr

This chapter concerns the work on two Raman fiber lasers (RFLs) emitting at a 1679 nm wavelength, and the subsequent investigation of a Raman amplifier (RA) operating from 1679 to 1900 nm. The work on RFLs resulted in the following publications [78–80], while the work concerning RAs resulted in the publications [81, 82].

The Raman gain as function of wavelength is described (section 3.2) and is followed by a description of the utilized polarization maintaining (PM) Raman fiber (section 3.3). The experimental results for a PM RFL with an 1679 nm emission wavelength are presented in section 3.4. The utilized pump sources are presented in section 3.4.1 while the experimental setup for the RFL is shown in section 3.4.1. Two different RFL cavities are investigated with emphasis on the laser stability and spectral broadening; a 61 m cavity (section 3.4.2) and a 140 m cavity (section 3.4.3). This is followed by an investigation of the laser stability (section 3.4.4) and a discussion of the RFL results (section 3.4.5).

The 1679 nm RFL was used as a pump for a PM RA characterized from 1679 to 1900 nm (section 3.5). After a description of the experimental setup (section 3.5.1), the results for both linearly co-polarized and orthogonal pump and signal are presented (section 3.5.2). The noise properties are described in section 3.5.3. The chapter is summarized in section 3.6.

3.1 Introduction

Following the discovery of stimulated Raman scattering (SRS) [7, 27] and the first demonstration of an all-fiber cavity utilizing fiber Bragg gratings (FBGs)

as cavity reflectors [28], RFLs have been studied extensively. Gain is obtained through SRS which offers versatility in the wavelength of operation, and can in principle provide gain at any wavelength, assuming that a suitable pump laser exists. The SRS process can also be used for frequency down-conversion of ultrafast pulses through the soliton self-frequency shift (SSFS) for propagation in fibers with anomalous dispersion [83, 84].

However, in this work SRS is investigated in the continuous wave (CW) regime. For silica based fibers the Raman gain peaks at a ∼13.2 THz frequency-downshift. Furthermore, the process can be cascaded to provide extended wavelength coverage [29].

Distributed Bragg reflector RFLs have recently been demonstrated with picometer linewidths [75, 85], along with distributed feedback RFLs enabling further linewidth reduction [86]. A result of the narrow linewidth design is an increased sensitivity towards alignment of the cavity defining FBGs. This is a result of a high mechanical and thermal sensitivity of the FBG, which is described in section 2.2.6, towards the central wavelength of the FBG. Previous studies on RFL stability have reported large variations in the output power over time, with up to 40% power variations on an hour scale [85]. The high enviromental FBG sensitivity motivates the implementation of a method for stabilizing and alligning the RFL FBGs.

When scaling RFLs to longer wavelengths above 1550 nm, the Raman gain coefficient decreases while the transmission loss in germanium-doped silica fibers increases. This impose a limit on how long the cavity can be with reasonable pump power levels.

Longer cavities require comparable weak output FBGs for optimal performance, which yields a low Q-factor cavity with a corresponding low intra-cavity optical power. However, as the cavity length is reduced the round-trip gain can be raised by increasing the fiber cavity Q-factor with the inscription of high-reflectivity FBGs. For shorter RFL cavities the increased intra-cavity optical power may impair performance through spectral broadening. The spectral broadening occurs due to four-wave mixing between adjacent cavity modes, which broadens the output spectrum beyond the output FBG bandwidth [87–89]. In addition to deteriorating the output spectrum, the laser performance is also affected from the so-called nonlinear effective reflectivity of the output FBG. The spectral shape of the intra-cavity Stokes wave of the RFL is defined by the effective FBG loss profile [88]. As the pump power is increased and the spectrum of the Stokes wave broadens, the effective FBG reflectivity is reduced [90]. This effect can be quite pronounced if the output FBG bandwidth is small. For a 100 pm FBG bandwidth a decrease from 70% output FBG reflectivity to 20% was observed when the RFL output power was increased from 0 to 400 mW [87].

3.2 Scaling of the Raman gain

One approach to the description of Raman amplification, is by a set of coupled power equations [91]. For low undepleted signal powers, the Raman gain in

units of dB is given by the following expression [91]:

$$G_{\mathrm{R,dB}} = 4.343 \cdot g_R P_p L_{\mathrm{eff}} \quad , \tag{3.1}$$

where g_R is the Raman gain coefficient, P_p the injected pump power and L_{eff} the effective length given by $L_{\mathrm{eff}} = 1\left[-\exp(-\alpha_p L)\right]/\alpha_p$, which depends on the length, L, and the pump propagation loss, α_p. The Raman gain coefficient depends on the fiber core and cladding material, and is typically described by the third order susceptibility $\chi^{(3)}$ of the germanosilicate glass, the optical frequency of the signal ω_s and the effective area of the signal and pump A^{ps}_{eff}. The Raman gain coefficient can be increased by raising the germanium concentration in the fiber core. A Raman gain coefficient of 300 dB/(W · km) was reported for a high 75% mol GeO_2 doping level [92]. For an unpolarized pump the Raman gain is described by the following expression [93]:

$$g_R = \frac{-3\omega_s}{\varepsilon_0 c^2 n_p n_s} \frac{\mathbf{Im}\left[\chi^{(3)}_{iiii} + \chi^{(3)}_{ijji}\right]}{2A^{ps}_{\mathrm{eff}}} \quad , \tag{3.2}$$

where ε_0 is the vacuum permittivity, c the speed of light, $n_{s/p}$ denote the signal and pump refractive index. In this case the Raman gain coefficient simply depends on the average of the two susceptibilities $\chi^{(3)}_{iiii}$ and $\chi^{(3)}_{ijji}$, corresponding to the Raman interaction when the pump and signal are polarized along the same axis or if they are orthogonal to each other, respectively. The Raman gain response in optical fibers scales when changing the pump wavelength, based on the changes in optical frequency of the pump and the change in effective area of the signal and pump [93]:

$$g_R(\Delta\nu, \Lambda_p) = g_R(\Delta\nu, \lambda_p) \cdot \left(\frac{\lambda_s}{\Lambda_s}\right) \cdot \left[\frac{A^{ps}_{\mathrm{eff}}(\Delta\nu, \lambda_p)}{A^{ps}_{\mathrm{eff}}(\Delta\nu, \Lambda_p)}\right] \quad , \tag{3.3}$$

where $\Delta\nu$ is the frequency offset between the signal and pump, $\lambda_{p,s}$ is the specified signal and pump wavelength and $\Lambda_{p,s}$ is the scaled signal and pump wavelength.

3.3 The polarization maintaining Raman fiber

The PM Raman Speciality fiber is provided by *OFS Fitel Denmark*, has a 18.7 μm^2 effective area at 1550 nm and a specified 2.5 $(W \cdot\ km)^{-1}$ Raman gain efficiency when using a depolarized pump at 1453 nm. The fiber is based on the panda layout, containing B_2O_3 doped stress rods inducing a birefringence specified at $2.8 \cdot 10^{-4}$.

The measured transmission loss of the PM Raman fiber is shown in fig. 3.1, which is characterized from 1200 nm to 1900 nm. At wavelengths below 1700 nm, the propagation loss was characterized utilizing a superluminescent light emitting diode (SLED) source (measurements from OFS Fitel Denmark). At wavelengths above 1700 nm the propagation loss was characterized using

a Thulium based amplified spontaneous emission (ASE) source (See fig. B.3). The fiber has an 0.4 dB/km loss minimum at 1600 nm, with propagation losses increasing drastically above 1700 nm, due to the increase in infrared (IR) absorption in the germanosilicate fiber [94].

The effective area of the fiber along with the calculated scaled Raman gain coefficient [95] is plotted for the OFS PM Raman fiber in fig. 3.1(a) which was utilized in the following experiments. The calculations were based on the specified Raman gain of 2.5 $W^{-1}km^{-1}$ for an unpolarized pump, corresponding to approximately 5 $W^{-1}km^{-1}$ for linearly and co-polarized signal and pump, when neglecting the much smaller contribution from $\chi^{(3)}_{ijji}$. In fig. 3.1 a large reduction in the Raman gain coefficient is predicted for longer wavelengths, due to the decrease in signal frequency and the increased effective area of the fiber.

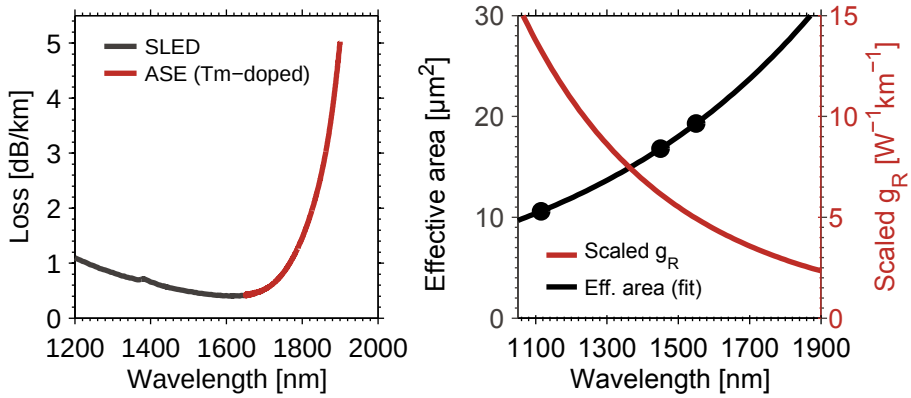

Figure 3.1: ***(left)*** *Transmissio loss measured along the slow axis of the PM Raman fiber from OFS. The transmission is measured using different light sources; an SLED source and a home build Tm-doped ASE source.* ***(right)*** *Estimated effective area and scaled Raman gain coefficient.*

3.4 Raman fiber laser

This section describes the experimental results for the investigated RFLs, following a description of the experimental setup.

3.4.1 Experimental setup

Pump sources

Two different 1564 nm pump sources, shown in fig. 3.2a and fig. 3.2b, were used to pump the different RFL configuration. For the 61 m cavity the pump source outlined in fig. 3.2a was used. Here, a 1564 nm pump seed is amplified in an Erbium doped fiber amplifier (EDFA) before it is coupled into a PM fiber using a linear polarizer which is aligned to the slow axis of the fiber. An isolator at the output attenuates any back-reflected pump light.

The pump source shown in fig. 3.2b, used for the 140 m RFL cavity, required additional measures to limit stimulated Brillouin scattering (SBS) due to the longer cavity length. The reduction in SBS is provided by using two pump seeds that are centered around 1564 nm, with a 20 pm displacement, along with a phase modulation of the pump seeds at three discrete frequencies f_{1-3} [96]. This provided an increase in the SBS threshold to above the level of available pump power.

Raman fiber laser

The experimental setups of the RFLs are shown in fig. 3.2c. The laser cavity is defined by FBGs inscribed in a segment of polarization maintaining (PM) Raman specialty fiber from OFS Fitel Denmark, described in section 3.3. Two FBGs, FBG1 and FBG2, are inscribed at a 1679 nm design wavelength, along with a pump reflector grating, FBG3, at 1564 nm. The inscribed pump FBG increases the conversion efficiency of the laser by increasing the pump absorption providing dual-pass amplification in the cavity. The gratings are inscribed directly in the PM Raman fiber, to avoid excess splice losses. Both RFLs emits at a 1679 nm wavelength. A typical output spectrum, measured for a 140 m cavity length, is shown in fig. 3.3.

Tuning the FBG central wavelength by controlling the temperature is described in section 2.2.6. Thermal tuning and stabilization of the FBGs is implemented by enclosing each FBG in a temperature controlled aluminum mount. To monitor the FBG temperature, a thermocouple is embedded inside the mount. The temperature T_{1-3} of the three gratings is controlled by a temperature active feedback control system, relying on a proportional-integral-derivative (PID) controller. This enables fine-tuning of the FBG central wavelength, with a 12 pm/^{o}C sensitivity, which is stabilized to a $\sim$15 mK temperature std. variation. These variations correspond to a sub-pm wavelength stability.

The measured transmission loss for the PM Raman fiber, described in section 3.3, is 0.42 and 0.46 dB/km at the pump and signal wavelength, respectively. The estimated effective area and Raman gain coefficient, described in section 3.3, is $g_R = 4.8\ (\mathrm{W}\cdot\mathrm{km})^{-1}$ and $A_{\mathrm{eff}} = 19.7\ \mu\mathrm{m}^2$ at the 1564 nm pump wavelength. Two cavity designs were investigated; one cavity containing 61 m fiber and a longer cavity containing 140 m fiber. The reflection coefficient of the output signal FBG was optimized to the cavity length. Each cavity contains a high reflectivity (HR) signal FBG and a low reflectivity (LR) signal output grating. Additionally, a HR pump FBG at the output enables dual-pass amplification while filtering away the unabsorbed pump at the output. Inscription of the cavity FBGs was described in section 2.2.7. The two HR gratings, FBG1 and FBG3, have a $\geq$99% reflectivity for both cavity lengths. The LR signal output grating (FBG2) has a reflectivity of 94% for the 61 m cavity and 68% for the 140 m cavity. The LR FBG reflectivity is optimized to each cavity, to account for the different cavity round-trip gain and loss.

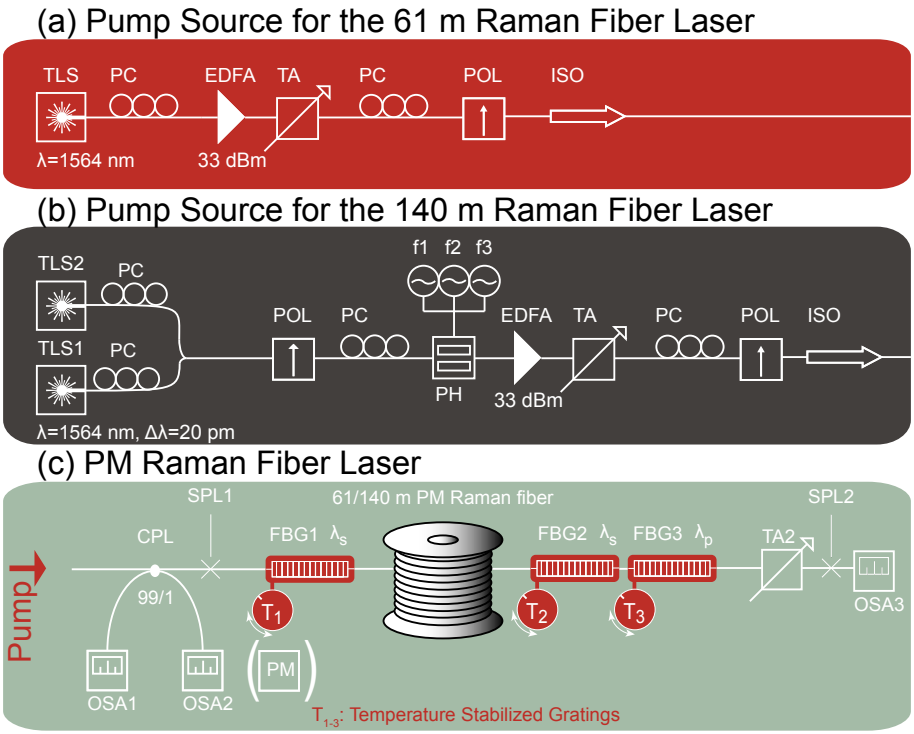

Figure 3.2: (a) Pump source without SBS suppression. (b) Pump source with SBS suppression and two pump seed. Both sources are amplified in a 33 dBm EDFA, and transmitted through a linear polarizer aligned with the principal fiber axis of the PM Raman fiber. (c) Experimental setup of the RFL, showing the 3 temperature stabilized and controlled FBGs. SPL: splice, PC: Polarization controller, POL: Polarizer, PH: Phase modulator, f1-3: RF frequency generators, EDFA: Erbium doped fiber amplifier, TA: Tunable attenuator, ISO: optical isolator, CPL: coupler.

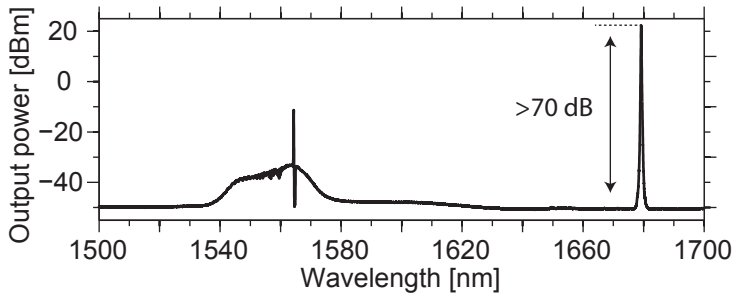

Figure 3.3: Typical laser output spectrum, measured for the 140 m laser cavity.

3.4.2 61 m cavity length

The first investigated high-Q RFL configuration, contained a 61 m long cavity with an output FBG reflectivity estimated to 94%, for which the lasing-characteristics is presented in fig. 3.4a. The lasing-characteristics is initially shown for single pass pump (□ in fig. 3.4a). Utilizing a pump reflector FBG at the output, pump recycling was enabled. The resulting dual pass amplification provided an increase in the conversion efficiency as depicted by the ◇ symbols in fig. 3.4. Both lasing-characteristics were measured with identical signal FBG alignment. As a result the slope efficiency was increased from 20 to 37%, in addition to a decrease in the lasing threshold pump power. The roll-off in the slope efficiency near the maximum output power level (◇ in fig. 3.4a), is caused by the onset of SBS which reduces the effective pump power level, beyond 900 mW pump power. At this setting, both the output power and output spectrum was very sensitive to the wavelength alignment of the two signal FBGs. The color plot in fig. 3.4b shows the output spectrum measured at 293 mW pump power, for different relative alignment of the two cavity FBGs. No significant changes in the output spectrum are observed when the FBG alignment is adjusted.

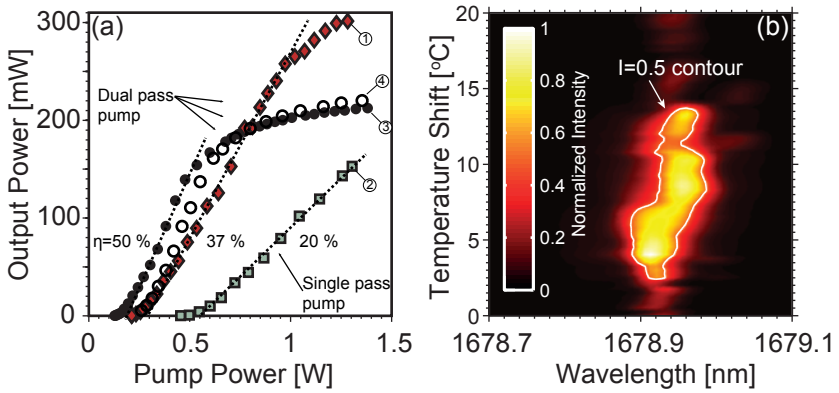

Figure 3.4: (a) Lasing-characteristics for different relative alignments between the HR and LR cavity FBGs for the 61 m cavity length. (b) Color plot of the laser output spectrum for different relative FBG alignment. The FBG alignment is controlled by adjusting the relative FBG temperature difference. Measured at a 293 mW pump power.

In fig. 3.5a the output spectrum at the highest output power is compared for □ and ◇ from fig. 3.4, depicting several distinct peaks. The multi-peak output spectrum suggests that several fringes from the spectral shape of the FBG contribute to the resonant cavity modes. This becomes more clear when considering the color plot in fig. 3.5d, which depicts the normalized output spectrum as a function of the pump power. Figure 3.5d illustrates that the output spectrum is uniform and spectrally narrow, with a 21 pm linewidth, at the lowest pump power setting. When the pump power is increased the complexity of the spectrum increases along with the spectral width.

By changing the relative FBG alignment, the slope efficiency was increased

Figure 3.5: (a-c) Output spectrum measured at the highest output power from fig. 3.4 in the dual pass pump configuration (full lines). Here a/b/c corresponding to ◇/●/○ in fig. 3.4, respectively. The dashed line in (a-c) depicts the output spectrum at the lowest power setting. The spectral FWHM is indicated by the two arrows. (d-f) The measured and normalized output spectrum is plotted as a function of the pump power above the lasing threshold for 3 configurations, with d/e/f corresponding to ◇/●/○ in fig. 3.4, respectively.

from 37% to 50%, as depicted for the • and ○ symbols in fig. 3.4. A saturation in output power is observed for pump powers exceeding 500 mW. Furthermore, the associated output spectrum at the highest output power setting is shown in fig. 3.5b and fig. 3.5c, respectively. The linewidth of the two respective output spectra is 118 and 146 pm, correspondingly, thus exceeding the ∼50 pm bandwidth of the output FBG.

Examination of the color plot of the normalized output spectrum in fig. 3.5e and f show that both configurations display a steady increase in the linewidth as the pump power is increased. However, in fig. 3.5f (○) a gradual two-peak formation in the output spectrum is observed.

The decrease in slope efficiency is consistent with a reduction in effective reflectivity as spectral broadening increases the RFL output bandwidth beyond the FBG FWHM bandwidth [97]. Due to the narrow HR FBG, the onset of spectral broadening is expected to decrease the laser emission. The part of the circulating cavity light that exceeds the HR FBG bandwidth, will "leak" from the cavity where it is attenuated in the isolator. The gradual splitting in the output spectrum observed in fig. 3.5c and fig. 3.5f, is the result of the emission spectrum exceeding the bandwidth of the output FBG [98].

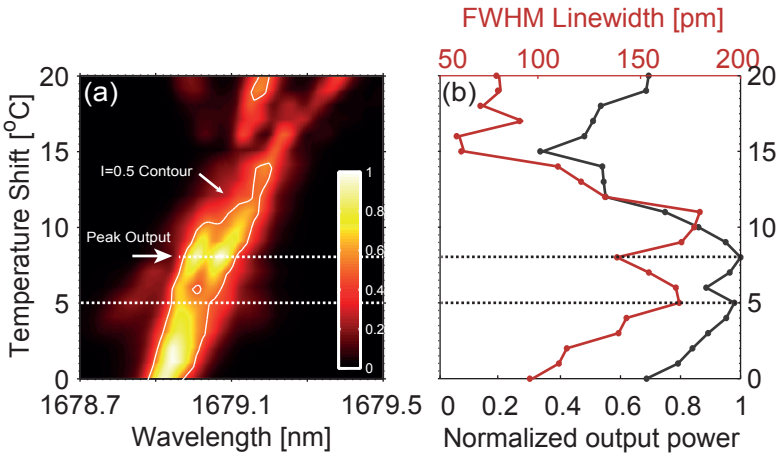

Figure 3.6: (a) Color plot showing the output spectrum as the relative temperature difference between the HR and LR cavity FBG is tuned for the 61 m cavity length. (b) Plot of the normalized output power along with the FWHM linewidth as a function of the relative temperature detuning of the cavity FBGs. Measured at a 1.42 W pump power.

In fig. 3.4 and fig. 3.5, three different regions of operation were observed. The color plot in fig. 3.6a shows the output spectrum as a function of the temperature shift varying from 0 to 20^{o}C between the two signal FBGs in the cavity. The temperature was increased incrementally and allowed to stabilize, before each output spectrum was recorded. Therefore, the color plot shows the development of the output spectrum as the cavity resonance is tuned thermally. In comparison, the normalized output power and linewidth is plotted in fig. 3.6b.

When adjusting the relative alignment of the cavity FBGs the output

FWHM linewidth varies between 50 and 180 pm. From the color plot it is seen that a uniform output spectrum can be obtained at a temperature shift (ΔT) from 0 to 4^{o}C. Further detuning of the FBGs leads to an increased linewidth where the output spectrum splits up as shown in fig. 3.5c and fig. 3.5f. Adjusting the relative grating alignment modifies the effective grating reflectivity, which in turn affects the amount of absorbed pump power and the final output power.

3.4.3 140 m cavity length

To reduce the effects of spectral broadening a low-Q cavity was constructed and characterized in a similar manner. The laser cavity is 140 m long and contains a weaker output FBG with an estimated reflectivity of 68%, as shown in section 2.2.7. The lasing-characteristics shown in fig. 3.7a have a 850 mW lasing threshold. The slope efficiency is 67%, and the maximum output power is 275 mW. The spectral shape at the highest output power setting is shown in fig. 3.7b, where the linewidth is 27 pm. In fig. 3.7c it is shown that the output wavelength is tunable across a 2 nm range from 1678.8 to 1680.8 nm by thermal alignment of the cavity FBGs. The lasing-characteristics remains linear with no roll-off in the slope efficiency at higher powers, in contrast to the 61 m high-Q cavity. The high lasing threshold indicates that the output coupling, through the LR FBG, is to high. This was confirmed when considering the level of unabsorbed pump, which was $\sim$ 500 mW at the highest pump power setting (see appendix B.3). An increase in conversion efficiency could be obtained by an increase in the output FBG reflectivity, which would require inscription of a new grating.

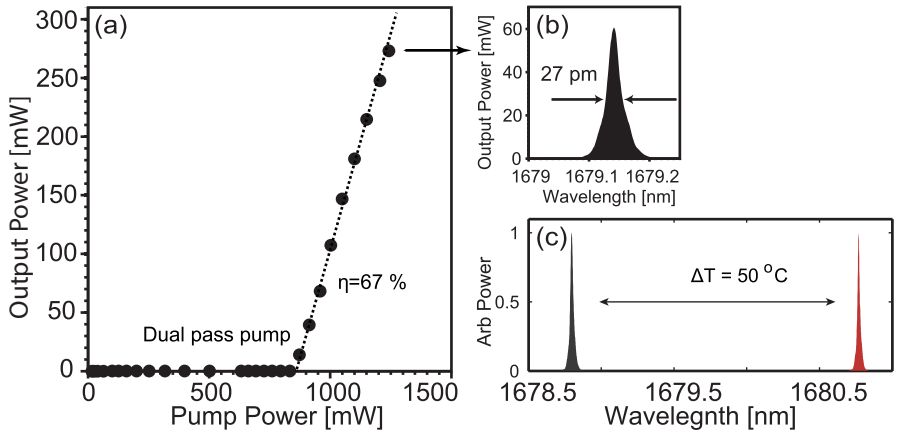

Figure 3.7: (a) Lasing-characteristics showing the output power for increasing pump power. (b) Measured output spectrum at the highest output power setting. (c) Tunability in the output wavelength by temperature tuning of the cavity FBGs.

The output linewidth, measured for each of the measurement points in fig. 3.7a, increases gradually from 18 to 26 pm as the pump power is raised. The results are shown in fig. 3.8a. The color plot in fig. 3.8b shows the normalized

output spectrum as a function of the pump power. The output spectrum remains stable with no changes in the output spectrum as the the pump power is increased. The output spectrum FWHM remains lower than the LR output FBG FWHM which is estimated to ∼28 pm based on the test FBG shown in section 2.2.7.

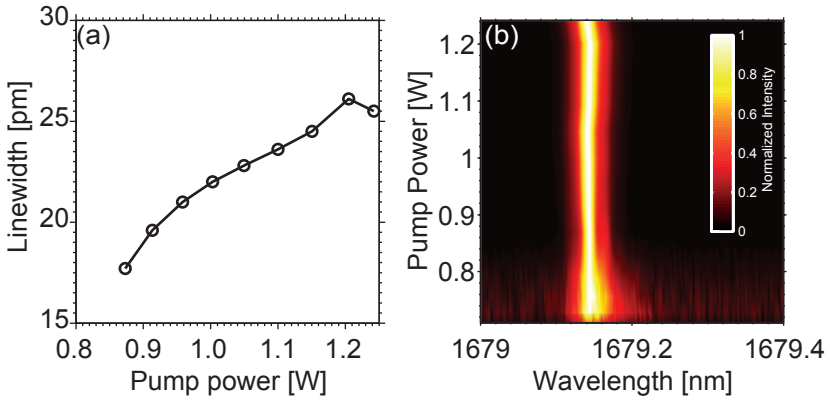

Figure 3.8: (a) *Measured output FWHM linewidth for increasing pump power. (b) Corresponding normalized output spectrum as the pump power is increased.*

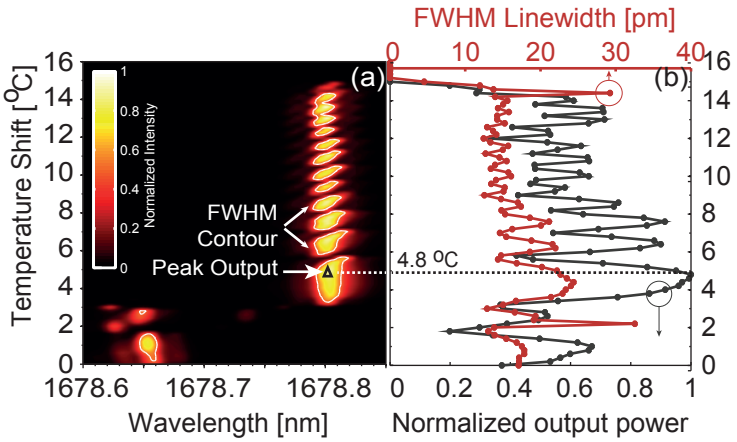

Figure 3.9: (a) *Color plot showing the output spectrum as the relative temperature difference between the HR and LR cavity FBG is tuned for the 140 m cavity length. (b) Plot of the normalized output power along with the FWHM linewidth as a function of the relative temperature detuning of the cavity FBGs. Measured at a* ∼ 1.8 *W pump power, with a 517 mW output power and 24 pm linewidth at 4.8°C temperature detuning.*

The FBG alignment was investigated by tuning the relative temperature between the two cavity signal FBGs. The output FBG temperature is fixed while the high reflectivity signal FBG is tuned, such that the emission wavelength remains constant. The results are represented in a color plot in fig. 3.9a.

It is seen that the output spectrum changes in a periodic manner as the FBG temperature difference is increased. The oscillation in output power with increasing detuning of the cavity FBG, verifies the presence of side-lobes in the FBG reflectivity, which were also observed for the test FBGs described in section 2.2.7. The highest output power is obtained at $\Delta T = 4.8^o$C as shown in fig. 3.9b. The white contour lines enclose the area where the normalized intensity surpasses 0.5. The laser linewidth is plotted along with the normalized output power in fig. 3.9b. The lower limit of the measured linewidth is limited by the 10 pm OSA resolution. At the highest output power setting at 4.8^oC the output power is 500 mW, while the linewidth is close to 20 pm. From fig. 3.9b it is evident that a slight $\sim 0.8^o$C shift in FBG temperature, relative to the optimal FBG alignment at 4.8^oC, leads to a 50% reduction in output power.

3.4.4 Stability

The temperature feedback control system described in section 2.2.6, was used to accurately align and stabilize the FBGs for the experiments described in sections 3.4.2 and 3.4.3. An example of the FBG temperature stability over

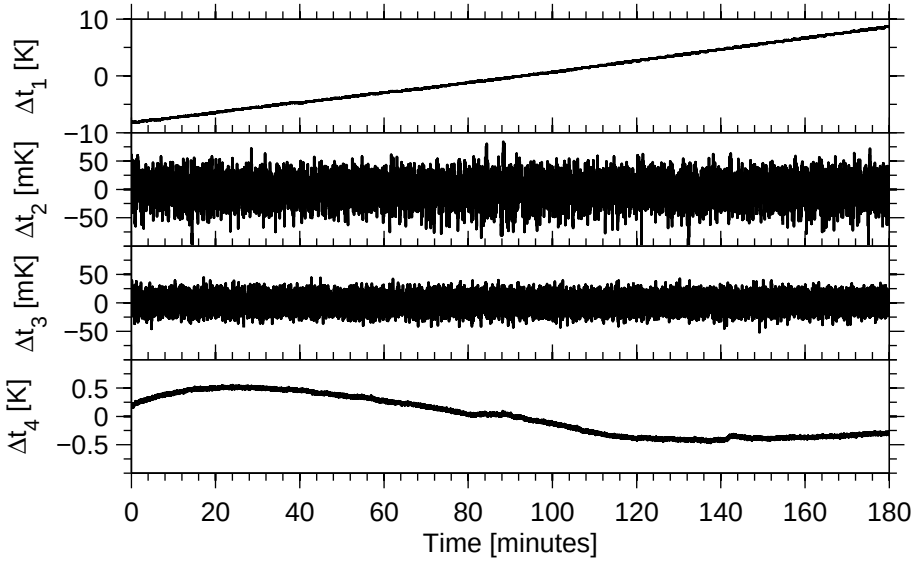

Figure 3.10: Measured FBG mount temperature (Δt_{1-3}) versus time, plotted along with the change in ambient temperature (Δt_4). Δt_1 is the HR FBG, Δt_2 is the pump reflector FBG, and Δt_3 is the LR FBG.

time, measured for the results shown in fig. 3.9, is shown in fig. 3.10. The temperature of the three FBG mounts, which should reflect the temperature of the FBG, is plotted along with the measured ambient temperature. The measurements were performed at a 2.5 Hz sampling rate. The HR signal FBG (Δt_1) is adjusted incrementally across the measurement session. A magnified view is shown in fig. 3.11.

The temperature stability is quantified in terms of the standard deviation in the measured temperature over time, and is 21 mK and 11.9 mK for the the pump reflector FBG (Δt_2) and the LR FBG (Δt_3), respectively. Across the 3 hour measurement session, the ambient temperature (Δt_4) varies slowly within a 1^oC range. The increased standard deviation measured for the pump HR FBG is caused by a higher average FBG operating temperature (40.60^oC), compared to the HR FBG (24.15^oC).

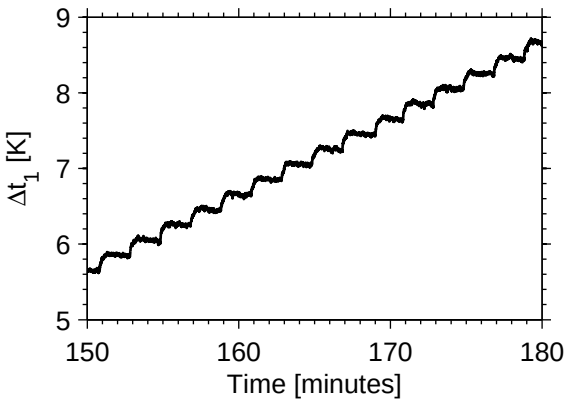

Figure 3.11: *Magnified view of the HR FBG temperature in fig. 3.10*

During the characterization of the FBG alignment, the relative FBG temperature of the HR FBG was adjusted in 0.2^oC increments across a 17^oC range. For each step the temperature is allowed to stabilize for one minute, after which the output spectrum is recorded. During this time the temperature remains stable, typically within 20 mK. This behavior is also evident from the magnified view of the temperature versus time plot shown in fig. 3.11.

Impact on the laser power and spectral stability

Studies on the laser power and spectral stability over time were conducted for the 140 m cavity [79]. The results show that the implemented PID temperature control proved very insensitive to environmental changes. A comparison of different methods for aligning the cavity gratings was conducted.

Initially, the output FBG was adjusted using a micrometer-stage and a strain gauge providing a few mN of accuracy in the wavelength tuning of the FBG. The results are shown in fig. 3.12a, for which the measured standard deviation is indicated for both the injected pump power, the output power, the change in linewidth and the shift in emission wavelength. An output power stability is 0.2% is obtained, whereas a clear shift in emission wavelength and a change in linewidth is evident.

Subsequently, thermal alignment of the FBGs was implemented by mounting the FBG in the active temperature feedback controlled mount. Tuning the FBG temperature without feedback control, provided an increase in both the linewidth and central emission wavelength stability as depicted in fig. 3.12b,

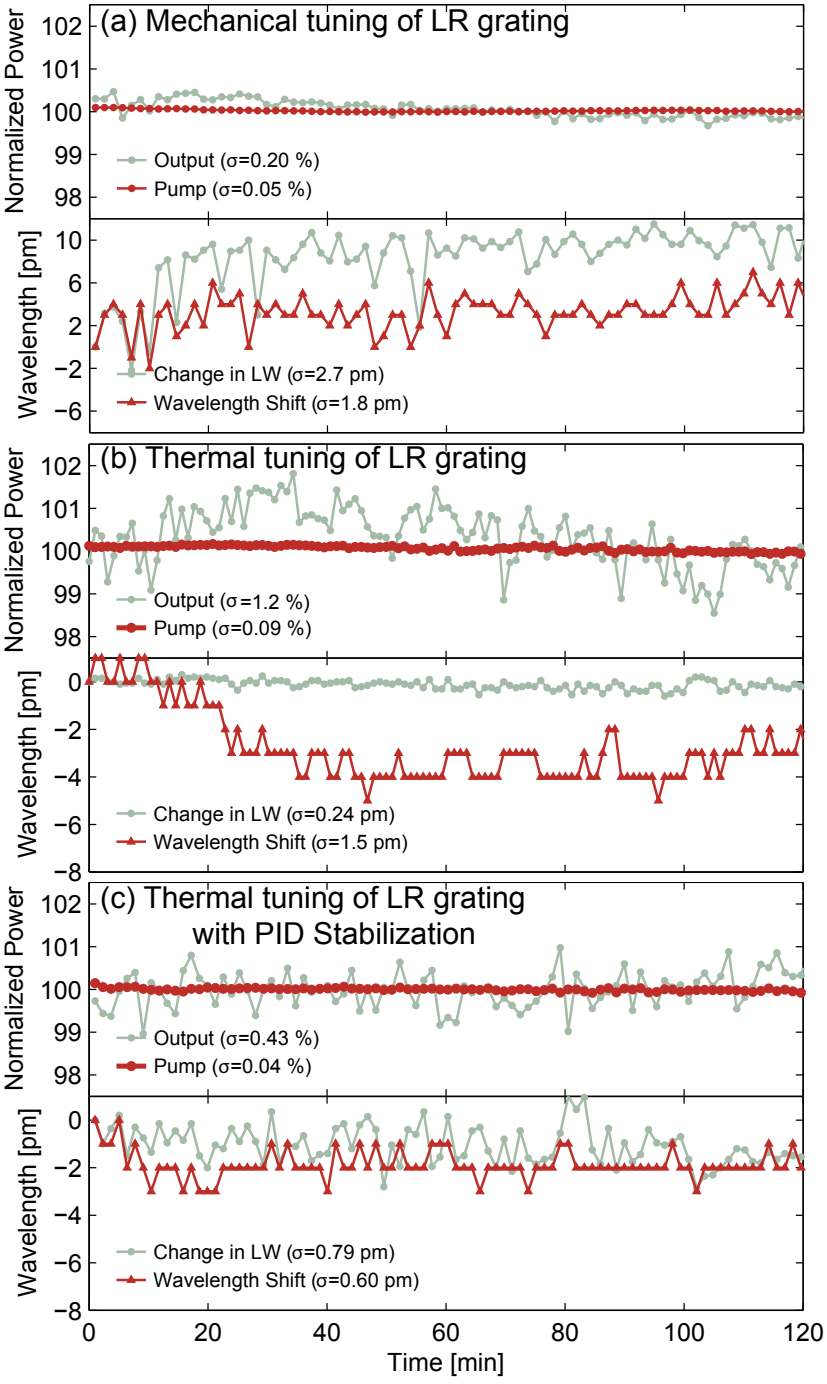

Figure 3.12: Plot of the laser output power and spectral stability versus time, for three different methods of aligning and stabilizing the LR FBG.

when compared to the results obtained for alignment by mechanical stretching of the fiber.

Temperature stabilization utilizing feedback from a thermocouple sensor enclosed in the heatsink along with PID control was realized, enabling accurate control and stabilization of the FBG. The results are shown in fig. 3.12c. During the measurements, the average output power was 680.5 mW for an average linewidth of 29 pm. A standard deviation in the measured FBG temperature of less than 20 mK was obtained, resulted in a power stability of 0.43% along with both a linewidth and emission wavelength stability below 1 pm.

3.4.5 Discussion

Two different RFL cavities were investigated, and efficient lasing was obtained for slope efficiencies ranging from 37 to 67% using the dual pass pump configuration.

The performance of the 61 m high-Q cavity was limited by the quality of the FBGs that could be inscribed. The short cavity length required an output grating with a strong reflectivity of 94%, which showed the appearance of strong side-lobes. Subsequent testing of two similar phase-masks revealed that manufacturing imperfections in the phase-mask leads to distorted FBGs with pronounced side-lobe structure. The combined effect of imperfect FBGs and spectral broadening at higher pump power levels, resulted in sensitive alignment of the cavity with varying emission spectrum and slope efficiency. To reduce the amount of spectral broadening, a 140 m low-Q cavity was constructed in a similar manner. The increased round-trip gain obtained for the longer cavity, required a weaker output grating with a less pronounced side-lobe structure.

However, both cavities had residual unabsorbed pump power, indicating that the conversion efficiency could be improved by further optimization of the grating reflectivity. The observed issue with recurring side-lobes may be mitigated by use of a better phase-mask, and by the use of Gaussian apodization for the FBG inscription process. Further optimization of the LR grating could be done by post-processing, where for example the grating reflectivity could be reduced by subsequent UV exposure without a phase-mask [75] or thermal annealing.

For the high-Q cavity it was shown that smaller changes in relative grating alignment caused large variations in the output spectrum and power. The results suggest that the increased alignment sensitivity is due to spectral broadening, which cause the decrease in slope efficiency observed for some configurations. In comparison, the low-Q cavity displayed increased slope efficiency with no signs of spectral broadening and with an output linewidth lower than the output FBG bandwidth. The issue of spectral broadening was therefore reduced by the decrease in circulating cavity power occurring as a result from the longer cavity and a lower output FBG reflectivity.

The challenge when using FBGs with a narrow bandwidth to define a cavity is, apart from the potential spectral broadening, that small perturbations in the FBG alignment leads to a large variation in both emission spectrum and output power. The stability analysis demonstrate that relative alignment between the

two FBGs is crucial to both the output power and the shape and quality of the output spectrum. While the complexity of the output spectrum is affected by the presence of recurring side-lobes in the FBG spectrum, this issue may be mitigated by use of a better phase-mask.

As a consequence of the improved cavity design including active feedback temperature control, a driftless output was obtained for 680 mW output power at 1680 nm. A high spectral stability was obtained, with a sub-pm standard deviation in the emission wavelength and linewidth. Furthermore, a 0.43% standard deviation in the measured output power could be obtained.

3.5 Raman Amplifier

This section concerns the work on RAs which resulted in the following publications [81, 82]. Stimulated Raman scattering (SRS) has been subject to much attention within the field of fiber lasers and amplifiers as it provides an extended wavelength coverage in comparison to rare-earth based devices. Motivated by the projected capacity crunch [22], different approaches are being explored to increase the capacity of communication systems [99, 100], both long and short range systems.

One approach is by exploiting new optical wavelength bands, outside the conventional communication window from 1530 nm to 1625 nm. In the development of lasers and amplifiers in the short wave IR above the Erbium band, SRS appears a promising candidate. We demonstrate a PM RFL, which acts as a pump for a RA at 1810 nm. The lasing wavelength of a RFL, thus also for a RA, can in principle be designed arbitrarily within the entire wavelength range from the Erbium band up to the Thulium/Holmium band by the utilization of cascaded SRS [29]. The main challenge when designing a long wavelength RA is the increased intrinsic fiber attenuation which as a consequence leads to an increase in the pump power requirement and deteriorated noise properties. To balance the increasing loss, a high Raman gain coefficient is required, and can be realized by higher Germanium doping concentration and smaller effective area of the fiber. Furthermore there is an inherent scaling of the Raman gain coefficient, which as a consequence reduces the Raman efficiency for longer wavelengths.

Distributed RAs are known to have superior noise properties when compared to discrete rare earth based amplifiers, such as the Erbium doped fiber amplifier (EDFA) [101]. The best reported EDFA noise figures are just above the quantum noise limit [102], whereas a recent demonstration of a long wavelength Thulium doped fiber amplifier (TDFA) operating between 1910 and 2020 nm, showed a 6.3 dB noise figure (NF) for 30 dB gain [103]. Whereas discrete EDFAs are limited to the 3 dB quantum noise limit, the effective noise figure (NF) for a distributed RA may below this limit and can even be negative [104]. In this work we present a distributed RA operating around a 1810 nm wavelength which provides an on/off gain exceeding 20 dB with an effective NF below 3 dB.

3.5.1 Experimental Setup

The experimental setup is shown in fig. 3.13. The RFL outlined in fig. 3.13a is pumped at 1564 nm and lases at the first stokes shift which peaks at 1679 nm (i.e. 13 THz lower than the pump), and was described in section 3.4. The monolithic RFL has a 140 m cavity length and consists solely of PM fiber. The output is linearly polarized with a polarization extinction ratio (PER) exceeding 20 dB. The RFL was described in section 3.4.

The RA is pumped by the RFL, and is based on a 4.2 km length of identical PM Raman fiber from OFS Fitel Denmark. The effective area and Raman gain coefficient for the fiber was shown in fig. 3.1a on page 30 , along with the measured transmission loss in fig. 3.1b. Pumped at 1679 nm, The amplifier gain peaks at 1810 nm. The fiber has a transmission loss of 0.46 dB/km at the 1679 nm pump wavelength and 1.64 dB/km at 1810 nm. Based on the specified effective area of the fiber, the effective area was extrapolated in section 3.3 and estimated to 27.7 μm^2 at 1810 nm. Based on Eq. eq. (3.3) and the estimated effective area of the fiber at 1810 nm, the specified Raman gain was scaled to the signal wavelength. From the ~ 5 $W^{-1}km^{-1}$ Raman gain coefficient specified for a 1453 nm pump wavelength, a 3.32 $W^{-1}km^{-1}$ Raman gain coefficient is predicted at a 1679 nm pump wavelength.

A Thulium based ASE source is used for the characterization of the fiber transmission loss, and as the signal for the characterization of the RA gain. The source utilizes a segment of highly doped Thulium fiber from OFS Fitel Denmark, and is shown in the outline of the experimental setup in fig. 3.13b. The fiber is pumped through a circulator with a 1600 nm pump amplified with an L-band EDFA. The unpolarized ASE emission is polarized utilizing a fiber polarizer, with an output spectrum that remained stable in time throughout the duration of the experiments. The ASE emission spectrum is shown in fig. 3.13a and extends from 1600 nm to 2000 nm, peaking near 1820 nm.

In the first configuration of the RA illustrated in fig. 3.13c, the pump is linearly polarized and is propagated along the slow axis of the fiber. The injected signal is also linearly polarized and launched along the same axis. The Raman gain in this configuration depends on $\chi^{(3)}_{iiii}$, and has a maximum at a 13 THz frequency downshift from the 1679 nm pump at 1810 nm. The amplifier is pumped backwards with respect to the signal propagation direction, to avoid the issue of intensity noise transfer from the RFL to the RA.

In the second RA configuration illustrated in fig. 3.13d, the pump is linearly polarized and launched along the fast axis of the fiber. The signal is linearly polarized but aligned orthogonal to the pump in the slow axis. The pump and signal are combined using a PM fiber polarization beam splitter and are propagating along the same direction. A PM polarizer at the output of the RA is utilized to filter out the residual pump but also the dominant part of the ASE which is generated along the fast (pump) axis. In this configuration the Raman gain depends solely on $\chi^{(3)}_{ijji}$ which is smaller by more than a factor of ten compared to $\chi^{(3)}_{iiii}$, and has a different frequency response [105].

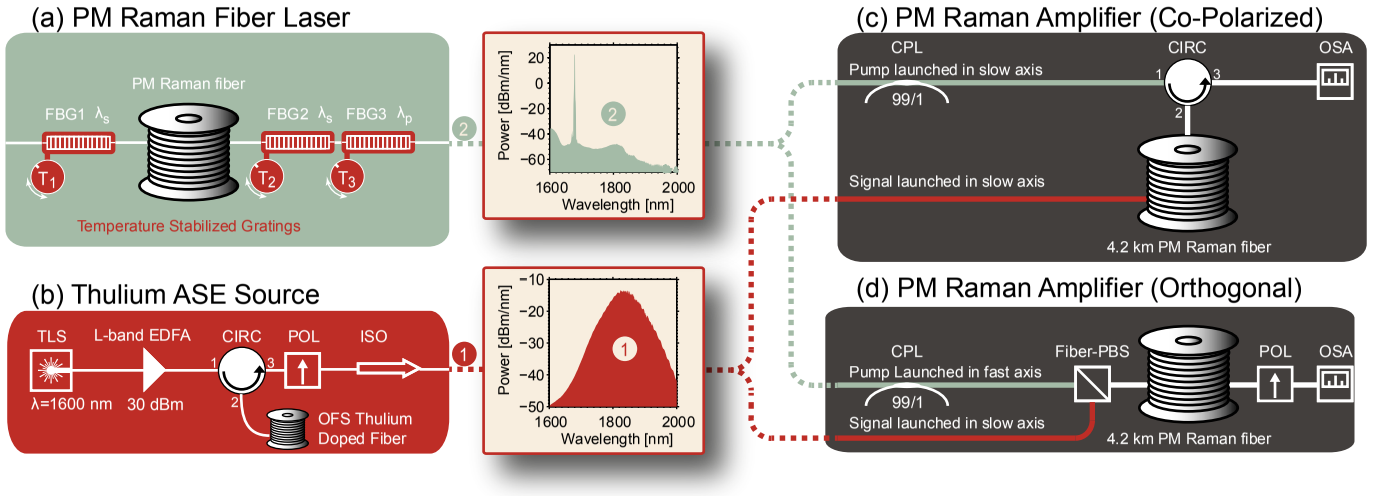

Figure 3.13: Experimental setup of the PM Raman fiber amplifier. (a) Raman fiber laser at a 1679 nm wavelength, acting as pump for the RA, shown along with the pump output spectrum. (b) Thulium based ASE source plotted along with the ASE output spectrum. The ASE source is pumped by a 1600 nm pump laser, using a circulator to remove the pump seed. The ASE is linearly polarized using a PM fiber coupled polarizer. (c) Setup used to characterize the co-polarized Raman gain, when launching both the signal and pump along the slow axis of the fiber. (d) Setup used to characterize the orthogonal Raman gain, when the pump is launched along the slow axis, and the ASE signal is launched along the fast axis. In both (c) and (d) a 4.2 km segment of OFS PM Raman fiber is used, where the pump is launched in the reverse direction with respect to the signal.

3.5.2 Experimental results

Based on the experimental setup shown in fig. 3.13, the Raman gain was characterized in the two amplifier configurations. The Raman gain was measured for a range of pump powers up to $\sim$ 400 mW for both linearly co-polarized and orthogonal pump and signal, as shown in figure fig. 3.14. A peak gain of 20.8 dB is obtained for 377 mW injected pump power at 1810 nm for the co-polarized configuration, as shown in fig. 3.14(a). For the on/off gain measurements the signal power was adjusted to be above the amplifier ASE power level throughout the characterized wavelength span.

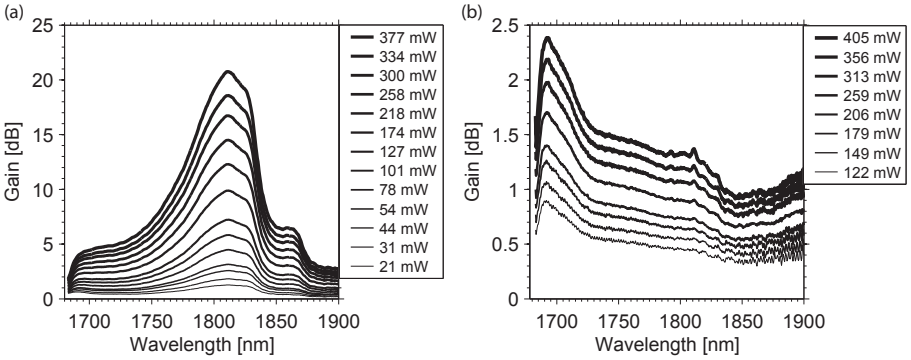

Figure 3.14: (a) Measured Raman gain for linearly co-polarized pump and signal for the listed range of injected pump powers. (b) Measured Raman gain for linearly polarized orthogonal pump and signal.

For the measured orthogonal Raman gain plotted in fig. 3.14b the gain peaks at 1693 nm with a 2.4 dB maximum gain for 405 mW injected pump power. Around 1810 nm some residual ASE is seen at increased pump powers. This part of the ASE is generated in the fast (pump) axis, and is not filtered out completely due to decreased polarizer performance at this wavelength.

The Raman gain coefficient, g_R is calculated from eq. (3.1) based on a linear fit to the measured Raman gain from eq. (3.1)a and eq. (3.1)b. The calculated Raman gain coefficient is plotted in fig. 3.15a, along with the linear correlation coefficient R from the fit. For the measured linearly co-polarized Raman gain, a peak gain coefficient of 3.76 $\mathrm{W^{-1}km^{-1}}$ was found. For the orthogonal configuration the Raman gain coefficient is shown in fig. 3.15b, with a 0.36 $\mathrm{W^{-1}km^{-1}}$ peak Raman gain coefficient. No saturation of the amplifier was observed, which is also confirmed by the high linearity ($R > 0.9999$) of the fit to the gain curve at the peak gain at 1810 nm. Based on the measured parameters, calculations using the coupled power equations [91] have shown signal transparency at 1810 nm for a distributed Raman amplifier for fiber lengths up to 40 km for the same amount of pump power.

The polarization dependence of the Raman gain is important in Raman amplifiers as it requires accurate control of the polarization of the signal and pump. For Raman amplifiers utilizing a depolarized pump, the polarization sensitivity can be avoided at the cost of a reduction in the overall Raman gain

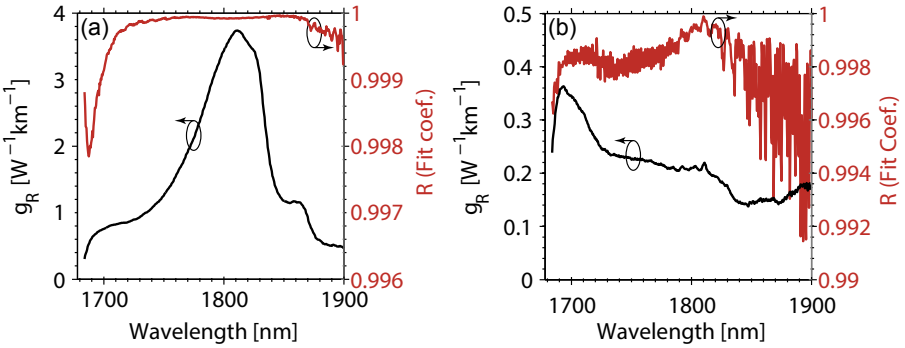

Figure 3.15: Measured Raman gain coefficient calculated based on Eq. eq. (3.1)*, along with the linear correlation coefficient R from the linear fit. (a) Co-polarized configuration. (b) orthogonal configuration.*

coefficient. The reduction comes from the average of the susceptibilities $\chi^{(3)}_{iiii}$ and $\chi^{(3)}_{ijji}$ for a depolarized pump in shown in Eq. eq. (3.2). For short pulses the Raman gain can cause the soliton self-frequency shift, for which energy within the pulse is transferred from higher to lower frequencies [84]. Therefore, as the co-polarized and orthogonal Raman gain is of similar magnitude close to the pump, the polarization sensitive nature of the Raman gain should be considered as it might affect the polarization properties of the signal.

3.5.3 Measured noise figure

The NF is a quantification of the degradation in the signal to noise (SNR) ratio of the signal when it is amplified, and is given by [91]:

$$\mathrm{NF} = \frac{2 \cdot \tilde{n} + 1}{G} \quad , \quad \tilde{n} = \frac{P_{\mathrm{ase}}}{h\nu B_0} \quad , \tag{3.4}$$

where G is the gain, $\tilde{n}$ is the number of noise photons, P_{ase} is the measured ASE power in the amplifier, h is plancs constant, ν is the frequency and B_o is the bandwidth. To compare the NF of a distributed Raman amplifier with a discrete amplifier, such as an EDFA or TDFA, the effective NF should be calculated [91]:

$$\mathrm{NF}_{\mathrm{eff}} = F \cdot \exp(-\alpha_s L) \quad , \tag{3.5}$$

where α_s is the signal transmission loss and L is the fiber length. The amplifier NF, calculated based on Eq. eq. (3.4) and eq. (3.5), is plotted in fig. 3.16(a) for the co-polarized configuration and in fig. 3.16(b) for the orthogonal configuration. The NF was calculated from the measured gain spectrum from fig. 3.14, along with the measured ASE spectrum of the amplifier in absence of a signal. The effective NF for the co-polarized Raman gain is plotted for three different signal wavelengths in fig. 3.16(a), where the dashed line corresponds to the wavelength where the gain is maximum. It can be seen that the NF decreases as the pump power and the corresponding on/off gain is increased.

At the Raman Gain peak with a 20.8 dB on/off gain the NF is 2.1 dB, with a NF between 1.3 and 2.9 dB across a 20 nm wavelength span from 1800 nm to 1820 nm.

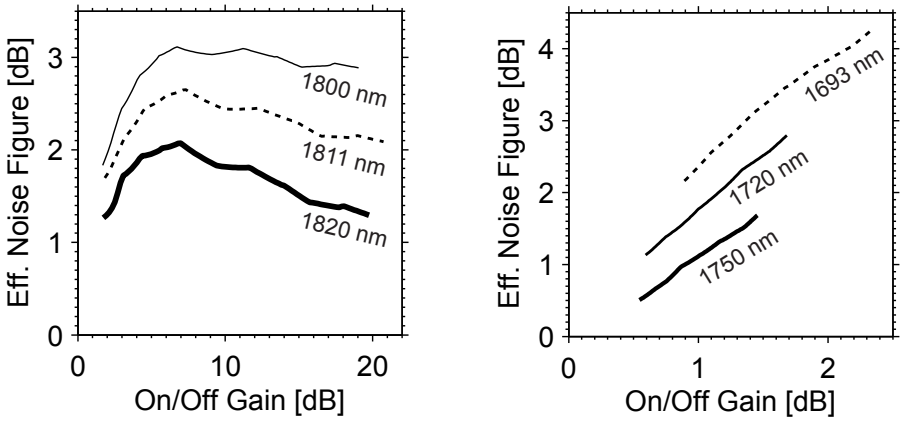

Figure 3.16: Measured effective noise figure of the Raman amplifier for the two characterized configurations, plotted as a function of the Raman gain. The noise figure was measured for different wavelengths, as indicated, where the dotted line corresponds to the wavelength of maximum gain. (a) Effective noise figure for the co-polarized configuration. (b) Effective noise figure for the orthogonal configuration.

For the orthogonal configuration the NF is plotted in fig. 3.16(b), at three wavelengths within the Raman gain. The dashed line corresponds to the gain peak located at 1693 nm. In this case the effective NF is found to increase with the pump power and associated on/off gain. More detailed measurements of the RA NF are included in appendix B.1 on page 142.

3.6 Summary

Two RFLs with different cavity designs were investigated. Due to a narrow spectral bandwidth of the cavity FBGs, spectral broadening was found to limit the performance of the investigated 61 m high-Q cavity. To investigate this further, a low-Q cavity was realized by increasing the cavity length to 140 m and using an weaker output FBG with a lower reflectivity. The improved cavity design mitigated the issues resulting from spectral broadening in the RFL cavity.

The investigation demonstrated that accurate alignment and stabilization by temperature control of the cavity FBGs was crucial to the laser performance. It was found that a $\sim 0.8^o$C increase in the grating temperature caused a 50% reduction in output power. A driftless output was obtained for 680 mW output power at 1679 nm along with a high spectral stability. A sub-pm standard deviation in the emission wavelength and linewidth was demonstrated in addition to a 0.43% standard deviation in the measured output power.

Subsequently, the 140 m RFL emitting at a 1679 nm wavelength was used for realizing a RA operating around a 1810 nm wavelength. The Raman gain of

the amplifier was characterized from 1680 to 1900 nm for different polarization configuratons, and a Raman gain exceeding 20 dB at 1810 nm along with a <3 dB effective noise figure was demonstrated.

Part II

Femtosecond fiber laser for tunable fiber-optic Cherenkov radiation

Chapter 4

Passively mode-locked femtosecond laser source

> A scientific truth does not triumph by convincing its opponents and making them see the light, but rather because its opponents eventually die and a new generation grows up that is familiar with it.
>
> Max Planck

This chapter describes the fiber laser system that was used for the experiments demonstrated in chapter 6. The laser oscillator and chirped pulse amplification (CPA) is described in sections 4.2 and 4.3, and the autocorrelation (AC) and frequency-resolved optical gating (FROG) pulse characterization techniques are described in section 4.4. The final pump pulses are characterized in section 4.5, where the tunability of the final pulse duration and power is investigated. The laser performance using two different fiber compressor fibers is compared in section 4.5.1 and section 4.5.2. Some efforts were invested in making a copy of the laser oscillator, which is described in section 4.6.

The oscillator and CPA is build by Xiaomin Liu and Dmitry Turchinovich, and my contribution to the work described in this chapter, is focused on the characterization and optimization of the combined laser system described in sections 4.5 and 4.6.

4.1 Introdution to mode-locked lasers

The modern development of nonlinear optics and ultrafast fiber laser phenomena is build upon the pioneering work from the beginning of the 1960s, from the first demonstration of light generated by a nonlinear process in 1961 by Franken *et al.* [6], the development of the first fiber laser by Koester *et al.* in

1964 [8] and the first demonstration of the ultrafast laser in 1966 by De Maria [9]. The development of different mode-locking techniques has lead to further advancements in ultrafast lasers [106, 107]. The generation of ultrashort pulses was dominated by the passively mode-locked dye laser until the end of the 1980s [108], and enabled the first generation of sub-picosecond pulses in 1974 [109], subsequently for pulse durations down to 27 fs [110]. During the 1990s, the dye laser was surpassed by the Ti:sapphire laser for the role of being the lab workhorse, with pulse durations down to the two-cycle regime [111]. The development of ultrafast fiber lasers has progressed far from the miliwatt average power level in the 1960s [112–116]. Current state-of-the-art systems have average powers in the kW range, and peak powers in the tens of GW range [117].

Modern ultrafast fiber lasers normally rely on passive mode-locking techniques, using either a saturable absorber such as the semiconductor saturable absorber mirror (SESAM), or a so-called artificial saturable absorber. The artificial saturable absorber is realized by nonlinear optics, i.e. Kerr lens mode-locking or nonlinear polarization evolution nonlinear polarization evolution (NPE). NPE mode-locking, also termed polarization additive-pulse mode-locking (APM), relies on nonlinear polarization rotation and can provide sub-100 fs pulse durations [113, 118, 119]. Mode-locked soliton lasers [120], such as the figure-eight laser [121] rely on the nonlinear amplifying loop mirror (NALM) mode-locking technique [122], are limited in output power, and are therefore typically used in a CPA configuration. However, dispersion managed soliton lasers, operating in the stretched pulse regime, can reach higher pulse energies [123].

Within the last decade, several new fiber laser designs have been demonstrated [124]. Work on self similar pulse propagation in fiber lasers have attracted a lot of attention [125–127], and permit much higher oscillator pulse energies than the previous soliton lasers and dispersion managed soliton lasers [128]. The all normal dispersive (ANDi) laser, which relies on a propagating dissipative soliton, permits scaling of the pulse energy to unprecedented levels, with pulse energies exceeding 100 nJ [129–132]. However, such laser systems typically rely on free-space components for the NPE saturable absorber and the compressor. In the following section the all-fiber laser system used for the experiments is described.

4.2 The master oscillator

The oscillator design itself is described in detail by Xiaomin *et al.* in [133–135] and is investigated further in section 4.6. The all-fiber oscillator, which is polarization maintaining (PM), has a small net anomalous dispersion, and is therefore operated in the weakly stretched pulse regime [136]. Passively mode-locking is initiated by a SESAM and a solid core photonic bandgap (SC-PBG) fiber is used for dispersion control. The gain and spectral filtering both helt to increase the mode-locking stability [123]. The oscillator design is similar to previous demonstrated non-PM fiber lasers, that rely on the SC-PBG fiber [137, 138]. The layout of the passively mode-locked all-fiber oscillator is shown

in fig. 4.1.

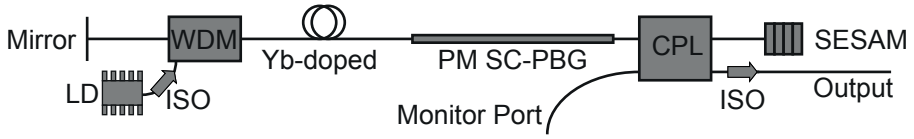

Figure 4.1: Experimental setup of the oscillator. The cavity contains a high-reflectivity fiber-coupled mirror, a laser diode (LD) coupled to wavelength demultiplexer (WDM) for separation of the 980 nm pump light and the light emitted at 1035 nm, a section of highly Ytterbium doped fiber, a section of PM solid core photonic bandgap (PM SC-PBG) fiber, a 20/80% coupler for extracting the output and monitor signal (CPL), a semiconductor saturable absorber mirror (SESAM). The output port is spliced directly to an isolator (ISO), while the end facet of the monitor output has an 8° angle cleave.

The oscillator has a 3.6 m cavity length of which contains a 32-cm segment of Yb-doped PM gain fiber [139] and a 1.21 m segment of SC-PBG fiber from *NKT Photonics A/S* for dispersion management and stabilization [140]. The residual 207 cm fiber in the cavity, mainly fiber leads connecting the different fiber-components, is PM980 Panda fiber. The dispersion for the different fiber elements is shown in fig. 4.2, with the net cavity dispersion being slight anomalous at the 1033 nm emission wavelength.

The pump LD for the Yb gain-fiber is grating stabilized, is centered at 976 nm and has a 120 mW operating power [141], delivered by a single moded *puremode HP980* pigtail. The LD is coupled into the cavity through a 980 nm isolator using a wavelength-division multiplexing (WDM). The LD isolator was found to be crucial as the LD output would otherwise become unstable, thus prohibiting stable mode-locking. It is believed that back-reflections at the pump wavelength causes instabilities in the LD, which as a result breaks the stable mode-locking.

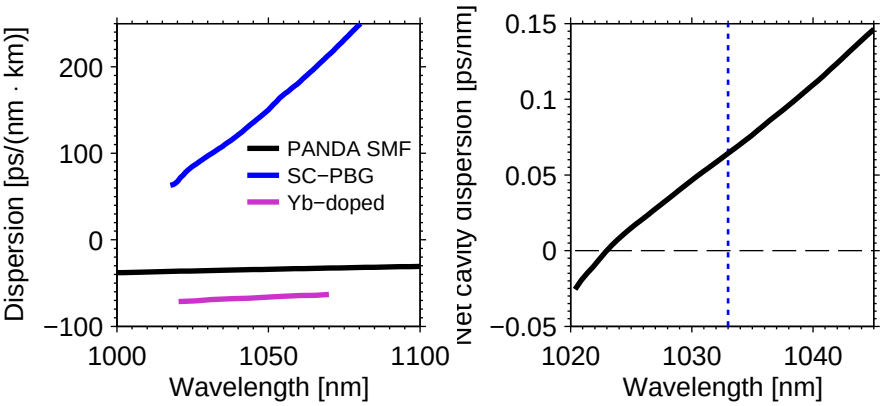

*Figure 4.2: **(left)** Comparison of the dispersion for the different optical fibers within the cavity. **(right)** Estimated net cavity dispersion.*

Passive mode-locking of the oscillator is initiated by a fiber-coupled SESAM,

manufactured by Batop, designed for 1040 nm operation with a 500 fs relaxation time, 40% absorbance, and 24% modulation depth [142].

The output and monitor signals are extracted using a 80 : 20 coupler (CPL). The monitor-port output is cleaved at an 8° angle to minimize back-reflections. The output signal passes through an isolator, also for the purpose of eliminating back-reflections, which would otherwise cause instabilities of the oscillator.

The oscillator emits a 28.77 MHz mode-locked pulse train, depicted in fig. 4.3, with an average output power of 1-1.5 mW. The pulses emitted from the oscillator are centered around 1033 nm, with a 7 nm full-width half maximum (FWHM) output bandwidth and an auto-correlation FWHM of 328 fs, as depicted in fig. 4.5. With the AC having a near Gaussian shape in the time domain, and thus assuming a $\sqrt{2}$ deconvolution ratio (see section 4.4.1), the corresponding FWHM pulse duration is 232 fs.

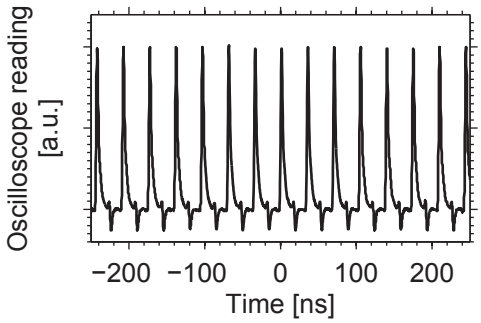

Figure 4.3: Measured 28.77 MHz repetition rate pulse train, measured at the monitor port of the oscillator.

4.3 The chirped pulse amplifier (CPA)

To amplify the ∼1 mW fs pulses from the oscillator, a chirped pulse amplifier system is utilized [143, 144]. To achieve a robust system with a compact footprint and a high degree of environmental stability, the CPA is fully monolithic, and relies fiber based stretcher and compressor, instead of free-space prism [145] or grating based compressors [146]. The experimental setup for the complete pump laser system is shown in fig. 4.4, and uses a hollow-core (HC) photonic crystal fiber (PCF) is used for the pump pulse recompression [147].

In the first stage of the CPA, the fs pulses emitted from the oscillator are stretched by approximately 75× to a ∼ 24.5 ps pulse duration, in a 35 m segment of PM980 Panda fiber in order to decrease he nonlinear effect in the following amplifier and compressor parts. The stretched pulse is then amplified in a pre-amplifier and a power-amplifier, based on highly doped Yb gain fiber [148] containing 80 cm and 1 m Yb-doped fiber, respectively. The power-amplifier stage is pumped through a PM WDM by a 750 mW grating stabilized PM980 pigtailed 974 nm laser pump diode [149]. The pump pulses are subsequently compressed in a HC PCF from NKT photonics A/S, termed HC-1060-02 and

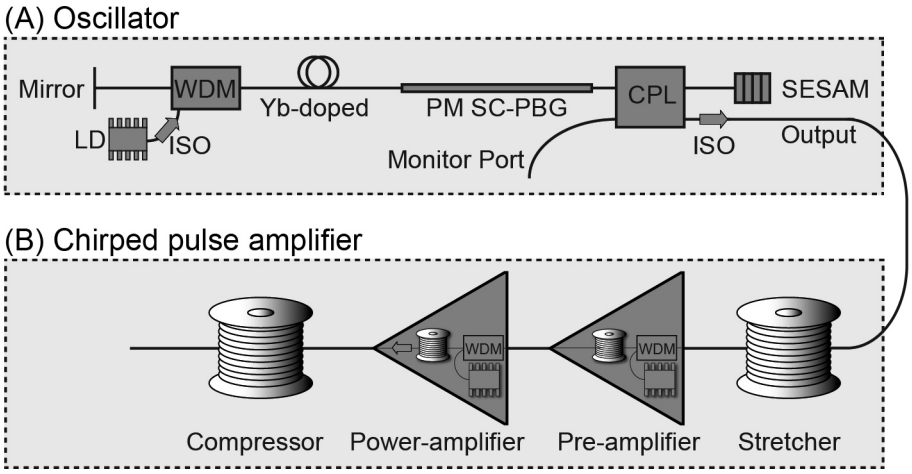

Figure 4.4: Illustration of the combined oscillator, CPA and compressor setup. The setup of the oscillator was described in fig. 4.1. The Chirped pulse amplifier consists of a segment of PM980 stretcher fiber, a pre- and power amplifier setup each pumped using a WDM and a 974 nm pump diode, before entering the pulse compression fiber through a high power fiber isolator.

is described in more detail in section 4.3.1. The transmission loss of the HC PCF compressor is approximately 2.2 dB, including the PM980 to HC PCF splice loss, with final average output powers up to ∼230 mW.

The AC trace and optical spectrum is plotted for different positions along the CPA chain in fig. 4.5. The modulation in the output spectrum introduced at the amplifier output is caused by the isolator.

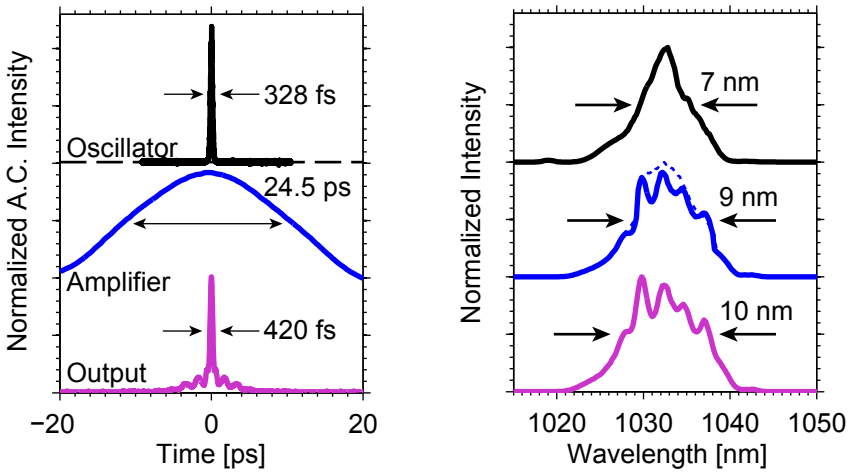

*Figure 4.5: **(left)** Measured AC at the oscillator, amplifier and final output. **(right)** Measured corresponding output spectrum. The dashed line shows the measured output spectrum before the isolator. Measurements at the courtesy of Xiaomin Liu [133].*

4.3.1 The hollow-core compression fiber

The HC fiber used as compressor for the all-fiber CPA, has a positive dispersion of the order 70-100 $\mathrm{ps \cdot nm^{-1} \cdot km^{-1}}$ around the 1033 nm wavelength, enabling it to balance the chirp induced by the panda PM980 stretch fiber. The fiber parameters for the HC-1060-02 fiber are presented in table 4.1.

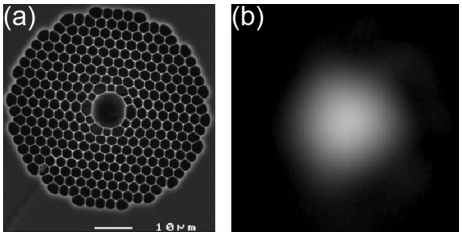

Figure 4.6: (a) SEM image of the microstructured part of the HC fiber [150]. (b) Measured HC output near-field at the pump wavelength.

In the experiments described in chapter 6, two different HC fibers, termed HC-1060-02 and HC-1060-03-FUD were used. The structure of the HC-1060-02 fiber is shown in fig. 4.6, which shows both a scanning electron microscope (SEM) image of the HC end-facet and the measured output near-field at the pump wavelength.

Dispersion @1060 nm	120	$\mathrm{ps \cdot nm^{-1} \cdot km^{-1}}$
Dispersion slope @1060 nm	1	$\mathrm{ps \cdot nm^{-2} \cdot km^{-1}}$
Mode field diameter	7.5 ± 1	μm
Zero dispersion wavelength	1010.5	nm
Core diameter	10 ± 1	μm

Table 4.1: Fiber parameters specified for HC-1060-02 [150].

The transmission window of the HC-1060-02 fiber extends across 100 nm, with a $\leq$0.1 dB/m transmission loss from 1010 to 1110 nm. If properly spliced and aligned, the $\Delta n = 1.65 \cdot 10^{-4}$ [151] birefringence of the fiber would maintain the linear polarizaiton of the pulses emitted from the amplifier, with a polarization extinction ratio (PER) between 10 and 14 dB. The splicing of the HC PCF and P980 panda fiber was performed on a *Ericsson FSU 995 PM Arc Fusion splicer*, with a typical splicing loss of 0.62 ± 0.24 dB and a PER of 19 ± 0.68 dB [151].

The quality of the final pulse shape at the CPA output, depends on the level of self-phase modulation (SPM) in the amplifier and on how well the dispersion of the HC PCF matches the stretch fiber. The second order dispersion, also termed the group velocity dispersion (GVD), can be compensated by selecting the right length of the compression fiber relative to the fiber stretcher, whereas uncompensated third order dispersion (TOD) deteriorate the final pulse shape. By modifying the compression fiber length the pulse duration can be optimized for a given power.

Output facet degradation

Experimental observations showed that following a fresh cleave of the HC-1060-02 output fiber facet, the output power would degrade in the matter of hours or days, depending on the usage. Visual inspection of the output facet with an infrared fiber scope, revealed a noticeable increase in scattered light. The increased scattering is suspected to be caused by glass chemistry in the HC-1060-02 host glass occurring under use [152].

For the measurements described in chapter 6 that were carried out using the HC-1060-02 compression fiber, a re-cleave of the HC-1060-02 end-facet prior to each measurement session is required, followed by a re-alignment of the coupling to the fiber under test (FUT). The HC PCF was cleaved with a ceramic tile or fiber-scribe, shortening the fiber by as little as possible and typically ∼2-5 mm, to limit the changes of the pulse shape and duration.

Revised hollow core pulse compression fiber (HC-1060-03-FUD)

To avoid re-alignment of the experimental setup prior to each measurement session, a new pulse compression fiber with similar specifications was investigated. The fiber, termed HC-1060-03-FUD, is a test fiber from NKT Photonics A/S, and is manufactured from a different glass composition that should offer improved long-term reliability by eliminating output facet degradation. The performance of the HC-1060-02 and HC-1060-03-FUD is compared in section 4.5.2.

4.4 Pulse characterization techniques

4.4.1 Intensity auto-correlation

When dealing with ultra short pulses in the fs-range, the response time of photo-diodes, and the speed of electronics becomes a limiting factor. Even with a *state of the art* 50 GHz oscilloscope and a 60 GHz photodetector, measuring a 5 ps pulse will yield a signal FWHM of 12.2 ps [153]. The standard method for characterizing short pulses and the workhorse in many labs, is the intensity or interferometric AC setup [154, 155]. The technique is widely adopted as the setup is simple, easy to operate, and offers a fast and sub-Hz measurement speed. The major drawback of this method, is that estimating the temporal pulse shape based on the measured AC trace, requires some assumptions to the expected pulse shape. This poses some limits to the insight gained when dealing with more complex pulses.

In the intensity AC setup, a second harmonic generation (SHG) signal which proportional to $E(t)E(t-\tau)$is generated, where τ is the delay, $E(t)$ is the signal input and $E(t-\tau)$ is the delayed signal:

$$I_{\mathrm{sig}}^{\mathrm{SHG}}(t,\tau) \propto I(t)I(t-\tau) \quad . \tag{4.1}$$

When measuring the SHG signal with a photodiode (PD), which is inherently slow compared to the pulse duration (t), the measured AC signal at a

delay τ is given by the integral:

$$I_{\mathrm{AC}}(\tau) \propto \int_{-\infty}^{\infty} I(t)I(t-\tau)dt \quad , \tag{4.2}$$

which is defined as the intensity AC. It should be noticed that following from eq. (4.2), the AC is always symmetric, which can be shown by a simple variable change from t to $t-\tau$. The conversion between the measured AC FWHM and the pulse duration FWHM, depends on the pulse shape and the associated deconvolution factor. For a Gaussian pulse shape the deconvolution factor is $\sqrt{2}$, for $\mathrm{sech}^2(t)$ shaped pulses the deconvolution factor is 1.543.

The AC setup used for all subsequent pulse characterization, is home build, with the experimental setup outlined in fig. 4.7. The collimated beam is passed through a polarizer and a half-wave plate, to ensure the alignment of the linearly polarized signal. The depicted setup can be used for both AC or FROG measurements, as it contains both an oscillating corner mirror and a high precision stage. When the setup is used for AC measurements, the stage remains fixed.

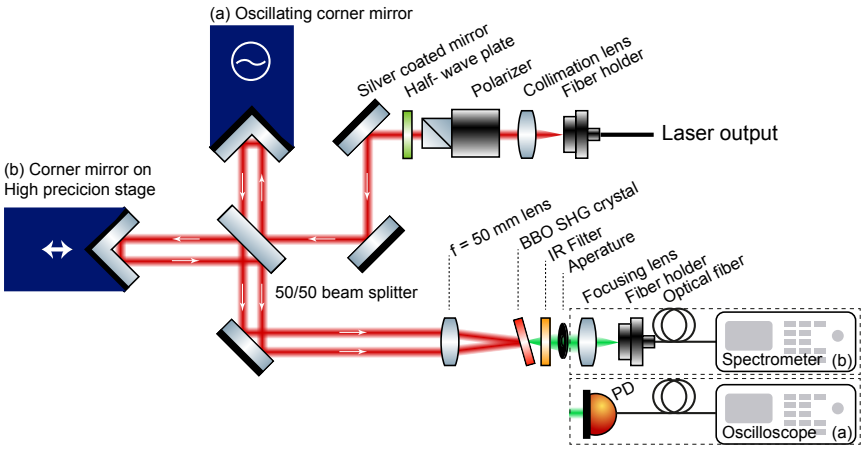

Figure 4.7: Illustration of the combined (a) AC and (b) FROG setup. The oscillating corner mirror is used for the AC measurement, whereas the corner mirror on the high precision translation stage is used for the FROG measurement. Both systems rely on the same beta barium borate (BBO) SHG crystal, however with different detection systems. The AC setup uses a PD and an oscilloscope, while the FROG setup uses a spectrometer.

The beam-splitter divides the signal beams to the two arms in a 50:50 ratio, with one half going to the oscillating mirror, and the other half going to the stage, now acting simply as a delay stage. When the beams are combined with the beam-splitter, half of the signal from each arm is lost. The two beams are then focused with a $f = 50$ mm lens into a BBO crystal for SHG.

Phase-matching of the SHG signal is obtained by rotating the BBO crystal relative to the incident beam. An infrared (IR) filter is used to remove any residual signal from the green SHG signal. Besides the intensity AC SHG signal which oscillates according to the corner mirror, two constant SHG signals

generated from each of the two arms are located spatially and symmetrically on each side of the intensity AC SHG signal. These are filtered out using an aperture placed in front of the PD. For the AC measurements, a biased Silicon based photo detector (*Thorlabs DET36A/M*) with a sensitivity from 350 to 1100 nm was used.

The oscillator, a *ScanDelay 150* from German *APE*, provides a close to linear displacement in time with a scan range up to 11.25 mm, corresponding to 150 ps in the time domain. When connected to an oscilloscope, a *Tektronix TDS2024B*, it provides a live 'displacement versus time' output. When combined with the PD signal, it provides an $I_{\mathrm{SHG}}(z)$ signal which is captured and processed by LabView. The measurement speed is dependent on the APE ScanDelay oscillation frequency, which is between 0.1 and 10 Hz.

4.4.2 Frequency resolved optical gating (FROG)

The FROG measurement technique is a method capable of retrieving both the temporal shape and phase of a pulse without any knowledge or assumptions to the pulse shape [156]. This is a problem that cannot be solved by only knowing the measured AC and spectrum for a pulse. The FROG method is based on the measurement of a spectrogram of the pulse, which can be done by using either a gate pulse or the pulse itself, followed by the solving the "two-dimensional phase-retrieval problem," which is a well known problem that occurs commonly in astronomy and x-ray diffraction [156]. The algorithm used to retrieve the pulse shape and phase is based on [157], and is described in detail by Trebino [156]. Alternative solutions include cross correlation FROG [158] which requires a gate pulse shorter that the investigated pulse, and the fringe resolved AC method [155].

The experimental implementation of FROG is using SHG, which can be described as the spectrally resolved AC. For the FROG measurement the measured spectrum detected by the spectrometer can be expressed as:

$$I_{\mathrm{FROG}}^{\mathrm{SHG}}(\omega, t) \propto \left| \int_{-\infty}^{\infty} E_{\mathrm{sig}}(t, \tau) \exp\left(-i\omega t\right) dt \right| \quad , \tag{4.3}$$

where $E_{\mathrm{sig}}(t, \tau) = E(t)E(t - \tau)$. The measured time and frequency data is the spectrogram of the pulse. Similar to the AC measurements the measured spectrogram is symmetric in time, hence providing an ambiguity to the direction of time and the sign of the retrieved phase. In this work a commercial software package from *FemtoSoft* is used to retrieve the pulse shape and phase from the measurement data.

In comparison to the AC measurement the FROG measurement technique, provides more detailed and unambiguous information regarding the pulse. While the AC measurement is performed live with a ∼Hz sampling rate, measuring the pulse using the FROG setup in its current implementation is time consuming. Measuring the FROG trace generally takes a few minutes, while the required data analysis can take between a few minutes and up to an hour, which limits its use to some degree. There are however commercial solutions, capable of performing live measurements with sub-Hz sampling rates [159].

As touched upon in section 4.4.1, the pulse characterization setup shown in fig. 4.7 can be used for either auto-correlations or FROG measurements. When performing FROG measurements the mirror oscillator remains fixed while a high precision stage[1], with 1μm stepsize, provides incremental translation steps. For each translation step the filtered SHG signal is measured with an *Ocean optics HD2000+* spectrometer. Typical parameters for the FROG setup, are 5-10 μm translation increments and between 64 and 512 steps depending on the complexity of the pulse and the pulse length.

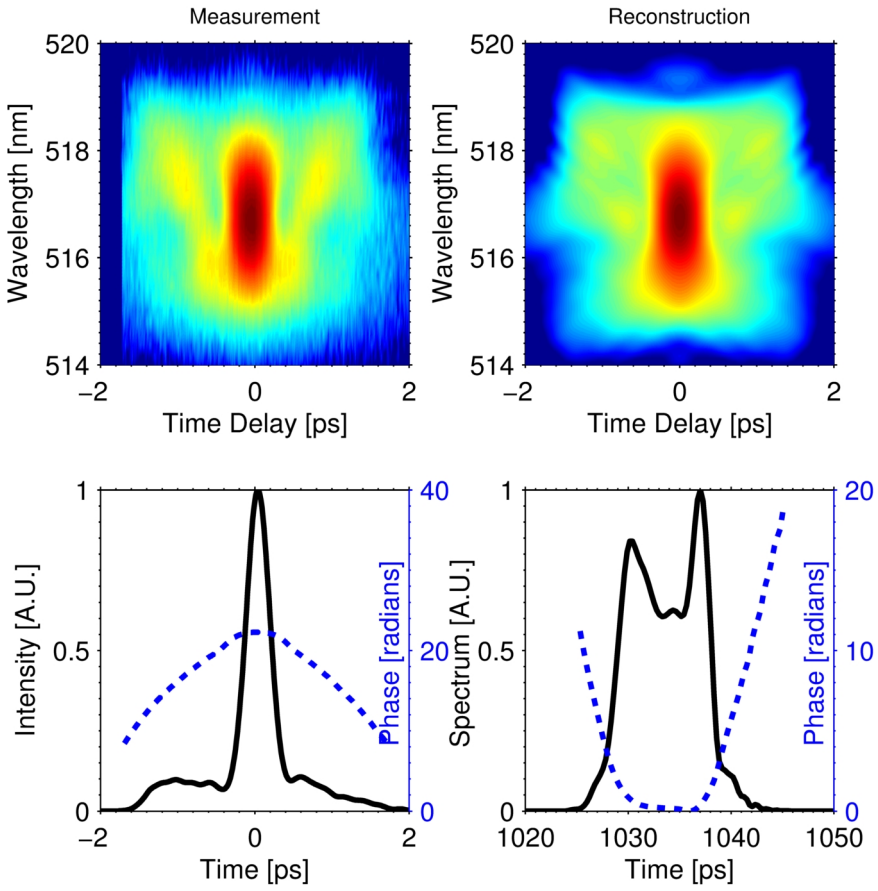

Figure 4.8: Color plot of the measured FROG spectrogram shown in comparison to the FROG reconstruction. The derived temporal pulse shape is plotted along with the phase in addition to the spectral shape and phase. The pulse compression was performed using the HC-1060-02 fiber. The error in the FROG retrieval is 0.55%.

In fig. 4.8 an example of a measured SHG FROG spectrogram is plotted along with the FROG reconstruction. The retrieved temporal pulse shape and

[1]Newport M-ILS250CC

phase is shown along with the spectrum and spectral phase.

Integration of the recorded SHG spectrum in the FROG trace, allows comparison between the computed intensity AC from the FROG setup with the discrete auto-correlation setup. This comparison is plotted in fig. 4.9, showing close correspondence between the two AC traces. The retrieved temporal pulse shape and phase is plotted along with the intensity AC in fig. 4.9. Upon examination of the FROG retrieved pulse shape, the comparison shows that the broader background on the AC trace is caused by long uniform pulse pedestal. Similar to the SHG AC the SHG FROG method has an ambiguity to the direction of time.

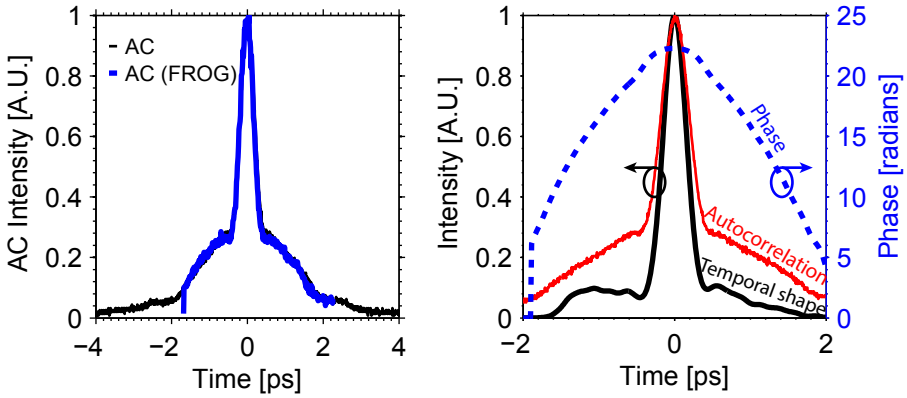

Figure 4.9: ***(left)*** *Intensity AC trace measured with the autocorrelator using a PD and an oscilloscope, shown in comparison with the AC trace derived from the FROG measurement using the sp ectrometer and translation stage.* ***(right)*** *Direct comparison between the measured AC trace from the AC setup and the FROG derived temporal pulse shape and phase.*

The SHG FROG method relies on phase-matching in the BBO crystal across the whole pulse spectrum. To investigate the dependence upon phase-matching different parts of the spectrum, three FROG measurements were performed and compared. The FROG trace was measured by optimizing the phase matching angle for the blue, central and red part of the spectrum. The pulse-retrieval algorithm was used individually on all three discrete measurements, and compared with the retrieved pulse-shape from an average of the three measurements above. In spite of a noticable difference in the recorded spectrogram, the findings showed small variation in the retrieved pulse shape, and are shown in appendix C.6.

4.5 Pump pulse characterization

The final duration of the emitted pulses, is the result of an interplay between the initial seed pulse from the oscillator and the CPA system. As will be shown in section 4.5.1, the properties of the pulses emitted from the laser can be modified electronically, by adjusting and balancing the LD pump power to the

oscillator, pre-amplifier and power-amplifier, respectively. The motivation for controlling the emitted pulse duration, is that for applications such as fiber-optic Cherenkov radiation (FCR) which may have a strong reaction to the changes in pulse-duration. This is a topic that will be discussed in greater in chapter 5.

4.5.1 The output pulse duration

Within the stable mode-locking regime, it was found that the oscillator LD could be adjusted to affect the seed pulse. This section deals with the laser performance, including the effects of the CPA, while using the HC-1060-02 fiber.

An example is shown in fig. 4.10, where the retrieved pulse shape from a FROG measurement is shown for two different configurations of the oscillator and CPA, demonstrating a change in the final pulse duration from 393 to 664 fs.

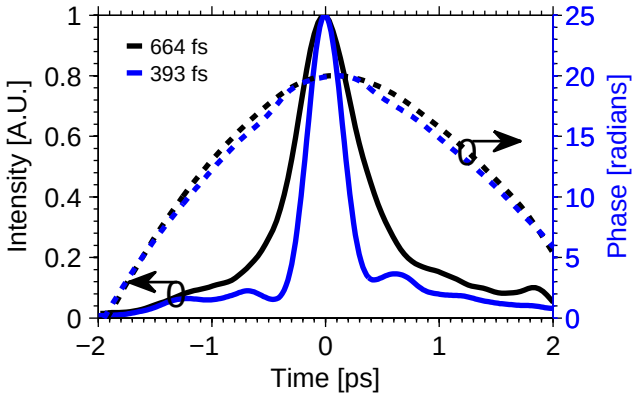

Figure 4.10: Comparison of the temporal pulse shape and phase for two different laser configurations, where the pulse duration is varied from 393 to 664 fs.

By adjusting the pump power of the individual LDs, it is possible to modify the pulse duration and output power. The trends are shown in fig. 4.11, where each of the three LDs for the oscillator, pre- and power-amplifier were adjusted individually.

This provides 3 degrees of freedom in controlling the pump pulse properties. The interplay of adjusting the oscillator and the pre- and power-amplifier pump levels simultaneously, allows for accurate control of both the pump pulse duration and output power. This can for instance be used as a method for adjusting the pulse duration while keeping the output power level constant.

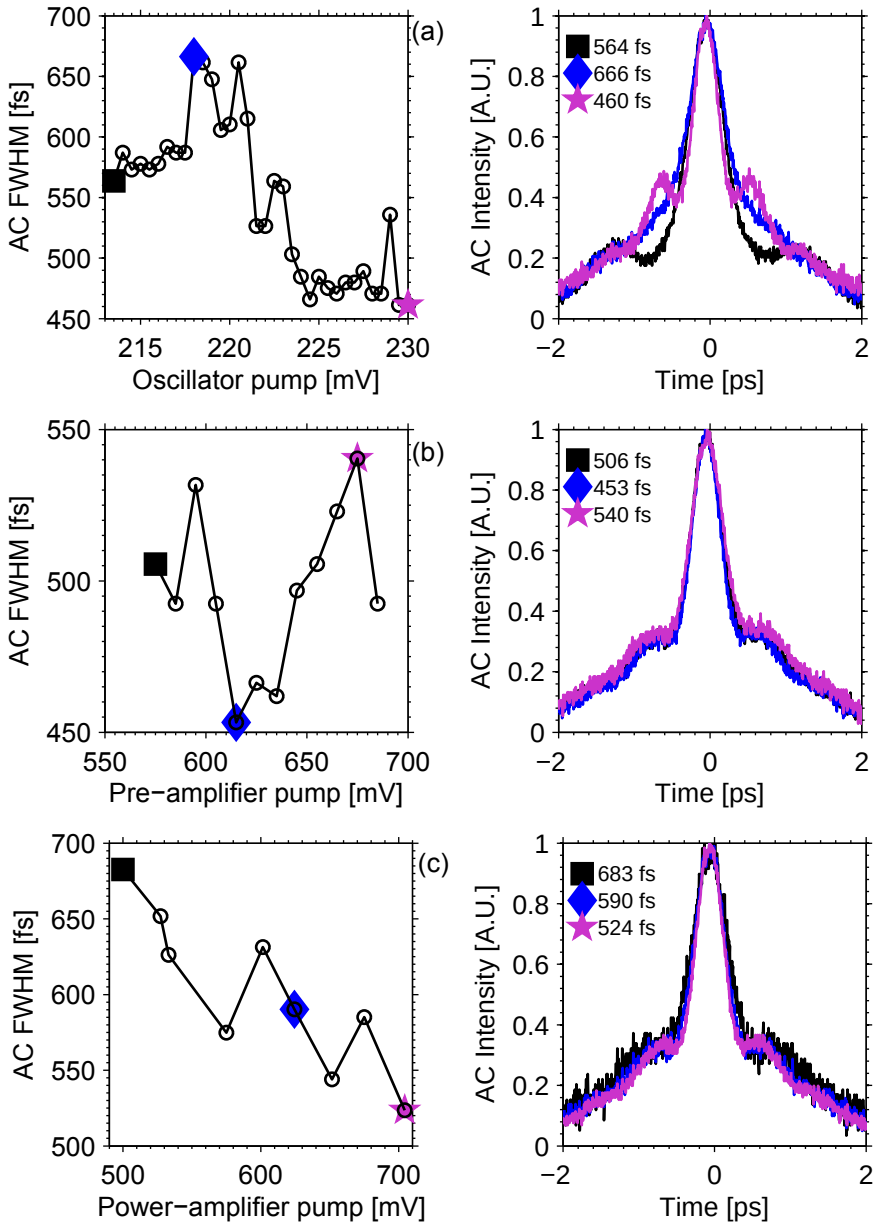

Figure 4.11: Auto-correlation of the final output from the HC-1060-02 fiber when tweaking each of the laser LDs individually. The measured AC FWHM is plotted in addition the AC trace for three different settings for (a) the oscillator LD, (b) the pre-amplifier LD and (c) the power-amplifier LD.

4.5.2 Performance with the new compression fiber

The HC-1030-03-FUD fiber, which is a development fiber from NKT Photonics, was supplied without any specifications. Apart from the different glass composition, it was expected to have similar properties to the HC-1060-02 fiber it replaces.

For the HC-1060-02 based compressor, a 21 m fiber length was required for pulse re-compression. Due to a different dispersion for the HC-1060-03-FUD fiber, a shorter fiber length was required.

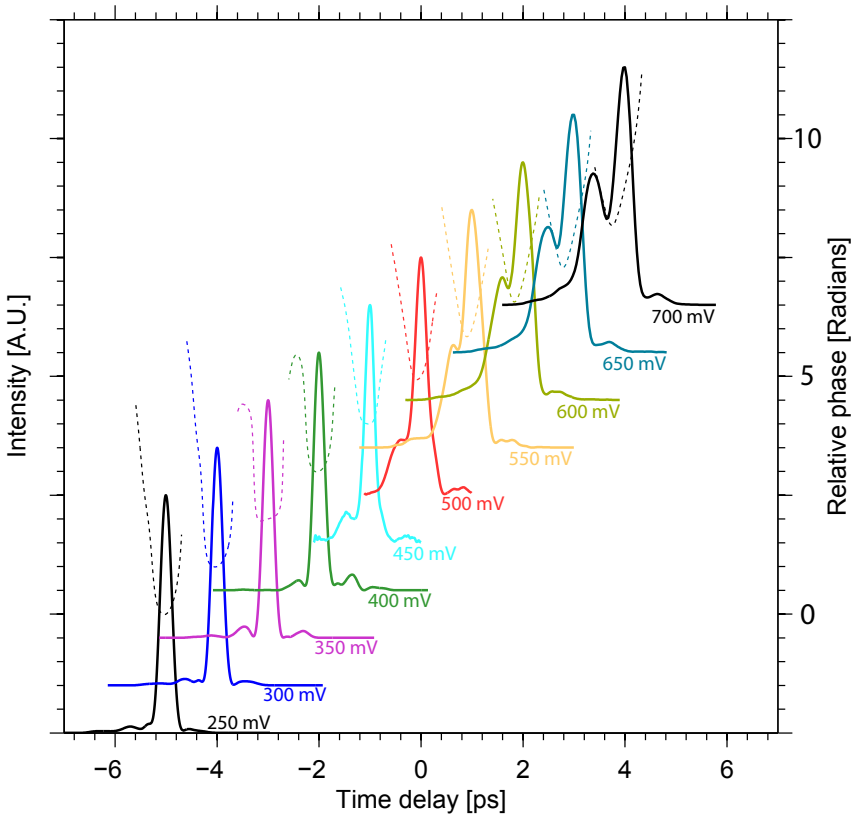

Figure 4.12: Retrieved temporal pulse shape (solid lines) plotted for a range of pump powers along with the temporal phase in radians (dashed line). The amplifier LD pump power is increased incrementally (see labels), with output powers ranging between ∼ 70 and ∼ 230 mW (see appendix C.5). Measured for 226 mV oscillator setting and 639 mV pre-amplifier setting.

During the optimization of the length of the compression fiber, both the output pulses were characterized with AC and FROG measurements for each consecutive cutback. The initial HC compressor fiber length was 20.6 m. Autocorrelation and FROG measurements indicated that further cutback was required (see appendix C.2). After a total cutback length of 6.58 m, and a final

HC fiber length of 14.0 m, the optimum compressor length was obtained for a 450 mV power-amplifier setting at 157 mW average output power.

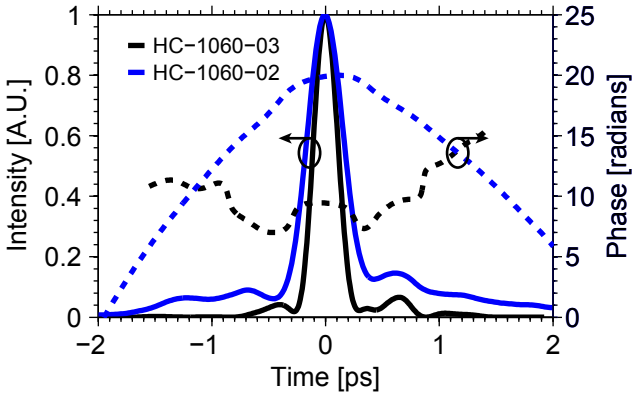

Figure 4.13: Retrieved pulse shape and phase using the HC-1060-02 and HC-1060-03 compression fibers, for the shortest possible pulse duration. The pulse duration is 379 fs for the HC-1060-02 fiber and 239 fs for the HC-1060-03 fiber.

It turned out that in addition to a higher dispersion, the dispersion profile of the HC-1060-03 was also slightly different from that of the HC-1060-02, which provided better compensation for the chirp induced by the stretcher fiber. The result is shown in fig. 4.13, comparing the shortest output pulse that could be obtained with the HC-1060-02, which is 397 fs. Using the new HC-1060-03 compression fiber the pump pulses could be compressed down to a 239 fs pulse duration, presumably due to better higher order dispersion compensation.

The temporal pulse shape and phase across the power-amplifier tuning range is plotted in fig. 4.12. From the plot it is evident that the pulse duration decreases as the pump power is increasing from a 250 mV to 450 mV power amplifier setting. At higher pump powers, the pulse duration increases while an increasing chirp across the pulse starts to appear. The output power increases very close to linearly from $\sim$ 70 mW at a 250 mV power amplifier setting to $\sim$ 230 mW at a 700 mV power amplifier setting, but depends on the setting of both the oscillator and the CPA which remained fixed. The output power versus amplifier power setting is listed for different configurations in appendix C.5.

The results from fig. 4.12 are summarized in fig. 4.14 for the lower power range, which show the pulse duration measured by both FROG and AC for different settings. The results in fig. 4.14 are plotted for two different pre-amplifier values and are shown for the a 250 to 500 mV power-amplifier range. The shortest pulse duration could easily be shifted to a higher output power by changing the HC PCF length relative to the stretcher fiber length. However, the 239 fs pulse duration obtained with a 157 mW average output power is sufficient for the experiments carried out in chapter 6. A full comparison of the pump pulses across the whole power-amplifier span is listed in figs. C.3 and C.4.

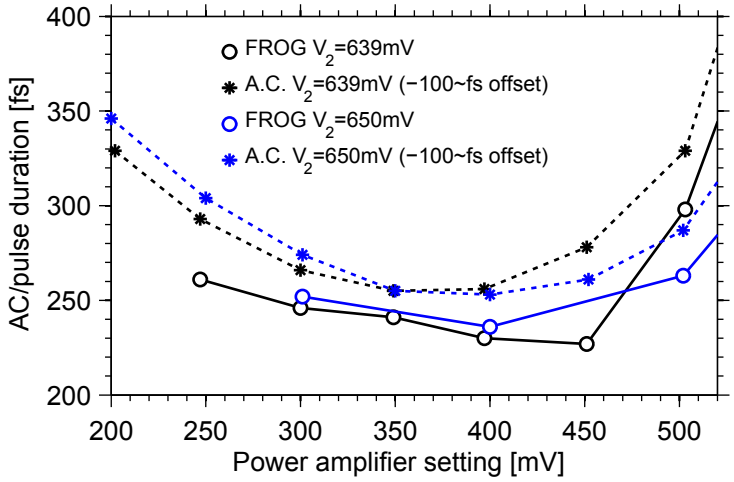

Figure 4.14: Comparison of the measured AC duration and the retrieved pulse duration using FROG for different power amplifier settings. The AC duration is offset by −100 fs. The pulses where characterized for two different pre-amplifier settings, while the oscillator setting remained fixed at 230 mV. The corresponding output powers are listed in the appendix in appendix C.5.

4.6 Replicating the all-fiber laser oscillator

This chapter is an account on the efforts invested to replicate the fs oscillator described in section 4.2, and is motivated by the need of having an additional fs laser system working in tandem for the experiments on FCR.

The operating principles of the oscillator is described in section 4.2, and the experimental layout of the setup is identical to the setup shown in fig. 4.1. Throughout the following chapter the oscillator described in section 4.2 is referred to as the *reference oscillator*. The crucial components, such as the SESAM, PM SC-PBG dispersion compensation fiber and the Yb-doped gain fiber have the same specifications as the components used in the reference oscillator.

As the cavity was constructed, each component was tested rigorously, before each fiber-coupled component was spliced. The splicing of the PM Panda fibers was performed on a *Ericsson FSU 995 PM Arc Fusion splicer*, where each splice was inspected both by IR scope and by inspecting the recorded heat-image recorded on the fiber splicer during the fusion splicing process. Only splices that upon inspection looked perfect and which had an estimated PER$\geq$ 35 dB were accepted.

The PM SC-PBG fiber manufactured by *NKT Photonics* which is used for dispersion compensation and spectral filtering in the cavity, was from the same spool as the fiber used for the oscillator described in section 4.2. Therefore it was expected that the dispersion properties would be similar to the reference oscillator. The splicing of the PM Panda fiber to the PM SC-PBG fiber were performed on a *Vytran FFS 2000* splicer at *Danish fundamental metrol-*

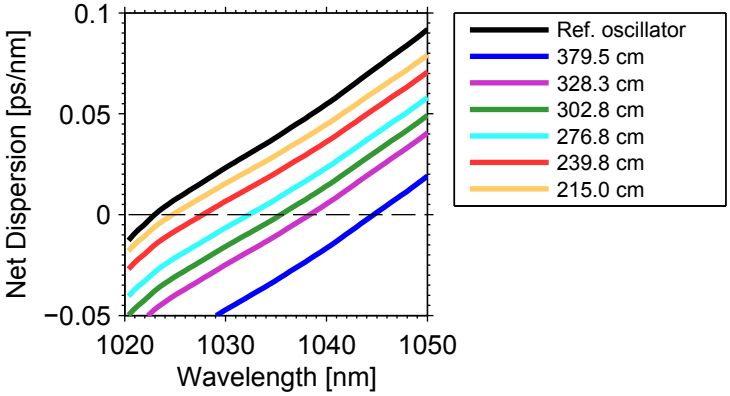

Figure 4.15: Estimated net dispersion for the oscillator cavity denoted (a) for different PM Panda fiber cutbacks. For comparison the net cavity dispersion for the reference oscillator is shown. The legend denotes the length of PM980 fiber in the cavity. The cavity contains 112 cm SC-PBG fiber and 24 cm Yb-doped gain fiber (30 cm for the ***blue*** *curve). The repetition rate varies from 19.7 MHz for 379.5 cm PM panda fiber to 30.97 MHz at 215 cm PM panda fiber.*

ogy (DFM), while the transmission, PER and near-field output images were monitored.

As previous attempts on reproducing the oscillator have failed, also while using the same SC-PBG dispersion compensation fiber, it was later suspected that there were variations in the fiber parameters along the length of the SC-PBG fiber spool. As a result, iterative cutback of the PM980 fiber in the cavity was performed, to test the laser for a broad range of different net cavity dispersion.

In fig. 4.15 the estimated net cavity dispersion is listed for a range of cutbacks of the PM Panda fiber. The net cavity dispersion is calculated from the dispersion profiles shown in fig. 4.2, and are shown in comparison with the reference oscillator. The accumulated round-trip loss of the oscillator is shown in fig. 4.16, measured without the Yb-doped gain fiber, and plotted along with the PM SC-PBG transmission. The loss window is quite flat between 1025 and 1045 nm with a normalized transmission $\geq$95%.

A total of 5 cavities were investigated, containing different lengths of SC-PBG fiber and for different net cavity dispersion:

Cavity (a): 112 cm SC-PBG fiber (19.7 to 30.97 MHz repetition rate)

Cavity (b): 121 cm SC-PBG fiber

Cavity (c): 112 cm SC-PBG fiber (23.15 to 33.5 MHz repetition rate)

Cavity (d): 177 cm SC-PBG fiber (13.07 to 28.07 MHz repetition rate)

Mode-locking

For cavity (a), two short instances of mode-locking was observed at two different cavity lengths corresponding a 23.13 and a 30.97 MHz repetition rate,

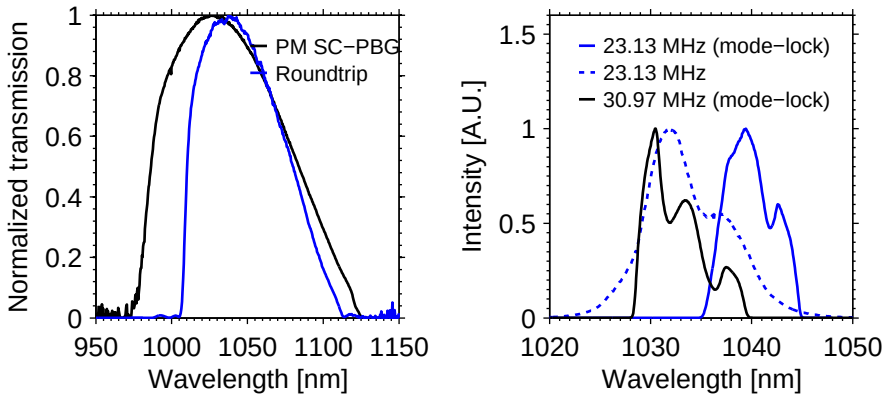

Figure 4.16: ***(left)*** *Shows the measured normalized transmission loss of the PM SC-PBG fiber along with the normalized cavity round-trip loss, measured excluding the Yb-doped gain fiber.* ***(right)*** *The output spectrum for cavity a shown for two different instances of mode-locking. The dashed line shows the output spectrum at a 23.13 MHz repetition rate without mode-locking for comparison.*

respectively. The change from Q-switching to stable mode-locking was clearly identified on the oscilloscope which was used to monitor the laser output using a PD. These two cavity lengths corresponds to the net dispersion profiles shown in **purple** and yellow in fig. 4.15, respectively. See table C.3 for a table listing the cutback lengths and repetition rates.

At a 23.13 MHz repetition rate, where stable mode-locking was obtained initially, the corresponding output spectrum is shown in fig. 4.16. The dashed line in fig. 4.16 shows the output spectrum obtained for Q-swtiching, which is blue-shifted by ∼10 nm relative to the mode-locked output spectrum. The laser remained mode-locked for a few hours, but not long enough for conducting an AC measurement.

As further mode-locking could not be obtained, subsequent cut-back measurements lead to a cavity length having a 30.97 MHz repetition rate, where mode-locking was obtained once again. The mode-locking remained stable across a range of pump powers, with Q-switching at higher pump powers up to a point where mode-locked double pulsing was observed. Examples of the pulse trains measured using the oscilloscope is shown for Q-switching and the regime of Q-switched mode-locking in appendix C.7, and for stable mode-locking for single and double pulsing in appendix C.8. These where measured for the cavity denoted (a) at 30.97 MHz repetition rate. Due to unknown reasons, the laser ceased mode-locking after a few days, despite rigorous attempts, and replacing the SESAM did not re-initiate mode-locking.

To rule out that the PM SC-PBG fiber or the two connecting splices had deteriorated in the course of the testing process, the PM SC-PBG fiber was removed from the cavity and replaced. A new 121 cm segment PM SC-PBG fiber was spliced to two short PM panda pigtails, repeating the above mentioned splicing and characterization process. Upon splicing into the cavity, denoted cavity (b), the cavity length was varied once again in vicinity of the

net cavity dispersion for the last obtained mode-locking. As these attempts did not facilitate mode-locking, it was decided to do a systematic replacement of the cavity components. Characterization of the replaced 112 cm PM SC-PBG fiber, revealed no deterioration in the transmission or PER properties.

Following the approach described for cavity (a), the cavity was build up again from scratch with the 112 cm PM SC-PBG fiber, while each fiber component was exchanged one at a time. For this cavity, denoted (c), five subsequent cutbacks were performed with a repetition rate ranging from 23.15 to 33.5 MHz. See table C.4 for a table listing the cavity details. During the cutbacks for cavity (c), no observations of mode-locking were found.

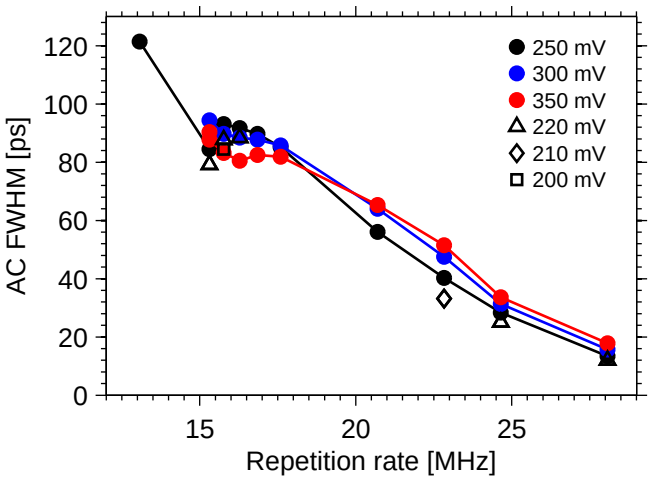

Figure 4.17: Measured AC pulse duration for the cavity denoted (d), plotted for different oscillator LD settings (i.e. pump power levels), and is based on a cavity containing 177 cm SC-PBG fiber. The pulse duration was measured for different repetition rates, during the process of shortening the cavity by iterative cutbacks of the cavity PM980 fiber.

A fourth cavity, denoted cavity (d), was assembled containing a much longer 177 cm PM SC-PBG fiber. During the subsequent cutback measurements of the PM980 fiber in the cavity, the pulse auto-correlation was measured for different oscillator pump settings, to quantize the change in pulse duration. This is shown in fig. 4.17. Here it is evident that the AC duration decreases as the repetition rate is increased.

Quantifying the pulse to pulse variation

When viewing the pulse train on a normal oscilloscope, a single-shot measurement of the pulse train provides some insight into the mode-locking stability. On a normal oscilloscope, a proper mode-locked pulse train is easily identified due to the high uniformity of the pulse train. However, outside the regime of stable mode-locking, a high speed sampling oscilloscope offers insight into the shot to shot variation, as it samples the pulse intensity from a series of pulses. To gain more insight into the laser stability, the *Tektronix TDS2024B*

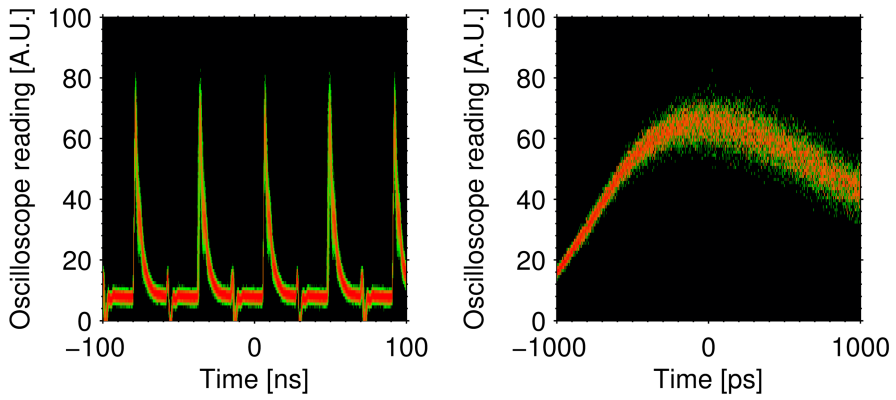

Figure 4.18: ***(left)*** *Color plot of the pulse train depicting the number of counts on a digital sample oscilloscope plotted as a function of relative trigger delay and intensity.* ***(right)*** *Color plot with a magnified view of the pulse peak.*

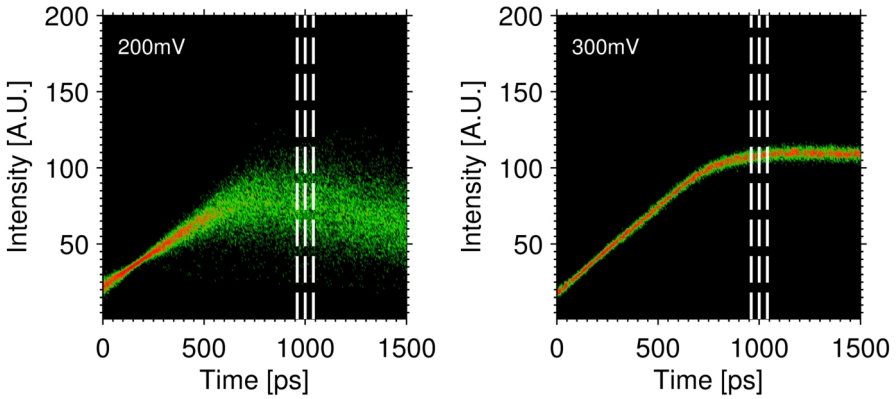

Figure 4.19: Color plot depicting the number of counts on a digital sample oscilloscope plotted as a function of relative trigger delay and intensity. The plot shows a magnified view of the pulse train, and compares the difference between a 200 mV ***(left)*** *and 300 mV* ***(right)*** *LD pump setting. The vertical resolution is 200, whereas the time resolution is 4 ps. The measurements are shown for cavity (d) at a 15.31 MHz repetition rate.*

oscilloscope was therefore replaced by a high speed digital phosphor oscilloscope (*Tektronix TDS7104 1 GHz 10 G/s*), that could be used to characterize the stability of the pulse train. An InGaAs PD with a 10 ns rise time was used (*Thorlabs DET10C/M*). An example of such a measurement is shown in fig. 4.18, where the sampled pulse train is plotted on a color plot, shows for both the pulse train, and a magnified view at the pulse peak. The plot is therefore a representation of the number of counts at a certain delay relative to the trigger time at a given PD intensity.

Measurements conducted for cavity (d) are shown in fig. 4.19 at a 15.31 MHz repetition rate, before the first cutback was performed. The plot shows a magnified view centered on the pulse peak from the oscilloscope, where the

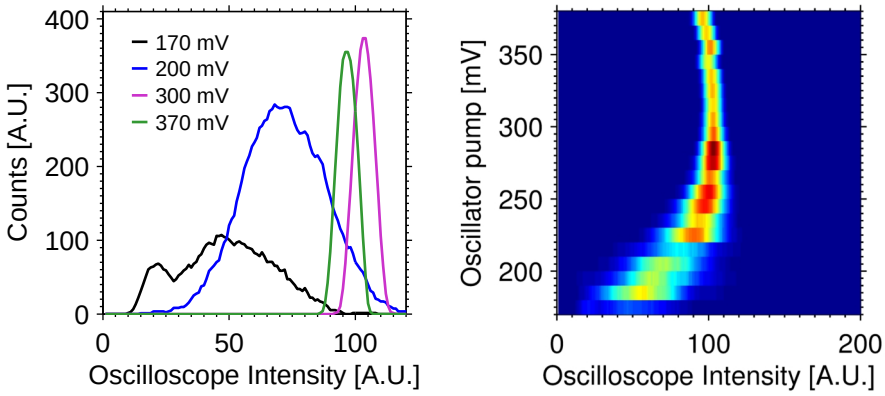

Figure 4.20: ***(left)*** *A plot of the counts at the intensity peak in fig. 4.19 averaged across the indicated 40 ps window, shown for four different LD pump settings.* ***(right)*** *Color plot depicting the variance in pulse power for a range of LD pump settings. Both plots are shown for cavity (d) at a 15.31 MHz repetition rate, before the first cutback*

intensity is resolved in 200 points and the time resolution is 4 ps. The two plots in fig. 4.19 shows a comparison for two different LD pump levels. At the 200 mV setting, there is a large shot to shot variation in the pulse duration, whereas at a 300 mV setting the variation is much smaller.

These results are summarized in fig. 4.20, which shows the average distribution across a small delay window at the peak oscilloscope signal marked with the dashed lines in fig. 4.19. By measuring the number of counts at a given oscilloscope intensity for a range of oscillator pump settings, the color-plot in fig. 4.20 can be computed. This color plot is a measure of the variance in the pulse to pulse power across a wide range of oscillator pump levels. From this plot it is evident that the pulse to pulse variation is smallest around a 300 mV LD setting.

By repeating this measurement for consecutive cutbacks of cavity (d), changes in the stability can be quantified. This is shown in fig. 4.21 for different cutback lengths with repetition rates ranging from 15.31 and 28.07 MHz. For the longest cavity, with a 15.31 MHz repetition rate, there seems to be a local minimum in the pulse to pulse variation around 300 mV oscillator LD setting. When comparing the measured pulse duration plotted in fig. 4.17 with the measure for the pulse to pulse variation in fig. 4.21, it is seen that while the pulse duration decreases when the repetition rate is increased, the pulse to pulse variation increases steadily. During the course of the performed measurements and cutback, there were no indications that the laser stability was improving, as the repetition rate and the net cavity dispersion was changed.

Summary

During the efforts of duplicating the reference oscillator, a total of four different cavities were tested. Under the course of testing, every single component in the cavity have been exchanged or replaced. The stable mode-locking that

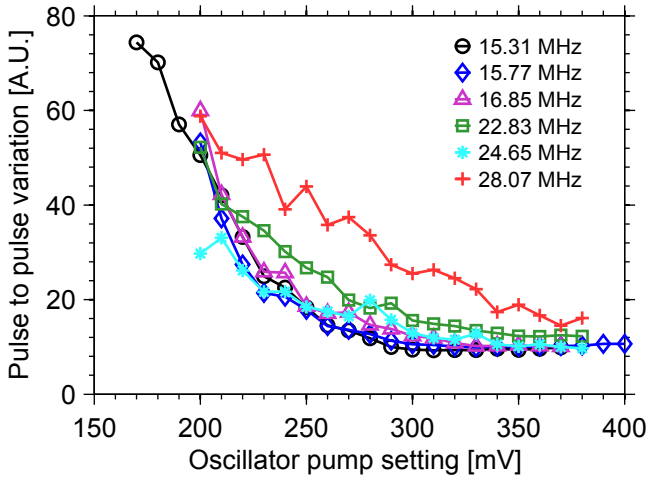

Figure 4.21: Measure of the pulse to pulse variation for different repetition rates for the cavity denoted (d), measured for a range of oscillator LD power settings.

was obtained at 1040 and at 1033 nm for the first of the four tested cavities, could not be reproduced. After exchanging all cavity components, the only components left are the PM SC-PBG segments which all come from the same fiber spool and batch. However, no plausible explanations could be found to answer why the cavity would suddenly cease to mode-lock, and why the repeated attempts did fail. Due to time constraints and because we wanted to proceed with the Cherenkov experiments described in chapters 5 and 6, this remains an unanswered question.

Chapter 5

The generation of Cherenkov radiation in optical fibers

> A scientist in his laboratory is not a mere technician: he is also a child confronting natural phenomena that impress him as though they were fairy tales.
>
> Marie Curie

This chapter is based on the publications [160–162] and describes the theory behind the generation of fiber-optic Cherenkov radiation (FCR) to provide a proper context for the experimental results presented in chapter 6. After a brief motivation of the FCR source (section 5.1) follows an introduction to a range of nonlinear phenomena and processes. The concept of optical solitons (section 5.2) and the mechanisms of soliton compression is described (section 5.2.1), which is the process responsible for the very localized nature of FCR generation obtained when pumping in the anomalous dispersion regime. The spatial pump compression point (CP) is described, and how it can be translated along the nonlinear fiber by controlling the properties of the pump pulse (section 5.2.2)

The basic principles behind supercontinuum (SC) generation are presented (section 5.3), leading to a discussion and comparison of the fundamental principles and noise properties of the FCR source (section 5.4). The noise properties for FCR are described and how it relates to the soliton order (N). To better understand these noise properties, the onset of modulation instability (MI) is described, thus motivating the use of ultrafast (fs) pump pulses for low noise applications.

The theory of Cherenkov phase-matching is described (section 5.5), in order to estimate the emission wavelength for the nonlinear fiber investigated in chapter 6. It is also demonstrated how the FCR phase-matching wavelength is affected when scaling the fiber structure down, e.g. by tapering down the nonlinear fiber. A discussion of reported ultrafast FCR systems is presented

in section 5.6. This is followed by numerical simulations on FCR generation based on the parameters for the pump laser system described in chapter 4 and the investigated nonlinear fiber. The presented results (figs. 5.1, 5.2, 5.7, 5.8 and 5.11 to 5.13) are obtained by solving the nonlinear Schrödinger equation (NLSE) numerically and were carried out by Jesper Lægsgaard. Predictions of FCR generated in a uniform nonlinear fiber are shown in section 5.7.

A method is proposed for extending the tunability of a FCR source. The concept is presented in section 5.8 and relies on a tapered fiber structure along with a pump laser system where the pump CP can be translated along the taper structure by modifying the pump pulse properties. Numerical results for FCR generated in different taper structures is described throughout section 5.9. These results seeks to shed light on the differences in the dynamics of the generated localized FCR along different parts of the taper; describing results for FCR generated along the down-taper (section 5.9.1) and up-taper (section 5.9.2).

5.1 Motivation and Background

From the invention of the low loss optical fiber by Kapron *et al.* in 1970 [163] and the mode-locked ultrafast laser by Ippen *et al.* in 1975 [164], the field of nonlinear optics has evolved rapidly. The invention of the nonlinear pure-silica photonic crystal fiber (PCF) fibers in the 1990s [19, 165] has attracted a lot of attention [166], especially due to their broadband transmission properties, endlessly single mode operation [18] and the possibility of dispersion engineering [167]. The development of PCFs lead to the first demonstration of SC generation in a PCF by Ranka *et al.* in 2000 [33], which sparked the so-called "supercontinuum revolution" in the start of the 21st century [168].

Many applications have benefited greatly from the availability of fiber based SC generation sources. Current commercial systems are characterized by a high spatial coherence and high spectral brightness along with an octave spanning emission spectrum. These properties makes SC usefull for a range of spectroscopy and imaging techniques, such as optical coherence tomography (OCT) [169, 170], two-photon excitation fluorescence (TPEF) [171, 172], fluorescence lifetime imaging microscopy (FLIM) [173, 174], stimulated emission depletion (STED) microscopy [175], and coherent anti-stokes Raman spectroscopy (CARS) [176, 177].

However, the stochastic nature of the large number of solitons comprising the SC output spectrum which are colliding and interacting, contribute to the noise properties that can limit some applications. The impact on relative intensity noise (RIN) from the SC source was investigated by Wang *et al.* [178], where it was demonstrated that RIN would degrade the performance for OCT applications. There should however be differentiated between the performance of typical commercial ps-pumped SC systems, and results on SC obtained using ultrafast pump fs pulses. The spectral coherence and RIN properties of such SC sources are described further in section 5.4.

Within the range of biophotonics there exists a number of applications that require low noise sources in the visible (VIS). FCR sources with emission in the

VIS are known to posses high coherence and low RIN [179, 180]. This topic is described in more detail in section 5.4.

Also, some applications in two-photon fluorescence (TPF) microscopy for biological samples require visible ultrafast pulses below 700 nm in the VIS [180, 181]. The ideal optical source for combined laser confocal scanning microscopy (LCSM) and FLIM [182] requires a picosecond or femtosecond narrowband pulse source, that is tunable across a wide wavelength range extending across the ultraviolet (UV) and VIS region (350-700 nm) [183]. The impact on RIN and spectral coherence for TPF and OCT using different FCR sources is described in great detail by Haohua *et al.* [180]. Recent results reported by Chan *et al.* [184] on nonlinear light microscopy (NLM) demonstrated TPF and second harmonic generation (SHG) microscopy techniques utilizing a FCR source. Further discussion of potential applications of FCR in biophotonics is presented in reference [183], while a detailed review on coherent SC and FCR for biophotonic applications is included in the reference [185].

5.2 Solitons and pulse compression

The soliton phenomena was first discovered as water-waves in the 1800s [186], and observed in optical fibers in 1980 by Mollenauer *et al.* [187]. Launching a pulse with sufficient pulse energy into an optical fiber with anomalous dispersion ($\beta_2 < 0$, $D > 0$), can lead to the excitation of a soliton [188], which is supported by a balance of dispersion and self-phase modulation (SPM). For a sech-shaped pulse with the temporal profile $\sqrt{P_0}\,\mathrm{sech}(t/t_0)$ launched in the anomalous dispersion regime, a soliton can be quantified by a soliton number:

$$N = \sqrt{\frac{\gamma P_0 t_0^2}{|\beta_2|}} \quad , \tag{5.1}$$

with t_0 being the pulse duration, P_0 the peak power, β_2 being the second order dispersion given by $\beta_2 = \mathrm{d}^2\beta/\mathrm{d}\omega^2$, where $\beta = n_{\mathrm{eff}}\frac{2\pi}{\lambda}$ is the propagation constant. γ is the nonlinear coefficient, which is given as $\gamma = k_0 n_2/A_{\mathrm{eff}}$, for a fiber with propagation constant k_0, with a nonlinear coefficient n_2 and an effective area A_{eff}.

5.2.1 Soliton pulse compression

For $N = 1$ in eq. (5.1) the solution is a stable fundamental soliton. If $N > 1$ a higher-order soliton can be excited. The solution to a higher-order soliton can be shown to oscillate periodically in the temporal and spectral domain [14].

In the most simple case, and in absence of other nonlinear effects, the soliton will simply oscillate back and forth in the spectral and temporal domain. The period of oscillations is given by the soliton period $z_{\mathrm{sol}} = \frac{\pi}{2}L_D$, with the dispersion length being defined as $L_D = T_0^2/|\beta_2|$. This approximation holds for longer pulse durations, low values of N, no loss, in absence of Raman scattering, and higher order dispersive effects.

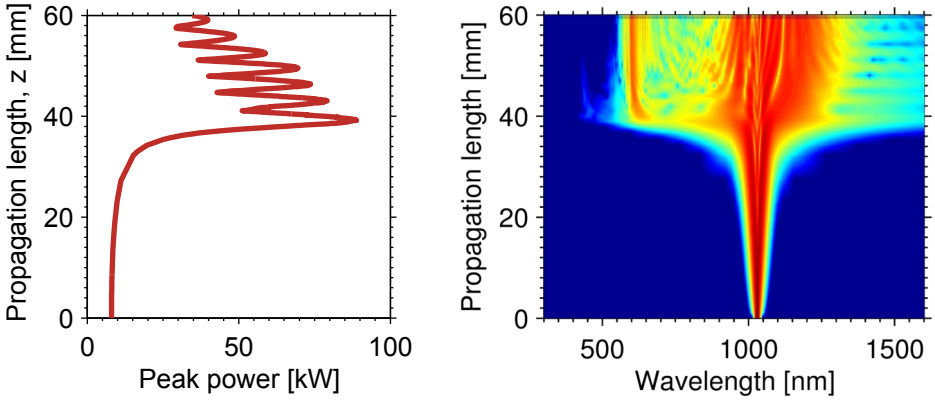

Figure 5.1: ***(left)*** *Temporal peak power along the fiber length.* ***(right)*** *Color plot of the output spectrum plotted along the fiber length. Calculated by Jesper Lægsgaard for a uniform fiber modeled after the NL-3.0-850 fiber described in section 6.1.1 with a 234 fs pump pulse duration, 2 nJ pulse energy and 8 kW peak power, corresponding to a 58 mW average power at a 29 MHz repetition rate.*

During the first part of the soliton period the pulse will undergo spectral broadening, effectively compressing the pulse temporally, which can increase the pulse peak power manifold. It was shown by Satsuma *et al.* [189] that the higher order solitons provides an 4.1×N pulse compression. The spatial point along the fiber where the the temporal pulse compression is highest is from hereon termed the CP. The propagation length at which the CP occurs can be parametrized in terms of the soliton number (N) of the input pump pulse [190]. For shorter pulse durations this initial compression, along with the presence of Raman scattering and higher order dispersion, will initiate a pulse break-up.

An example is shown in fig. 5.1, where the peak power along with the spectral evolution of the pump is shown for propagation along a nonlinear fiber. The results are based on numerical simulations obtained by solving the generalized nonlinear Schrödinger equation (GNLSE), for the parameters listed in the legend of fig. 5.1. The initial spectral broadening from 0 to 39 mm occurs due to SPM, culminating in a temporal peak power of $\sim$ 89 kW at 39 mm propagation length denoted the CP, that has increased by more than one order of magnitude from the 8 kW the input peak power. It is also evident from fig. 5.1 that the initial compressing point is accompanied by recurring recompression that are decreasing in peak power along the propagation length.

From the colorplot of spectral evolution shown in fig. 5.1, the initial SPM is clearly visible, and is followed by more complex dynamics from the initial pump CP and forwards. The emission of FCR generation, also known as dispersive wave (DW) generation, is visible at 610 nm. This VIS 610 nm light is generated spatially at the pump CP due to phase-matching in the nonlinear fiber. This particular phenomena is described in greater detail in section 5.5.

The localized pump CP is described by Austin *et al.* [191] with respect to both DW and SC generation. The DW generation region can be quantized

by defining the measured dispersive wave generation region (DWGR), as the spatial region along the fiber where the DW energy increases from 20% to 80% of its final value. Here, a 2-8 mm DWGR was obtained for pump pulses with soliton numbers (N) up to 10 [191].

5.2.2 Tuning the soliton compression point

Changing the input pump pulse parameters can lead to a change in the propagation length that is required to obtain pulse compression. The translational tuning of the pump pulse CP is shown in fig. 5.2, which is predicted for a 234 fs full-width half maximum (FWHM) pulse duration when varying the input peak power 4/6/8 kW, and with a corresponding 1/1.5/2 nJ pulse energy. The results show a 20 mm translational tuning when changing the pump power a factor of 2. This property can be exploited when using optical fiber tapers, a topic that is discussed in greater detail in section 5.8.

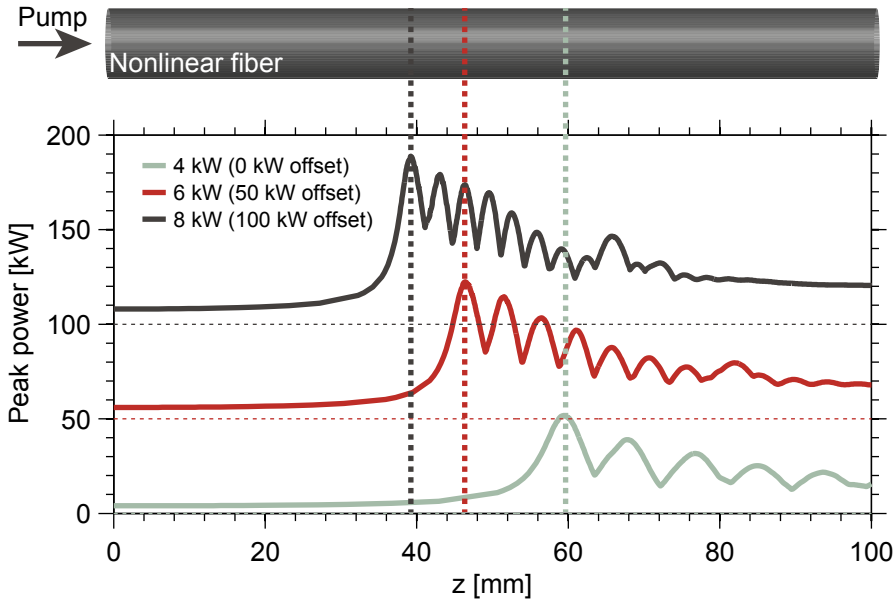

Figure 5.2: Numerical simulations for a 234 fs FWHM pump pulse duration, 4/6/8 kW input peak power at 1/1.5/2 nJ corresponding pulse energy. Calculated by Jesper Lægsgaard for a uniform fiber modeled after the NL-3.0-850 fiber described in section 6.1.1.

5.3 Supercontinuum generation

A SC source is characterized by a broad, typically octave-spanning output spectrum, and has come a long way since the first bulk demonstration in 1970 [192] and the first fiber-based demonstration in 1976 by Lin *et al.* [193, 194].

Accelerated by the development of PCFs [33] and advances in mode-locked all-fiber laser systems [34, 35] the SC source has matured into a commercially available product [36], now found on many lab benches and as turnkey systems e.g. in biology labs. The theory behind SC generation has been described extensively in the litterature [195]. Most of the currently available commercial systems, are ps pumped, and relies on MI to break up the initial pump pulse, which subsequently form a variety of "soliton-like-pulses" [196, 197]. These solitons, supported in the anomalous dispersion regime, generate dispersive waves in the normal dispersion regime. As the solitons propagate further, they redshift due to the stimulated Raman induced soliton self frequency shift [83, 84], but also blue-shift the dispersive waves due to a so-called trapping effect [198, 199]. In silica based systems, the red-part of the SC spectrum is limited by the increasing infrared transmission loss, which provides a cutoff around $\sim$ 2400 nm. This effectively limits the blue edge of the spectrum due to the trapping effect between the solitons and DWs [200].

5.4 Low noise Cherenkov radiation

The topic of noise in FCR and SC sources is not covered easily, and can be studied numerically by solving the NLSE [195]. The noise dynamics in SC can be quite complex, and depends highly on the system parameters. Determining the dominating noise source, also requires further insight.

In the temporal domain, the parametric process of degenerate four-wave mixing [14, 96] is termed modulation instability when the process is seeded by noise [195, 201, 202]. This process can, in case of phase-matching [96], provide a large gain across a broad bandwidth. If the aim is to generate low noise FCR in the VIS domain, the MI process can provide a significant noise contribution.

In SC generation, the main noise contributor is typically due to either MI or soliton fission [195, 203]. While the noise properties of FCR have not been investigated as a part of this thesis, this work is motivated by the potential low noise properties for FCR, when compared with typical SC sources.

The noise for SC sources has been studied in great detail theoretically [195, 204], and also experimentally for both commercial picosecond pumped SC [205] and for fs pump pulses [206, 207]. It is well known that typical SC sources suffer from a high RIN in addition to low spectral coherence [195]. While the RIN and spectral coherence describe different noise types, i.e., intensity and phase fluctuations, respectively, they are typically interrelated and follow similar trends. As a result, the spectral coherence is typically used as a benchmark for noise in SC emission. The first-order spectral coherence is a measure of the phase stability stability, and is defined as [204]:

$$|g_{12}(\lambda, t_1 - t_2)| = \left| \frac{\langle E_1^*(\lambda, t_1) E_2(\lambda, t_2) \rangle}{\sqrt{\langle |E_1^*(\lambda, t_1)|^2 \rangle \langle |E_2(\lambda, t_2)|^2 \rangle}} \right| \quad , \tag{5.2}$$

The g_{12} parameter denotes the mutual spectral coherence between adjacent pulses, where the times t_1 and t_2 denote different times for the electric fields

E_1 and E_2.

Studies by Dudley *et al.* [195] describes the general noise trends, and proposes a rule of thumb for obtaining high spectral coherence in SC. The noise is generally lower for SC when pumped in the normal group velocity dispersion (GVD) regime, but with the cost of a much smaller SC generation bandwidth [195]. It was found that for SC generated using pump pulses with N<10 provides a high spectral coherence, while the generated SC for N>30 possesses low coherence. These generalizations are also applicable when considering FCR.

However, for FCR generated using ultrafast fs pump pulses, the noise contribution is dominated by the onset of MI, which may break up the pump pulse. The MI process is inherently noisy, as it entails amplification of quantum noise. Investigation of the RIN noise in VIS FCR sources have demonstrated increased noise performance compared to ps-based commercial SC sources [179, 180].

A study by tu *et al.* [180] shows a comparison of the RIN between a spectrally sliced ps-based SC source, similar to the current commercial SC sources, with different FCR based sources. The findings showed up to ~ 30 dB/Hz advantage for the FCR source in the measured RIN. These results were obtained using sub 100 fs pump pulses with soliton orders $N \sim 5$.

From the calculated dispersion profiles for the NL-850-3.0 fiber shown in fig. 5.4 of chapter 5, the soliton number (N) is estimated as a function of the pulse duration using a 1033 nm pump. The pulse peak power is calculated using eq. (5.1) under the assumption of a Gaussian pulse shape with the expression; $P_p \simeq 0.94 \cdot \frac{E_p}{\tau_p}$, where E_p is the pulse energy, and τ_p is the FWHM pulse duration. In fig. 5.3 the soliton number (N) is plotted as a function of the

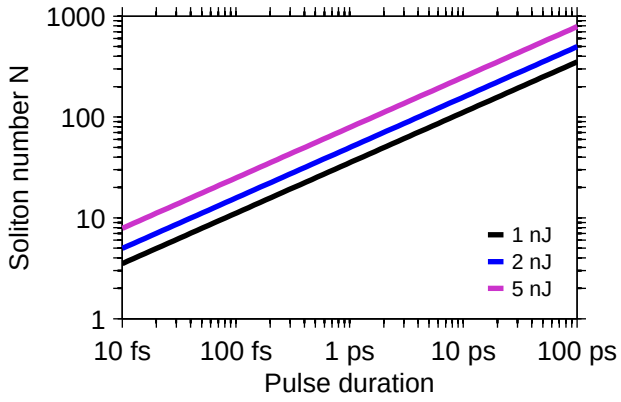

Figure 5.3: Scaling of the soliton number (N) for varying pulse durations and pulse energies, calculated for $\beta_2 = -30$ ps^2/km and $\gamma = 40$ $1/(W \cdot km)$.

pulse duration. While the absolute values depends on the fiber parameters, the generic trend is clear. Utilizing pump pulses with a very short pulse duration, allows low soliton order (N) for high (i.e. nJ level) pulse energies.

5.5 Cherenkov radiation phase-matching

Traditionally, Cherenkov radiation (CR) is light that is produced by charged particles passing through a dielectric medium while travelling at speeds above the phase velocity of light in that medium [208]. For solitons propagating in optical fibers, it has been shown that the emission of a dispersive wave is equivalent to the CR process [209]. The CR in optical fibers, denoted FCR, arise due to the perturbation of an optical soliton by higher order dispersion, and is well-described by the NLSE [188]. In literature concerning super-continuum generation, this phenomena is typically termed DW generation.

Based on the NLSE, the phase-matching relation governing the FCR process can be derived [209]. Following the notation from [191] the phase-matching is described by:

$$\tilde{\beta}(\omega) \equiv \beta_s(\omega) - \beta(\omega_s) - \beta_1(\omega_s)(\omega - \omega_s) = \frac{\gamma(\omega_s)P_s}{2} \quad , \tag{5.3}$$

where ω_s is the soliton frequency and P_s is the soliton peak power, γ is the nonlinear coefficient, $\beta_s(\omega)$ is the soliton wavenumber at a frequency ω. $\beta(\omega_s)$ is the linear dispersion curve of the fiber, with $\beta_1(\omega_s)$ being the derivative hereof evaluated at the soliton frequency.

The analytic expressions used to predict the linear and nonlinear phase-matching wavelength, shown in eq. (5.3), has proved to reliable predict the FCR wavelength [210, 211].

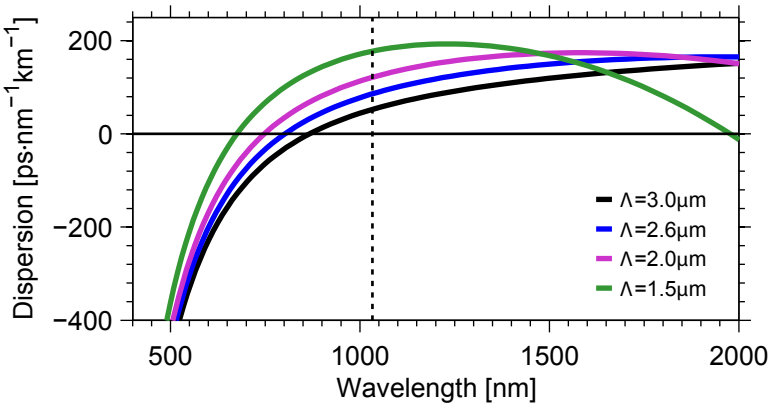

Figure 5.4: Calculated group velocity dispersion profiles for different fiber dimensions. $\Lambda = 3.0|\mu m$ corresponds closely to the PCF fiber NL-3.0-850 from NKT Phononics described in section 6.1.1. The curves for $\Lambda < 3.0$ μm reflects how the fiber disperison is modified if the fiber dimension is scaled down.

The dispersion profiles shown in fig. 5.4 were calculated based on the method in [212], with results provided by Jesper Lægsgaard. The calculations have been made to mimic the nonlinear PCF, termed NL-3.0-850, from NKT Photonics which is described in more detail in section 6.1.1. The NL-3.0-850 fiber has a specified 850 nm zero-dispersion wavelength, a 3 μm pitch, and a high air-filling

fraction > 90%. Based on scanning electron microscope (SEM) images of the fiber, the physical layout was replicated using a cobweb PCF fiber structure. The model takes into account various fine details regarding the fiber structure, including the rounding of the hexagonal hole structure.

In fig. 5.4 where the dispersion is plotted, only the fiber pitch is varied, with the black curve having a pitch (Λ) of 3.0 μm, which corresponds closely to the NL-3.0-850 fiber. The other three dispersion profiles, shows the blue-shift in the zero-dispersion wavelength that is obtained when scaling down the fiber structure. This can be done by a fiber tapering process and is described in section section 5.9. Scaling the fiber down to 4/5, 2/3 and 1/2 of the original fiber diameter, entails a corresponding scaling in Λ, down from $\Lambda = 3.0$ μm to $\Lambda = 2.6, 2.0$, and 1.5 μm, respectively.

The linear FCR phase match, corresponding to $P_p = 0$, is calculated from eq. (5.3) for the different dispersion profiles, and is shown in fig. 5.5. A phase-matching region close to the pump wavelength at 1033 nm is seen along with a phase-matching region in the VIS region around 400-600 nm.

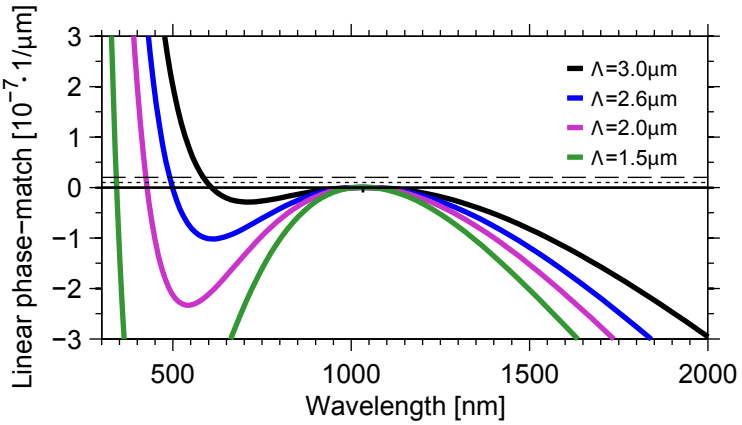

Figure 5.5: Linear FCR phase-matching curve for different fiber dimensions. When the pitch is decreased, the linear FCR phase-matching is blueshifted. The dotted and dashed line corresponds to the nonlinear induced shift in phase-matching for 50 and 100 kW peak power, respectively.

When reducing the fiber pitch, the linear FCR phase-matching wavelength shifts to lower wavelengths. If the non-linear FCR phase-matching is considered, corresponding to the term γP_P from eq. (5.3), phase-matching shifts to slightly positive values of $\tilde{\beta}(\omega)$. Therefore, an increasing blue-shift in the FCR phase-matching wavelength is expected for increasing pulse power.

The results are summarized in fig. 5.6 for a 1033 nm pump wavelength, where the zero-dispersion wavelength, as well as the linear FCR phase-match is plotted as a function of the fiber pitch.

As evident from the phase-matching in eq. (5.3), the FCR emission can also be affected by changing the pump wavelength. While this approach can be used to tune the emission wavelength for Ti:Sapphire based systems, it is not suitable for femtosecond fiber lasers. These systems are typically confined to

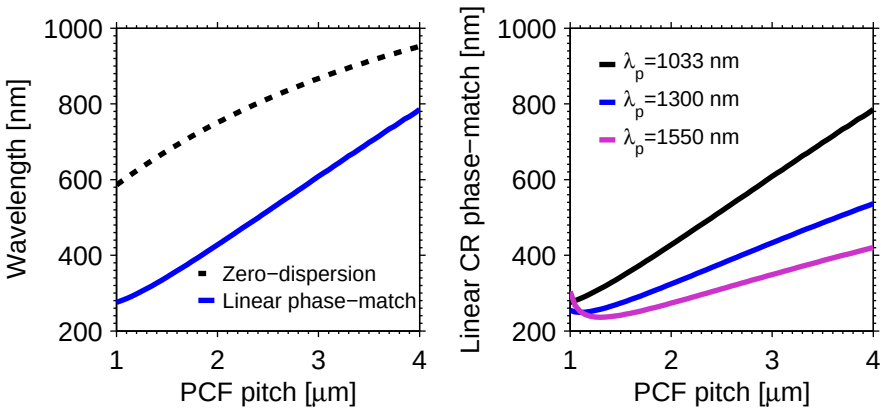

Figure 5.6: ***(left)*** *The calculated zero-dispersion wavelength is plotted for the cobweb fiber structure as a function of the PCF pitch. The predicted linear FCR phase-matching wavelength is shown for a 1033 nm pump wavelength.* ***(right)*** *Predicted linear FCR phase-matching wavelength for different pump wavelengths for a cobweb PCF structure with a 3 µm pitch.*

the gain bandwidth of rare-earth dopants such as Ytterbium or Erbium which are not tunable in emission wavelength.

5.6 Overview of current ultrafast Cherenkov radiation systems

An overview of ultrafast FCR systems is listed in table 5.1. While most of the reported systems relies on solid-state pump lasers in references [183, 210, 213–224], some fiber based pump systems were reported [37, 38, 184, 225, 226]. In this section follows a description of selected examples.

Previous work by Liu *et al.* [37] demonstrated the generation of up to 4.2 mW isolated FCR in a monolithic fiber laser system with selective tunability around 600 nm using the nonlinear fiber described in section 6.1.1. The pulse duration of the emitted FCR emission was ∼100 fs, much shorter that the duration of the pump pulse, owning to the temporal pump compression during the FCR process.

The group of Kärtner [223] have investigated the FCR generated using few cycle pulses from a Ti:sapphire pump source. The dependence on pump parameters, such as pulse duration, pulse energy, and pump wavelength were investigated both theoretically and experimentally [227]. Generation of up to 70 nm broad FCR was obtained for conversion efficiencies up to 40%, using sub nJ pump pulse energies. The scaling in pump pulse duration showed that a decreasing 100 to 10 fs pump pulse duration, provided an increase in FCR conversion efficiency from 20 to >40%.

Also, impressive results were demonstrated by Chen *et al.* [226], based on a 3 GHz pump source [228], where broadband FCR was generated across a bandwidth exceeding 200 nm and leading to compressed pulses of 14 fs. Extensive

work on FCR has been done by the group of Stephen Boppart, which a strong emphasis on applications in biophotonics [220]. Similar selective tunability of FCR emission was demonstrated using range of different nonlinear fibers using a Ti:Sapphire pump [210]. A combined FCR emission range from 485 to 690 nm was obtained utilizing three different nonlinear fibers, with different phase-matching regions, while exploiting the 690 to 1020 nm wavelength tuning range of a Ti:Sapphire pump source [211]. Subsequent work demonstrated similar results using a *state-of-the-art* 1550 nm Er:fiber laser pump source with a 80 fs pulse duration, where FCR was generated using pump pulse soliton orders of $N{\sim}5$ along with pulse energies between 5.8 and 32.8 nJ [38].

The results reported by Zhang *et al.* [225] are obtained for an Yb-doped PCF laser, emitting 100 fs pulses. A high 40% conversion efficiency was reported, which was enabled due to a 2 m PCF fiber length for the FCR generation and by pumping deep in the anomalous dispersion regime.

Very recent results by Chan *et al.* [184] demonstrate up to 40% conversion efficiency, along with short pulse durations, using a commercial fs Yb-based pump source [229].

Pump Laser source				Nonlinear fiber(s)			FCR wave.	Eff.	Ref.
Type	Wavelength [nm]	Duration [fs]	Rep. rate [MHz]	Type	λ_{ZDW} [nm]	Length [cm]	[nm]	[%]	
Ti:sapphire	800	190	80	PCF	700	40	430	25	[213]
Ti:sapphire	820	35	100	PCFs	680	10	490 & 510	20	[214]
Cr:forserite	1240	100	10^{-3}	Specific PCFs	1035 & 1075	8	530-720	1	[215]
Ti:sapphire	880-900	100	80	Tapered PCFs	630	0.5-1	538 & 600	20	[216]
Ti:sapphire	800	20	85	2 PCFs	670 & 735	0.5	470-500	-	[217]
Ti:sapphire	880-900	100	80	Tapered PCFs	865-630	1-2	385-625	-	[218]
Ti:sapphire	690-1020	100	80	2 PCFs	770 & 845	10	485-690	10	[219]
Ti:sapphire	1020	170	80	Series PCFs	670-890	15-18	347-680	2-6	[183, 210, 220]
Er:fiber laser	1550	80	50	low-nonlinearity fibers	890-1313	9	370-850	7	[38]
Ti:sapphire	800	80	10^{-3}	gas-filled HC-PCFs	700	10-90	176-550	8	[221, 222]
Ti:sapphire	800	10	85	PCF	710	2	450-550	40	[223]
Ti:sapphire	800	120	76	PCF	760	50	545-580	8-31	[224]
Yb-doped PCF laser	1038	95	49	two-ZDW PCF	852 & 2539	200	410 & 423	40	[225]
Yb-doped laser	1027	140	$3 \cdot 10^3$	PCF	945	2.8-4.8	750-950	-	[226]
Yb-doped laser	1030	250	54.77	PCF	975	8.5	670-790	40	[184]
all-fiber Yb-doped laser	1035	300	28	Spliced on PCF	850	10	580-630	1	[37]

Table 5.1: Comparison of different ultrafast FCR laser systems.

5.7 Cherenkov radiation in a uniform nonlinear fiber

Based on eq. (5.3) and the fiber and pulse parameters, the phase matching can be predicted. The fiber parameters from the nonlinear fiber (NL-3.0-850) used in the experiments in chapter 6, are described in section 6.1.1. Insertion of the parameters in eq. (5.3) yields a linear phase-matching point at 610 nm as show in fig. 5.5. By inclusion of the power dependent nonlinear term, it becomes evident that increasing the peak power shifts the phase matching to shorter wavelengths.

In fig. 5.7 the spectral and temporal evolution is shown for 300 mm propagation distance in a NL-3.0-850 fiber. The fiber dispersion is calculated from a 3.1 μm cobweb fiber modeled to match the NL-3.0-850 fiber (see section 5.5). The initial 234 fs pump pulse is fully compressed after 39 mm propagation, at which point there is overlap between the now broad pump pulse and the phase-matched wavelength for the FCR emission occurring at 600 nm. The localized nature of the FCR process is evident from fig. 5.7, where the spectral evolution shows that the VIS FCR emission is generated across a few mm from the CP. The corresponding temporal evolution also shown in fig. 5.7, shows the initial pump pulse breakup by soliton fission following near the pump CP. From the pump CP, a fast temporal walk-off between the FCR wave and the pump is seen, due to the large group velocity mismatch.

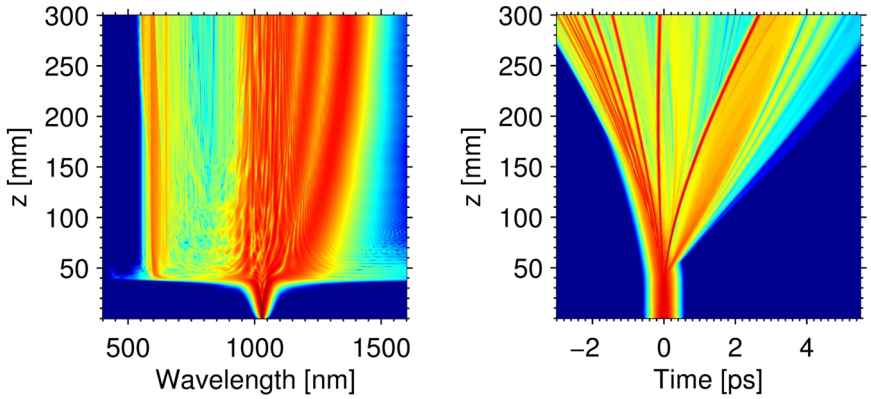

Figure 5.7: ***(left)*** *Spectral and* ***(right)*** *temporal evolution for 300 mm propagation along a NL-3.0-850 fiber. Simulations are carried out for a 234 fs FWHM pump pulse centered at 1033 nm with 8 kW peak power, 2 nJ pulse energy, 58 mW average power at a 29 MHz rep rate.*

The spectrogram representation is a convenient way to illustrate the pulse dynamics, and can be calculated based on the field along with a variable delay gate function [195]. The spectrogram has been computed at z=300 mm, shown in fig. 5.8, where the wavelength dependent parabolic group delay is visible. The individual solitons are clearly identified at the high-wavelength side of the pump. Similarly, the group velocity matched dispersive waves are located on the low-wavelength side.

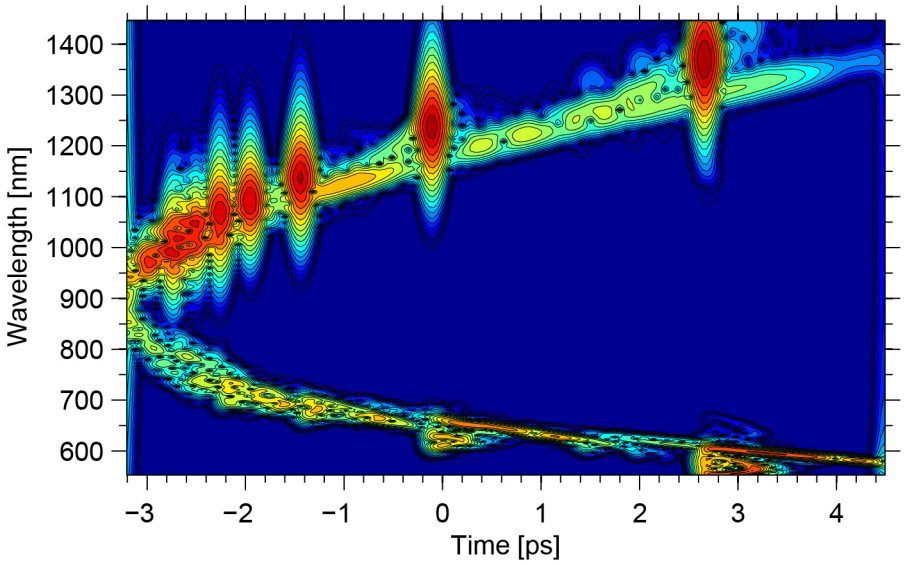

Figure 5.8: Spectrogram of the fiber output at z= 300 mm, for the same parameters as in fig. 5.7.

In fig. 5.8 it is seen that as the solitons red-shift they pull the FCR wave further down in frequency towards the blue, due to the coupling from the pump to the FCR wave by cross phase modulation (XPM).

5.8 Increasing the Cherenkov radiation wavelength tunability

For practical applications and in order to be competitive to current broadband SC sources, a FCR wavelength tuning range beyond the tens of nm is desirable. One approach suggested by Tu *et al.* [38] that enables coverage of the VIS domain with a FCR source, is to use a modular system consisting of a pump laser source along with a series of different nonlinear fibers with different dispersion properties. By switching between a series of 6 different optical fibers with a phase-match covering individual discrete regions, each with limited wavelength-tunability in the tens of nm range, an overall tuning range covering from the UV to the beginning of the infrared (IR) was obtained.

However, the wide tuning range in [38] comes at the cost of increased system complexity, due to coupling to the array of required fiber, and increased environmental sensitivity due to the required free-space components, i.e. non-monolithic design. The ideal FCR source should therefore be fully monolithic with no free-space components to increase the stability, ease of operation and to decrease the physical footprint, and have an increased wavelength tuning range, better than the current 30-40 nm range [37].

The tapering of optical fibers enables the variation of the dispersion as a function of the fiber length. As a result, the phase-matching wavelength for FCR generation will vary throughout the taper. Previous work have demonstrated that optical fiber taper structures can be used to increase the performance of both SC and FCR systems.

In field of SC generation, also relying on DW generation, tapers have been used as a method to extend the generation bandwidth using meter-long tapers [230–233]. The group of Knox demonstrated that by using millimeter-long microstructured optical fiber tapers, the spectral width of the generated FCR could be increased [234–236].

In section 5.9 the method of increasing the wavelength tuning range of FCR emission by the use of optical fiber tapers is proposed.

5.9 Cherenkov radiation in optical nonlinear fiber tapers

The proposed method for extending the wavelength tuning range of FCR emission relies on:

- **localized** CP of the pump laser due to soliton pump compression along with the localized FCR generation on a millimeter length scale
- **translational** tuning of the pump CP along the fiber when changing the pump pulse duration and/or power
- **taper** structure that provides a translational dependence of the phase-matching wavelength for FCR emission

The concept of the VIS Cherekov laser based on a taper is outlined in fig. 5.9. A femtosecond IR pump pulse is launched into a PCF having a tapered fiber geometry. Due to the anomalous fiber dispersion at the pump wavelength, temporal compression of the pump pulse takes place in the fiber. At the spatially very localized peak in pump power, termed the pump CP, generation of phase-matched FCR can take place. Due to the tapered fiber structure, the fiber dispersion varies along the fiber, and therefore also the FCR phase-matching wavelength. By changing the power and/or pulse duration of the pump pulse, the CP can be translated along the fiber. This is illustrated in fig. 5.9 for $P_2 > P_1$. As the FCR generation occurs very localized, a translation in the CP entails a tuning in the FCR emission wavelength.

In section 5.5 the calculated dispersion curves and corresponding phase-matching diagrams, show that a down-tapering of the NL-3.0-850 fiber to 2/3 of its diameter, would shift the zero-dispersion wavelength and corresponding linear phase-matching wavelength from 610 nm to 430 nm. In chapter 4 it was demonstrated how electrical tuning of the oscillator and amplifier laser diode (LD) enables control of the pulse duration and power. In section 5.2 describing the soliton pulse compression and translational tuning of the CP, a 20 mm translational tuning of the CP was predicted when tuning the pulse energy from 1 to 2 nJ. Taking into account the localized nature of the FCR

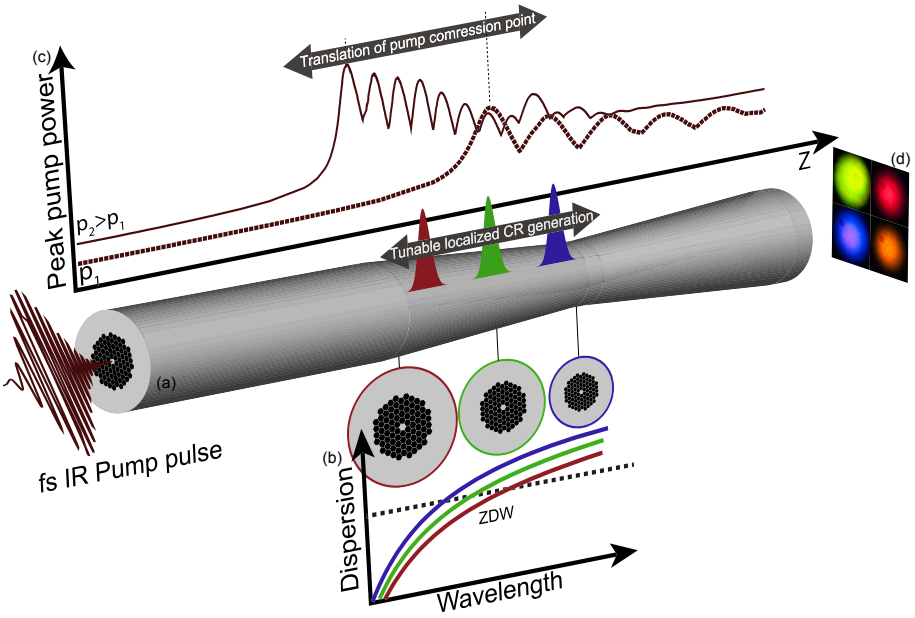

Figure 5.9: Illustration of the concept behind the tunable visible Cherenkov laser. (a) Tapered photonic crystal fiber. (b) Dispersion along different parts of the fiber taper, illustrating the blue-shift of the zero dispersion wavelength (ZDW) as the fiber dimensions are scaled down. (c) Plot of the peak pump power along the fiber length for different pump powers. (d) Examples of generated Cherenkov radiation for different fiber structures.

generation, done in a NL-3.0-850 fiber tapered down to 2/3 of its diameter, should potentially allow for FCR generation across an much wider wavelength range.

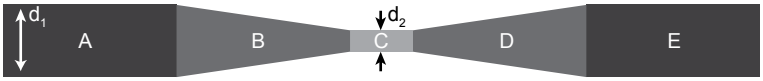

Figure 5.10: Schematic of the optical fiber taper structure.

The structure of the optical fiber taper, described in this thesis, can be generalized to the following shape that is outlined in fig. 5.10. Two leads (A & E) with the fiber diameter d_1 connects to a taper structure, containing a down-tapering section (B), a taper waist section (C) and an up-tapering section (D). The up- and down-tapering sections each transitioning from the lead diameter d_1 to the taper waist width d_2. The tapers that were realized experimentally, described in sections 6.5 to 6.7, have tapering ratios $R = d_2/d_1$ between $\frac{1}{2}$ and $\frac{2}{3}$, taper waist lengths from 1-10 mm, and up- and down-tapering sections from 2-25 mm. The fiber tapers will be named according to the length of the three taper segments, i.e. a 10-2-30 mm taper is a taper having a 10 mm down-tapering section, followed by a 2 mm taper waist, and a 30 mm up-tapering section.

As described in section 6.1.1 the utilized NL-3.0-850 fiber is single-moded at the 1033 nm pump wavelength. Transmission through such a structure can be of negligible loss if the tapering structure is sufficiently gradual [237]. This can be quantified by a adiabactic criterion that the taper should satisfy [238, 239]. It also follows that if the taper profile is adiabatic, there should be no power transfer between modes [240].

In the following sections FCR generated along different parts of the taper is described and discussed.

5.9.1 Compression point in the down-taper

By proper selection of the fiber lead length (segment A in fig. 5.10) before the down-tapering section, the pump pulse can be made to compress along the down-tapering section.

For a down-taper the zero-dispersion wavelength decreases along z, meaning that $\lambda_{\mathrm{zdw}}(z_2) > \lambda_{\mathrm{zdw}}(z_1)$. The change in CP for increasing pump powers will therefore red-shift the phase-matching wavelength. This behavior is opposite to the blue-shift in the generated FCR light, originating from the power-dependent phase-matching in eq. (5.3). In the end, the balancing of these two counteracting effects in a down-taper will determine the net blue-shift or red-shift in the FCR light with increasing pump power, and depends on both the pump pulse parameters and the taper-dimensions.

As an example, the simulated spectral and temporal evolution for FCR generation along a down-taper is shown in fig. 5.11. The taper contains a 20 mm lead, followed by a 30 mm linear down-taper to 2/3 of the original fiber diameter.

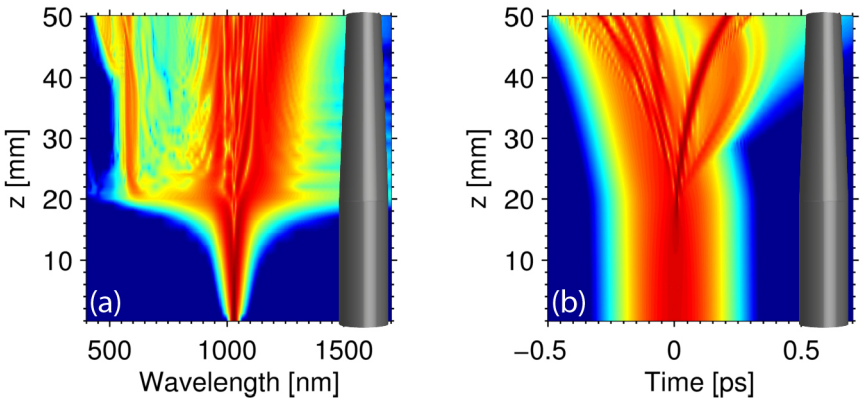

Figure 5.11: ***(left)*** *Spectral and* ***(right)*** *temporal evolution for propagation along a 20 mm fiber lead, followed by a 30 mm linear down-taper. The fiber parameters are based on the NL-3.0-850 fiber tapered down to 2/3 diameter. Simulations are carried out for a 129 fs FWHM pump pulse and 1.36 nJ pulse energy.*

For the taper structure shown in fig. 5.11, the pump pulse parameters should ideally be chosen freely to allow translational tuning of the pump CP across the whole 30 mm length of the down-taper in order to obtain the highest degree of

wavelength tunability. For this particular example with a 2/3 down-tapering, the zero-dispersion wavelength (ZDW) is reduced from 867 to 750 nm, with a corresponding approximated linear phase match at 610 nm and 430 nm. FCR emission in blue edge of the tuning range should occur for a pump CP near the taper end at $\sim$ 50mm for the appropriate pump pulse. While little distortion is expected for the limited subsequent propagation of the generated FCR pulse along the blue limit, light generated at the red side of the wavelength tuning range is generated near the taper start and propagates a longer distance.

By considering the worst case scenario, where the FCR light is generated at a CP around z=20 mm and thereafter propagates an additional 30 mm along the down-taper, further insight into the distortion of the generated FCR light is gained from fig. 5.11 and fig. 5.12. For the simulations a 129 fs pulse duration and a 1.36 nJ pulse energy were chosen to obtain a CP around z=20 mm. From fig. 5.11 it is evident that the FCR spectrum is generated in the first few mm of the down-taper, after which the subsequent propagation leads to significant distortion of the FCR spectrum starting at 42 mm near the taper end. This particular example was chosen to illustrate the problem of re-collision of the FCR wave with the pump which is evident from the temporal plot in fig. 5.11.

As the pump and FCR wave propagates along the down-taper, the relative group velocity between the two waves changes due to the changes in dispersion. Initially, the FCR wave lags behind the pump pulse as illustrated in the temporal plot of fig. 5.11. Along the down-taper structure the pump group velocity decreases while the group velocity of the FCR wave increases. As a result, a

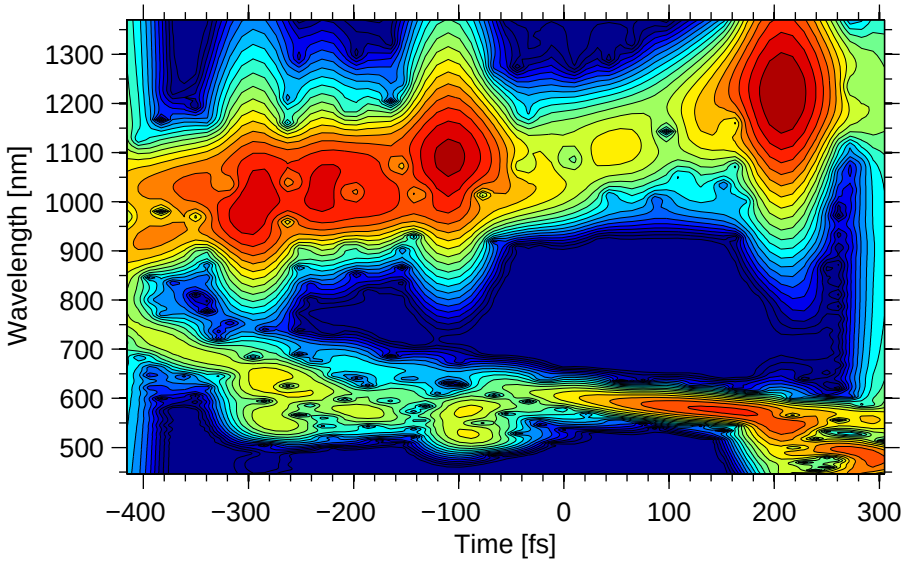

Figure 5.12: Spectrogram showing the collision of the pump and the FCR wave at the fiber output at z= 50 mm, calculated for the simulations shown in fig. 5.11.

collision between the pump and FCR wave occurs before the end of the fiber end, where the pump and FCR wave interact through XPM which broadens

and blue-shift the final FCR spectrum. A spectrogram calculated for the output at $z = 50$ mm, just after the collision, is plotted in fig. 5.12. On the red wavelength side it is evident that the initial pump pulse has split up into a few discrete solitons that are slightly separated in time. The spectrogram shows some temporal overlap following the collision between the furthest red-shifted soliton and the FCR wave, along with what appears to be partial trapping of the FCR wave which is blue-shifted slightly.

Numerical simulations not shown here suggests that this re-collision could be avoided for similar taper dimensions by utilizing a nonlinear down-taper structure, where the tapering rate is varied along the taper, as opposed to the linear taper structures that are presented in this chapter.

Cherenkov radiation in the up-tapering part of a taper

5.9.2 Compression point in the up-taper

In a similar manner, the generation of FCR light can take place along the up-taper section, where again the translational tuning of the pump CP is exploited. For this configuration the length of the taper structure and fiber leads should be prepared in such a way that the pump CP at the lowest power setting occurs at the end of the fiber up-taper.

When increasing the pump power the CP will shift to an earlier point along the taper z_1. For this case, the resulting shift in ZDW and corresponding phase-matching wavelength will be opposite the behavior that of the down-taper structure described in section 5.9.1.

An increase in the pump power will result in an increase in λ_{zdw} as $\lambda_{\mathrm{zdw}}(z_2) < \lambda_{\mathrm{zdw}}(z_1)$. The result is a blue-shift in the phase-matched FCR light as the pump power is increased. This power-dependent blue-shift in phase matching due to the translational power dependence in the CP will add constructively to the nonlinear term in the FCR phase-matching, which also induces a blue-shift in the FCR phase-matching for increasing pump powers. As a result an overall enhanced tuning behavior is expected for FCR along the up-tapering part of a fiber taper.

When tuning the FCR emission wavelength furthest towards the blue, analogous to adjusting the translational location of the pump CP to the taper waist, both the pump and the generated FCR wave travels along the up-taper. For this situation, subsequent recompression of the pump along the up-taper can give rise to secondary FCR emission. This is illustrated in fig. 5.13b for a short taper, having 10 mm fiber lead followed by a 10 mm down-taper and a 10 mm uptaper.

While the peak power for the additional subsequent recompression of the pump is usually decreasing monotonically after the initial CP, the power may be high enough to generate additional FCR light along the up-taper. Generation of FCR along the up-taper is more prone to secondary FCR emission as the phase-matching wavelength moves closer to the pump along the up-taper. Even though the peak-power of the pump may be lower for the following recompression, the power required for FCR emission also decreases along the up-taper. The resulting output spectral evolution for the short taper in fig. 5.13b

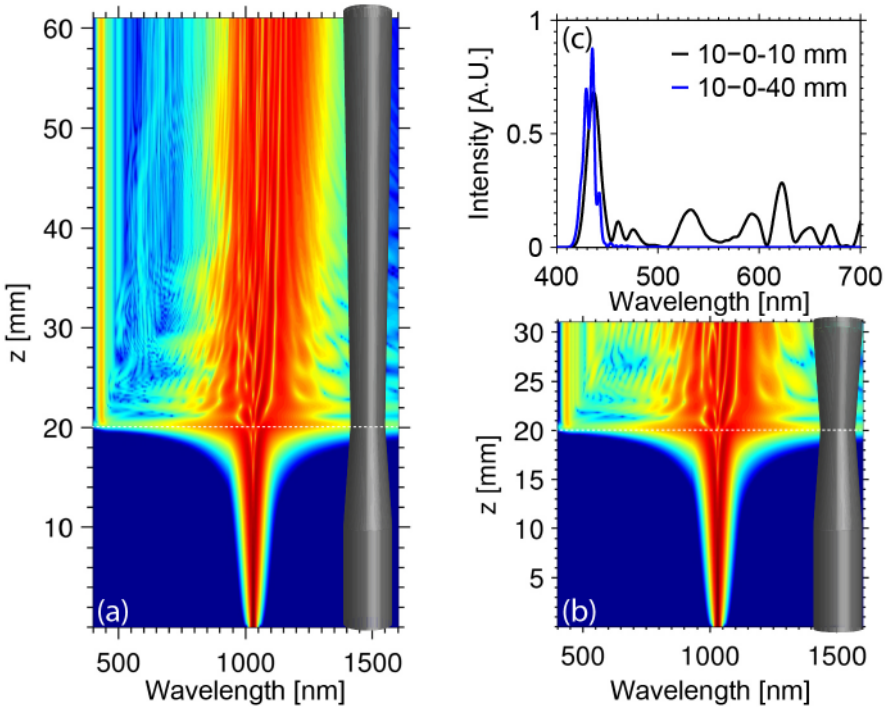

Figure 5.13: (a) Spectral evolution for a 10 mm lead followed by 10 mm linear down-taper and a 10 mm up-taper. (b) Spectral evolution for a 10 mm lead followed by 10 mm linear down-taper and a 40 mm up-taper. (c) comparison of the output spectrum for the two taper structures. For both tapers the pitch along the taper varies from 3.1 μm to 2.0 μm. The pump pulse FWHM duration is 163 fs and the pulse energy is 1.72 nJ.

is messy, and the output spectrum is shown in fig. 5.13c.

This issue can be avoided by introducing an asymmetric taper shape, with an extended up-tapering region as shown in fig. 5.13a. By decreasing the taper slope, the change in phase-matching wavelength is much slower, meaning that the peak power for the subsequent pump recompression along the fiber up-taper is to low for significant FCR generation. Thus, when comparing the output spectra for the two taper-structures in fig. 5.13c a much cleaner output spectrum can be obtained.

Chapter 6

Experimental results on FCR

> What we observe is not nature itself, but nature exposed to our method of questioning.
>
> Werner Heisenberg

The following chapter is based on the publications [160–162], and deals with the experimental results on FCR generated in both non-tapered and tapered fibers. The experimental setup used for the FCR experiments is introduced in section 6.1, followed by a description of the utilized nonlinear fiber section 6.1.1. Experimental results for a non-tapered fiber segment is presented in section 6.3. The degree of tunability that can be obtained as a result of the non-linear phase-matching is demonstrated by varying the pump pulse duration and power. This is done to provide a point of reference for the investigation of fiber tapers. This section is followed by section 6.4, where the tapered nonlinear fibers are described, and the results for the generated of fiber-optic Cherenkov radiation (FCR) in different tapers are presented.

6.1 Experimental setup

In section 5.8 it was described how this work was motivated towards broad visible (VIS) FCR tunability in a fully monolithic fiber laser system. However, as a testing platform, a free-space setup enables easier characterization of nonlinear fibers and taper structures. A free-space testing platform also offers the benefit and possibility of characterizing and monitoring the pump pulses.

The experimental setup is outlined in fig. 6.1. The pump light is collimated from the hollow-core (HC) compression fiber (described in section 4.3.1), using a 3-axis fiber launch stage and an $f = 11$ mm aspheric lens (L_1). The pump light is coupled into the fiber under test (FUT) utilizing an aspheric lens (L_2) with a 3.1 mm focal length and a 0.68 numerical aperture (NA). The FUT is based on the NL-3.0-850 fiber, either in a tapered or non-tapered form, but with all samples having an input facet with 2.1 μm mode field diameter (MFD)

and 0.17 NA. To enable efficient coupling, the provided $\frac{3.1\ mm}{11\ mm} = 0.282X$ magnification, matches the $0.28X$ MFD mismatch between the HC fiber (7.5 μm) [150] and the nonlinear (NL) fiber [241] closely.

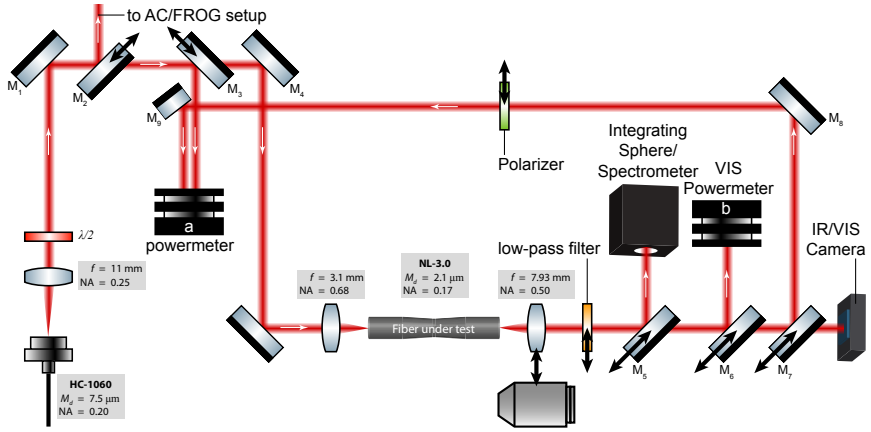

Figure 6.1: Experimental setup for the FCR generation, where the 1035 nm pump is coupled to the FUT. P_b

The FUT remains stationary, while both the input lens L_2 and the collimation lens L_3 at the FUT output, are mounted on separate 3-axis stages (*Thorlabs Flexture MBT616D*). Coupling to the FUT is optimized by alignment of the collimation lenses, and using the beam-walk technique for the mirrors M_4 and M_5. The input power was monitored by utilization of an integrating-sphere power meter (P_a) in fig. 6.1, using the flip-mirror M_3. For measuring and optimizing the FUT insertion loss, transmitted pump power was monitored using the same reference power meter (P_a) with mirrors M_{8-10}. Coupling efficiencies for the 1033 nm pump were typically in the $60-70\%$ range. However, some degradation in the coupling efficiency was observed over time.

Lenses L_{1-3} were anti-reflection (AR) coated, providing $\sim 0.25\%$ reflection at the pump wavelength, but with higher reflection for the light in the visible range with R$\leq$ 1% from 600 to 700 nm, but increasing to R$\geq$ 10% below 500 nm.

The accumulated transmission loss, measured at the pump wavelength for the setup outlined in fig. 6.1, is listed in table 6.1, with α_{FUT} denoting the FUT insertion loss (including collimation lenses).

When characterizing the FCR light emitted from the FUT. a short-pass filter was used, having a 750 nm cutoff with $\geq$ 97% transmission from 400-700 nm. An optical density (OD) higher than 5, above the cutoff wavelength, ensures strong filtering of the pump. The VIS output spectrum was measured with flip mirror M_6 and an integrating sphere connecting to an *Ocean Optics HR2000+* spectrometer, having a 0.222 nm resolution from 376 to 815 nm. The visible output power was measured using flip-mirror M_7 and power-meter P_b.

Following alignment of the pump relative to the FUT in order to maximize the transmission, the output collimation lens L_3 was corrected for the

		Loss [dB]
(a)	After HC collimator	Reference
(b)	After half-wave plate	0.06
(c)	Monitor (power meter)	0.16
(d)	Before taper input lens	0.33
(e)	After taper output lens	0.33+α_{FUT}
(f)	Output (power meter)	0.51+α_{FUT}

Table 6.1: Measured accumulated transmission loss for the experimental setup at the 1033 nm pump wavelength. α_{FUT} denotes the insertion loss of the FUT.

$\sim$ 0.1 mm focal length shift between the generated VIS FCR light and the pump wavelength.

For measuring the near- and far-field of the FUT output, a camera behind flip-mirror M_8 along with a 50x or 100x objective was used. The cameras used was either a monochrome charge-coupled device (CCD) camera for characterization at the pump wavelength, sensitive up to 1100 nm, while an RGB camera (Thorlabs DCU224C) was used for near- and far-field imaging of the generated VIS FCR.

To align the input polarization with respect to the parasidic principal axis of the FUT a half-wave plate ($\lambda/2$) was used, positioned just after the pump collimator. By utilizing a polarizer before or after the FUT. the incident and output polarization angle and polarization extinction ratio (PER) could be characterized using power-meter P_a. Characterizations of the pump pulses were done with either the autocorrelation (AC) or frequency-resolved optical gating (FROG) setup, described in section 4.5, using flip-mirror M_2.

6.1.1 The nonlinear fiber (NL-3.0-850)

The fiber utilized for all subsequent FCR experiments, both for tapered and non-tapered fibers, is a nonlinear photonic crystal fiber (PCF) from NKT with the model name NL-3.0-850 [241]. The fiber parameters are listed in table 6.2, with a dispersion profile similar to the profile shown in fig. 5.4 in section 5.5.

There is no designed structural elements to enforce polarization maintaining properties, By characterization of the PER of the pump before and after coupling into the fiber, it was found that the fiber is birefringent. The polarization of the pump is preserved if aligned properly along the principal fiber axis. This is described in further details in section 6.6.1, which shows the high sensitivity in FCR towards changes in polarization for fiber taper structures.

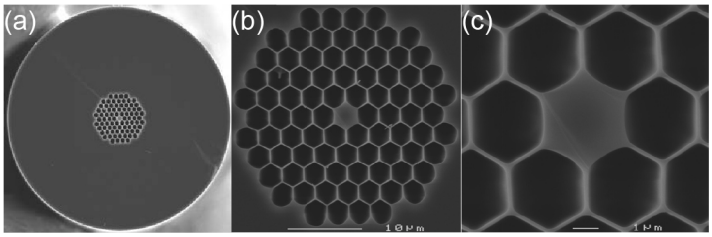

Figure 6.2: scanning electron microscope (SEM) images showing the transverse shape of the fiber facet (a), along with magnified images of the holey region (b) and core region (c) [241].

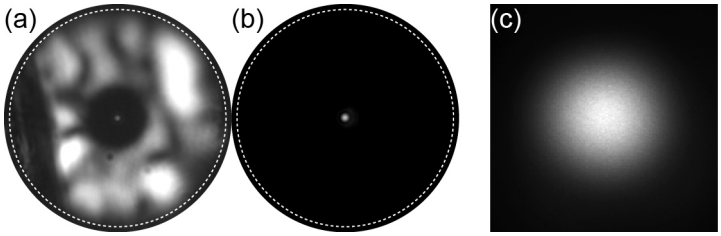

Figure 6.3: Near-Field at the output of a fiber taper, measured at the pump wavelength. The dashed line in (a) & (b) outlines the outer fiber circumference. (a) Measured during the alignment process, showing the transmission of additional cladding modes. (b) Measured after further alignment where only the core-mode is exited. (c) Measured for optimum alignment where only the core mode is excited, showing only the core region.

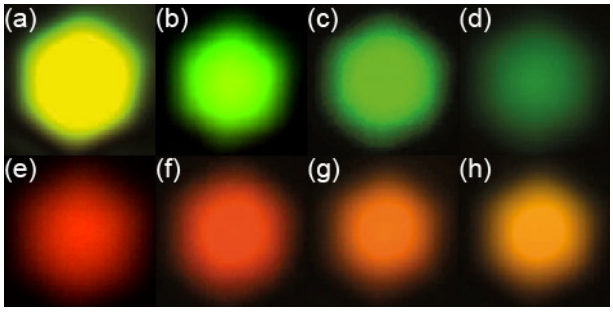

Figure 6.4: The images (a-h) shows the near-field image of the output facet for different colors of the generated FCR light, measured with an RGB camera after the low-pass infrared (IR) filter.

As evident from the images of the transverse fiber shape shown in fig. 6.2, the fiber has a high air filling factor exceeding 90%. The fiber could be cleaved with a clean end facet using both tension cleavers but also by hand using either a ceramic cleaving tile or a Ruby tipped fiber scribe. The latter two methods proved very useful when dealing with short and delicate fiber or taper segments. The core of the fiber is single-mode at the pump wavelength due to the small core area.

Nonlinear coefficient	40	$\mathrm{W}^{-1} \cdot \mathrm{km}^{-1}$
Effective nonlienar area	4.6	$\mu\mathrm{m}^2$
Numerical aperature	0.17	
Mode field diameter	2.0 ± 0.1	μm
Zero dispersion wavelength	850 ± 5	nm
Core diameter	3.1 ± 0.1	μm
Pitch	3.0 ± 0.1	μm

Table 6.2: Fiber parameters, specified at the ZDW for NL-3.0-850 [241].

When optimizing the coupling to the FUT. both the near-field and the transmitted power is evaluated during the alignment process. The measured near-field measured at the pump wavelength is shown in fig. 6.3. The near-field image of the generated VIS FCR in a tapered NL-3.0-850 fiber, is show for different FCR emission wavelengths in fig. 6.4. While the images shown in fig. 6.4 reflects the typical taper-output near-field, the emission of VIS FCR along higher order LP_{02} like modes were observed in some cases with poor coupling and are fig. 6.5.

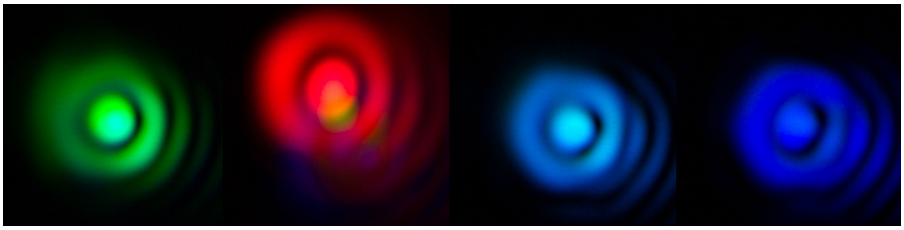

Figure 6.5: Near-field images captured with a RGB camera of VIS generated FCR for instances of low taper transmission.

6.2 Localized pump compression point and Cherenkov generation

In chapter section 5.2.1 the soliton pulse compression phenomena was described. The simulations predicts a very localized maximum value in the pulse peak power. Assuming sufficient peak power for the pump to couple the phase-matched dispersive wave, the emission of visible light from the FCR generation at the compression point (CP) is visible to the naked eye.

The motivation for the visual inspection of the localized FCR, is that it enables experimental verification of the pump CP localization, and how it can be translated along the fiber length. This becomes increasingly relevant with the introduction of tapered fiber structures described in section 6.4.

By mounting a high resolution camera with a high magnification lens above the FUT in the experimental setup (fig. 6.1 in section 6.1), the power-dependent displacement in the CP and FCR point is visible. This power-dependent trans-

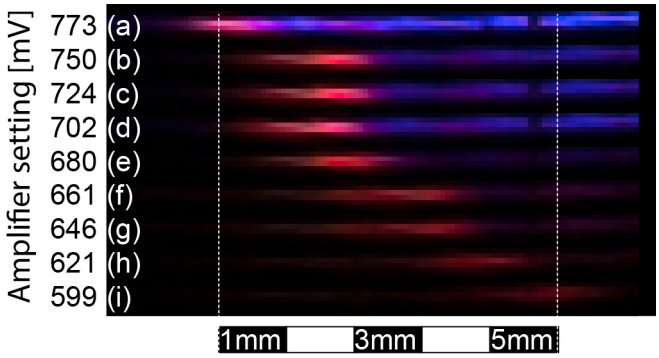

Figure 6.6: How the CP is translated along the fiber with increasing pump power. This example is shown for a fiber taper, with pump compression near the taper waist at ∼47% taper transmission (including collimation lenses). The photos (a-i) shows images of the FUT exposed with a RGB camera (a Canon 5D with an IR filter) mounted above the fiber, where the number in mV next to each label denotes the power amplifier pump diode monitor voltage. The pump power increases linearly with the monitor voltage, until it starts to saturate above 700 mV. A 600 mV setting corresponds to ∼195 mW and 720 mV corresponding to ∼228 mW.

lation is shown in fig. 6.6 for a tapered NL-3.0-850 fiber at a range of pump powers. The output power increases linearly from 600 to 700 mV, after which the amplifier starts to saturate. The pulse duration decreases monotonically as the pump power is increased. This behavior is described in further detail in section 6.3. The increase in pump power along with the decreasing pulse duration, results in a ~ 5 mm displacement in the FCR CP along the fiber.

When viewing a larger section of the FUT. recurring compression points can be visible for some set of parameters. A comparison is shown in fig. 6.7 where only a single CP is visible in (a), and multiple compression points are shown along the FUT in (b) and (c).

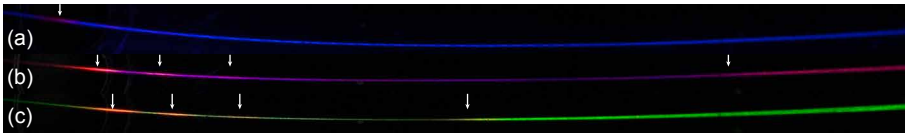

Figure 6.7: Images showing multiple compression points along a fiber taper, for different pump parameters, with the images captured as in fig. 6.6. The pump is launched from the left side, and only the part of the fiber near the CP is shown.

These recurring compression points have decreasing peak pump power, and can lead to additional FCR emission at different wavelengths, due to the power-dependent term in the phase-matching relation described in section 5.5. However, for a tapered structure which has a z-dependent phase-matching, the recurring pump compression points can shift the emission wavelength considerably.

For the example in fig. 6.7, shown for a 25-2-25 mm taper, significant emission at a later CP in the fiber is observed. In spite of a lower peak pump power at a later pump CP, the red-shift in the zero-dispersion wavelength (ZDW)

further up along the up-taper, causes an enhanced emission in the red/green in fig. 6.7b/c. This behavior can be understood from the increase in conversion efficiency as the FCR phase-match moves closer to the pump wavelength along the up-taper, and the conversion BW is reduced.

6.3 Results for non-tapered fibers

These findings presented in this section provides a preliminary estimate of the degree of translational tunability in the CP that can be realized.

The first experiments were performed on a non-tapered segment of NL-3.0-850. From the linear phase-match (described in section 5.5), the NL-3.0-850 should emit FCR light around 610 nm. An initial 38 cm segment of the fiber was mounted in the experimental setup shown in fig section 6.1.

The coupling to the FUT was optimized as described in section 6.1, while both the FUT near-field and transmitted power was monitored continuously, to ensure coupling to only the fundamental mode along with the highest possible transmission.

After alignment of the FUT. where a 65.9% transmission was obtained, both the pump pulse and the VIS FCR was characterized for each consecutive measurement. The transmission is measured at the pump wavelength and includes the two collimation lenses. For the experiment presented in figs. 6.8 to 6.11 the results obtained for the 38 cm segment are shown in comparison to a subsequently cutback to a 17.5 cm fiber length. After the cutback a similar transmission of 66.6% was measured for the shorter fiber segment.

The output spectrum is plotted for a range of pump powers in fig. 6.8, measured with an integrating sphere and an ocean optics spectrometer, with the corresponding pump power and pump pulse duration listed in fig. 6.10. The emitted VIS FCR far-field, captured with an RGB camera, is shown in fig. 6.9. The residual pump is removed by a short-pass filter, which only transmits ≤ 750 nm. The VIS FCR power is measured with a discrete power-meter and is listed in fig. 6.11 along with the FCR full-width half maximum (FWHM) emission BW.

Both the 37 and 17.5 cm fiber segment shows a 20 nm blue-shift in the emission wavelength, due to the nonlinear phase-match, as the pump power is increased. The FCR emission wavelengths is centered at 605 nm at $\sim$165 mW monitor pump power and decreases to 585 nm at $\sim$229 mW monitor pump power. The monitor pump power and AC are monitored and measured continuously for the duration of the measurement session. While the pump power is increased, the pump pulse duration decreases from 837 fs AC FWHM at the lowest power setting down to 583 fs AC FWHM at highest power setting, as shown in fig. 6.10. This behavior was also described in chapter 4. The full AC traces for the minimum and maximum pulse duration is shown in fig. 6.10. The AC trace has a pedestal, which is most pronounced for the longest pulse duration. The pulse pedestal arises in the chirped pulse amplification (CPA) and is believed to be caused by uncompensated third order dispersion (TOD) for the stretcher and compressor fiber. As many different pulse shapes can provide the identical auto-correlation trace, it is necessary to confer with the

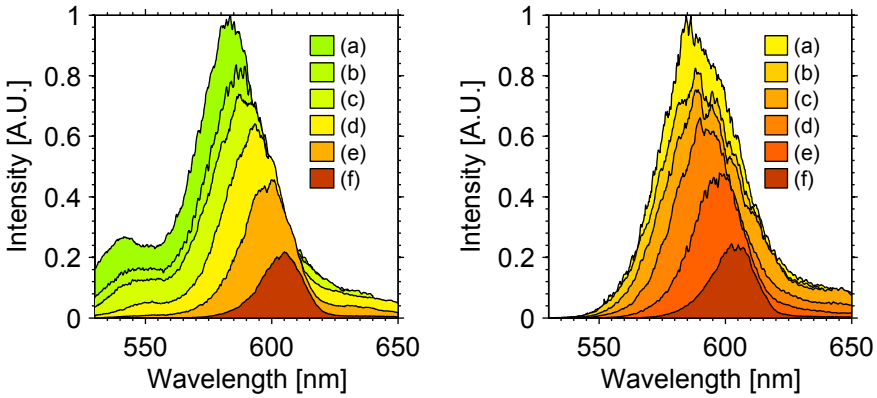

Figure 6.8: Measured VIS FCR output spectrum for different pump power levels decreasing monotonically from a-f. The corresponding pump parameters are shown in fig. 6.10. ***(left)*** *Output spectrum obtained for a 37 cm long nonlinear fiber segment measured before cutback.* ***(right)*** *Output spectrum measured after cutback of the nonlinear fiber to a 17.5 cm fiber length.*

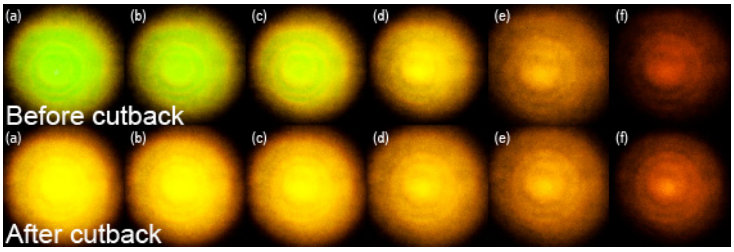

Figure 6.9: Photos of output far-field before and after cutback of the nonlinear fiber corresponding to measurement a-f in fig. 6.8

pulse shape retrieved from a FROG measurement, as described in section 4.4.2 and section 4.5.

The optical power of the generated FCR light increases with the amount of pump power, exceeding 3 mW, while the FWHM emission bandwidth seems to saturate at the highest pump power at a FWHM bandwith above 30 nm.

For the longer 37 cm segment, a secondary peak around 550 nm appears at higher pump power levels, that is also observed clearly in the far-field images shown in fig. 6.9. The numerical simulations presented in section 5.7 for slightly different pump parameters, indicate that a secondary peak arise after about 200 mm propagation. This corresponds well with the experimental observations, which show the disappearance of the 550 nm peak when the fiber length was cut-back to 17.5 cm as shown in fig. 6.8.

In this experiment, visual inspection revealed that for the highest pump power, corresponding to setting (a) in fig. 6.8 and 229 mW monitor pump power, the FCR was generated at a point 59 mm into the fiber. Reducing the power to the lowest setting corresponding to (f) in fig. 6.8 at 167 mW, further translated the CP and FCR to a point 82 mm into the fiber.

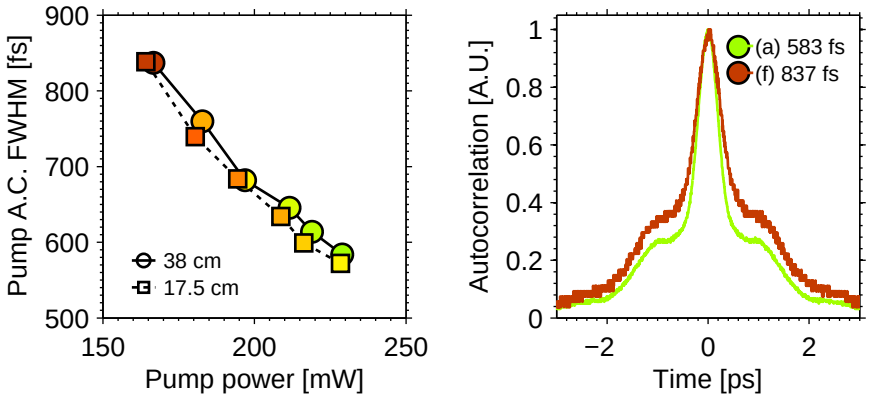

Figure 6.10: Pump parameters corresponding to the measurements a-f shown in fig. 6.9 and fig. 6.8. ***(left)*** *Measured pump FWHM AC plotted with respect to the pump power.* ***(right)*** *AC traces for the shortest and longest pump pulse durations measured for the 38 cm fiber (before cutback).*

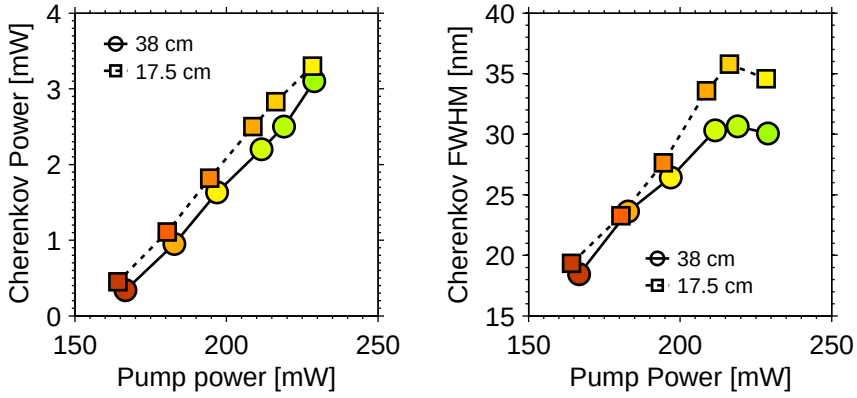

Figure 6.11: Measurement parameters for the FCR output corresponding to the measurements a-f shown in fig. 6.9 and fig. 6.8. ***(left)*** *Measured VIS FCR output power.* ***(right)*** *Measured FCR output spectrum FWHM .*

For practical applications of the generated FCR light, a cutback of the fiber should preferably be made as close as possible to the point where the FCR is generated, to obtain the cleanest output spectrum along with the shortest possible output pulse duration.

While the pulses are expected to compress faster in a tapered fiber structure, due to the increased fiber nonlinearity, these results indicate that it should be possible to obtain a few centimeter of translational tuning of the CP along the taper structure for the available laser pump parameters.

6.4 CR generation in a tapered fibers

The theory and operating principles for FCR in optical fiber tapers was discussed in chapter 5. The following sections describe in detail selected experimental results that demonstrating the tunability of the generated FCR. The manufacturing of optical fiber tapers from PCF fibers is described in section 6.5. This is followed by a review of the experimental results on FCR generation obtained for two taper structures, having 25-2-25 mm and 10-2-10 mm dimensions, in sections 6.6 and 6.7, respectively.

The concept of tuning of the FCR emission wavelength by adjusting the pulse duration and thus translating the CP point along the taper is shown in section 6.6. The effect of birefringence upon the FCR emission, and the dependence upon the pump launch angle relative to the principal fiber axis is described in section 6.6.1, while the polarization for the generated VIS FCR emission is described in section 6.6.2. The characteristic wavelength tuning behavior for FCR generated along the down-taper and up-taper is compared in section 6.6.3 and section 6.6.4, respectively. These results are then compared to a taper having different dimensions in section 6.7. The section is concluded by the description of the manufactured asymetric tapers in section 6.8, which could not be characterized due to equipment failure, along with a discussion of the results in section 6.8.

6.5 Manufacturing and characterization of fiber tapers

The following section deals with the manufacturing of micro-structured optical fiber tapers, which are used to increase the tunability of FCR.

For the tapering of the micro-structured nonlinear fiber, a commercial *Vytron LDS-1250* tapering station was used. A Tungsten or Irridium filament heats up the fiber to the softening point in a small chamber purged with Argon gas, while two stepper motor blocks move the fiber along the filament. The taper width is adjusted by controlling the relative velocity of the two blocks during the process. While the tapering station did not allow for pressurization of the air-hole microstructure during the tapering, no damages to the microstructure were observed.

After each tapering, the FUT was investigated from the side using a *Carl Zeiss Axioskop 40* with either a $50X/0.8$ *Carl Zeiss Epiplan-Neofluar* or a $100X/0.75$ *Carl Zeiss Epiplan* objective. In this way both the taper dimensions, as well as the micro-structure of the fiber could be examined. Small discontinuities in the taper structure could be identified, as well as damages to the micro-structuring of the fiber; partial and complete hole collapse.

Once a tapering recipe was developed for a particular fiber type and heating filament, the taper machine can produce taper structures of high quality. Two examples are shown in fig. 6.12, showing the taper target along with the measured taper profile. Here, the 10-10-10 mm and 25-2-25 mm labels reflect the taper dimenstions, defining the length of the down-taper, taper waist, and

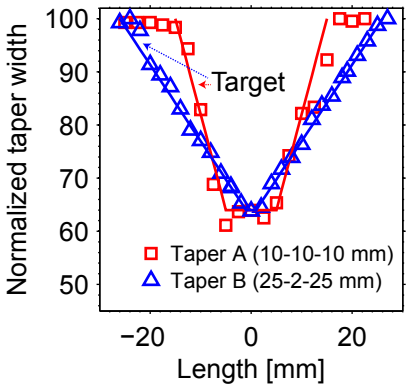

Figure 6.12: The taper target (full lines) along with the measured taper dimensions for a 25-2-25 mm taper (blue) and a 10-10-10 mm taper (red).

the up-taper, respectively.

The tapering system is quite sensitive to changes in the filament, and must be calibrated before each use. If the taper machine parameters were not properly calibrated, either the taper structure would be compromised or the fiber would simply break during the tapering process. Mechanical alignment of the motor block holding the fiber was found to be an important prerequisite. Over time the alignment would drift, such that the two motor blocks would no longer pull along the same axis. The result hereof can degrade the taper quality and cause the fiber to break prematurely during the tapering process.

The power of the filament is a crucial parameter to calibrate, as it controls the softening of the FUT. Depending on the filament material and dimensions, the power required for softening the FUT ranged from 85 W to 140 W for the Tungsten filament [1]. The following list describes the experimental observations when dialing in the filament power for a new filament and/or fiber:

1. **Below softening point (to low power)** The FUT will not soften sufficiently, and will break or slide in the groves of the two motor blocks.

2. **Lower end of softening point (near optimum power)** The FUT can be tapered, but the tapering profile can be uneven, and oscillate (see fig. 6.13a,b).

3. **Optimum softening point (optimum power)** The lowest power where the FUT tapering fits the target profile. (see fig. 6.13c).

4. **Above softening point (power to high)** The FUT might still fit the target tapering profile, but the power is so high that the microstructuring is damaged.

[1] Filament type E125-12525-N30

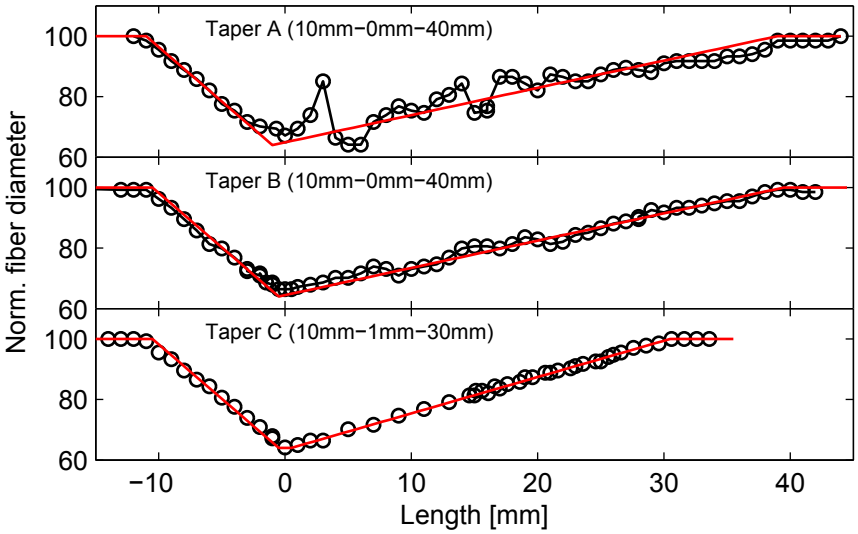

Figure 6.13: Measured taper profiles plotted along with the designed target dimensions while optimizing the taper parameters on the Vytran LDS-1250. *Whereas the down-tapering section is close to the target dimensions for taper A and B, the up-tapering section is uneven. When the parameters have been adjusted, the resulting tapers follow the target profile very well, as depicted for Taper C.*

6.6 Results for the 25-2-25 mm taper

The initial measurements were carried out on a taper having a 25 mm linear down- and up-tapering section, with a 2 mm long taper waist, hence referred to as the 25-2-25 mm taper. The taper dimensions, and micro-structure integrity was investigated as described in section 6.5. The taper structure is shown in fig. 6.14, showing both an image stack of microscope images measured at 0.5 mm increments along the taper profile along with a plot of the measured taper diameter. The taper segment shown in fig. 6.14 depicts sample (c) in fig. 6.15.

The NL-3.0-850 fiber, described in section 6.1.1, was tapered down to 2/3 of the original fiber diameter. This corresponds to 3.1 μm pitch tapered down to $\sim$ 2 μm. From the CP observed for the non-tapered samples, the required lead length before the 25-2-25 mm taper was estimated, to provide a CP near the taper waist. The taper leads were initially cut-back according to fig. 6.15a, with 28 mm fiber before the waist, and a 95 mm fiber lead length after the taper.

From the phase-matching diagram (fig. 5.6 in section 5.5) the $\sim$610 nm estimated linear phase-match in the non-tapered fiber, is reduced to around $\sim$ 430 nm for the estimated 2 μm PCF pitch at the taper waist. Varying the pulse duration from the main oscillator, by adjusting the oscillator pump diode as described in section 4.5.1, allows to shift the CP along the fiber taper. This does not affect the pump power, which remains constant.

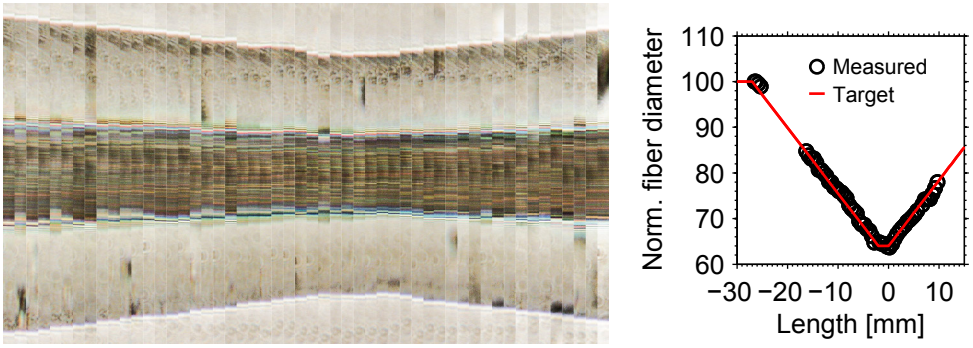

Figure 6.14: 25-2-25 mm taper measured at 0.5 mm interval. The side-view images were captured with bottom lighting using a 50X objective on a Zeiss Axioskop 40 *microscope.*

Figure 6.15: The estimated taper shape and lead length for different cutbacks of Taper 11.

In fig. 6.16 the output spectrum for FCR generated in the taper is shown for different pump pulse durations, all at the same pump power. The pump AC trace is plotted next to the corresponding output spectrum. For fig. 6.16a,b the main peak is situated at 417 and 454 nm respectively, but with a secondary region containing additional sub-peaks centered at 617-620 nm. For fig. 6.16c,d only a single main peak situated at 547 nm and 592 nm is observed.

The difference in pump CP for the different pump pulses, causes the difference in phase-matching for fig. 6.16a-d due to the z-dependance of the phase-matching for the taper as described in section 5.9. The main blue peak in fig. 6.16a,b corresponds to phase-matching near the taper waist, with the secondary peaks originating due subsequent recompression of the pump pulse in the fiber lead. The peaks in fig. 6.16c,d with FCR emission at 547 and 592 nm corresponds to phase-matching much closer to the taper leads.

The far-field from the taper in fig. 6.17, measured for different pump pulse parameters, show output FCR light ranging from the blue, red and orange.

6.6.1 Effects of the taper birefringence on the generated Cherenkov radiation

In the experiments performed on non-tapered fibers, a clear dependence on the pump launch angle was observed, and is touched upon briefly in section 6.1. When rotating the incident pump polarization angle while monitoring the FCR generation, the effects of the fiber birefringence was clearly observed. The FCR output power was found to depend on the pump polarization angle relative to the principal axis of the birefringent nonlinear fiber. In a crude approximation, this is explained from a scaling in the effective non-linearity of the fiber, which provides a reduced nonlinear response as the pump is launched at an angle to

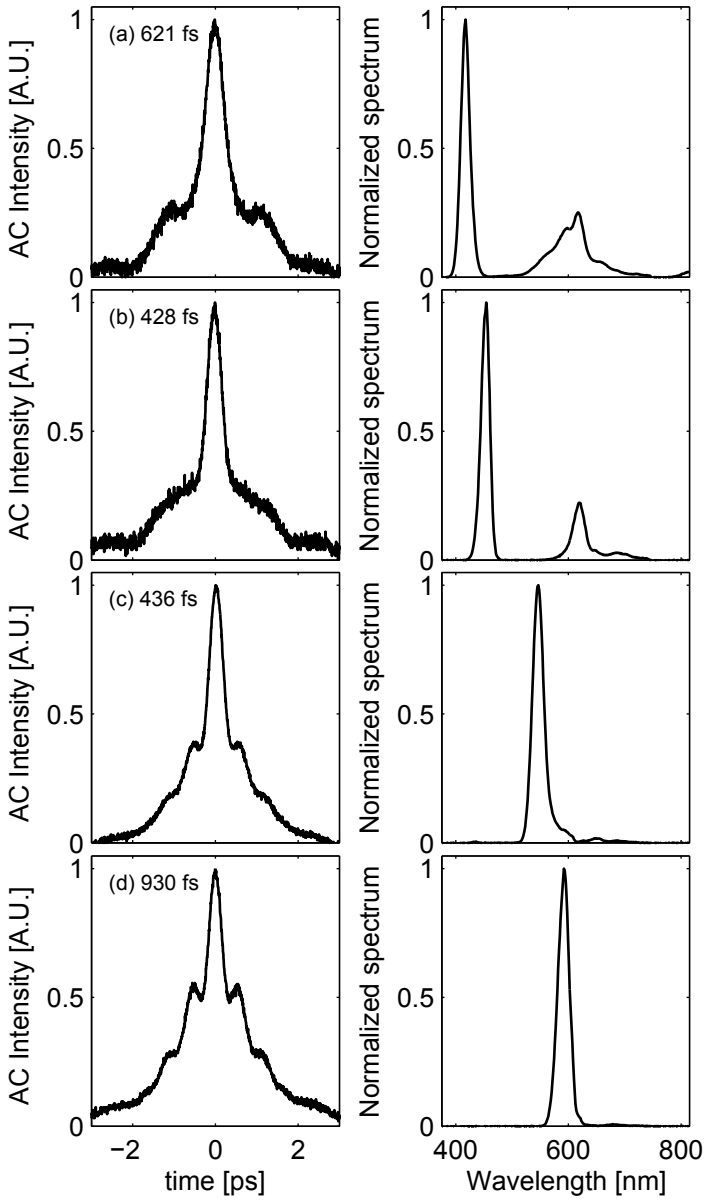

Figure 6.16: 2014-02-17: The visible FCR output spectrum is plotted along with the pump AC trace for different input pump pulses (a-d). The pump power level is fixed at 225 mW with 44.6% coupling efficiency (a-d). The pump pulse AC FWHM is indicated next to the label. The main peak for subfigure (a-d) is centered at 417,454,547 and 592 nm.

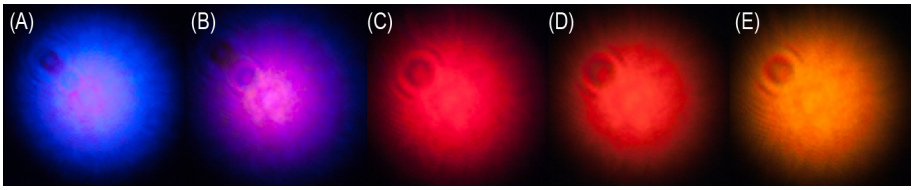

Figure 6.17: Examples of the collimated output for a tapered fiber structure for different pump parameters, projected onto a white background and exposed with an RGB camera.

the principal fiber axis. As a result, optimizing the pump polarization launch angle was required to get the most efficient FCR.

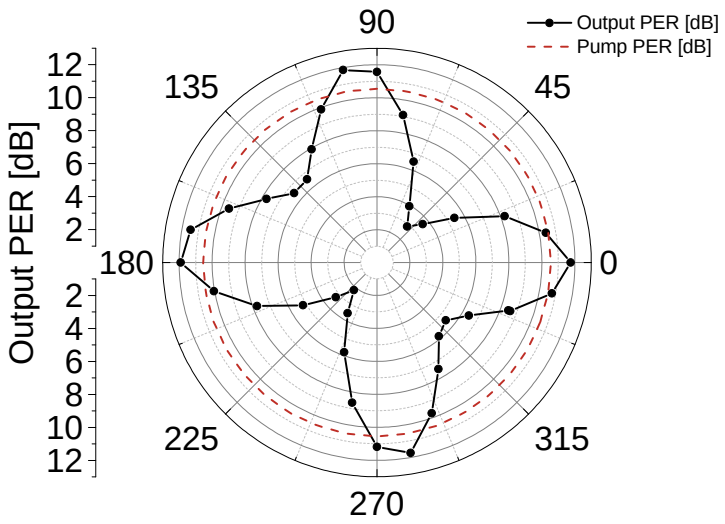

Figure 6.18: The PER of the pump measured at output of the taper, as a function of the incident pump polarization angle (degrees). The input pump PER is indicated by the dashed line and remains constant at 10.5 dB as the pump polarization angle is rotated.

The effects of the birefringence for the NL-3.0-850 fiber, has an increased impact for tapered fiber structures opposed to straight non-tapered fibers, due to the z-dependence of the phase-matching for taper structures. The birefringence of the NL-3.0-850 fiber was touched upon briefly in section 6.3 concerning non-tapered fibers. By rotation of a half-wave-plate after the HC pump output and rotation of the linearly polarized pump incidence angle, as indicated in fig. 6.1 of the experimental setup. While the launch angle of the pump was varied, the pump PER measured at the fiber taper output was investigated.

Manual measurement of the PER, using a power-meter and a linear polarizer proved more reliable and repeatable than using a discrete extinction ration meter (*OZ Optics Ltd. Er-100-IR*). As a result, the PER was measured by hand for each pump polarization angle, as shown in fig. 6.18. This measurement was performed for a 25-2-25 mm fiber taper and reflects the observed experimental trend. For a 10.5 dB pump input PER The PER varies periodically between

2.2 dB and 11.9 dB as the pump polarization angle for the incident pump is rotated. As expected the measured PER maximum has a period of 90^o, with similar PER along the slow and fast axis. However, there is a difference in the minimum PER obtained when launching 45^o from the slow or fast axis, which is alternating between 2.2 and 6.6 dB, and could originate from the input pump which is not perfectly linearly polarized.

In fig. 6.19 the measured PER of the pump is plotted along with a contour plot of the output spectrum centered around the blue phase-matching region. The total output power is integrated from the contour plot for each angle and is shown in fig. 6.19c. Three dashed blue lines indicate different local maxima in the output power, whereas the two red lines indicate two local minima in the output power.

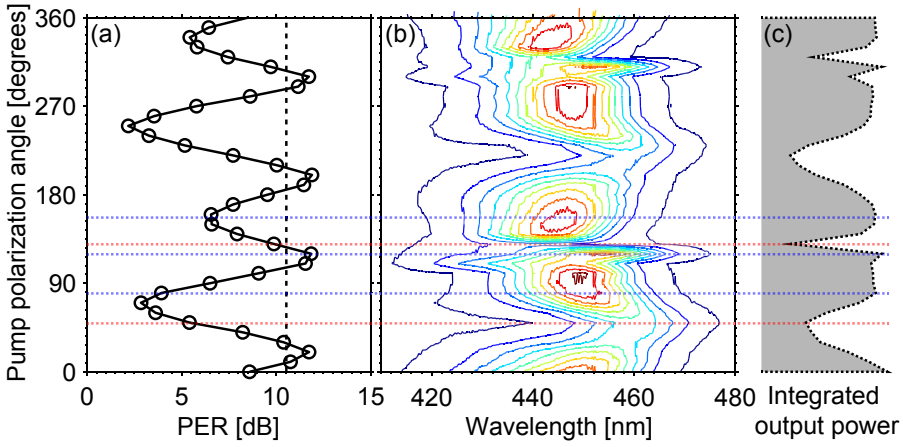

Figure 6.19: (a) Pump PER measured in dB at the output of the taper for different incident pump polarization angles. The dashed line denotes the PER of the pump before the taper. (b) Contour plot of the blue part of the output spectrum as the incident pump angle is rotated. (c) Integrated output power from 400 to 500 nm from the contour plot measurements in (b). Measured for 230 mW pump power and 42.6 coupling efficienty.

The rotational invariance between the two principal polarization axes that was lacking in the PER measurements, is also reflected in the FCR output spectrum. It appears that FCR generated when the pump launched along the two different principal axes is different, e.g. at 20^o and 110^o in fig. 6.19a.

At a pump angle near 110^o where the pump polarization is aligned along a principal fiber axis (see the blue dashed line in fig. 6.19b), a peak in the output power is observed. This behavior is expected, as the effective fiber nonlinearity is maximized when launching along the principal fiber axis. However, a 90^o rotation of the pump to the complimentary principal fiber axis, provides an unexpected near-minimum in the output power.

From the measurements in fig. 6.19, it is evident that the polarization dynamics for the fiber taper is not trivial. It is believed that the complex polarization behavior is caused by the fact that the nonlinear fiber is not intentional polarization maintaining, and because the pump is not perfectly linearly polarized.

Preliminary numerical studies were performed by Jesper Lægsgaard, taking the weak birefringence of the nonlinear fiber into account, along with the fact that the pump is not perfectly linearly polarized. Here it was found that changes in the pump launch angle relative to the fiber taper had a large impact on the generated FCR light. While these results did reproduce some of the experimental observations, further investigation is outside the scope of this thesis.

The experimental results showed a high sensitivity in the generated FCR to the pump polarization angle. This polarization nature could be exploited as a degree of freedom for the sake of tuning the FCR emission wavelength. However, as the end goal for the FCR laser is a fully spliced and all-fiber based setup, tuning the emission wavelength using polarization does not seem practical. For such a system the method of electrical tuning the pump pulse parameters to control the emission wavelength, as described in chapter 5, seams more feasible.

In the continued experimental studies, the polarization nature is taken into account when adjusting and optimizing the performance of the FCR generation. The pump launch angle relative to the principal fiber axis of the nonlinear fiber is used as a parameter that is optimized, in order to obtain the highest conversion efficiency and the widest wavelength tuning range possible, for the emitted FCR light.

6.6.2 Polarization of the generated Cherenkov radiation

Motivated by the high sensitivity in the generated FCR towards changes in the pump polarization, the polarization of the generated VIS FCR light was investigated. By insertion of a free-space polarizer after the taper and before the spectrometer, the polarization nature of the emitted FCR light was characterized. This is shown in fig. 6.20 where the generated FCR output spectrum in the 25-2-25 mm taper is plotted for three different angles of the polarization analyzer. The output spectrum corresponding to the angle of maximum and minimum transmission through the polarizer, at 90^o separation, is compared with the output measured without the polarizer. For the main FCR peak centered at 438 nm a PER of 6.5 dB was found. From the figure it is evident that the polarization for the peak at 438 nm and the broader 570-660 nm region is different.

By incremental rotation of the polarizer angle while measuring the output spectrum, enabled the measuring the PER across the output spectrum at each wavelength. In fig. 6.21 the PER is plotted along with the output spectrum, measured without the polarizer. It was found that the PER was largest in the vincinity of the 438 nm peak, but varied across the output spectrum.

Mapping out the polarization angle across the spectrum revealed a variation in the polarization angle by $\sim 15^o$ across the 438 nm peak. Furthermore, the emission polarization angle of the 438 nm peak differs from the polarization angle of the smaller sub-peaks in the 570-660 nm region (supplementary figure listed in fig. D.1).

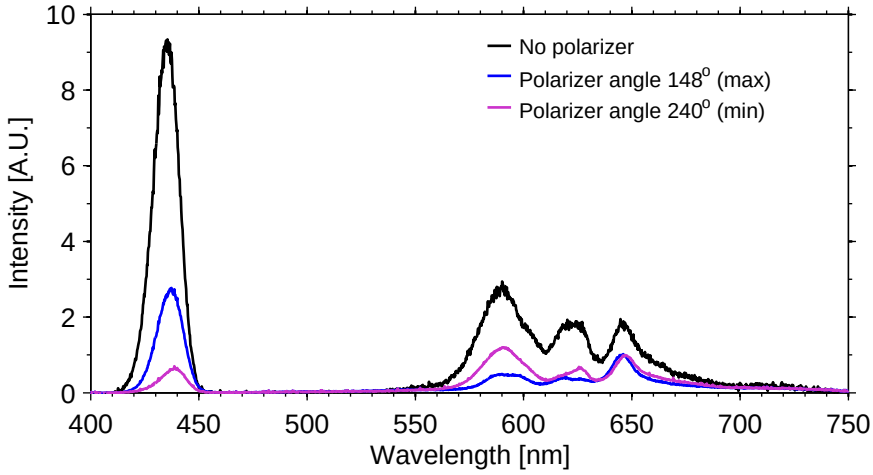

Figure 6.20: Characterization of the emitted FCR polarization. The output spectrum, showing an FCR emission peak at 440 nm along with a broader FCR region from 570 to 660 nm.

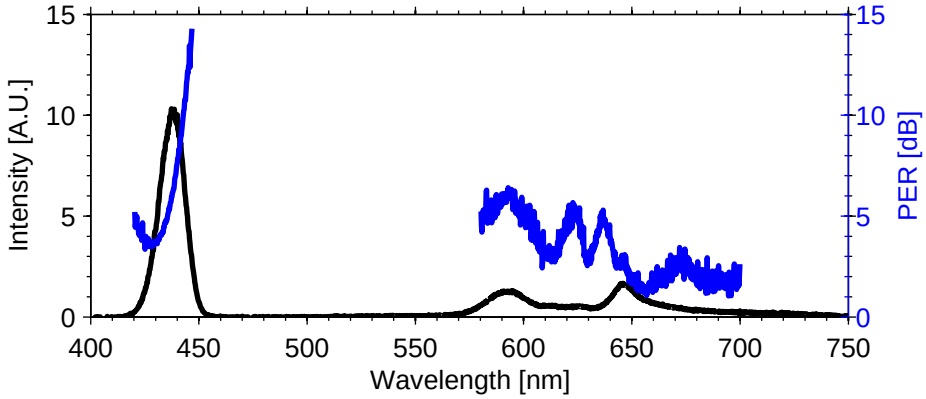

Figure 6.21: Measured FCR output spectrum plotted along with the measured PER.

6.6.3 (a) Pump-compression along the down-taper

This section presents the results obtained for the 25-2-25 mm taper structure outlined in fig. 6.15a, which has a 25 mm long lead before the down-taper, followed by 95 mm lead after the end of the up-taper. The results show FCR generation along the down-tapering section of said taper.

The measurements were carried out in rapid succession of each other, to avoid any drift in the coupling coefficient across the duration of the measuring session. The pump power was monitored with a power-meter as shown in the experimental setup in section 6.1.

From the previous experiments on non-tapered fibers, it is expected that with 25 mm lead prior to the taper, the pump CP should be located along the down-tapering section. The output spectrum in fig. 6.22, plotted for increasing pump power, contains two spectrally isolated peaks. The main blue peak is accompanied by a secondary peak around 600 to 640 nm.

A red-shift in the central FCR wavelength of the main peak, is observed when increasing the pump power. A 27 nm tuning range extending from 421 to 448 nm is obtained, when increasing the pump power from 197 to 228.7 mW. The pump AC FWHM decreases from 550 fs at the lowest power setting to 510 fs at the highest pump power setting. As discussed in section 5.9.1 this red-shift with increasing pump power suggests that the FCR emission is originating from the down-tapering section.

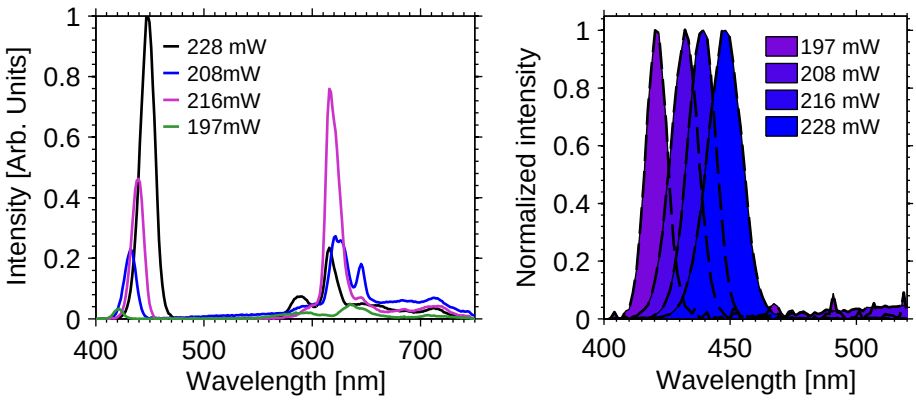

*Figure 6.22: Measured output spectrum **(left)** plotted for different pump power levels, plotted along with the normalized intensity vs wavelength (right). These measurements show that as the pump power is increased, the FCR wavelength red-shifted. The pump launch angle remained constant at a 355^o wave-plate angle. The pump monitor power was increased from 197-228.7 mW, at a power amplifier setting of 601.4-703.5 mV. The pump AC FWHM decreased from 550 fs at the lowest power setting to 510 fs at the highest pump power.*

Numerical simulations indicated that the secondary peak around 600-650 nm, originated due to recompression of the pump pulse further along the taper. This was tested by doing a cutback of the fiber in the middle of the up-tapering region, as illustrated in fig. 6.15b.

A comparison of the output spectrum before and after cutback at the taper waist is shown in fig. 6.23 for different pump launch angles relative to the FUT. The results shown in fig. 6.23a show spectrally isolated emission both around 440 nm and around 600 nm. The results obtained after a cutback along the up-taper in fig. 6.23b, show suppression of the secondary emission around 600 nm.

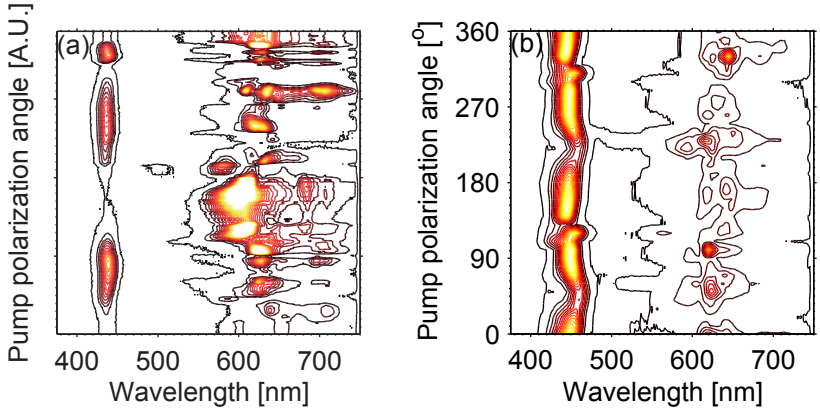

Figure 6.23: Measurement of the output spectrum for varying angles of the input pump polarization. ***(a)*** *Before cutback along the up-taper (see fig. 6.15a).* ***(b)*** *after cutback at the taper waist (see fig. 6.15b).*

6.6.4 (b) Pump-compression along the up-taper

Following a cut-back of the lead prior to the taper structure, corresponding to the shape outlined in fig. 6.15c, shifted the CP to the up-tapering part of the fiber taper. From the photos of the taper shown along side the estimated taper shape in fig. 6.24, makes it possible to identify the CP in the up-tapering part of the taper structure.

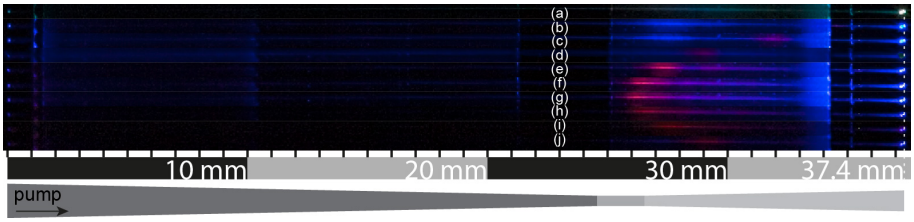

Figure 6.24: The photos (a-k) are captured with an RGB camera and are all exposed at identical settings, and can thus be compared directly. The pump power is lowest for (a) and increases monotonically towards (j).

For this experiment an improved pulse compression fiber was utilized, described in more detail in section 4.3.1. The HC-1060-03 fiber replaces the HC-1060-02 fiber and provides a lower pump pulse duration, which as a result lowers the average power required for FCR in the following experiments, in comparison to the results shown in the previous chapter. The new and improved pulse compression scheme is described in detail in section 4.5.2. The pump pulse duration, measured by FROG, decreases from 260 fs down to 230 fs from a 92.3 to 139.6 mW average pump power, after which the pulse duration increases towards 900 fs at 220 mW.

The output spectrum corresponding to the taper photos in fig. 6.24, is shown in fig. 6.25. For this taper configuration, only a single and isolated FCR

spectum is observed.

The central wavelength is blue-shifted from 493 nm at 92.3 mW average pump power, down to 413 nm at 157.1 mW average pump power. These two spectra corresponds to (a) and (e) in fig. 6.24, respectively. From the photos shown in fig. 6.24 it becomes evident that for higher pump powers the central wavelength remains constant the as the CP moves down into the taper waist region. However, due to degradation of the taper transmission which was reduced to 48%, poor conversion efficiency was obtained. For the measurements shown in fig. 6.25, the output powers was in the μW range.

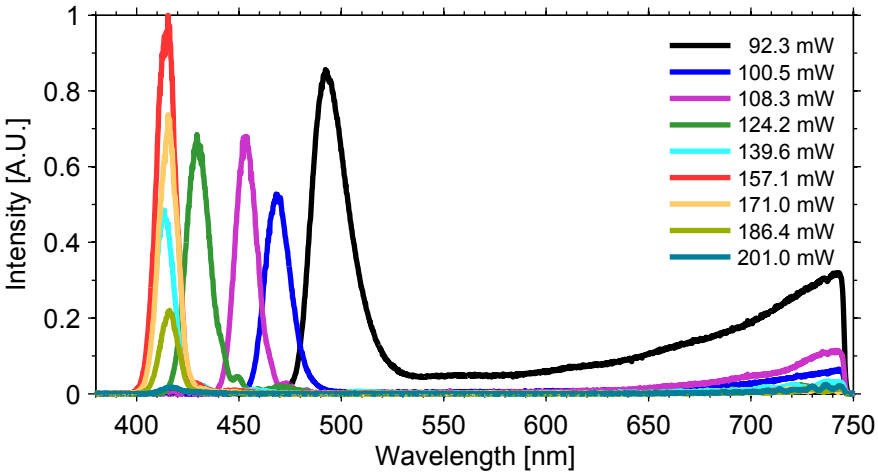

Figure 6.25: Measured FCR output spectrum for increasing pump power at a 48% coupling efficiency.

6.7 Results for the 10-2-10 mm taper

A shorter 10-2-10 mm taper structure, was tested in similar fashion as for the 25-2-25 mm taper described in section 6.6. The taper dimensions is shown in fig. 6.26, and has a 50.5 mm fiber lead before the down-taper starts, and a 121.7 mm total length.

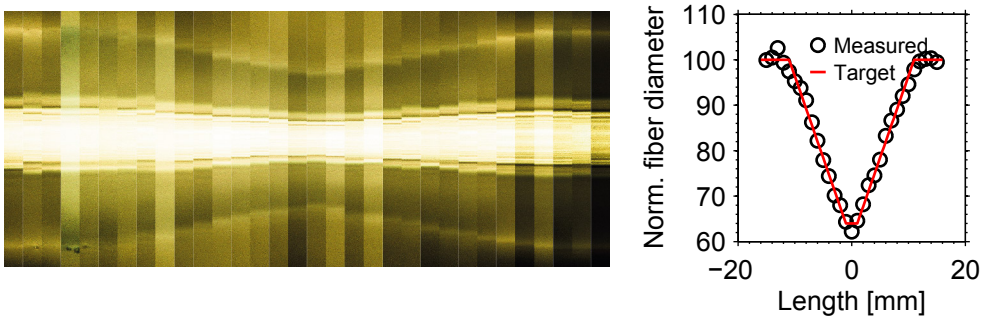

Figure 6.26: Measurement of the fiber dimensions for fiber the tested 10-2-10 mm taper structure. ***(left)*** *Images of the taper dimensions using a 50x objective.* ***(right)*** *Measured taper dimensions shown along with the 10-2-10 mm target.*

The taper location and lead length is shown in fig. 6.27 for two different cutbacks of the fiber length. The taper alignment was done by adding markers on the taper structure with a pen under the microscope. When mounted in the experimental setup, the fiber could be cleaved with the intended length of fiber lead before the taper waist, to obtain a pump CP along the taper structure. The measurements relating to the taper in configuration A (fig. 6.27a) are shown in section 6.7, while the results relating to the taper in configuration B (fig. 6.27b) are shown in section 6.7.

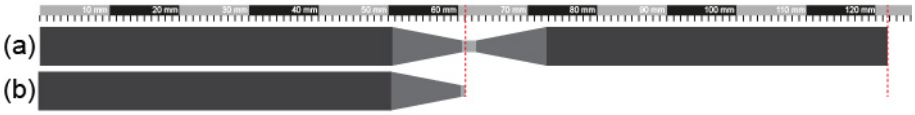

Figure 6.27: Schematic of the dimension and positioning of the taper and the lead length (a) before cutback and (b) after cutback at the taper waist. The pump light is launched from the left side.

Configuration A (Before cutback)

The taper shape and lead length for configuration A is outlined in fig. 6.27a. A taper transmission of 71% was obtained, which includes the transmission loss of the input and output collimation lenses. The measured output spectrum is plotted for a range of pump powers in fig. 6.28a-k along with the corresponding photos showing the pump CP in fig. 6.29a-k. During the experiments the CPA parameters were fixed at a ∼235 fs pulse duration, while the final pump power

injected into the FUT was adjusted using a linear polarizer and a half-wave plate.

At the lowest power setting, corresponding to the plot fig. 6.28a, a single isolated green-colored peak is observed centered at 518 nm. The corresponding pump power and output power is listed in section 6.7. This measurement corresponds to the photo in fig. 6.29a showing an image of the taper exposed with an RGB camera from a top-view perspective of the fiber taper. It is seen that the pump CP is located 3-4 mm into the down-taper, followed by emission of green light which is scattered out of the fiber taper structure.

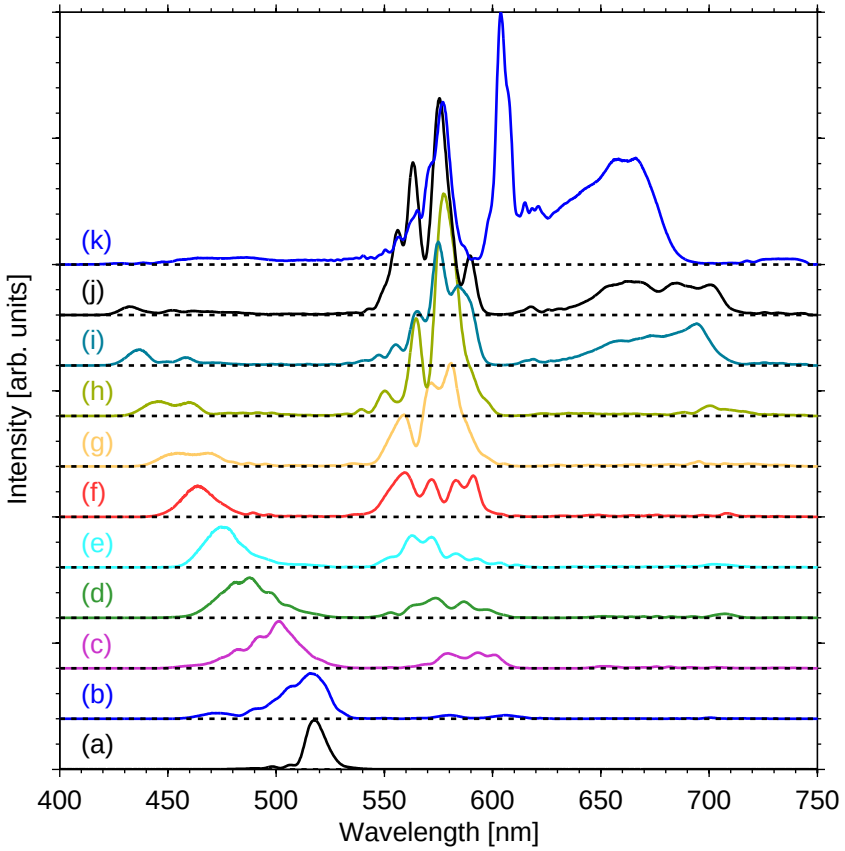

Figure 6.28: Measured output spectrum for a range of pump powers that increase from (a) towards (k), and are listed in fig. 6.29.

As the pump power is increased monotonically in fig. 6.28a-k the output spectrum gets increasingly complicated. the spectral peak in fig. 6.28a at 518 nm is continuously blue-shifted down to 432 nm in fig. 6.28j with increasing pump power. As the power is increased, isolated FCR emission at a secondary spectral region starts to appear at 580-610 nm, as shown in fig. 6.28b. When

the pump power is increased further, the spectrum blue-shifts monotonically towards 550-590 nm in fig. 6.28k. At the highest power settings a broader continuum starts to appear, shown in fig. 6.28h-k.

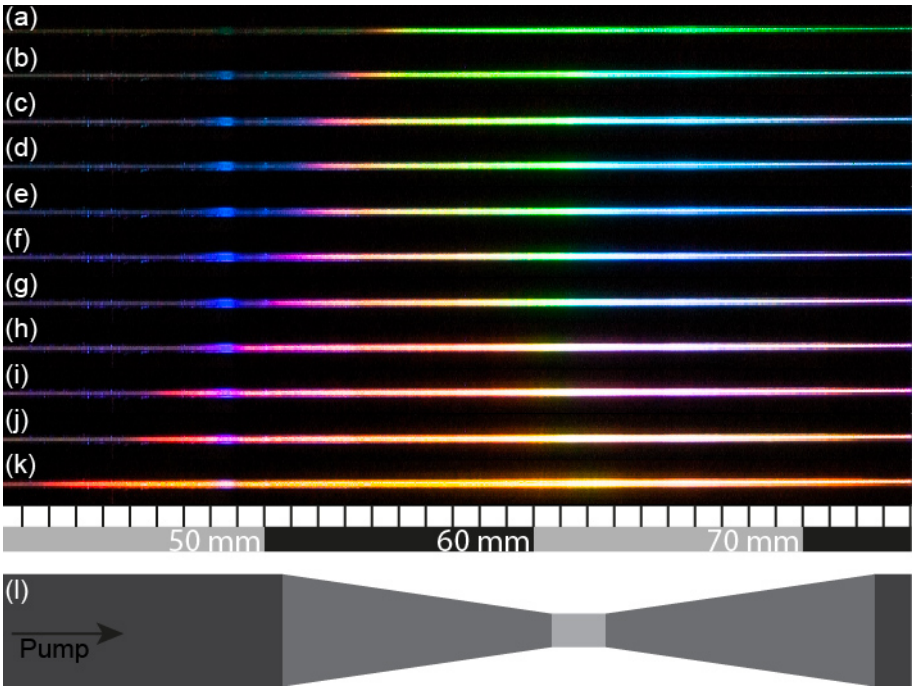

Figure 6.29: Results on 2014-07-31-16 before cutback of taper13. The 11 photos (a-k) shown in the top are exposed at identical settings, and can be compared directly. The pump power is lowest for (a) and is increased mononotically towards (k).

In fig. 6.29a-k the initial CP and associated FCR emission is visible. It is observed how this point translates to earlier positions along the fiber when the pump power is increased, with the translation spanning ~ 13 mm for the 58.6 to 89.9 mW change in pump power.

ID	Pump power [mW]	VIS Output power [mW]	ID	Pump power [mW]	VIS Output power [mW]
(a)	58.6	0.13	(g)	67.0	0.72
(b)	60.9	0.26	(h)	72.2	1.06
(c)	62.7	0.39	(i)	76.5	1.37
(d)	63.9	0.43	(j)	78.8	1.65
(e)	64.7	0.46	(k)	89.9	2.53
(f)	66.0	0.57			

Table 6.3: List of the measured pump power and VIS output power for measurement (a-k) in fig. 6.28 and fig. 6.29.

While the secondary region could be the result of subsequent pump recompression along the taper profile, it is difficult to make any conclusions based on the presented measurements. However, by performing a cutback at the taper waist, the potential FCR generation along the up-taper and fiber lead tail can be avoided.

Configuration B (after cutback)

Following a cutback at the taper waist, as illustrated in fig. 6.27, the taper was characterized as shown in fig. 6.30. The corresponding pump parameters are listed in table 6.4, with a pulse duration decreasing monotonically from 255 fs at the lowest pump power to 228 fs at the highest pump power setting.

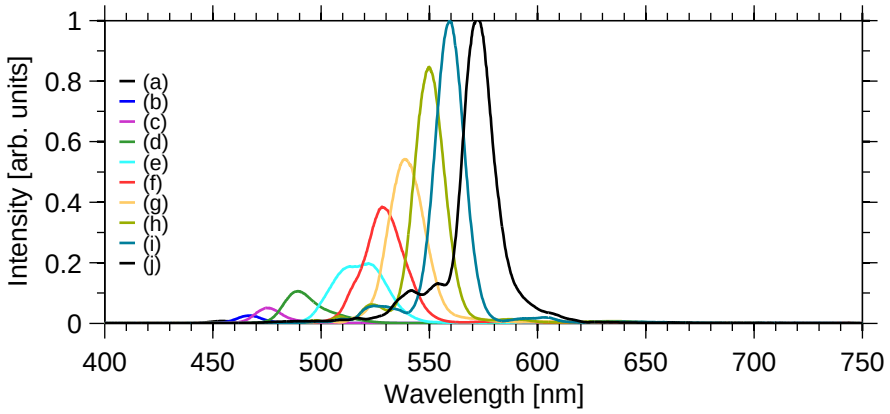

Figure 6.30: Output spectrum for increasing power from (a) to (j), with pump pulse parameters listed in table 6.4 at a 61.3% taper coupling efficiency.

In comparison to the results obtained for configuration A, the output spectrum is reduced to a single output peak, across the pump power range. The FCR output spectrum and output power is shown in fig. 6.31. Considering the normalized output spectrum, a 118.4 nm tuning range is obtained, extending from 454.1 to 572.5 nm. The output FWHM bandwidth varies from 12.9 to 30.8 nm across the tuning range, while the VIS output power increases monotonically from 20 μW to 1.93 mW.

The power dependent tunability in the FCR emission wavelength was reduced by from 118.4 nm reported here to 86.2 nm by rotation of the pump launch angle by 22^o. These results have been included in the appendix (appendix D.4).

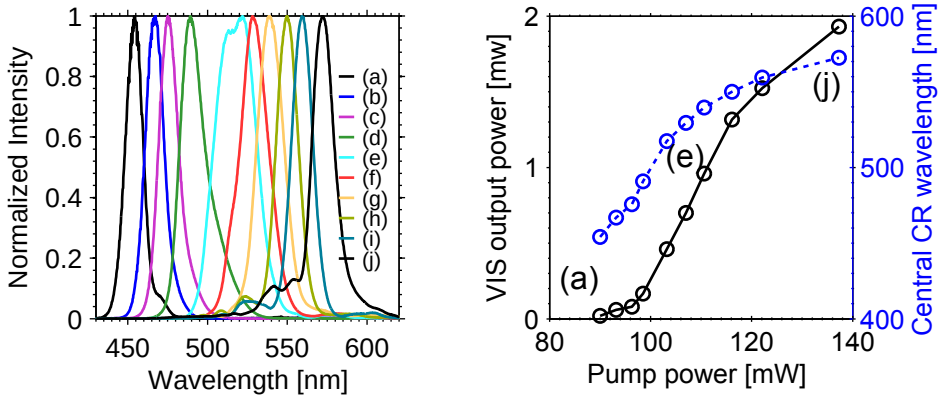

Figure 6.31: ***(left)*** *Measured normalized FCR emission spectrum.* ***(right)*** *Measured visible FCR output power and central FCR emission wavelength versus pump power. The pump parameters are listed in table 6.4.*

ID	Monitor [mW]	Monitor [mV]	Pump AC [fs]	Pump FROG [fs]	VIS Output [mW]	λ_c [nm]	BW [nm]
(a)	90.0	269	382	255	0.02	454.1	12.9
(b)	93.2	280	376	252	0.06	466.9	13.8
(c)	96.3	290	371	249	0.08	475.6	14.7
(d)	98.5	301	366	246	0.17	490.8	18.9
(e)	103.2	316	362	244	0.46	517.4	30.8
(f)	107.0	326	360	243	0.70	529.4	21.6
(g)	110.6	339	357	242	0.96	539.5	20.2
(h)	116.1	359	355	239	1.32	550.0	16.8
(i)	122.1	381	356	234	1.52	559.4	16.3
(j)	137.3	436	372	228	1.93	572.5	16.8

Table 6.4: Table of the measurement parameters for fig. 6.30 and fig. 6.31.

6.8 Discussion

The results for the FCR source are evaluated according to the following criteria:

I All-fiber pump source with no free-space components

II fully monolithic FCR setup, i.e. direct splicing of the FCR generation fiber to the pump source

III All-electrical tunability of the FCR emission wavelength, i.e. no free-space gratings, attenuators etc.

IV Broad wavelength tuning bandwidth

V Single peaked and isolated emission spectrum

VI Short temporal pulse shape of the generated FCR across the wavelength tuning range

VII Similar output power levels across the wavelength tuning range

The experiments were conducted based on fulfilling I. While the testing-platform for investigating the fiber tapers is implemented using a free-space setup, the nonlinear tapers could easily be spliced to the end-facet of the HC compression fiber using an intermediate fiber. This was also reported in previous results within the group [37], and entails that item II could fairly easily be fulfilled. Control of the duration and energy of the pump pulse is crucial to the working principles of the improved FCR source. Fulfilling item I and II confines the degree of tunability in the pump pulse parameters to what can be achieved by electrical control of the oscillator and amplifier laser diodes III. The items I-III defines the obtainable pump pulse parameters, and set the overall limitations of the FCR source (in item IV-VII).

The FCR wavelength tuning range IV depends on the synergy between the properties of the pump source and the dimensions and corresponding phase-matching regions for the given taper structure.

The experimental results showed that a single peaked and isolated emission spectrum V could be obtained for different FCR configurations. In the study of FCR generated along different parts the taper, it was found that proper cutback of the fiber taper was essential to obtain single peaked and isolated FCR emission. Shortening any excessive lengths of fiber, following the relevant region of FCR generation along the taper, was crucial to avoid the issue of recurring pump compression that could lead to secondary FCR emission. These observations were also supported by numerical simulations. While the emission of a set of synchronized and spectrally isolated ultrafast pulses may be beneficial for some specialized applications, such as stimulated emission depletion (STED) microscopy, this work is focused on obtaining spectrally isolated emission.

The translational tuning of the localized FCR impacts the temporal properties of the FCR emission VI. A consequence of the high normal fiber dispersion in the generated VIS wavelength range, which increases towards the blue edge of the wavelength tuning range, is a rapid broadening of the generated FCR

pulse for subsequent propagation after the localized point of generation. The underlying principle of the improved FCR source entails that light at different frequencies is generated at different positions along the fiber. As a result, the different emission frequencies will exhibit different dispersion induced temporal broadening. This broadening is much stronger for light at blue frequencies than for light at red frequencies. Therefore, the temporal pulse quality is highly depended on the taper shape. For FCR generated along the down-tapering region the light at blue frequencies would be generated close to the end facet, while the light at red frequency is generated earlier in the taper. In a down-taper the light at blue frequencies, which has the highest sensitivity towards subsequent propagation, has to travel a much shorter distance than the light at red frequencies. In such a system the overall temporal broadening across the wavelength system will be reduced. If FCR is generated along the up-tapering part of a nonlinear fiber taper, the situation is reversed, and the light at blue frequencies will experience much stronger broadening. In this situation the light at red frequencies is generated close to the fiber end, while light at the blue frequencies has to propagate from near the taper waist to the fiber output at the end of the up-taper.

To obtain a higher degree of uniformity in the output power levels across the wavelength tuning range (item VII) would require a more detailed investigation. While a taper design optimized to the pump pulse parameters is expected to improve upon the results, further improvements could also be obtained with better individual control of the pump pulse duration and energy.

Asymmetric tapers

Numerical simulations presented in section 5.9.2 suggested futher improve upon the results for FCR generated along an up-taper profile. This lead to the manufacturing of a set of asymmetric taper profiles, where the issue of secondary FCR emission should be reduced. The measured taper profiles are included in appendix D.5 for the parameters listed in appendix D.1. Due to equipment failure characterization of said tapers is beyond the scope of this thesis.

Chapter 7

Conclusion and outlook

> Nothing in life is to be feared, it is only to be understood. Now is the time to understand more, so that we may fear less.
>
> Marie Curie

The overall aim of this PhD thesis is the investigation of nonlinear frequency conversion in different types of fiber lasers. The study focuses on two different methods for the frequency conversion of light, which are briefly presented in the following. Raman fiber lasers are examined for their frequency down-conversion ability, where infrared (IR) pump light from the Erbium band is converted to longer wavelengths. A fiber-optic Cherenkov radiation (FCR) source was explored for its ability for generating light at visible (VIS) wavelengths using an infrared Ytterbium pump source.

The investigation of Raman fiber lasers and amplifiers, leads to the characterization of two different laser cavities emitting at a 1679 nm wavelength; a 61 m high-Q cavity with a weak output coupling and a longer 140 m low-Q cavity having a larger output coupling. Subsequently, a Raman amplifier, pumped with the 1679 nm Raman fiber laser (RFL), is investigated at a wavelength range from 1679 to 1900 nm.

During the study, the performance of the 61 m high-Q cavity was found to be limited by the quality of the inscribed gratings. The shorter cavity length required an output fiber Bragg grating (FBG) with a strong reflectivity of 94%, showing strong side-lobes. The combined effect of imperfect fiber Bragg gratings and spectral broadening at higher pump power levels, resulted in high alignment sensitivity for the cavity, with a varying emission spectrum and slope efficiency. To reduce the amount of spectral broadening, a 140 m low-Q cavity was constructed using a similar method. The increased round-trip gain obtained for the longer cavity, required a weaker output grating with a less pronounced side-lobe structure. The spectral broadening issue was alleviated by reducing the circulating cavity power through the use of a weaker output

FBG. When compared with the high-Q cavity, the low-Q cavity displayed increased slope efficiency showing no signs of spectral broadening and having an output linewidth which was lower than the output FBG bandwidth.

A challenge when using FBGs with a narrow spectral bandwidth to define a cavity is, apart from the potential spectral broadening, that small perturbations in the FBG spectral alignment leads to a large variation in both emission spectrum, and output power. Apart from the potential spectral broadening, one of the main challenges, when using FBGs with a narrow spectral bandwidth to define a cavity, is that small perturbations in the FBG spectral alignment lead to large variations in both the emission spectrum, and the output power. Therefore, accurate active feedback temperature stabilization of the gratings defining the cavity was implemented; a typical 10-20 mK standard deviation in the grating temperature was achieved, ensuring accurate alignment stability.

In the stability analysis, the impact of the relative grating alignment is investigated. The results emphasize the importance of precise alignment of the cavity gratings; which was found to be crucial to both the output power and the shape and quality of the output spectrum. For the low-Q cavity, it was found that a $\sim 0.8^{o}$C increase in the grating temperature caused a 50% reduction in output power.

As a consequence of the improved cavity design, including active feedback temperature control, a driftless output was obtained for 680 mW output power at 1679 nm. A high spectral stability was obtained, having a sub-pm standard deviation in the emission wavelength and linewidth. Furthermore, a 0.43% standard deviation in the measured output power was also obtained.

A Raman amplifier (RA) having a peak gain at 1810 nm was realized experimentally. The amplifier is polarization maintaining (PM) and is pumped by the 1679 nm RFL. The Raman gain of the amplifier was characterized from 1679 to 1900 nm, and a Raman gain exceeding 20 dB at 1810 nm along with a <3 dB effective noise figure was demonstrated. The findings show that in spite of high transmission losses at 1810 nm, a high Raman gain coefficient provided by the OFS PM Raman fiber in conjunction with the developed RFL, has the potential to provide a high discrete gain, but also has the ability to provide distributed Raman amplification across tens of kilometers at reasonable pump powers levels. The RA offers improved noise performance when compared to rare earth doped amplifiers, but also provides flexibility in operation wavelength and can be used to bridge the gap between the Erbium and the Thulium band.

The VIS FCR source can be considered for a broad range of applications in the field of biophotonics. The FCR emission is characterized by having a high coherence, short temporal pulse duration, and a tunable bandwidth in the tens of nanometer range, along with the potential for very low noise properties. The pursuit of a compact and robust VIS FCR source, which is suited for applications outside of the optical lab, lead to the work on an all fiber based system. Increasing the selective tunability of current fiber laser pumped FCR systems, involved working on extending the wavelength tunability of such systems.

To achieve this, a FCR source emitting light at visible wavelengths ranging

from 420 to 610 nm is demonstrated. FCR is obtained by pumping a nonlinear photonic crystal fiber (PCF) with a 1030 nm Ytterbium based pump source. The fiber laser pump system delivers femtosecond pump pulses with pulse durations down to 234 fs and pulse energies up to 8 nJ. This system utilizes an all-fiber based pulse stretcher and compressor scheme, with pulse delivery through a hollow-core fiber.

An initial 20 nm tuning range in VIS FCR emission is obtained across a 585 to 605 nm wavelength range generated in a uniform nonlinear PCF. Tunability is obtained by varying the launched pump power, and by utilizing the power dependent phase-matching governing the FCR process. VIS output powers exceeding 3 mW are obtained across a 20-35 nm spectral bandwidth. The conversion efficiency is of the order of $\sim$1% and is limited by the pump pulse duration and energy.

To extend the wavelength tunability of the FCR source, a tapered nonlinear PCF is utilized. The operating principles of the improved FCR source relies upon the localized nature of FCR, which is provided by the soliton pump compression obtained when pumping in the anomalous dispersion regime. Controlling the localized FCR generation point along the tapered fiber structure provides a spatial dependence upon the phase-matched emission wavelength. Phase-matching at different positions along the fiber taper is dictated by the local fiber taper dispersion profile. The translational control of the pump compression point (CP) is demonstrated by exploiting a combination of control over the pulse duration and power. This control is provided by means of electrical tuning of the laser oscillator and of the amplifier system.

A series of nonlinear fiber tapers with different parameters were manufactured and investigated. During the course of the experimental investigation FCR emission across a 420 to 610 nm wavelength range is observed. This wavelength range is consistent with the theoretically predicted 430 to 610 nm linear phase-matching obtained when tapering down the nonlinear fiber from a core diameter of 3.0 to 2.0 μm.

The experimental results for two different taper structures are presented, and the difference in pump power tuning behavior for FCR generated in different parts of the taper is illustrated; i.e. the combined effect of (a) nonlinear phase matching and (b) the change in linear phase match with translation of the pump CP along the taper structure. The observations confirm that FCR is indeed generated along either the up- or down-taper; this is also supported by side-view images of the fiber taper structure. The localized FCR generation is visible to the naked eye due to scattering in the fiber core, and allows mapping of the localized FCR generation region relative to the fiber taper dimensions by use of a camera.

The results for FCR generated along both a down-taper and an up-taper section demonstrate a much improved wavelength tuning range; when compared to the results obtained using a uniform fiber. The widest tuning range is obtained for FCR generated in a 10 mm down-taper with a core diameter decreasing from 3 to 2 μm. A wavelength tunability of 118 nm, across a 454 to 572 nm wavelength range, is shown along with a maximum VIS output power of 2 mW.

Theoretical predictions provide further insight into the relevant processes and a better understanding of the underlying mechanisms that govern the potential degradation in the temporal and spectral properties of the generated FCR. For FCR generated along an up-taper, the predictions suggested using asymmetric fiber tapers, i.e. a short 10 mm down-taper followed by a longer 30-50 mm up-taper, to avoid secondary FCR emission. Unfortunately, despite the preparation of these asymmetric fiber tapers, equipment failures and time constrains prevented an experimental investigation. The results demonstrate that the use of optical fiber tapers is a promising method for extending the wavelength tuning range for FCR sources. The provision of highly tunable VIS FCR having low noise and ultrafast temporal pulse properties could be used in advancing a range of spectroscopy and microscopy techniques for biophotonic applications.

7.1 Outlook and future perspectives

For the work on RFLs a significant level of unabsorbed pump power was obtained in spite of the dual pass configuration utilizing a pump reflector FBG. This would suggest that further optimization of the FBG reflectivity, relative to the cavity length, could lead to an increased conversion efficiency.

The inscribed FBGs suffered from strong side-lobes in the reflectivity spectrum. The somewhat irregular performance, which was obtained in some cases for the high-Q RFL cavity, could be mitigated by further optimization of the inscribed FBGs. Apodization of the FBGs could potentially provide a high side-lope suppression and hence enhancing the laser performance.

Further experimental investigation of FCR generation in optical fiber tapers, should include the characterization and comparison of the temporal pulse properties of the FCR generated for different taper structures. After unsuccessful attempts on replicating the femtosecond laser oscillator further investigation into the matter is advised. A list of suggested approached to improve upon the experimental results is presented in the following.

Increased control of the pump pulse parameters: The current pump laser system could be improved by exploiting the three degrees of freedom available when calibrating the relative laser diode (LD) setting of the oscillator, pre-amplifier, and power-amplifier, facilitating further parametrization of the final pump pulse duration and energy that could be obtained. Separate control of the pulse energy and pulse duration would provide better control of the FCR generation in fiber tapers, which could improve the obtained wavelength tuning range. Separate control of the pulse energy and pulse duration would provide better control of the FCR generation in the fiber tapers, which could also improve on the obtained wavelength tuning range.

Further optimization between the taper structure and the pump source: During the course of the experiments two different taper profiles were investigated. Numerical calculation suggests that further optimization of

the taper layout structure, relative to the parameter range of the pump source, will increase performance.

More advanced taper shapes: Preliminary numerical results have also shown that in order to avoid some of the issues that were predicted, more exotic taper shapes could be utilized to provide possible solutions. This could for example be used as a method for avoiding re-collision between a pump and FCR pulse along the down-taper.

Enhanced pump laser performance: Further improvement of the combined laser oscillator and chirped pulse amplification (CPA) system, that could lead to even shorter pulse durations with higher pulse energies, would allow for lower soliton orders (N), improved conversion efficiency and better noise properties.

Part III

Appendix

Acronyms

AC	autocorrelation.
ANDi	all normal dispersive.
APM	additive-pulse mode-locking.
AR	anti-reflection.
ASE	amplified spontaneous emission.
BBO	beta barium borate.
CARS	coherent anti-stokes Raman spectroscopy.
CCD	charge-coupled device.
CP	compression point.
CPA	chirped pulse amplification.
CR	Cherenkov radiation.
CW	continuous wave.
DW	dispersive wave.
DWGR	dispersive wave generation region.
EDFA	Erbium doped fiber amplifier.
FBG	fiber Bragg grating.

FCR fiber-optic Cherenkov radiation.

FLIM fluorescence lifetime imaging microscopy.

FROG frequency-resolved optical gating.

FUT fiber under test.

FWHM full-width half maximum.

GNLSE generalized nonlinear Schrödinger equation.

GVD group velocity dispersion.

HC hollow-core.

HOM higher-order mode.

HR high reflectivity.

IR infrared.

LCSM laser confocal scanning microscopy.

LD laser diode.

LR low reflectivity.

MFD mode field diameter.

MI modulation instability.

NA numerical aperture.

NALM nonlinear amplifying loop mirror.

NF noise figure.

NL nonlinear.

NLM nonlinear light microscopy.

NLSE nonlinear Schrödinger equation.

NPE nonlinear polarization evolution.

OAM orbital angular momentum.

OCT optical coherence tomography.

OD optical density.

OSA optical spectrum analyzer.

PCF photonic crystal fiber.

PD photodiode.

PER polarization extinction ratio.

PID proportional-integral-derivative.

PM polarization maintaining.

RA Raman amplifier.

RFL Raman fiber laser.

RIN relative intensity noise.

SBS stimulated Brillouin scattering.

SC supercontinuum.

SC-PBG solid core photonic bandgap.

SEM scanning electron microscope.

SESAM semiconductor saturable absorber mirror.

SHG second harmonic generation.

SLED superluminescent light emitting diode.

SNR signal to noise.

SPM self-phase modulation.

SRS stimulated Raman scattering.

SSFS soliton self-frequency shift.

STED stimulated emission depletion.

TDFA Thulium doped fiber amplifier.

TLS tunable laser source.

TOD third order dispersion.

TPEF two-photon excitation fluorescence.

TPF two-photon fluorescence.

UV ultraviolet.

VCSEL vertical-cavity surface-emitting laser.

VIS visible.

WDM wavelength-division multiplexing.

XPM cross phase modulation.

ZDW zero-dispersion wavelength.

Appendix A

Supplementary figures concerning chapter 2

A.1 Photos of the temperature stabilized fiber Bragg grating setup

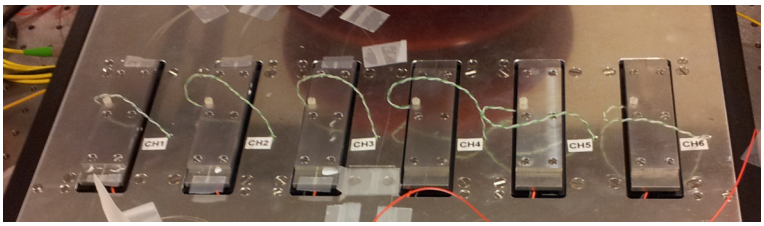

Figure A.1: Photos of the fiber Bragg grating temperature control setup, used to align and stabilize the laser cavity gratings.

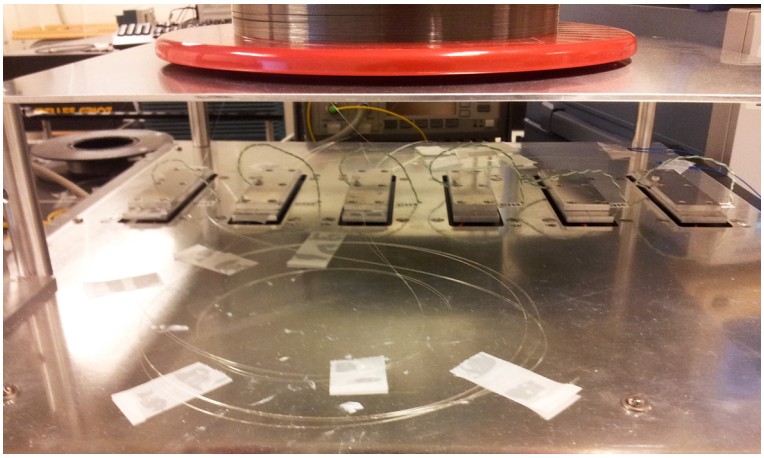

Figure A.2: Photos of the fiber Bragg grating temperature control setup, used to align and stabilize the laser cavity gratings.

A.2 Tuning of the fiber Bragg grating by stretching the fiber

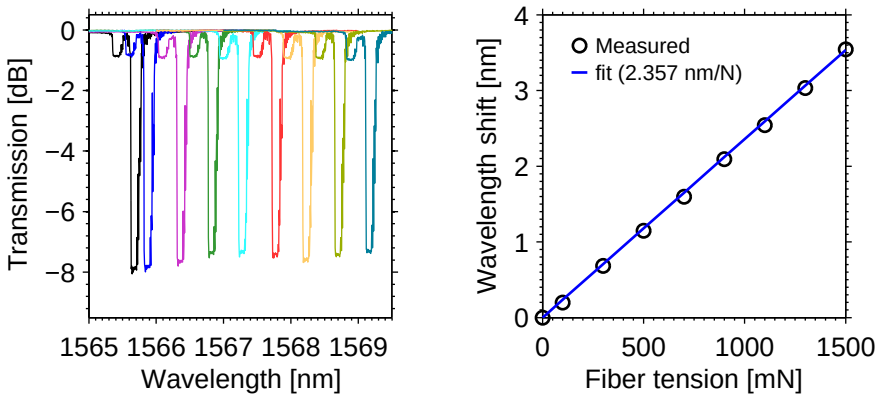

Figure A.3: ***left*** *Transmission spectrum for a FBG with increasing fiber tension.* ***(right)*** *Shift in FBG central wavelength as a function of the tension.*

A.3 Post UV illumination of the fiber Bragg grating to decrease the reflectivity

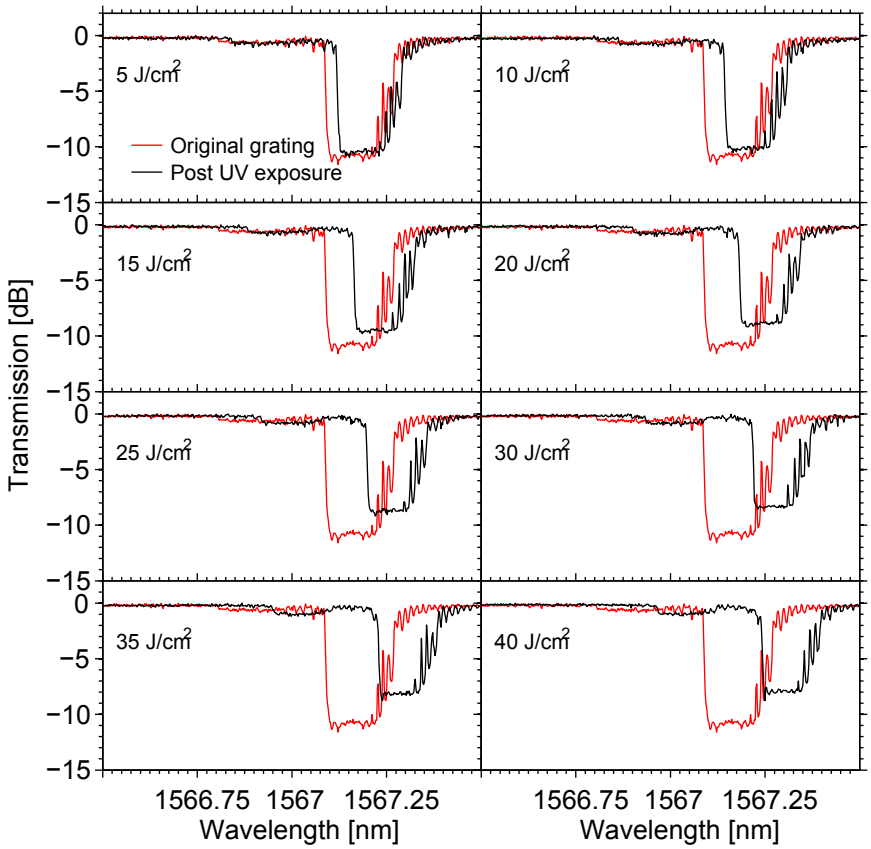

Figure A.4: Measurements showing how the grating strength can be reduced by subsequent UV exposure without a phase-mask.

A.4 Comparison of the fiber Bragg grating reflectivity

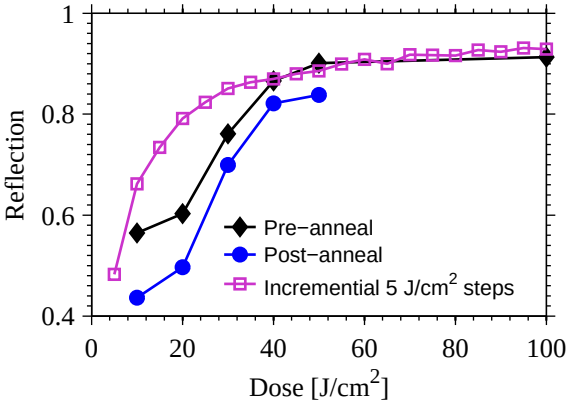

Figure A.5: Measured fiber Bragg grating reflectivity inscribed in a non D_2 loaded segment of PM Raman fiber. The reflectivity is estimated from the measured grating transmission. The gratings reflectivity is plotted versus the accumulated UV dose in 5 J/cm^2 increments (purple line), and for individually inscribed fiber Bragg gratings prior (black line) and followint (blue line) annealing of the grating.

A.5 Comparison of the inscribed fiber Bragg gratings with and without fiber hydrogenation

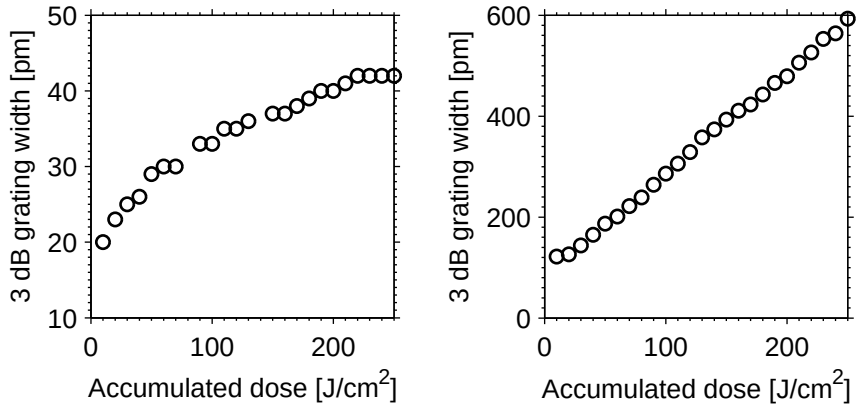

*Figure A.6: Measured fiber Bragg grating width versus the accumulated UV write dose. Comparison between non D_2 loaded **(left)** and D_2 loaded fiber **(right)**.*

the wavelength shift for increased ultraviolet (UV) dose is shown in fig. A.7

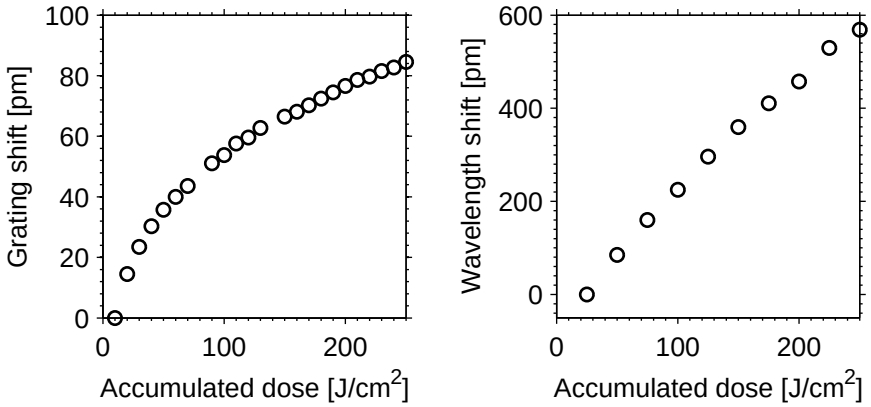

*Figure A.7: Measured shift in the central wavelength of the fiber Bragg grating versus the accumulated UV dose for a non D_2 loaded **(left)** and D_2 loaded fiber **(right)**.*

A.6 Comparison of fiber Bragg grating reflectivity and transmission

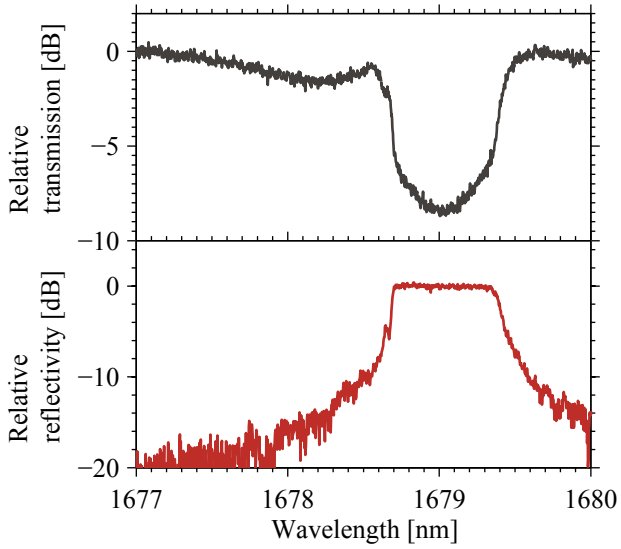

Figure A.8: Comparison of the measured grating reflectivity and transmission measured with a circulator and a broadband supercontinuum source.

A.7 Supplementary information concerning section 2.1.3

The parameter $\eta(V)$ represents the fraction of the integrated fundamental-mode intensity contained in the core, and is an approximation that is made for the LP_{01} mode, where $V \leq 2.4$ [65]

$$\eta(V) = 1 - \frac{1}{V^2}, \qquad V \leq 2.4 \tag{A.1}$$

where the V parameter defined as:

$$V = \frac{2\pi a}{\lambda}\sqrt{n_{\mathrm{co}}^2 - n_{\mathrm{cl}}^2} \tag{A.2}$$

where a is the core radius, n_{co} is the maximum core index, n_{cl} is the cladding index.

Appendix B

Supplementary figures concerning chapter 3

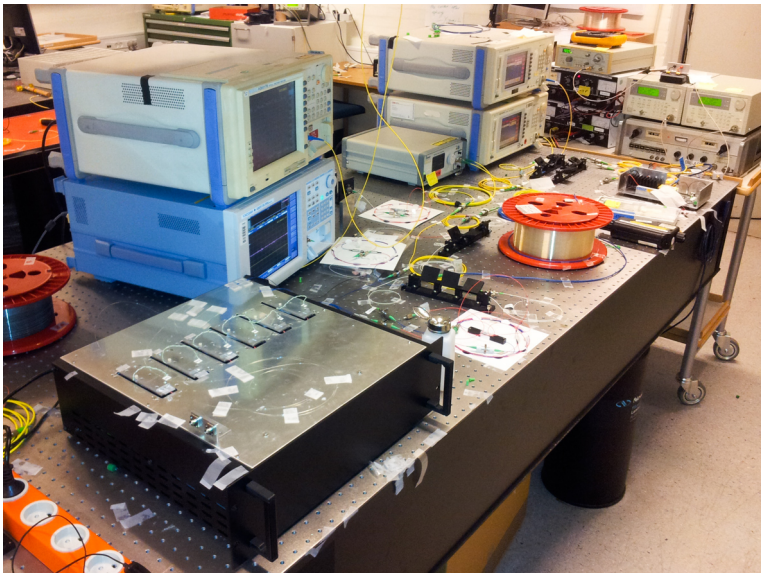

Figure B.1: Photo of the Raman fiber laser and the Raman amplifier setup.

B.1 Additional figures of the measured noise figure for the 1810 nm Raman amplifier

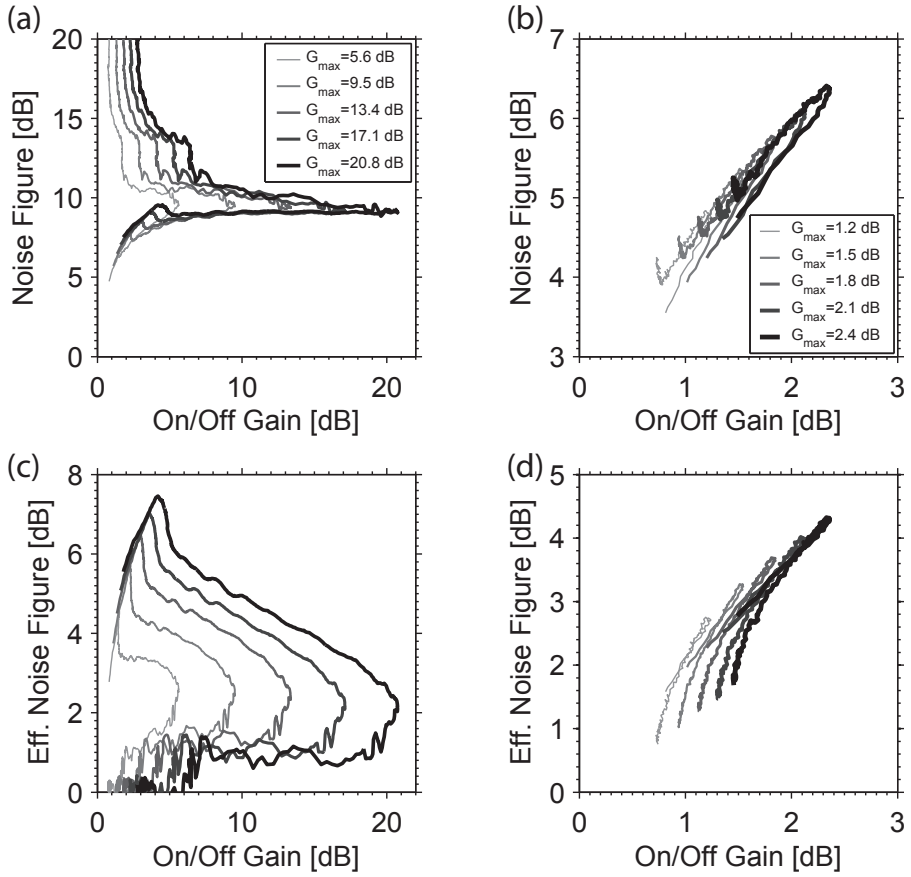

Figure B.2: Measured noise figures and effective noise figures for Raman amplification with a 1679 nm pump. The noise was characterized for linear co-polarized pump and signal (a,c) and for linear but orthorgonal polarization between the pump and signal (b,d).

B.2 Thulium ASE source

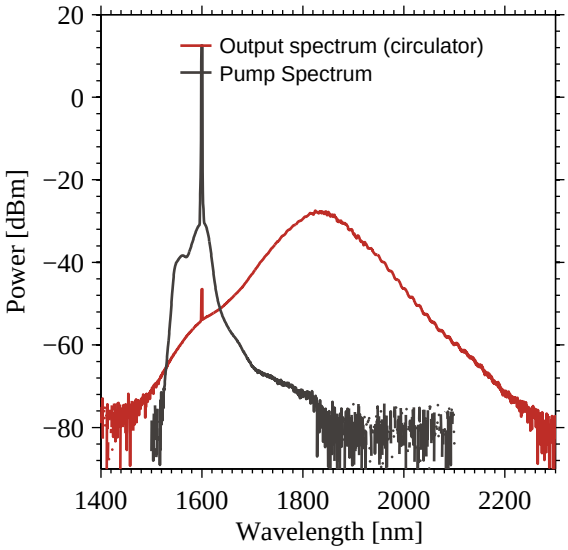

Figure B.3: Output spectrum of the Thulium amplified spontaneous emission (ASE) source, plotted along with the pump spectrum.

B.3 Unabsorbed pump power for the 140 m Raman fiber laser cavity

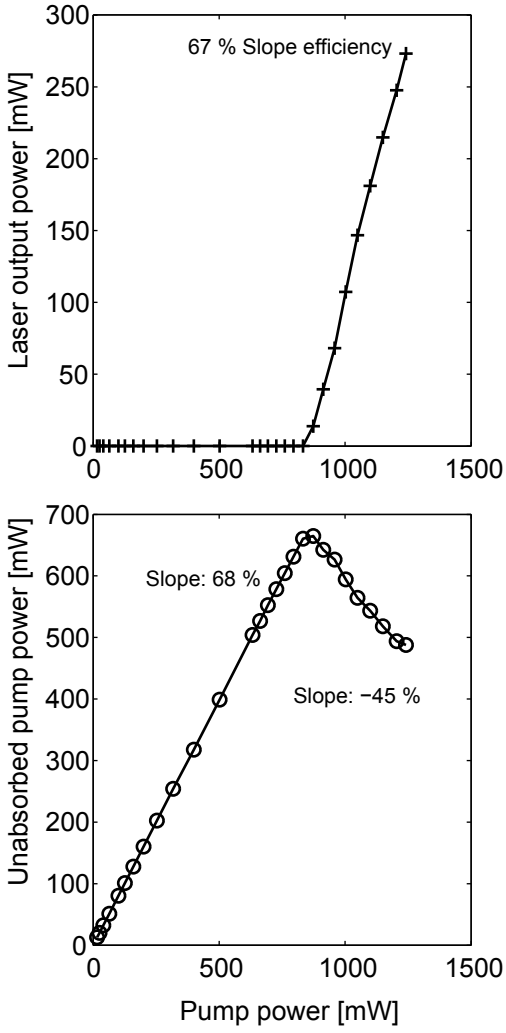

Figure B.4: Comparison of the measured laser output power and the level of unabsorbed pump power versus pump power for the investigated 140 m Raman fiber laser cavity.

Appendix C

Supplementary figures concerning chapter 4

C.1 Final pulse duration using the HC-1060-02 compression fiber

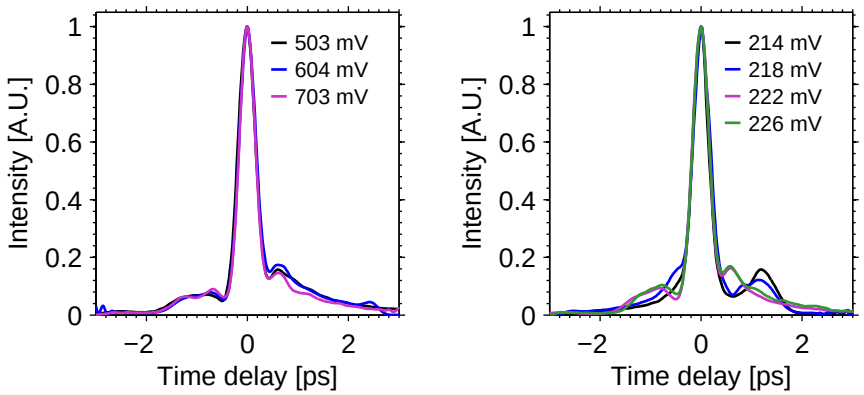

Figure C.1: The retrieved pulse shape using frequency-resolved optical gating (FROG) for compression with a HC-1060-02 fiber. ***(left)*** *Results for different power amplifier settings. The oscillator and pre-amplifier monitor LD power remains fixed at 226 mV and 615 mV, respectively.* ***(right)*** *Results for different oscillator LD power settings, while the pre- and power-amplifier LD remains constant at 615 mV and 705 mV, respectively.*

Oscillator pump [mV]	AC FWHM [fs]	Temporal FWHM [fs]
214	638	373
218	741	409
222	653	392
226	683	391

Table C.1: Measured autocorrelation duration using the HC-1060-02 compression fiber for different oscillator settings.

Amplifier pump [mV]	AC FWHM [fs]	Temporal FWHM [fs]
0	3150	1214
503	671	406
549	640	391
600	682	396
655	614	379
702	622	375

Table C.2: Measured autocorrelation duration using the HC-1060-02 compression fiber for different power amplifer settings.

C.2 Cutback of the HC-1060-03-FUF compression fiber

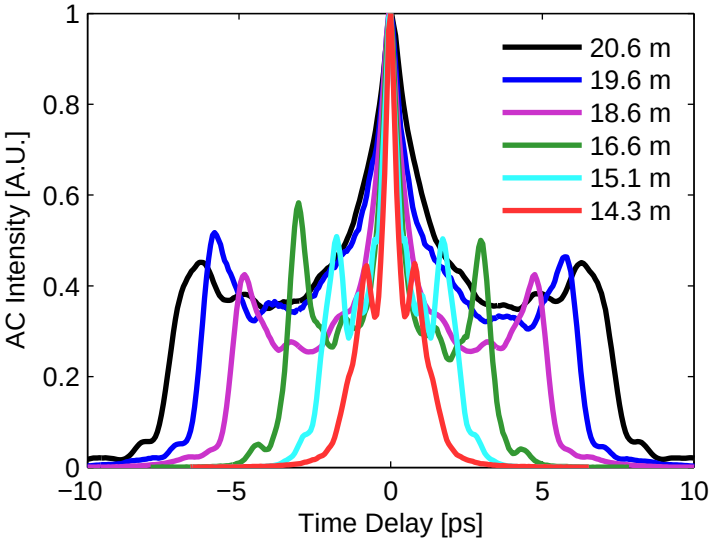

Figure C.2: Measured autocorrelation traces for different HC-1060-03-fud compressor fiber lengths.

C.3 Final output pump pulse shape with the HC-1060-03-FUD compression fiber

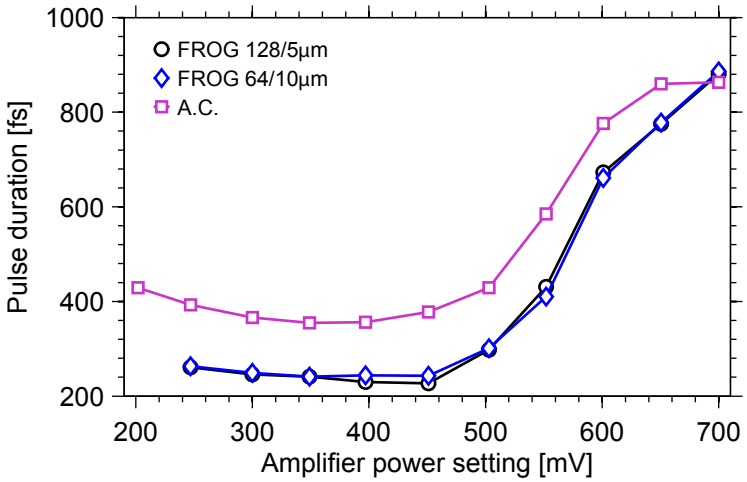

Figure C.3: Comparison of the retrieved pulse duration using FROG at two different measurement and retrieval configurations, with the label indicating the grid-size and the step-size, respectively. These are compared to the measured autocorrelation duration, and is measured with respect to the power amplifier setting. Measured for a 639 mV pre-amplifier setting.

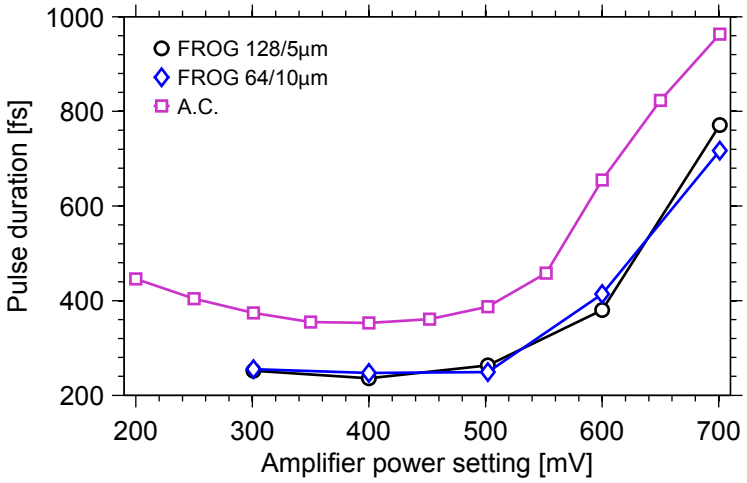

Figure C.4: Comparison of the retrieved pulse duration using FROG at two different measurement and retrieval configurations, with the label indicating the grid-size and the step-size, respectively. These are compared to the measured autocorrelation duration, and is measured with respect to the power amplifier setting. Measured for a 650 mV pre-amplifier setting.

C.4 Details regarding the cutback of the oscillator cavity length

Cutback	Panda [cm]	SC-PBF [cm]	Yb [cm]	Rep. rate [MHz]
0	379.5	112	30	
1	328.3	112	24	23.13
2	302.8	112	24	24.46
3	276.8	112	24	26.17
4	239.8	112	24	28.90
5	215.0	112	24	30.97

Table C.3: Parameters concerning the cutback of PM980 fiber from the cavity denoted (a), described in section 4.6.

Cutback	Panda [cm]	SC-PBF [cm]	Yb [cm]	Tot [cm]	Rep Calc	Rep [MHz]
0	297.7	112	33.4	443.1	23.19	23.15
1	263.5	112	33.4	408.9	25.13	25.1
2	229.7	112	33.4	375.1	27.39	27.36
3	205.0	112	33.4	350.4	29.32	29.3
4	180.0	112	33.4	325.4	31.57	31.4
5	160	112	33.4			33.5

Table C.4: Parameters concerning the cutback of PM980 fiber from the cavity denoted (c), described in section 4.6.

C.5 Output power versus amplifier power setting for the HC-1060-03-FUD compression fiber

650 mV pre-amplifier setting		639 mV pre-amplifier setting	
Power amplifier setting [mV]	Pump power [mW]	Power amplifier setting [mV]	Pump power [mW]
202	73.7	202	76.1
252	90.5	247	91.3
301	106.4	300	108.6
351	122.8	349	124.6
402	138.6	397	139.8
452	154.5	451	157.5
500	169.0	503	172.7
550	184.5	552	187.9
603	198.9	601	201.3
651	212.1	651	215.2
701	226.3	700	229.9

Table C.5: Measured collimated pump power for different power-amplifier settings, measured for two pre-amplifier configurations.

C.6 Phase matching sensitivity for the SHG crystal

Both of the autocorrelation (AC) and FROG techniques rely on the phase matching condition of the BBO crystal used for generation of the second harmonic generation (SHG) signal. The phase matching of the SHG crystal was optimized, by rotating the crystal at the pulse center, e.g. at 0 time delay. In fig. C.5 the SHG angle was optimized for optimum phase-matching for different parts of the FROG spectrum; the blue, central and red part of the spectrum. The retrieved temporal pulse shape and phase is plotted in fig. C.6 for the FROG measurement where the SHG angle was optimized for the central part of the spectrum, shown in comparison to retrieved pulse calculated for the average of the three different SHG phase-matching angles. The results show close correspondence between the two measurements.

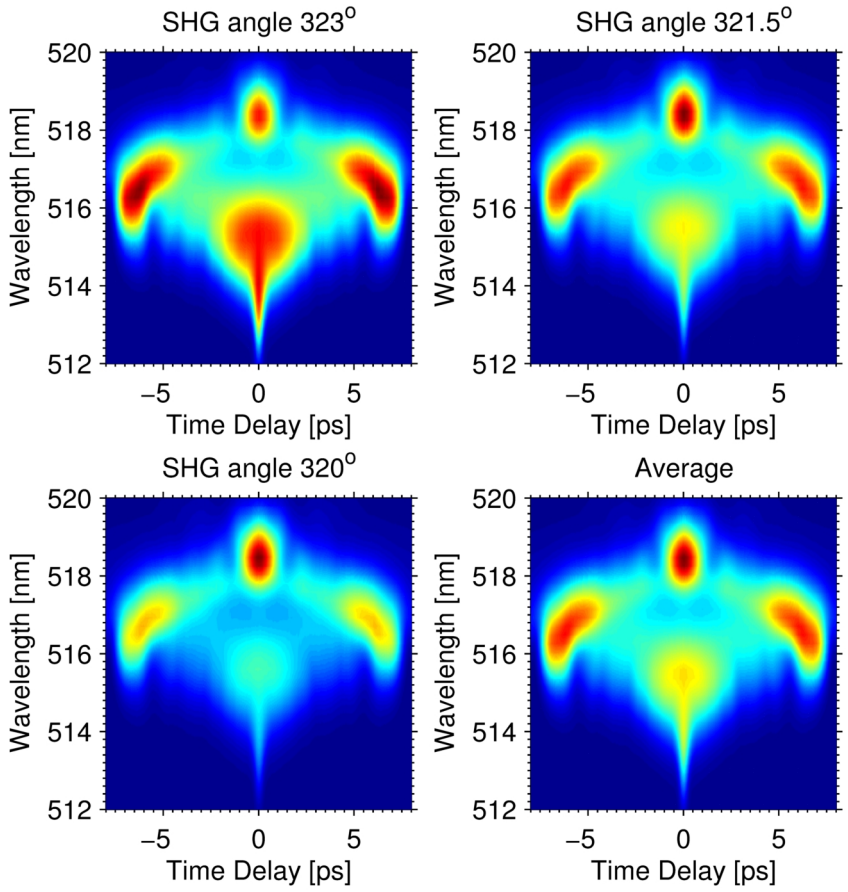

Figure C.5: Measured SHG FROG spectrograms for different SHG phase-matching angles, plotted along with an average of the three measurements.

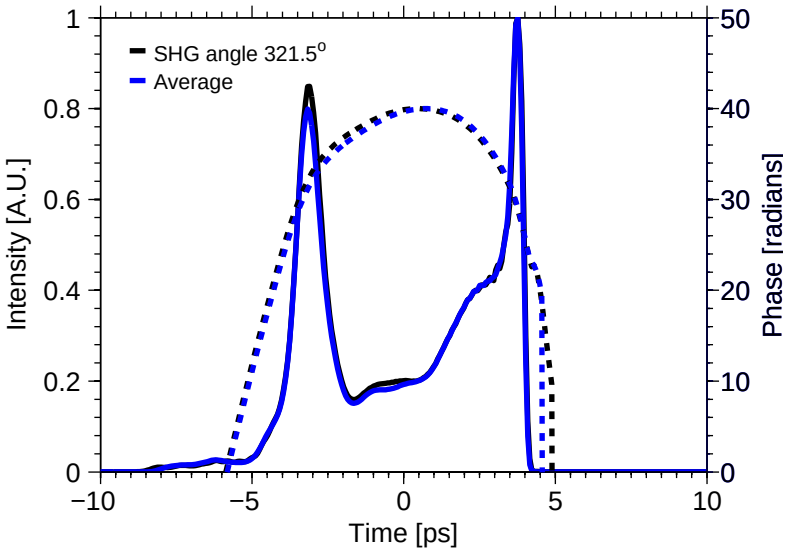

Figure C.6: Retrieved temporal pulse shape and phase compared for two retreived SHG FROG spectrograms. The first measured at 321.5° SHG angle, that was optimized for the center of the spectrum, and the other which is based on an average spectrogram of the three SHG angles shown in fig. C.5.

C.7 Examples for Q-switching

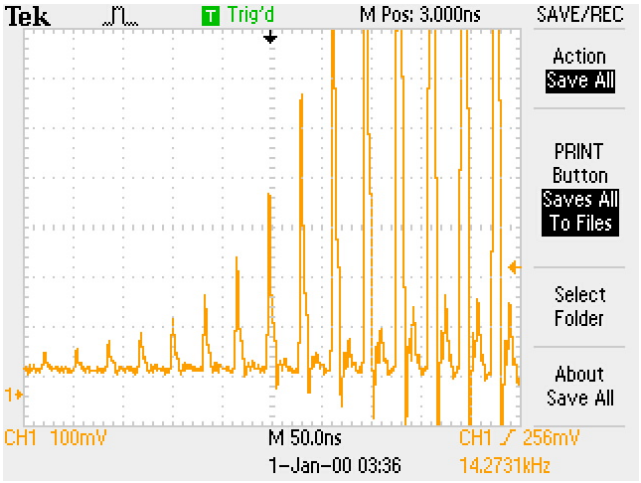

Figure C.7: Example of Q-switching at 30.97 MHz repetition rate for the cavity denoted (a) in section 4.6

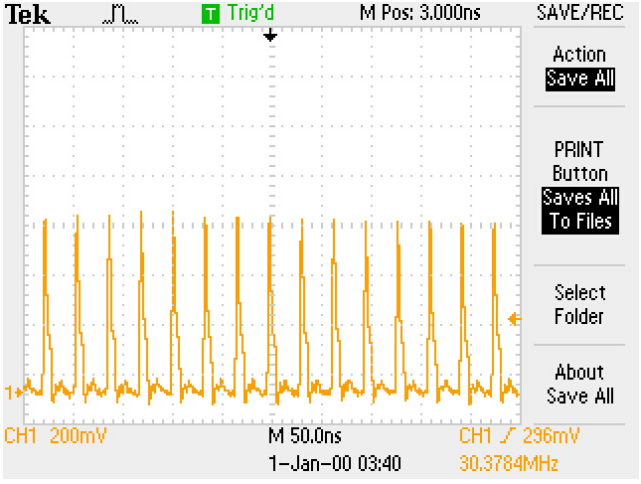

Figure C.8: Example of Q-swiched mode-locking at 30.97 MHz repetition rate for the cavity denoted (a) in section 4.6

C.8 Examples for mode-locking

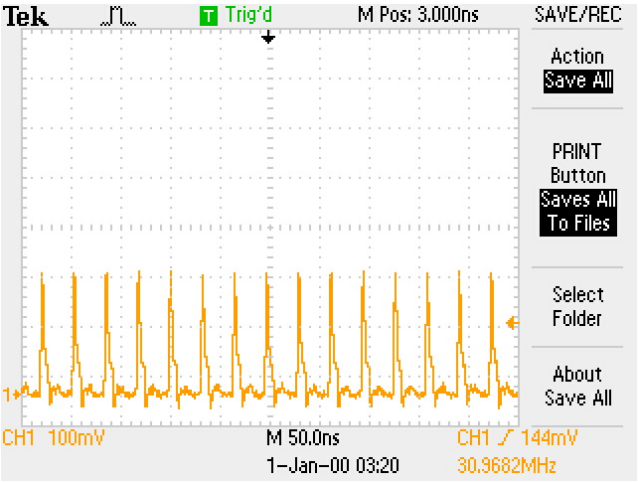

Figure C.9: Example of mode-locking at 30.97 MHz repetition rate for the cavity denoted (a) in section 4.6

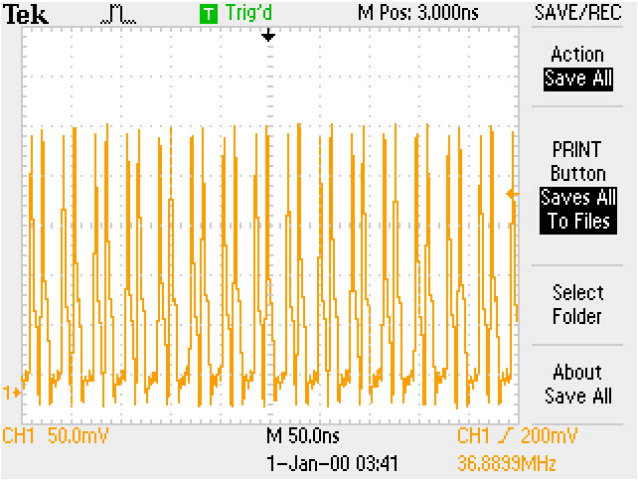

Figure C.10: Example of mode-locking with double pulsing at 30.97 MHz repetition rate for the cavity denoted (a) in section 4.6

Appendix D

Supplementary figures concerning chapter 6

D.1 Details regarding the taper machine parameters

The heating fillament is Ω shaped. The fillament with the ID E125-12525-N30, has the following dimensions: Width 3.175 mm, Thickness 0.635 mm, Neck opening width 0.762 mm and Outside diameter 3.175 mm. The parameters for the *Vytran LDS-1250* tapering machine are listed below in appendix D.1.

Parameter	Symmetric Tapers	Asymmetric Tapers
Original diameter	125 μm	125 μm
Final diameter	60/80 μm	80 μm
# Down taper stages	50	50
# Up taper stages	50	100
Constant pull velocity	0.5 mm/s	0.5 mm/s
Power	85-90 W	120-140 W
Pre-purge time	5 s	5 s
Post-purge time	10 s	10 s
Taper pull delay	1 s	1 s
Initial Furnace move	0 mm	0 mm
Power distribution	0	0
Fillament Type	-	E125-12525-N30 A/B

Table D.1: General parameters for the tapering machine.

D.2 Polarization of the generated Cherenkov radiation

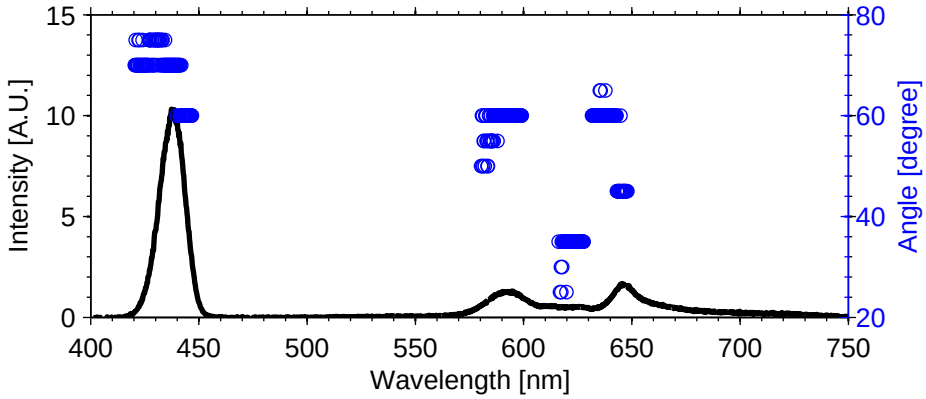

Figure D.1: Measured polarization angle for the generated Cherenkov radiation.

D.3 Cherenkov emission for different pump polarization alignments

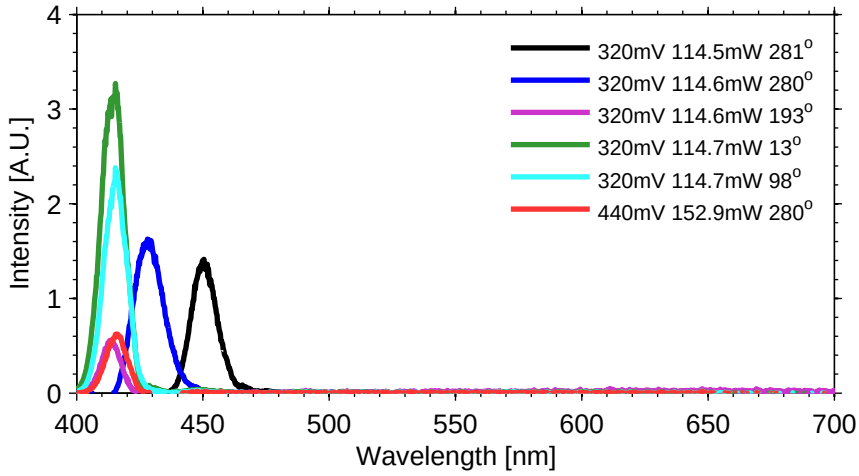

Figure D.2: Measured Cherenkov emission for different pump polarization angles relative to the principal fiber axis of the fiber under test. The legend denotes the power amplifier setting, the pump power and the angle of the half-wave plate, respectively.

D.4 Additional measurements for the configuration described in section 6.7

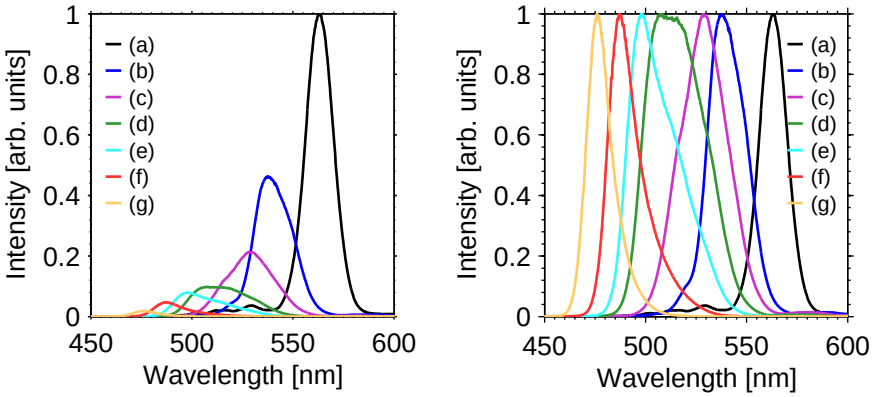

Figure D.3: ***(left)*** *Measured Cherenkov emission spectrum plotted along with the normalized output spectrum* ***(right)****, for the parameters listed in table D.2. The pump launch angle is rotated by* $\Delta\phi = 22^o$*, relative to the measurements shown in section 6.7.*

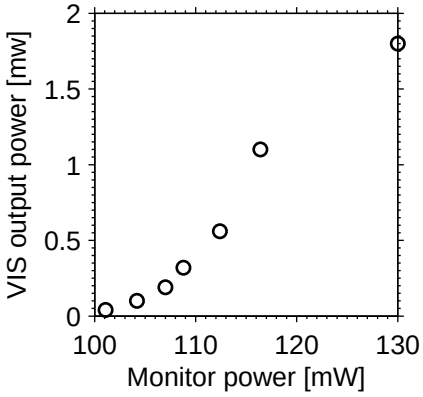

Figure D.4: Measured Cherenkov output power versus pump power, corresponding to the measurements shown in fig. D.3 and the paremeters listed in table D.2. The pump launch angle is rotated by $\Delta\phi = 22^o$*, relative to the measurements shown in section 6.7.*

ID	Monitor [mW]	Monitor [mV]	Pump AC [fs]	Pump FROG [fs]	VIS Output [mW]	λ_c [nm]	BW [nm]
(a)	101.1	300	366	246	0.04	563.2	17.0
(b)	104.2	311	363	245	0.10	540.6	23.5
(c)	107.0	320	362	244	0.19	528.6	29.7
(d)	108.8	326	360	244	0.32	515.3	37.5
(e)	112.4	337	358	242	0.56	504.0	29.2
(f)	116.4	350	355	241	1.1	489.0	17.9
(g)	130	399	357	230	1.8	477.0	14.3

Table D.2: Table of the measurement parameters for fig. D.3 and fig. D.4. The monitor power denotes the power of the pump prior to fiber-coupling, monitor voltage is the control voltage for the LD, and VIS output is the measured visible output power after filtering out the pump. The pump launch angle is rotated by $\Delta\phi = 22^o$, relative to the measurements shown in section 6.7.

D.5 Taper profiles for the manufactured asymmetric fiber tapers

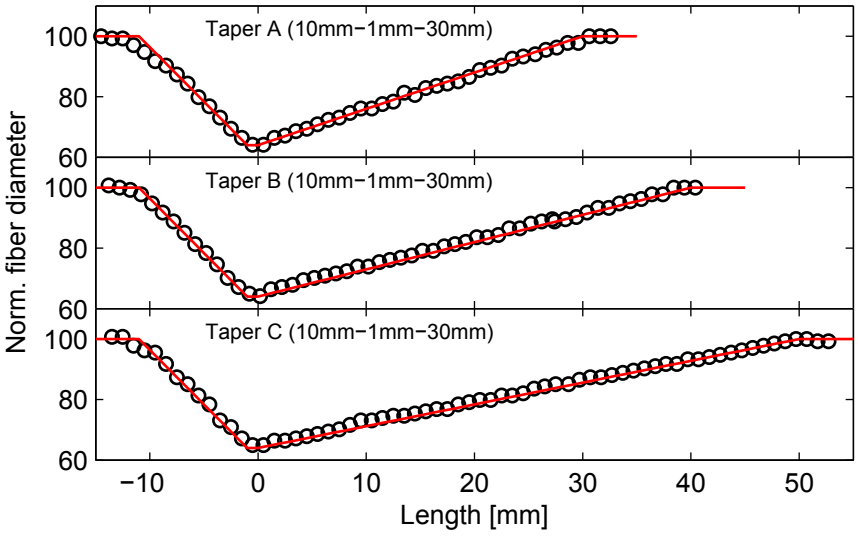

Figure D.5: Measured taper profiles plotted along with the design target dimensions for three different manufactured asymmetric fiber taper shapes.

Bibliography

[1] A. Einstein. “Quantum theory of radiation.” In: *Phys. Zeitschrift* 18 (1917), pp. 121–128.

[2] J. Gordon, H. Zeiger, and C. Townes. “Molecular Microwave Oscillator and New Hyperfine Structure in the Microwave Spectrum of NH3”. In: *Phys. Rev.* 95.1 (July 1954), pp. 282–284. ISSN: 0031-899X. DOI: 10.1103/PhysRev.95.282.

[3] A. Schawlow and C. Townes. “Infrared and Optical Masers”. In: *Phys. Rev.* 112.6 (Dec. 1958), pp. 1940–1949. ISSN: 0031-899X. DOI: 10.1103/PhysRev.112.1940.

[4] T. H. Maiman. “Stimulated Optical Radiation in Ruby”. In: *Nature* 187.4736 (Aug. 1960), pp. 493–494. ISSN: 0028-0836. DOI: 10.1038/187493a0.

[5] *"The Nobel Prize in Physics 1964". Nobelprize.org. Nobel Media AB 2014. Web. 26 Dec 2014.* http://www.nobelprize.org/nobel_prizes/physics/laureates/1964/.

[6] P. A. Franken, A. E. Hill, C. W. Peters, and G. Weinreich. “Generation of optical harmonics”. In: *Phys. Rev. Lett.* 7.4 (1961), pp. 118–119. ISSN: 0031-9007.

[7] G. Eckhardt, R. Hellwarth, F. McClung, S. Schwarz, D. Weiner, and E. Woodbury. “Stimulated Raman Scattering From Organic Liquids”. In: *Phys. Rev. Lett.* 9.11 (Dec. 1962), pp. 455–457. ISSN: 0031-9007. DOI: 10.1103/PhysRevLett.9.455.

[8] C. J. Koester and E. Snitzer. “Amplification in a Fiber Laser”. In: *Appl. Opt.* 3.10 (Oct. 1964), pp. 1182–1186. ISSN: 0003-6935. DOI: 10.1364/AO.3.001182.

[9] A. J. DeMaria, D. A. Stetser, and H. Heynau. “Self mode-locking of lasers with saturable absorbers”. In: *Appl. Phys. Lett.* 8.7 (Apr. 1966), pp. 174–176. ISSN: 03759601.

[10] M. J. Weber. “Glasses and Crystals of Glasses Nonlinear Refractive Index of”. In: *Opt. Eng.* 17.5 (Oct. 1978), p. 175463. ISSN: 0091-3286. DOI: 10.1117/12.7972266.

[11] R. Adair, L. Chase, and S. Payne. "Nonlinear refractive index of optical crystals". In: *Phys. Rev. B* 39.5 (Feb. 1989), pp. 3337–3350. ISSN: 0163-1829. DOI: 10.1103/PhysRevB.39.3337.

[12] M. Chini, K. Zhao, and Z. Chang. "The generation, characterization and applications of broadband isolated attosecond pulses". In: *Nat. Photonics* 8.3 (Feb. 2014), pp. 178–186. ISSN: 1749-4885. DOI: 10.1038/nphoton.2013.362.

[13] A. Bouchier, G. Lucas-Leclin, P. Georges, and J. M. Maillard. "Frequency doubling of an efficient continuous wave single-mode Yb-doped fiber laser at 978 nm in a periodically-poled MgO:LiNbO3 waveguide". In: *Opt. Express* 13.18 (2005), p. 6974. ISSN: 1094-4087. DOI: 10.1364/OPEX.13.006974.

[14] G. P. Agrawal. *Nonlinear Fiber Optics (4th edition)*. Elsevier, 2007. ISBN: 9780123970237. DOI: 10.1016/B978-0-12-397023-7.00006-1.

[15] C. V. Raman and K. S. Krishnan. "A new type of secondary radiation". In: *Nature* 121.3048 (1928), pp. 501–502. ISSN: 0028-0836.

[16] Y. R. Shen and N. Bloembergen. "Theory of Stimulated Brillouin and Raman Scattering". In: *Phys. Rev.* 137.6A (Mar. 1965), A1787–A1805. ISSN: 0031-899X. DOI: 10.1103/PhysRev.137.A1787.

[17] J. C. Knight, T. A. Birks, P. S. J. Russell, and D. M. Atkin. "All-silica single-mode optical fiber with photonic crystal cladding". In: *Opt. Lett.* 21.19 (Oct. 1996), p. 1547. ISSN: 0146-9592. DOI: 10.1364/OL.21.001547.

[18] T. a. Birks, J. C. Knight, and P. S. Russell. "Endlessly single-mode photonic crystal fiber". In: *Opt. Lett.* 22.13 (July 1997), p. 961. ISSN: 0146-9592. DOI: 10.1364/OL.22.000961.

[19] P. Russell. "Photonic crystal fibers." In: *Science* 299.5605 (Jan. 2003), pp. 358–62. ISSN: 1095-9203. DOI: 10.1126/science.1079280.

[20] D. Keck. "On the ultimate lower limit of attenuation in glass optical waveguides". In: *Appl. Phys. Lett.* 22.7 (1973), p. 307. ISSN: 00036951. DOI: 10.1063/1.1654649.

[21] J. Hecht. *City of Light: The Story of Fiber Optics*. Oxford University Press, 1999, p. 348. ISBN: 0195108183.

[22] D. J. Richardson. "Filling the light pipe." In: *Science* 330.6002 (Oct. 2010), pp. 327–8. ISSN: 1095-9203. DOI: 10.1126/science.1191708.

[23] *[Online, accessed 02-01-2015]*. http://www.cisco.com/c/en/us/solutions/collateral/service-provider/ip-ngn-ip-next-generation-network/white_paper_c11-481360.html.

[24] J. Sakaguchi, Y. Awaji, N. Wada, A. Kanno, T. Kawanishi, T. Hayashi, T. Taru, T. Kobayashi, and M. Watanabe. "109-Tb/s (7x97x172-Gb/s SDM/WDM/PDM) QPSK transmission through 16.8-km homogeneous multi-core fiber". In: *Opt. Fiber Commun. Conf. Fiber Opt. Eng. Conf. 2011*. c. Washington, D.C.: OSA, 2011, PDPB6. ISBN: 978-1-55752-906-0. DOI: 10.1364/OFC.2011.PDPB6.

[25] T. Morioka, Y. Awaji, R. Ryf, P. Winzer, D. Richardson, and F. Poletti. "Enhancing optical communications with brand new fibers". In: *IEEE Commun. Mag.* 50.2 (Feb. 2012), s31–s42. ISSN: 0163-6804. DOI: 10.1109/MCOM.2012.6146483.

[26] N. Bozinovic, Y. Yue, Y. Ren, M. Tur, P. Kristensen, H. Huang, A. E. Willner, and S. Ramachandran. "Terabit-scale orbital angular momentum mode division multiplexing in fibers." In: *Science* 340.6140 (June 2013), pp. 1545–8. ISSN: 1095-9203. DOI: 10.1126/science.1237861.

[27] R. Hellwarth. "Theory of Stimulated Raman Scattering". In: *Phys. Rev.* 130.5 (June 1963), pp. 1850–1852. ISSN: 0031-899X. DOI: 10.1103/PhysRev.130.1850.

[28] P. Kean, B. Sinclair, K. Smith, W. Sibbett, C. Rowe, and D. Reid. "Experimental Evaluation of a Fibre Raman Oscillator Having Fibre Grating Reflectors". In: *J. Mod. Opt.* 35.3 (Mar. 1988), pp. 397–406. ISSN: 0950-0340. DOI: 10.1080/09500348814550431.

[29] S. G. Grubb, T. Strasser, W. Y. Cheung, W. A. Reed, V. Mizrahi, T. Erdogan, P. J. Lemaire, A. M. Vengsarkar, D. J. DiGiovanni, D. W. Peckham, and B. H. Rockney. "High-Power 1.48 μm Cascaded Raman Laser in Germanosilicate Fibers". In: *Opt. Amplifiers Their Appl.* Washington, D.C.: OSA, 1995, SaA4. ISBN: 1-55752-406-8. DOI: 10.1364/OAA.1995.SaA4.

[30] R. A. Sims, P. Kadwani, L. Shah, and M. Richardson. "Generation and Amplification of 350 fs, 2 μm pulses in Tm:fiber". In: *Proc. SPIE 7914, Fiber Lasers VIII Technol. Syst. Appl. 79141L*. Ed. by J. W. Dawson. Vol. 7914. Feb. 2011, pp. 79141L–79141L–6. DOI: 10.1117/12.877765.

[31] P. Roberts, F. Couny, H. Sabert, B. Mangan, D. Williams, L. Farr, M. Mason, A. Tomlinson, T. Birks, J. Knight, and P. St J Russell. "Ultimate low loss of hollow-core photonic crystal fibres." In: *Opt. Express* 13.1 (Jan. 2005), pp. 236–44. ISSN: 1094-4087.

[32] A. T. Pedersen, L. Gruner-Nielsen, and K. Rottwitt. "Low Wavelength Loss of Germanium Doped Silica Fibers". In: *OFC/NFOEC 2008 - 2008 Conf. Opt. Fiber Commun. Fiber Opt. Eng. Conf.* IEEE, Feb. 2008, pp. 1–3. ISBN: 978-1-55752-856-8. DOI: 10.1109/OFC.2008.4528753.

[33] J. K. Ranka, R. S. Windeler, and A. J. Stentz. "Visible continuum generation in air-silica microstructure optical fibers with anomalous dispersion at 800 nm". In: *Opt. Lett.* 25.1 (Jan. 2000), p. 25. ISSN: 0146-9592. DOI: 10.1364/OL.25.000025.

[34] E. Taylor, L. Ng, J. Nilsson, R. Caponi, A. Pagano, M. Potenza, and B. Sordo. "Thulium-Doped Tellurite Fiber Amplifier". In: *IEEE Photonics Technol. Lett.* 16.3 (Mar. 2004), pp. 777–779. ISSN: 1041-1135. DOI: 10.1109/LPT.2004.823733.

[35] A. B. Rulkov, A. G. Getman, M. Y. Vyatkin, S. V. Popov, J. R. Taylor, and V. P. Gapontsev. "525-1800nm, watt-level, all-fibre picosecond source". In: *Conf. Lasers Electro-Optics/International Quantum Electron. Conf. Photonic Appl. Syst. Technol.* San Francisco, California: Optical Society of America, 2004, CPDC7.

[36] N. Savage. "Supercontinuum sources". In: *Nat. Photonics* 3.2 (Feb. 2009), pp. 114–115. ISSN: 1749-4885. DOI: 10.1038/nphoton.2008.286.

[37] X. Liu, J. Lægsgaard, U. Møller, H. Tu, S. a. Boppart, and D. Turchinovich. "All-fiber femtosecond Cherenkov radiation source." In: *Opt. Lett.* 37.13 (July 2012), pp. 2769–71. ISSN: 1539-4794.

[38] H. Tu, J. Lægsgaard, R. Zhang, S. Tong, Y. Liu, and S. A. Boppart. "Bright broadband coherent fiber sources emitting strongly blue-shifted resonant dispersive wave pulses." In: *Opt. Express* 21.20 (Oct. 2013), pp. 23188–96. ISSN: 1094-4087. DOI: 10.1364/OE.21.023188.

[39] J. Ballato, T. Hawkins, P. Foy, R. Stolen, B. Kokuoz, M. Ellison, C. McMillen, J. Reppert, a. M. Rao, M. Daw, S. R. Sharma, R. Shori, O. Stafsudd, R. R. Rice, and D. R. Powers. "Silicon optical fiber." In: *Opt. Express* 16.23 (Nov. 2008), pp. 18675–83. ISSN: 1094-4087.

[40] S. Morris, T. Hawkins, P. Foy, J. Hudson, L. Zhu, R. Stolen, R. Rice, and J. Ballato. "On loss in silicon core optical fibers". In: 2.11 (2012), pp. 195–197. DOI: 10.1016/j.optmat.2012.06.020.23..

[41] N. Healy, J. R. Sparks, P. J. Sazio, J. V. Badding, and A. C. Peacock. "Tapered silicon optical fibers." In: *Opt. Express* 18.8 (Apr. 2010), pp. 7596–601. ISSN: 1094-4087.

[42] N. Healy, L. Lagonigro, J. R. Sparks, S. Boden, P. J. a. Sazio, J. V. Badding, and A. C. Peacock. "Polycrystalline silicon optical fibers with atomically smooth surfaces." In: *Opt. Lett.* 36.13 (July 2011), pp. 2480–2. ISSN: 1539-4794.

[43] L. Lagonigro, N. Healy, J. R. Sparks, N. F. Baril, P. J. a. Sazio, J. V. Badding, and A. C. Peacock. "Low loss silicon fibers for photonics applications". In: *Appl. Phys. Lett.* 96.4 (2010), p. 041105. ISSN: 00036951. DOI: 10.1063/1.3294630.

[44] P. Mehta, M. Krishnamurthi, N. Healy, N. F. Baril, J. R. Sparks, P. J. a. Sazio, V. Gopalan, J. V. Badding, and A. C. Peacock. "Mid-infrared transmission properties of amorphous germanium optical fibers". In: *Appl. Phys. Lett.* 97.7 (2010), p. 071117. ISSN: 00036951. DOI: 10.1063/1.3481413.

[45] L. Shen, N. Healy, P. Mehta, T. D. Day, J. R. Sparks, J. V. Badding, and A. C. Peacock. "Nonlinear transmission properties of hydrogenated amorphous silicon core fibers towards the mid-infrared regime." In: *Opt. Express* 21.11 (June 2013), pp. 13075–83. ISSN: 1094-4087. DOI: 10.1364/OE.21.013075.

[46] P. Mehta, N. Healy, N. F. Baril, P. J. a. Sazio, J. V. Badding, and a. C. Peacock. "Nonlinear transmission properties of hydrogenated amorphous silicon core optical fibers." In: *Opt. Express* 18.16 (Aug. 2010), pp. 16826–31. ISSN: 1094-4087.

[47] P. Mehta, N. Healy, and R. Slav. "Nonlinearities in Silicon Optical Fibers". In: (2011), pp. 7–9.

[48] K. O. Hill, Y. Fujii, D. C. Johnson, and B. S. Kawasaki. "Photosensitivity in optical fiber waveguides: Application to reflection filter fabrication". In: *Appl. Phys. Lett.* 32.10 (1978), p. 647. ISSN: 00036951. DOI: 10.1063/1.89881.

[49] G. Meltz, W. W. Morey, and W. H. Glenn. "Formation of Bragg gratings in optical fibers by a transverse holographic method". In: *Opt. Lett.* 14.15 (Aug. 1989), p. 823. ISSN: 0146-9592. DOI: 10.1364/OL.14.000823.

[50] T. E. Tsai, E. J. Friebele, and D. L. Griscom. "Thermal stability of photoinduced gratings and paramagnetic centers in Ge- and Ge/P-doped silica optical fibers". In: *Opt. Lett.* 18.12 (June 1993), p. 935. ISSN: 0146-9592. DOI: 10.1364/OL.18.000935.

[51] M. J. Yuen. "Ultraviolet absorption studies of germanium silicate glasses." In: *Appl. Opt.* 21.1 (Jan. 1982), pp. 136–40. ISSN: 0003-6935.

[52] D. P. Hand and P. S. J. Russell. "Photoinduced refractive-index changes in germanosilicate fibers". In: *Opt. Lett.* 15.2 (Jan. 1990), p. 102. ISSN: 0146-9592. DOI: 10.1364/OL.15.000102.

[53] L. Dong, J. L. Archambault, L. Reekie, P. S. Russell, and D. N. Payne. "Photoinduced absorption change in germanosilicate preforms: evidence for the color-center model of photosensitivity." In: *Appl. Opt.* 34.18 (June 1995), pp. 3436–40. ISSN: 0003-6935. DOI: 10.1364/AO.34.003436.

[54] J. P. Bernardin and N. Lawandy. "Dynamics of the formation of Bragg gratings in germanosilicate optical fibers". In: *Opt. Commun.* 79.3-4 (Oct. 1990), pp. 194–199. ISSN: 00304018. DOI: 10.1016/0030-4018(90)90034-Q.

[55] R. Kashyap. "Photosensitive Optical Fibers: Devices and Applications". In: *Opt. Fiber Technol.* 1.1 (Oct. 1994), pp. 17–34. ISSN: 10685200. DOI: 10.1006/ofte.1994.1003.

[56] A. Othonos. "Fiber Bragg gratings". In: *Rev. Sci. Instrum.* 68.12 (1997), p. 4309. ISSN: 00346748. DOI: 10.1063/1.1148392.

[57] I. Bennion, J. Williams, L. Zhang, K. Sugden, and N. Doran. "UV-written in-fibre Bragg gratings". In: *Opt. Quantum Electron.* 28.2 (Feb. 1996), pp. 93–135. ISSN: 0306-8919. DOI: 10.1007/BF00278281.

[58] R. Kashyap. *Fiber Bragg Gratings (Second Edition)*. Academic Press, 2009, p. 632. ISBN: 9780123725790.

[59] K. Hill and G. Meltz. “Fiber Bragg grating technology fundamentals and overview”. In: *J. Light. Technol.* 15.8 (1997), pp. 1263–1276. ISSN: 07338724. DOI: 10.1109/50.618320.

[60] B. Malo, K. Hill, F. Bilodeau, D. Johnson, and J. Albert. “Point-by-point fabrication of micro-Bragg gratings in photosensitive fibre using single excimer pulse refractive index modification techniques”. In: *Electron. Lett.* 29.18 (1993), p. 1668. ISSN: 00135194. DOI: 10.1049/el:19931110.

[61] R. Kashyap, J. R. Armitage, R. J. Campbell, D. L. Williams, G. D. Maxwell, B. J. Ainslie, and C. A. Millar. “Light-sensitive optical fibres and planar waveguides : Advances in optical technology”. In: *BT Technol. J.* 11.2 (1993), pp. 150–160. ISSN: 1358-3948.

[62] K. O. Hill, B. Malo, F. Bilodeau, D. C. Johnson, and J. Albert. “Bragg gratings fabricated in monomode photosensitive optical fiber by UV exposure through a phase mask”. In: *Appl. Phys. Lett.* 62.10 (1993), p. 1035. ISSN: 00036951. DOI: 10.1063/1.108786.

[63] D. Anderson, V. Mizrahi, T. Erdogan, and A. White. “Production of in-fibre gratings using a diffractive optical element”. In: *Electron. Lett.* 29.6 (1993), p. 566. ISSN: 00135194. DOI: 10.1049/el:19930379.

[64] P. S. J. Russell, J.-L. Archambault, and L. Reekie. “Fibre gratings”. In: *Phys. World* 6 (1993), pp. 41–46.

[65] T. Erdogan. “Fiber grating spectra”. In: *J. Light. Technol.* 15.8 (1997), pp. 1277–1294. ISSN: 07338724. DOI: 10.1109/50.618322.

[66] M. M. Broer, R. L. Cone, and J. R. Simpson. “Ultraviolet-induced distributed-feedback gratings in Ce3+ -doped silica optical fibers”. In: *Opt. Lett.* 16.18 (Sept. 1991), p. 1391. ISSN: 0146-9592. DOI: 10.1364/OL.16.001391.

[67] P. Lemaire, R. Atkins, V. Mizrahi, and W. Reed. “High pressure H2 loading as a technique for achieving ultrahigh UV photosensitivity and thermal sensitivity in GeO2 doped optical fibres”. In: *Electron. Lett.* 29.13 (1993), p. 1191. ISSN: 00135194. DOI: 10.1049/el:19930796.

[68] V. Mizrahi, P. J. Lemaire, T. Erdogan, W. A. Reed, D. J. DiGiovanni, and R. M. Atkins. “Ultraviolet laser fabrication of ultrastrong optical fiber gratings and of germania-doped channel waveguides”. In: *Appl. Phys. Lett.* 63.13 (1993), p. 1727. ISSN: 00036951. DOI: 10.1063/1.110696.

[69] D. K. Lam and B. K. Garside. “Characterization of single-mode optical fiber filters.” In: *Appl. Opt.* 20.3 (Feb. 1981), pp. 440–5. ISSN: 0003-6935.

[70] N.-H. Sun, J.-J. Liau, Y.-W. Kiang, S.-C. Lin, R.-Y. Ro, J.-S. Chiang, and H.-W. Chang. “Numerical analysis of apodized fiber bragg gratings using coupled mode theory”. In: *Prog. Electromagn. Res.* 99 (2009), pp. 289–306. ISSN: 1559-8985. DOI: 10.2528/PIER09102704.

[71] S. J. Mihailov, F. Bilodeau, K. O. Hill, D. C. Johnson, J. Albert, and A. S. Holmes. “Apodization Technique for Fiber Grating Fabrication with a Halftone Transmission Amplitude Mask”. In: *Appl. Opt.* 39.21 (July 2000), p. 3670. ISSN: 0003-6935. DOI: 10.1364/AO.39.003670.

[72] W. H. Loh, M. J. Cole, M. N. Zervas, S. Barcelos, and R. I. Laming. “Complex grating structures with uniform phase masks based on the moving fiber-scanning beam technique”. In: *Opt. Lett.* 20.20 (Oct. 1995), p. 2051. ISSN: 0146-9592. DOI: 10.1364/OL.20.002051.

[73] R. Kashyap, a. Swanton, and D. Armes. “Simple technique for apodising chirped and unchirped fibre Bragg gratings”. In: *Electron. Lett.* 32.13 (1996), p. 1226. ISSN: 00135194. DOI: 10.1049/el:19960837.

[74] M. Matthewson, C. Kurkjian, and J. Hamblin. “Acid stripping of fused silica optical fibers without strength degradation”. In: *J. Light. Technol.* 15.3 (Mar. 1997), pp. 490–497. ISSN: 07338724. DOI: 10.1109/50.557565.

[75] A. Siekiera, R. Engelbrecht, R. Neumann, and B. Schmauss. “Fiber Bragg gratings in polarization maintaining specialty fiber for Raman fiber lasers”. In: *Phys. Procedia* 5 (Jan. 2010), pp. 671–677. ISSN: 18753892. DOI: 10.1016/j.phpro.2010.08.098.

[76] G. Meltz and W. W. Morey. “Bragg grating formation and germanosilicate fiber photosensitivity”. In: *Proc. SPIE 1516, Int. Work. Photoinduced Self-Organization Eff. Opt. Fiber*. Ed. by F. Ouellette. Vol. 1516. Dec. 1991, pp. 185–199. DOI: 10.1117/12.51164.

[77] A. G. Simpson, K. Kalli, L. Zhang, K. Zhou, and I. Bennion. “Type 1A fibre Bragg grating photosensitivity and the development of optimum temperature invariant type I â type IA strain sensors”. In: *Proc. SPIE*. Vol. 5459. Sept. 2004, pp. 118–127. DOI: 10.1117/12.545299.

[78] A. S. Svane and K. K. Rottwitt. “PM Raman fiber laser at 1679 nm”. In: *Adv. Photonics Congr.* Vol. 0. c. 2012, JTu5A.28. ISBN: 978-1-55752-946-6. DOI: 10.1364/ANIC.2012.JTu5A.28.

[79] A. S. Svane, X. Liu, and K. Rottwitt. “Highly Stable PM Raman Fiber Laser at 1680 nm”. In: *CLEO 2013*. Washington, D.C.: OSA, 2013, CW1M.6. ISBN: 978-1-55752-972-5. DOI: 10.1364/CLEO_SI.2013.CW1M.6.

[80] A. S. Svane and K. Rottwitt. “Design of an 1800nm Raman amplifier”. In: *Proc. SPIE*. Vol. 8915. Oct. 2013, p. 89150D. DOI: 10.1117/12.2035273.

[81] A. S. Svane. “Monolithic PM Raman fiber laser at 1679 nm for Raman amplification at 1810 nm”. In: *Cleo/europe 2013 - Eur. Conf. Lasers Electro-optics* (2013).

[82] A. S. Svane and K. Rottwitt. “Design of an 1800nm Raman amplifier”. In: *Proc. SPIE*. Oct. 2013, p. 89150D. DOI: 10.1117/12.2035273.

[83] F. M. Mitschke and L. F. Mollenauer. "Discovery of the soliton self-frequency shift". In: *Opt. Lett.* 11.10 (Oct. 1986), p. 659. ISSN: 0146-9592. DOI: 10.1364/OL.11.000659.

[84] J. P. Gordon. "Theory of the soliton self-frequency shift." In: *Opt. Lett.* 11.10 (Oct. 1986), pp. 662–4. ISSN: 0146-9592. DOI: 10.1364/OL.11.000662.

[85] A. Siekiera, R. Engelbrecht, A. Nothofer, and B. Schmauss. "Short 17-cm DBR Raman Fiber Laser With a Narrow Spectrum". In: *IEEE Photonics Technol. Lett.* 24.2 (Jan. 2012), pp. 107–109. ISSN: 1041-1135. DOI: 10.1109/LPT.2011.2173329.

[86] J. Shi, S. Alam, and M. Ibsen. "Raman DFB Fiber Laser with Truly Unidirectional Output". In: *Adv. Photonics Congr.* 1 (2012), BW3E.6. DOI: 10.1364/BGPP.2012.BW3E.6.

[87] J. C. Bouteiller. "Spectral modeling of Raman fiber lasers". In: *IEEE Photonics Technol. Lett.* 15.12 (Dec. 2003), pp. 1698–1700. ISSN: 1041-1135. DOI: 10.1109/LPT.2003.819758.

[88] S. A. Babin, D. V. Churkin, A. E. Ismagulov, S. I. Kablukov, and E. V. Podivilov. "Spectral broadening in Raman fiber lasers." In: *Opt. Lett.* 31.20 (Oct. 2006), pp. 3007–9. ISSN: 0146-9592.

[89] S. A. Babin, D. V. Churkin, A. E. Ismagulov, S. I. Kablukov, and E. V. Podivilov. "Four-wave-mixing-induced turbulent spectral broadening in a long Raman fiber laser". In: *J. Opt. Soc. Am. B* 24.8 (2007), p. 1729. ISSN: 0740-3224. DOI: 10.1364/JOSAB.24.001729.

[90] S. Babin. "Intensity interactions in cascades of a two-stage Raman fiber laser". In: *Opt. Commun.* 226.1-6 (Oct. 2003), pp. 329–335. ISSN: 00304018. DOI: 10.1016/j.optcom.2003.09.003.

[91] J. Bromage. "Raman Amplification for Fiber Communications Systems". In: *J. Light. Technol.* 22.1 (2004), pp. 79–93.

[92] V. M. Mashinsky, V. B. Neustruev, V. V. Dvoyrin, S. A. Vasiliev, O. I. Medvedkov, I. A. Bufetov, A. V. Shubin, E. M. Dianov, A. N. Guryanov, V. F. Khopin, and M. Y. Salgansky. "Germania-glass-core silica-glass-cladding modified chemical-vapor deposition optical fibers: optical losses, photorefractivity, and Raman amplification". In: *Opt. Lett.* 29.22 (2004), p. 2596. ISSN: 0146-9592. DOI: 10.1364/OL.29.002596.

[93] K. Rottwitt, J. Bromage, a.J. Stentz, M. Lines, and H. Smith. "Scaling of the raman gain coefficient: applications to germanosilicate fibers". In: *J. Light. Technol.* 21.7 (July 2003), pp. 1652–1662. ISSN: 0733-8724. DOI: 10.1109/JLT.2003.814386.

[94] T. Izawa, N. Shibata, and A. Takeda. "Optical attenuation in pure and doped fused silica in the IR wavelength region". In: *Appl. Phys. Lett.* 31.1 (1977), p. 33. ISSN: 00036951. DOI: 10.1063/1.89468.

[95] K. Rottwitt, J. Bromage, a.J. Stentz, M. Lines, and H. Smith. "Scaling of the raman gain coefficient: applications to germanosilicate fibers". In: *J. Light. Technol.* 21.7 (July 2003), pp. 1652–1662. ISSN: 0733-8724. DOI: 10.1109/JLT.2003.814386.

[96] J. Hansryd, P. A. Andrekson, M. Westlund, and P. O. Hedekvist. "Fiber-based optical parametric amplifiers and their applications". In: *IEEE J. Sel. Top. Quantum Electron.* 8.3 (May 2002), pp. 506–520. ISSN: 1077-260X. DOI: 10.1109/JSTQE.2002.1016354.

[97] Y. Feng, L. R. Taylor, and D. B. Calia. "150 W highly-efficient Raman fiber laser." In: *Opt. Express* 17.26 (Dec. 2009), pp. 23678–83. ISSN: 1094-4087.

[98] S. A. Babin, D. V. Churkin, A. E. Ismagulov, S. I. Kablukov, and E. V. Podivilov. "Broadening of the intracavity and output spectra of a raman fiber laser with a low-Q cavity". In: *Laser Phys.* 17.11 (Nov. 2007), pp. 1279–1285. ISSN: 1054-660X. DOI: 10.1134/S1054660X07110011.

[99] P. J. Winzer. "Modulation and multiplexing in optical communication systems". In: *IEEE Leos Newsl.* 23.1 (2009), pp. 4–10.

[100] S. Randel, R. Ryf, A. Sierra, P. J. Winzer, A. H. Gnauck, C. A. Bolle, R.-J. Essiambre, D. W. Peckham, A. McCurdy, and R. Lingle. "6x56-Gb/s mode-division multiplexed transmission over 33-km few-mode fiber enabled by 6x6 MIMO equalization". In: *Opt. Express* 19.17 (2011), pp. 16697–16707. ISSN: 1094-4087.

[101] S. Wabnitz. "Nonlinear and noise limitations in dispersion-managed soliton wavelength-division multiplexing transmissions with distributed Raman amplification". In: *Opt. Lett.* 26.11 (June 2001), pp. 777–9. ISSN: 0146-9592.

[102] R. Laming, M. N. Zervas, and D. N. Payne. "Erbium-doped fiber amplifier with 54 dB gain and 3.1 dB noise figures". In: *Photonics Technol. Lett. IEEE* 4.12 (1992), pp. 1345–1347. ISSN: 1041-1135.

[103] Z. Li, A. M. Heidt, J. M. O. Daniel, Y. Jung, S. U. Alam, and D. J. Richardson. "Thulium-doped fiber amplifier for optical communications at 2 μm". In: *Opt. Express* 21.8 (2013), pp. 9289–9297. ISSN: 1094-4087.

[104] B. Bristiel, P. Gallion, Y. Jaouen, and E. Pincemin. "Intrinsic noise figure derivation for fiber Raman amplifiers from equivalent noise figure measurement". In: *Light. Technol. Instrum. Meas. Conf. 2004. Proc.* IEEE, 2004, pp. 135–140. ISBN: 0780387228.

[105] R. Hellwarth. "Third-order optical susceptibilities of liquids and solids". In: *Prog. Quantum Electron.* 5.1 (1977), pp. 1–68. ISSN: 00796727. DOI: 10.1016/0079-6727(79)90002-8.

[106] U. Keller. "Recent developments in compact ultrafast lasers." In: *Nature* 424.6950 (Aug. 2003), pp. 831–8. ISSN: 1476-4687. DOI: 10.1038/nature01938.

[107] H. Haus. "Mode-locking of lasers". In: *IEEE J. Sel. Top. Quantum Electron.* 6.6 (Nov. 2000), pp. 1173–1185. ISSN: 1077-260X. DOI: 10.1109/2944.902165.

[108] C. V. Shank. *Ultrashort laser pulses and applications*. Ed. by W. Kaiser. Heidelberg: Springer, 1988.

[109] C. V. Shank and E. P. Ippen. "Subpicosecond kilowatt pulses from a mode-locked CW dye laser". In: *Appl. Phys. Lett.* 24.8 (1974), pp. 373–375. ISSN: 0003-6951.

[110] J. Valdmanis and R. L. Fork. "Design considerations for a femtosecond pulse laser balancing self phase modulation, group velocity dispersion, saturable absorption, and saturable gain". In: *Quantum Electron. IEEE J.* 22.1 (1986), pp. 112–118. ISSN: 0018-9197.

[111] D. H. Sutter, G. Steinmeyer, L. Gallmann, N. Matuschek, F. Morier-Genoud, U. Keller, V. Scheuer, G. Angelow, and T. Tschudi. "Semiconductor saturable-absorber mirror assisted Kerr-lens mode-locked Ti: sapphire laser producing pulses in the two-cycle regime". In: *Opt. Lett.* 24.9 (1999), pp. 631–633. ISSN: 1539-4794.

[112] M. Fermann, a. Galvanauskas, G. Sucha, and D. Harter. "Fiber-lasers for ultrafast optics". In: *Appl. Phys. B Lasers Opt.* 65.2 (Aug. 1997), pp. 259–275. ISSN: 0946-2171. DOI: 10.1007/s003400050272.

[113] L. Nelson, D. Jones, K. Tamura, H. Haus, and E. Ippen. "Ultrashort-pulse fiber ring lasers". In: *Appl. Phys. B Lasers Opt.* 65.2 (Aug. 1997), pp. 277–294. ISSN: 0946-2171. DOI: 10.1007/s003400050273.

[114] A. Tünnermann, T. Schreiber, F. Röser, A. Liem, S. Höfer, H. Zellmer, S. Nolte, and J. Limpert. "The renaissance and bright future of fibre lasers". In: *J. Phys. B At. Mol. Opt. Phys.* 38.9 (May 2005), S681–S693. ISSN: 0953-4075. DOI: 10.1088/0953-4075/38/9/016.

[115] J. Limpert, F. Roser, T. Schreiber, and A. Tunnermann. "High-power ultrafast fiber laser systems". In: *IEEE J. Sel. Top. Quantum Electron.* 12.2 (Mar. 2006), pp. 233–244. ISSN: 1077-260X. DOI: 10.1109/JSTQE.2006.872729.

[116] A. T(ünnermann, T. Schreiber, and J. Limpert. "Fiber lasers and amplifiers: an ultrafast performance evolution." In: *Appl. Opt.* 49.25 (Sept. 2010), F71–8. ISSN: 1539-4522.

[117] M. E. Fermann and I. Hartl. "Ultrafast fibre lasers". In: *Nat. Photonics* 7.11 (Oct. 2013), pp. 868–874. ISSN: 1749-4885. DOI: 10.1038/nphoton.2013.280.

[118] J. Buckley, A. Chong, S. Zhou, W. Renninger, and F. W. Wise. "Stabilization of high-energy femtosecond ytterbium fiber lasers by use of a frequency filter". In: *J. Opt. Soc. Am. B* 24.8 (2007), p. 1803. ISSN: 0740-3224. DOI: 10.1364/JOSAB.24.001803.

[119] F. Ilday, J. Buckley, L. Kuznetsova, and F. Wise. "Generation of 36-femtosecond pulses from a ytterbium fiber laser". In: *Opt. Express* 11.26 (Dec. 2003), p. 3550. ISSN: 1094-4087. DOI: 10.1364/OE.11.003550.

[120] J. N. Kutz. "Mode-Locked Soliton Lasers". In: *SIAM Rev.* 48.4 (Jan. 2006), pp. 629–678. ISSN: 0036-1445. DOI: 10.1137/S0036144504446357.

[121] D. Richardson, R. Laming, D. Payne, V. Matsas, and M. Phillips. "Self-starting, passively modelocked erbium fibre ring laser based on the amplifying Sagnac switch". In: *Electron. Lett.* 27.6 (1991), p. 542. ISSN: 00135194. DOI: 10.1049/el:19910341.

[122] M. E. Fermann, F. Haberl, M. Hofer, and H. Hochreiter. "Nonlinear amplifying loop mirror." In: *Opt. Lett.* 15.13 (July 1990), pp. 752–4. ISSN: 0146-9592.

[123] S. Namiki, E. P. Ippen, H. A. Haus, and C. X. Yu. "Energy rate equations for mode-locked lasers". In: *J. Opt. Soc. Am. B* 14.8 (Aug. 1997), p. 2099. ISSN: 0740-3224. DOI: 10.1364/JOSAB.14.002099.

[124] P. Grelu and N. Akhmediev. "Dissipative solitons for mode-locked lasers". In: *Nat. Photonics* 6.2 (Feb. 2012), pp. 84–92. ISSN: 1749-4885. DOI: 10.1038/nphoton.2011.345.

[125] F. Ilday, J. Buckley, W. Clark, and F. Wise. "Self-Similar Evolution of Parabolic Pulses in a Laser". In: *Phys. Rev. Lett.* 92.21 (May 2004), p. 213902. ISSN: 0031-9007. DOI: 10.1103/PhysRevLett.92.213902.

[126] M. Fermann, V. Kruglov, B. Thomsen, J. Dudley, and J. Harvey. "Self-Similar Propagation and Amplification of Parabolic Pulses in Optical Fibers". In: *Phys. Rev. Lett.* 84.26 (June 2000), pp. 6010–6013. ISSN: 0031-9007. DOI: 10.1103/PhysRevLett.84.6010.

[127] B. Oktem, C. Ulgudur, and F. O. Ilday. "Soliton-similariton fibre laser". In: *Nat Phot.* 4.5 (May 2010), pp. 307–311. ISSN: 1749-4885.

[128] J. R. Buckley, F. W. Wise, F. O. Ilday, and T. Sosnowski. "Femtosecond fiber lasers with pulse energies above 10 nJ". In: *Opt. Lett.* 30.14 (July 2005), p. 1888. ISSN: 0146-9592. DOI: 10.1364/OL.30.001888.

[129] A. Chong, J. Buckley, W. Renninger, and F. Wise. "All-normal-dispersion femtosecond fiber laser". In: *Opt. Express* 14.21 (2006), p. 10095. ISSN: 1094-4087. DOI: 10.1364/OE.14.010095.

[130] A. Chong, W. H. Renninger, and F. W. Wise. "All-normal-dispersion femtosecond fiber laser with pulse energy above 20nJ". In: *Opt. Lett.* 32.16 (2007), p. 2408. ISSN: 0146-9592. DOI: 10.1364/OL.32.002408.

[131] S. Lefrançois, K. Kieu, Y. Deng, J. D. Kafka, and F. W. Wise. "Scaling of dissipative soliton fiber lasers to megawatt peak powers by use of large-area photonic crystal fiber." In: *Opt. Lett.* 35.10 (May 2010), pp. 1569–71. ISSN: 1539-4794.

[132] D. S. Kharenko, E. V. Podivilov, A. A. Apolonski, and S. A. Babin. "20 nJ 200 fs all-fiber highly chirped dissipative soliton oscillator". In: *Opt. Lett.* 37.19 (Sept. 2012), p. 4104. ISSN: 0146-9592. DOI: 10.1364/OL.37.004104.

[133] X. Liu, J. Laegsgaard, and D. Turchinovich. "Highly-stable monolithic femtosecond Yb-fiber laser system based on photonic crystal fibers." In: *Opt. Express* 18.15 (July 2010), pp. 15475–83. ISSN: 1094-4087.

[134] X. Liu, J. Laegsgaard, and D. Turchinovich. "Self-stabilization of a mode-locked femtosecond fiber laser using a photonic bandgap fiber." In: *Opt. Lett.* 35.7 (Apr. 2010), pp. 913–5. ISSN: 1539-4794.

[135] X. Liu, J. Lægsgaard, and D. Turchinovich. "Monolithic Highly Stable Yb-Doped Femtosecond Fiber Lasers for Applications in Practical Biophotonics". In: *IEEE J. Sel. Top. Quantum Electron.* 18.4 (2012), pp. 1439–1450. DOI: 10.1109/JSTQE.2012.2183580.

[136] H. Haus, K. Tamura, L. Nelson, and E. Ippen. "Stretched-pulse additive pulse mode-locking in fiber ring lasers: theory and experiment". In: *IEEE J. Quantum Electron.* 31.3 (Mar. 1995), pp. 591–598. ISSN: 00189197. DOI: 10.1109/3.364417.

[137] C. K. Nielsen, K. G. Jespersen, and S. R. Keiding. "A 158 fs 5.3 nJ fiber-laser system at 1 um using photonic bandgap fibers for dispersion control and pulse compression". In: *Opt. Express* 14.13 (2006), p. 6063. ISSN: 1094-4087. DOI: 10.1364/OE.14.006063.

[138] A. Isomäki and O. G. Okhotnikov. "All-fiber ytterbium soliton mode-locked laser with dispersion control by solid-core photonic bandgap fiber". In: *Opt. Express* 14.10 (2006), p. 4368. ISSN: 1094-4087. DOI: 10.1364/OE.14.004368.

[139] *[Online, accessed 27-December-2014].* http://www.nufern.com/pam/optical_fibers/946/PM-YSF-HI/.

[140] J. K. Lyngsø, B. J. Mangan, and P. J. Roberts. "Polarization Maintaining Hybrid TIR/Bandgap All-Solid Photonic Crystal Fiber". In: *Conf. Lasers Electro-Optics/Quantum Electron. Laser Sci. Conf. Photonic Appl. Syst. Technol.* Optical Society of America, 2008, CThV1.

[141] *[Online, accessed 25-November-2014].* http://www.laserenterprise.com/resources/pdf/pump-laser/D00007-PB-08_LC94_datasheet.pdf.

[142] *[Online, accessed 20-December-2014].* http://www.batop.de/products/saturable-absorber/saturable-absorber-mirror/data-sheet/saturable-absorber-mirror-1040nm/saturable-absorber-mirror-SAM-1040-40-500fs.pdf.

[143] D. Strickland and G. Mourou. "Compression of amplified chirped optical pulses". In: *Opt. Commun.* 55.6 (1985), pp. 447–449. ISSN: 0030-4018.

[144] M. Pessot, P. Maine, and G. Mourou. "1000 times expansion/compression of optical pulses for chirped pulse amplification". In: *Opt. Commun.* 62.6 (1987), pp. 419–421. ISSN: 0030-4018.

[145] R. L. Fork, O. E. Martinez, and J. P. Gordon. "Negative dispersion using pairs of prisms". In: *Opt. Lett.* 9.5 (May 1984), p. 150. ISSN: 0146-9592. DOI: 10.1364/OL.9.000150.

[146] E. Treacy. "Optical pulse compression with diffraction gratings". In: *IEEE J. Quantum Electron.* 5.9 (Sept. 1969), pp. 454–458. ISSN: 0018-9197. DOI: 10.1109/JQE.1969.1076303.

[147] J. Limpert, T. Schreiber, S. Nolte, H. Zellmer, and A. Tünnermann. "All fiber chirped-pulse amplification system based on compression in air-guiding photonic bandgap fiber". In: *Opt. Express* 11.24 (Dec. 2003), p. 3332. ISSN: 1094-4087. DOI: 10.1364/OE.11.003332.

[148] *[Online, accessed 27-December-2014].* http://www.nlight.net/nlight-files/file/datasheets/Fibers/nLIGHT_LIEKKI-Yb1200-6-125_110211.pdf.

[149] *[Online, accessed 25-November-2014].* http://www.amstechnologies.com/fileadmin/amsmedia/downloads/3516_Oclaro_LC96Ux_r2_1.pdf.

[150] *[Online, accessed 23-November-2014].* www.nktphotonics.com/files/files/HC-1060.pdf.

[151] J. T. Kristensen, A. Houmann, X. Liu, and D. Turchinovich. "Fusion splicing of single-mode fibers and hollow-core photonic crystal fibers , relevant for monolithic fiber laser pulse compression". In: *Opt. Express* 16.13 (2008), pp. 9986–9995.

[152] *Private communication with Jens Kristian Lyngsø, NKT Photonics A/S.*

[153] *[Online, accessed 20-December-2014].* http://www.newport.com/High-Speed-Photodetectors-and-Photoreceivers-High/917754/1033/content.aspx.

[154] J. A. Armstrong. "Measurement of Picosecond Laser Pulse Widths". In: *Appl. Phys. Lett.* 10.1 (1967), p. 16. ISSN: 00036951. DOI: 10.1063/1.1754787.

[155] J.-C. M. Diels, J. J. Fontaine, I. C. McMichael, and F. Simoni. "Control and measurement of ultrashort pulse shapes (in amplitude and phase) with femtosecond accuracy". In: *Appl. Opt.* 24.9 (May 1985), p. 1270. ISSN: 0003-6935. DOI: 10.1364/AO.24.001270.

[156] R. Trebino. *Frequency-Resolved Optical Gating: The Measurement of Ultrashort Laser Pulses*. Boston: Springer, 2002, p. 425. ISBN: 1402070667.

[157] K. W. Delong, D. N. Fittinghoff, R. Trebino, B. Kohler, and K. Wilson. "Pulse retrieval in frequency-resolved optical gating based on the method of generalized projections." In: *Opt. Lett.* 19.24 (Dec. 1994), pp. 2152–4. ISSN: 0146-9592.

[158] S. Linden, J. Kuhl, and H. Giessen. "Amplitude and phase characterization of weak blue ultrashort pulses by downconversion". In: *Opt. Lett.* 24.8 (Apr. 1999), p. 569. ISSN: 0146-9592. DOI: 10.1364/OL.24.000569.

[159] *[Online, accessed 27-December-2014].* http://www.mesaphotonics.com/products-2/pulse-measurement/frogscan/.

[160] A. S. Svane, X. Liu, J. Lægsgaard, H. Tu, S. A. Boppart, and D. Turchinovich. "Electrically-Tunable Multi-Color Ultrafast Cherenkov Fiber Laser". In: *CLEO 2014*. Washington, D.C.: OSA, 2014, ATh3P.6. ISBN: 978-1-55752-999-2. DOI: 10.1364/CLEO_AT.2014.ATh3P.6.

[161] X. Liu, A. S. Svane, J. Lægsgaard, H. Tu, S. A. Boppart, and D. Turchinovich. "Tunable Femtosecond Cherenkov Fiber Laser". In: *IEEE/ICAIT 2014*. 2014.

[162] X. Liu, A. S. Svane, J. Lægsgaard, H. Tu, S. A. Boppart, and D. Turchinovich. "Progress in Cherenkov femtosecond fiber lasers". In: *[Being Prep. submission]* (2014).

[163] F. P. Kapron. "Radiation losses in glass optical waveguides". In: *Appl. Phys. Lett.* 17.10 (1970), p. 423. ISSN: 00036951. DOI: 10.1063/1.1653255.

[164] E. Ippen. "Passive mode locking of the cw dye laser". In: *Appl. Phys. Lett.* 21.8 (1972), p. 348. ISSN: 00036951. DOI: 10.1063/1.1654406.

[165] J. C. Knight. "Photonic crystal fibres." In: *Nature* 424.6950 (Aug. 2003), pp. 847–51. ISSN: 1476-4687. DOI: 10.1038/nature01940.

[166] P. S. Russell. "Photonic-Crystal Fibers". In: *J. Light. Technol.* 24.12 (Dec. 2006), pp. 4729–4749. ISSN: 0733-8724. DOI: 10.1109/JLT.2006.885258.

[167] D. Mogilevtsev, T. A. Birks, and P. S. J. Russell. "Group-velocity dispersion in photonic crystal fibers". In: *Opt. Lett.* 23.21 (Nov. 1998), p. 1662. ISSN: 0146-9592. DOI: 10.1364/OL.23.001662.

[168] J. M. Dudley and J. R. Taylor. "Ten years of nonlinear optics in photonic crystal fibre". In: *Nat. Photonics* 3.2 (Feb. 2009), pp. 85–90. ISSN: 1749-4885. DOI: 10.1038/nphoton.2008.285.

[169] I. Hartl, X. D. Li, C. Chudoba, R. K. Ghanta, T. H. Ko, J. G. Fujimoto, J. K. Ranka, and R. S. Windeler. "Ultrahigh-resolution optical coherence tomography using continuum generation in an air-silica microstructure optical fiber". In: *Opt. Lett.* 26.9 (May 2001), p. 608. ISSN: 0146-9592. DOI: 10.1364/OL.26.000608.

[170] B. Povazay, K. Bizheva, A. Unterhuber, B. Hermann, H. Sattmann, A. F. Fercher, W. Drexler, A. Apolonski, W. J. Wadsworth, J. C. Knight, P. S. J. Russell, M. Vetterlein, and E. Scherzer. "Submicrometer axial resolution optical coherence tomography". In: *Opt. Lett.* 27.20 (Oct. 2002), p. 1800. ISSN: 0146-9592. DOI: 10.1364/OL.27.001800.

[171] J. A. Palero, V. O. Boer, J. C. Vijverberg, H. C. Gerritsen, and H. J. C. M. Sterenborg. "Short-wavelength two-photon excitation fluorescence microscopy of tryptophan with a photonic crystal fiber based light source". In: *Opt. Express* 13.14 (2005), p. 5363. ISSN: 1094-4087. DOI: 10.1364/OPEX.13.005363.

[172] D. Li, W. Zheng, and J. Y. Qu. "Imaging of epithelial tissue in vivo based on excitation of multiple endogenous nonlinear optical signals." In: *Opt. Lett.* 34.18 (Sept. 2009), pp. 2853–5. ISSN: 1539-4794. DOI: 10.1364/OL.34.002853.

[173] G. McConnell. "Confocal laser scanning fluorescence microscopy with a visible continuum source". In: *Opt. Express* 12.13 (2004), p. 2844. ISSN: 1094-4087. DOI: 10.1364/OPEX.12.002844.

[174] J. H. Frank, A. D. Elder, J. Swartling, A. R. Venkitaraman, A. D. Jeyasekharan, and C. F. Kaminski. "A white light confocal microscope for spectrally resolved multidimensional imaging." In: *J. Microsc.* 227.Pt 3 (Sept. 2007), pp. 203–15. ISSN: 0022-2720. DOI: 10.1111/j.1365-2818.2007.01803.x.

[175] . E. Auksorius. "Multidimensional Fluorescence Imaging and Superresolution Exploiting Ultrafast Laser and Supercontinuum Technology". Ph.D. thesis. Imperial College London, 2008.

[176] A. De Angelis, A. Labruyere, V. Couderc, P. Leproux, A. Tonello, H. Segawa, M. Okuno, H. Kano, D. Arnaud-Cormos, P. Leveque, and H.-o. Hamaguchi. "Time-frequency resolved analysis of a nanosecond supercontinuum source dedicated to multiplex CARS application." In: *Opt. Express* 20.28 (Dec. 2012), pp. 29705–16. ISSN: 1094-4087. DOI: 10.1364/OE.20.029705.

[177] S. Murugkar, C. Brideau, A. Ridsdale, M. Naji, P. K. Stys, and H. Anis. "Coherent anti-Stokes Raman scattering microscopy using photonic crystal fiber with two closely lying zero dispersion wavelengths". In: *Opt. Express* 15.21 (2007), p. 14028. ISSN: 1094-4087. DOI: 10.1364/OE.15.014028.

[178] Y. Wang, I. Tomov, J. S. Nelson, Z. Chen, H. Lim, and F. Wise. "Low-noise broadband light generation from optical fibers for use in high-resolution optical coherence tomography". In: *J. Opt. Soc. Am. A* 22.8 (2005), p. 1492. ISSN: 1084-7529. DOI: 10.1364/JOSAA.22.001492.

[179] X. Liu, G. E. Villanueva, J. Lægsgaard, U. Møller, H. Tu, S. a. Boppart, and D. Turchinovich. "Low-Noise Operation of All-Fiber Femtosecond Cherenkov Laser." In: *IEEE Photonics Technol. Lett.* 25.9 (Mar. 2013), pp. 892–895. ISSN: 1041-1135. DOI: 10.1109/LPT.2013.2253765.

[180] H. Tu, Y. Zhao, Y. Liu, Y.-Z. Liu, and S. Boppart. "Noise characterization of broadband fiber Cherenkov radiation as a visible-wavelength source for optical coherence tomography and two-photon fluorescence microscopy". In: *Opt. Express* 22.17 (Aug. 2014), p. 20138. ISSN: 1094-4087. DOI: 10.1364/OE.22.020138.

[181] W. R. Zipfel, R. M. Williams, R. Christie, A. Y. Nikitin, B. T. Hyman, and W. W. Webb. "Live tissue intrinsic emission microscopy using multiphoton-excited native fluorescence and second harmonic generation." In: *Proc. Natl. Acad. Sci. U. S. A.* 100.12 (June 2003), pp. 7075–80. ISSN: 0027-8424. DOI: 10.1073/pnas.0832308100.

[182] P. Bastiaens and A. Squire. "Fluorescence lifetime imaging microscopy: spatial resolution of biochemical processes in the cell". In: *Trends Cell Biol.* 9.2 (Feb. 1999), pp. 48–52. ISSN: 09628924. DOI: 10.1016/S0962-8924(98)01410-X.

[183] H. Tu and S. a. Boppart. "Versatile photonic crystal fiber-enabled source for multi-modality biophotonic imaging beyond conventional multiphoton microscopy". In: *Versatile photonic Cryst. fiber-enabled source multimodality biophotonic imaging beyond Conv. Multiphot. Microsc.* Ed. by A. Periasamy, P. T. C. So, and K. König. Vol. 7569. Feb. 2010, pp. 75692D–75692D–9. DOI: 10.1117/12.841298.

[184] M.-C. Chan, C.-H. Lien, J.-Y. Lu, and B.-H. Lyu. "High power NIR fiber-optic femtosecond Cherenkov radiation and its application on nonlinear light microscopy". In: *Opt. Express* 22.8 (2014), pp. 9498–9507. ISSN: 1094-4087.

[185] H. Tu and S. A. Boppart. "Coherent fiber supercontinuum for biophotonics". In: *Laser Photon. Rev.* 7.5 (2013), pp. 628–645. ISSN: 1863-8899.

[186] J. S. Russell. "Report on waves". In: *14th Meet. Br. Assoc. Adv. Sci.* Vol. 311. 1844, p. 390.

[187] L. F. Mollenauer, R. H. Stolen, and J. P. Gordon. "Experimental Observation of Picosecond Pulse Narrowing and Solitons in Optical Fibers". In: *Phys. Rev. Lett.* 45.13 (Sept. 1980), pp. 1095–1098. ISSN: 0031-9007. DOI: 10.1103/PhysRevLett.45.1095.

[188] A. Hasegawa. "Transmission of stationary nonlinear optical pulses in dispersive dielectric fibers. I. Anomalous dispersion". In: *Appl. Phys. Lett.* 23.3 (1973), p. 142. ISSN: 00036951. DOI: 10.1063/1.1654836.

[189] J. Satsuma and N. Yajima. "B. Initial Value Problems of One-Dimensional Self-Modulation of Nonlinear Waves in Dispersive Media". In: *Prog. Theor. Phys. Suppl.* 55.55 (1974), pp. 284–306. ISSN: 0375-9687. DOI: 10.1143/PTPS.55.284.

[190] E. Dianov, Z. Nikonova, A. Prokhorov, and V. Serkin. "Optimal compression of multisoliton pulses in fiber-optic waveguides". In: *Pisma v Zhurnal Tekhnischeskoi Fiz.* 12 (1986), pp. 756–760.

[191] D. R. Austin, C. M. de Sterke, B. J. Eggleton, and T. G. Brown. "Dispersive wave blue-shift in supercontinuum generation". In: *Opt. Express* 14.25 (2006), p. 11997. ISSN: 1094-4087. DOI: 10.1364/OE.14.011997.

[192] R. Alfano and S. Shapiro. "Emission in the Region 4000 to 7000 Å Via Four-Photon Coupling in Glass". In: *Phys. Rev. Lett.* 24.11 (Mar. 1970), pp. 584–587. ISSN: 0031-9007. DOI: 10.1103/PhysRevLett.24.584.

[193] C. Lin and R. H. Stolen. "New nanosecond continuum for excited-state spectroscopy". In: *Appl. Phys. Lett.* 28.4 (1976), p. 216. ISSN: 00036951. DOI: 10.1063/1.88702.

[194] C. Lin, V. Nguyen, and W. French. "Wideband near-I.R. continuum (0.7-2.1 μm) generated in low-loss optical fibres". In: *Electron. Lett.* 14.25 (1978), p. 822. ISSN: 00135194. DOI: 10.1049/el:19780556.

[195] J. M. Dudley and S. Coen. "Supercontinuum generation in photonic crystal fiber". In: *Rev. Mod. Phys.* 78.4 (Oct. 2006), pp. 1135–1184. ISSN: 0034-6861. DOI: 10.1103/RevModPhys.78.1135.

[196] A. Hasegawa. “Generation of a train of soliton pulses by induced modulational instability in optical fibers”. In: *Opt. Lett.* 9.7 (July 1984), p. 288. ISSN: 0146-9592. DOI: 10.1364/OL.9.000288.

[197] E. M. Dianov, P. V. Mamyshev, A. M. Prokhorov, and S. V. Chernikov. “Generation of a train of fundamental solitons at a high repetition rate in optical fibers”. In: *Opt. Lett.* 14.18 (Sept. 1989), p. 1008. ISSN: 0146-9592. DOI: 10.1364/OL.14.001008.

[198] A. V. Gorbach and D. V. Skryabin. “Theory of radiation trapping by the accelerating solitons in optical fibers”. In: *Phys. Rev. A* 76.5 (Nov. 2007), p. 053803. ISSN: 1050-2947. DOI: 10.1103/PhysRevA.76.053803.

[199] A. V. Gorbach and D. V. Skryabin. “Light trapping in gravity-like potentials and expansion of supercontinuum spectra in photonic-crystal fibres”. In: *Nat. Photonics* 1.11 (Nov. 2007), pp. 653–657. ISSN: 1749-4885. DOI: 10.1038/nphoton.2007.202.

[200] P. Beaud, W. Hodel, B. Zysset, and H. Weber. “Ultrashort pulse propagation, pulse breakup, and fundamental soliton formation in a single-mode optical fiber”. In: *IEEE J. Quantum Electron.* 23.11 (Nov. 1987), pp. 1938–1946. ISSN: 0018-9197. DOI: 10.1109/JQE.1987.1073262.

[201] S. Liu. “Four-wave mixing and modulation instability of continuous optical waves in single-mode optical fibers”. In: *Appl. Phys. Lett.* 89.17 (2006), p. 171118. ISSN: 00036951. DOI: 10.1063/1.2369646.

[202] R. H. Stolen, J. P. Gordon, W. J. Tomlinson, and H. A. Haus. “Raman response function of silica-core fibers”. In: *J. Opt. Soc. Am. B* 6.6 (June 1989), p. 1159. ISSN: 0740-3224. DOI: 10.1364/JOSAB.6.001159.

[203] J. C. Travers. “Blue extension of optical fibre supercontinuum generation”. In: *J. Opt.* 12.11 (Nov. 2010), p. 113001. ISSN: 2040-8978. DOI: 10.1088/2040-8978/12/11/113001.

[204] J. M. Dudley and S. Coen. “Coherence properties of supercontinuum spectra generated in photonic crystal and tapered optical fibers”. In: *Opt. Lett.* 27.13 (July 2002), p. 1180. ISSN: 0146-9592. DOI: 10.1364/OL.27.001180.

[205] U. Møller, S. T. Sørensen, C. Jakobsen, J. Johansen, P. M. Moselund, C. L. Thomsen, and O. Bang. “Power dependence of supercontinuum noise in uniform and tapered PCFs.” In: *Opt. Express* 20.3 (Jan. 2012), pp. 2851–7. ISSN: 1094-4087. DOI: 10.1364/OE.20.002851.

[206] X. Gu, M. Kimmel, A. Shreenath, R. Trebino, J. Dudley, S. Coen, and R. Windeler. “Experimental studies of the coherence of microstructure-fiber supercontinuum”. In: *Opt. Express* 11.21 (Oct. 2003), p. 2697. ISSN: 1094-4087. DOI: 10.1364/OE.11.002697.

[207] F. Lu and W. H. Knox. “Generation of a broadband continuum with high spectral coherence in tapered single-mode optical fibers”. In: *Opt. Express* 12.2 (2004), p. 347. ISSN: 1094-4087. DOI: 10.1364/OPEX.12.000347.

[208] B. M. Bolotovskii and V. L. Ginzburg. "The Vavilov-Cerenkov Effect and the Doppler Effect in the Motion of Sources with Superluminal Velocity in Vacuum". In: *Sov. Phys. Uspekhi* 15.2 (Feb. 1972), pp. 184–192. ISSN: 0038-5670. DOI: 10.1070/PU1972v015n02ABEH004962.

[209] N. Akhmediev and M. Karlsson. "Cherenkov radiation emitted by solitons in optical fibers". In: *Phys. Rev. A* 51.3 (Mar. 1995), pp. 2602–2607. ISSN: 1050-2947. DOI: 10.1103/PhysRevA.51.2602.

[210] H. Tu and S. A. Boppart. "Ultraviolet-visible non-supercontinuum ultrafast source enabled by switching single silicon strand-like photonic crystal fibers." In: *Opt. Express* 17.20 (Sept. 2009), pp. 17983–8. ISSN: 1094-4087. DOI: 10.1364/OE.17.017983.

[211] H. Tu and S. A. Boppart. "Optical frequency up-conversion by supercontinuum-free widely-tunable fiber-optic Cherenkov radiation". In: *Opt. Express* 17.12 (May 2009), p. 9858. ISSN: 1094-4087. DOI: 10.1364/OE.17.009858.

[212] J. Lægsgaard, A. Bjarklev, and S. E. Barkou Libori. "Chromatic dispersion in photonic crystal fibers: fast and accurate scheme for calculation". In: *J. Opt. Soc. Am. B* 20.3 (2003), p. 443. ISSN: 0740-3224. DOI: 10.1364/JOSAB.20.000443.

[213] I. Cristiani, R. Tediosi, L. Tartara, and V. Degiorgio. "Dispersive wave generation by solitons in microstructured optical fibers". In: *Opt. Express* 12.1 (2004), pp. 124–135. ISSN: 1094-4087.

[214] M. Hu, L. Chai, and A. Zheltikov. "Frequency-tunable anti-Stokes line emission by eigenmodes of a birefringent microstructure fiber". In: *Opt. Express* 12.9 (2004), pp. 1932–1937. ISSN: 1094-4087.

[215] A. V. Mitrofanov, Y. M. Linik, R. Buczynski, D. Pysz, D. Lorenc, I. Bugar, A. A. Ivanov, M. V. Alfimov, A. B. Fedotov, and A. M. Zheltikov. "Highly birefringent silicate glass photonic-crystal fiber with polarization-controlled frequency-shifted output: A promising fiber light source for nonlinear Raman microspectroscopy". In: *Opt. Express* 14.22 (2006), pp. 10645–10651. ISSN: 1094-4087.

[216] F. Lu, Y. Deng, and W. H. Knox. "Generation of broadband femtosecond visible pulses in dispersion-micromanaged holey fibers". In: *Opt. Lett.* 30.12 (2005), pp. 1566–1568. ISSN: 1539-4794.

[217] A. A. Amorim, H. M. Crespo, M. Miranda, J. a. L. Silva, and L. M. Bernardo. "Study of non-solitonic blue-green radiation generated in mm-long photonic crystal fibers". In: *Photonics Eur.* International Society for Optics and Photonics, 2006, p. 618717.

[218] F. Lu and W. H. Knox. "Generation, characterization, and application of broadband coherent femtosecond visible pulses in dispersion micromanaged holey fibers". In: *JOSA B* 23.6 (2006), pp. 1221–1227. ISSN: 1520-8540.

[219] H. Tu and S. A. Boppart. "Optical frequency up-conversion by supercontinuum-free widely-tunable fiber-optic Cherenkov radiation". In: *Opt. Express* 17.12 (2009), pp. 9858–9872. ISSN: 1094-4087.

[220] H. Tu and S. A. Boppart. "Coherent fiber supercontinuum for biophotonics." In: *Laser Photon. Rev.* 7.5 (Sept. 2013), pp. 628–645. ISSN: 1863-8880. DOI: 10.1002/lpor.201200014.

[221] N. Y. Joly, J. Nold, W. Chang, P. Hölzer, A. Nazarkin, G. K. L. Wong, F. Biancalana, and P. S. J. Russell. "Bright spatially coherent wavelength-tunable deep-UV laser source using an Ar-filled photonic crystal fiber". In: *Phys. Rev. Lett.* 106.20 (2011), p. 203901.

[222] K. F. Mak, J. C. Travers, P. Hölzer, N. Y. Joly, and P. S. J. Russell. "Tunable vacuum-UV to visible ultrafast pulse source based on gas-filled Kagome-PCF". In: *Opt. Express* 21.9 (2013), pp. 10942–10953. ISSN: 1094-4087.

[223] G. Chang, L.-J. Chen, and F. X. Kärtner. "Highly efficient Cherenkov radiation in photonic crystal fibers for broadband visible wavelength generation." In: *Opt. Lett.* 35.14 (July 2010), pp. 2361–3. ISSN: 1539-4794.

[224] J. Yuan, X. Sang, C. Yu, Y. Han, G. Zhou, S. Li, and L. Hou. "Highly efficient and broadband Cherenkov radiation at the visible wavelength in the fundamental mode of photonic crystal fiber". In: *Photonics Technol. Lett. IEEE* 23.12 (2011), pp. 786–788. ISSN: 1041-1135.

[225] X. B. Zhang, X. Zhu, L. Chen, F. G. Jiang, X. B. Yang, J. G. Peng, and J. Y. Li. "Enhanced violet Cherenkov radiation generation in GeO2-doped photonic crystal fiber". In: *Appl. Phys. B* 111.2 (2013), pp. 273–277. ISSN: 0946-2171.

[226] H.-w. Chen, Z. Haider, J. Lim, S. Xu, Z. Yang, F. X. Kärtner, and G. Chang. "3 GHz, Yb-fiber laser-based, few-cycle ultrafast source at the Ti:sapphire laser wavelength." In: *Opt. Lett.* 38.22 (Nov. 2013), pp. 4927–30. ISSN: 1539-4794.

[227] G. Chang, L.-J. Chen, and F. X. Kärtner. "Fiber-optic Cherenkov radiation in the few-cycle regime." In: *Opt. Express* 19.7 (Mar. 2011), pp. 6635–47. ISSN: 1094-4087.

[228] H.-w. Chen, G. Chang, S. Xu, Z. Yang, and F. X. Kärtner. "3 GHz, fundamentally mode-locked, femtosecond Yb-fiber laser." In: *Opt. Lett.* 37.17 (Sept. 2012), pp. 3522–4. ISSN: 1539-4794.

[229] *[Online, accessed 01-01-2015].* http://www.amplitude-systemes.com/client/document/mikan_4.pdf.

[230] A. Kudlinski, A. K. George, J. C. Knight, J. C. Travers, A. B. Rulkov, S. V. Popov, and J. R. Taylor. "Zero-dispersion wavelength decreasing photonic crystal fibers for ultraviolet-extended supercontinuum generation". In: *Opt. Express* 14.12 (2006), p. 5715. ISSN: 1094-4087. DOI: 10.1364/OE.14.005715.

[231] J. C. Travers, S. V. Popov, and J. R. Taylor. "Trapping of dispersive waves by solitons in long lengths of tapered PCF". In: *2008 Conf. Lasers Electro-Optics*. IEEE, May 2008, pp. 1–2. ISBN: 978-1-55752-859-9. DOI: 10.1109/CLEO.2008.4551413.

[232] S. T. Sørensen, A. Judge, C. L. Thomsen, and O. Bang. "Optimum fiber tapers for increasing the power in the blue edge of a supercontinuum-group-acceleration matching." In: *Opt. Lett.* 36.6 (Mar. 2011), pp. 816–8. ISSN: 1539-4794. DOI: 10.1364/OL.36.000816.

[233] S. T. Sørensen, U. Møller, C. Larsen, P. M. Moselund, C. Jakobsen, J. Johansen, T. V. Andersen, C. L. Thomsen, and O. Bang. "Deep-blue supercontinnum sources with optimum taper profiles - verification of GAM." In: *Opt. Express* 20.10 (May 2012), pp. 10635–45. ISSN: 1094-4087.

[234] F. Lu, Y. Deng, and W. H. Knox. "Generation of broadband femtosecond visible pulses in dispersion-micromanaged holey fibers". In: *Opt. Lett.* 30.12 (2005), p. 1566. ISSN: 0146-9592. DOI: 10.1364/OL.30.001566.

[235] F. Lu and W. H. Knox. "Low noise wavelength conversion of femtosecond pulses with dispersion micro-managed holey fibers". In: *Opt. Express* 13.20 (2005), p. 8172. ISSN: 1094-4087. DOI: 10.1364/OPEX.13.008172.

[236] F. Lu and W. H. Knox. "Generation, characterization, and application of broadband coherent femtosecond visible pulses in dispersion micromanaged holey fibers". In: *J. Opt. Soc. Am. B* 23.6 (2006), p. 1221. ISSN: 0740-3224. DOI: 10.1364/JOSAB.23.001221.

[237] T. Birks and Y. Li. "The shape of fiber tapers". In: *J. Light. Technol.* 10.4 (Apr. 1992), pp. 432–438. ISSN: 07338724. DOI: 10.1109/50.134196.

[238] J. Love and W. Henry. "Quantifying loss minimisation in single-mode fibre tapers". In: *Electron. Lett.* 22.17 (1986), p. 912. ISSN: 00135194. DOI: 10.1049/el:19860622.

[239] J. Love, W. Henry, W. Stewart, R. Black, S. Lacroix, and F. Gonthier. "Tapered single-mode fibres and devices. Part 1: Adiabaticity criteria". In: *IEE Proc. J Optoelectron.* 138.5 (1991), p. 343. ISSN: 02673932. DOI: 10.1049/ip-j.1991.0060.

[240] G. Brambilla, F. Xu, P. Horak, Y. Jung, F. Koizumi, N. P. Sessions, E. Koukharenko, X. Feng, G. S. Murugan, J. S. Wilkinson, and D. J. Richardson. "Optical fiber nanowires and microwires: fabrication and applications". In: *Adv. Opt. Photonics* 1.1 (Jan. 2009), p. 107. ISSN: 1943-8206. DOI: 10.1364/AOP.1.000107.

[241] *[Online, accessed 19-November-2014].* http://www.nktphotonics.com/files/files/NL-30-850.pdf.